Zhengru Ren

Advanced Control Algorithms to Support Automated Offshore Wind Turbine Installation

Zhengru Ren

Doctoral Thesis

NTNU
Norwegian University of
Science and Technology
Faculty of Engineering Science and Technology
Department of Marine Technology

◉ NTNU
Norwegian University of
Science and Technology

◉ NTNU

◉ NTNU
Norwegian University of
Science and Technology

Zhengru Ren

Advanced Control Algorithms to Support Automated Offshore Wind Turbine Installation

Thesis for the degree of Philosophiae Doctor

Trondheim, August 2019

Norwegian University of Science and Technology
Faculty of Engineering Science and Technology
Department of MarineTechnology

NTNU
Norwegian University of
Science and Technology

Abstract

The thesis presents the research on automated offshore wind turbine (OWT) installation. The aim of the project is to find innovative and cost-effective methods for installing and maintaining OWTs.

Utilization of wind energy grows quickly in the past two decades. The trend of increasing turbine size reduces the costs of installation and grid connection per unit energy produced. However, the growing installation height challenges the OWT installation. The target of the present thesis is to develop novel algorithms of real-time state estimation and control of the installation of bottom-fixed and floating OWTs (including individual components like blades or pre-assembled subsystems), by state-of-the-art automatic control theories, aiming for improved efficiency, increased operation safety, and reduced installation cost.

In the present thesis, two installation strategies are studied, i.e., single blade installation to a bottom-fixed OWT with a monopile foundation using a jackup vessel and tower-nacelle-rotor preassembly installation to a spar foundation using a catamaran. Depending on the level of onshore preassembly, they are two opposite extremes among all installation strategies. The former strategy has a wider application with the lowest operational efficiency, while the latter has the fewest offshore lifts but requires more specific equipment. The major emphasis is on automated single blade installation. Since blade is the component with the most complex aerodynamics characteristics and its installation is the most time-consuming and expensive, the research can be extended to other components can be easily solved. Furthermore, part of the effort is put on improving the performance of the novel wind turbine installation concept using a catamaran proposed by SFI MOVE.

A user-friendly numerical modeling framework for the offshore installation is developed for control design purposes. Various OWT installation models

have been investigated. Several controllers and estimators have been developed. Time-domain simulations and sensitivity studies have been conducted to verify the performance of the proposed algorithms.

Preface

This thesis is submitted in partial fulfilment of the requirements for the degree of Philosophiae doctor (PhD) at the Norwegian University of Science and Technology (NTNU). I have done this work at the Department at Marine Technology, NTNU. My main supervisor and co-supervisor have been Professor Roger Skjetne and Professor Zhen Gao from NTNU, respectively.

Acknowledgment

It is fate to make me come to NTNU and meet all people.

First and foremost, I would like to wholeheartedly express my deepest appreciation to three persons who significantly contribute to my PhD study and research. They are Professor Roger Skjetne, Professor Zhen Gao, and Associate Professor Zhiyu Jiang.

As my main supervisor and career mentor, Professor Roger Skjetne not only imparts professional advises but also impresses me with his strict attitudes to research. I appreciate for the open and friendly working environment that he provides to me, his knowledge, and all his patient and timely replies. It has been my honor and pleasure working with Roger in my master and PhD study. His guidance helped me in all the time of research and writing of this thesis.

I am deeply thankful to Professor Zhen Gao, my co-supervisor. His high efficiency and knowledge promote the workflow and improve the quality of my research. Without his guidance and constant feedback, this PhD would not have been achievable.

I am grateful to Associate Professor Zhiyu Jiang, who provides professional guidance and helps me overcome all the confusion and anxiety in the beginning of my PhD study. Full enjoyment of research was gained when I started cooperating with Zhiyu.

I wish to thank Associate Professor Karl Henning Halse and Professor Hans Petter Hildre who offered me a great and unforgettable experience in NTNU Ålesund campus from April to June, 2019.

I would also thank all my coauthors whom I had the pleasures to cooperate with. I would especially like to thank Associate Professor Bo Zhao, Associate Professor Wei Shi, Jiafeng Xu, and Amrit Shankar Verma. My

thanks also go out to my office mates, Svenn Are Værnø, Jon Bjørnø, and Hans-Martin Heyn for their friendliness and tolerant attitudes.

Nobody has been more important to me in the pursuit of this project than my family members. I would like to thank my parents, Xudong Ren and Lihong Wang, who love and support me to pursue lifelong meaning and happiness in the process of growing up. A special thank you to Ying Lu, my wonderful girlfriend, for her companion and for always being so supportive of my work.

Contents

List of Tables

List of Figures

Part I

Background and summary

Chapter 1

Introduction

1.1 Background and motivation

Utilization of wind energy grows quickly in the past two decades. A trend of steadily increasing wind energy's share of the worldwide electricity supply is noticed. Compared with onshore wind energy, offshore wind is stronger and more steady, resulting in higher and steadier energy production. In addition, OWTs do not occupy limited land areas and damage untouched nature. As most energy is consumed in developed cities, another advantage of OWT is the short distance between the wind farms and these cities. Furthermore, new industries and more jobs are created by this new business area.

In 2017, wind energy has the largest installed capacity and remains the second largest form of power generation capacity in Europe; see Figure 1.1. The percentage of offshore wind energy increase year by year; see Figure 1.2.
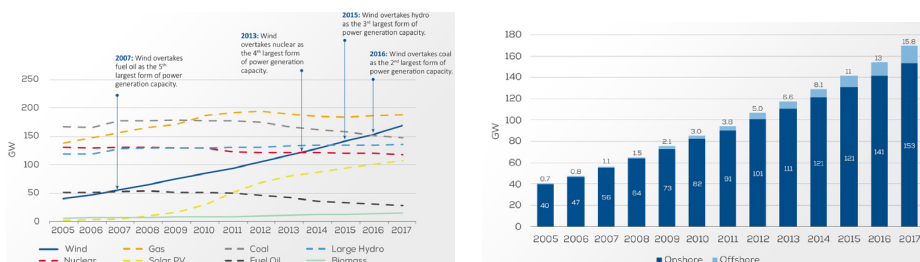
Figure 1.1: (Left) the growth of total power production in Europe 2005–2017, (right) cumulative installed onshore and offshore wind energy. Source: Wind Europe (2018).

Wind energy occupies more than half of the new installed capacity in 2017. In a long-term perspective, the amount of installed wind power capacity until 2050 will meets 50% of EU's electricity demand, of which 60% would be offshore wind (Wind Europe 2017). Thus, the offshore wind industry is promising.
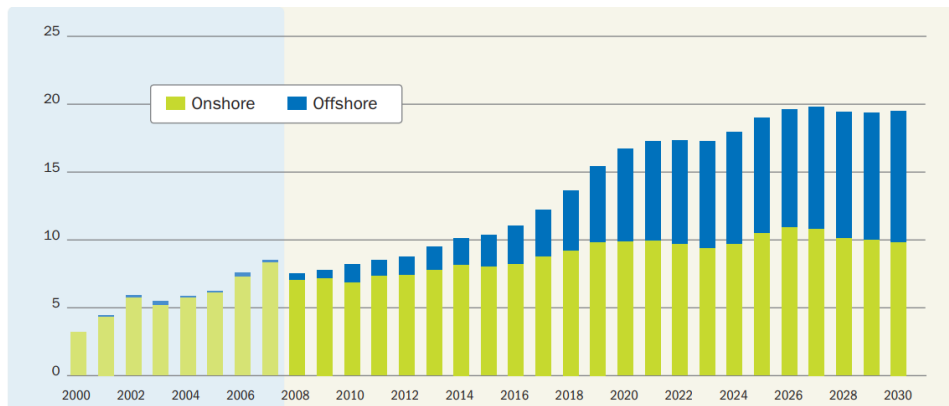
Figure 1.2: Wind energy annual installation 2000-2030 (in GW), source: Zervos & Kjaer (n.d.).

The price of electricity from offshore wind was typically two to three times greater than electricity from onshore wind in 2017 (Stehly et al. 2017). The first reason is the cost on design and construction of foundations. Moreover, OWT installation, including lifting and mating operations, is expensive (Kaiser & Snyder 2013). For an offshore wind farm project, capital expenditures (CapEx) and operational expenditures (OpEx) are the two main categories of the expenses. The assembly and installation cost is the third largest element in CapEx, accounting for 19% for bottom-fixed OWT and 11.3% for floating OWT. Because of the limitations of lifting and monitoring equipment, spending time waiting for the required weather window, by the offshore construction vessel, is not uncommon. However, the research on OWT installation is still not well addressed.

Shown in Figure 1.3(a), the wind turbine installation time is greatly reduced in the past two decades. This is not only because of the growing rated power capacity per unit turbine, but also technical advance and increasing gained project experience. The trend of reduction in installation time is more remarkable for larger OWTs. However, it is noticed that the reduction of turbine installation time per MW (55%) is much smaller than that of the foundation installation time per MW (87%). Comparing with

the foundation installation, there is still a lot of room for improvement of
OWT superstructure installation, including tower, nacelle, and rotor.

(a)

(b)

(c)
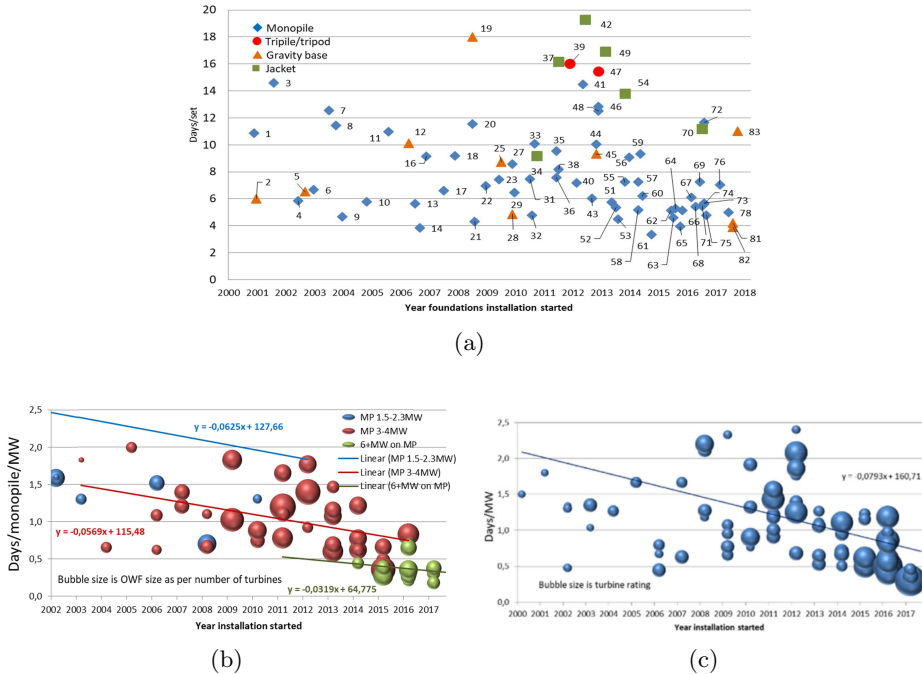
Figure 1.3: (a) Wind farm installation days per megawatt of installed capacity,
(b) monopile installation days per MW, (c) turbine-only installation days per MW.
Source: Lacal-Arántegui et al. (2018).

OWTs are categorized into bottom-fixed and floating wind turbines depend-
ing the foundation structures, e.g., monopile, gravity base, jacket as bottom-
fixed foundations and single point anchor reservoir (spar), semi-submersible,
tension leg platform as floating ones; see Figure 1.4.

The OWT installation can be conducted by either jack-up or floating instal-
lation vessels depending on the water depth for operation. At the moment,
jack-up works up to 40-50m of water depth. Floating installation vessel
should be used for deeper water depth. The challenges for floating installa-
tion vessel is the wave induced motions which cause pendular oscillation to
the payload through crane fixed on the vessel.

For a mainstreamed horizontal-axis three-blade wind turbine, the total num-
ber of the blades for each wind turbine is three. There exist several instal-
lation strategies depending on the level of onshore preassembly; see Fig-

(a) Bottom-fixed OWT   (b) Floating OWT
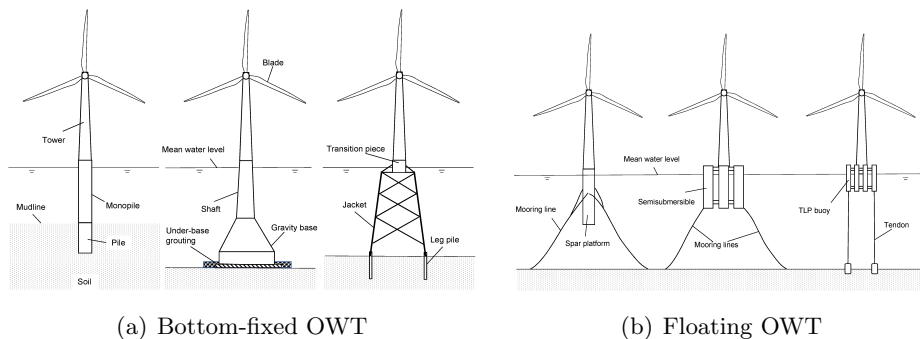
Figure 1.4: Various OWT foundations, source: Jiang et al. (2017).

ure 1.5. For example, (i) the blades can be installed to the hub separately, namely single blade installation; (ii) two blades can be preassembled on the hub with a bunny-ear configuration; (iii) all blades are assembled on the hub and the rotor is installed as a whole; (iv) all wind turbine components are preassembled and installed with one lift. The selection of the installation methods is a tradeoff among many aspects. The increasing number of offshore operations demands longer operation window, resulting in stricter requirement for the weather and onboard equipment. Hence, onshore preassembly shortens the expensive offshore operations. Typically, the most efficient solution is a fully preassembled structure with tower, nacelle, hub, and blades as a whole. However, such installation strategy faces two main challenges.

First of all, wind turbines are becoming bigger. The capability of wind turbines has more than doubled since 2001, while the number of wind turbines is 20% less (Energinet 2018). The trend of increasing turbine size reduces the costs of installation and grid connection per unit energy produced; see Figure 1.6. The records of OWT sizes have been broken again and again. The height of the current GE's Haliade-X 12 MW OWT reaches 260 meters, and the diameter of the rotor is 220 meters. The growing installation height and weight challenge the crane devices and lifting operation for most of the installation vessels. In addition, the communication between the crane operator and personnel in the hub is weakened.

Secondly, the deck utilization ratio reduces with the increasing level of preassembly. In other words, more turbine components can be carried from onshore to offshore installation site if components are not pre-assembled, resulting in shorter overall transport time; see Figure 1.5(a). However, the

(a) Pieces separately

(b) Bunny-ear configuration

(c) Pre-assembled rotor

(d) Pre-assembled turbine

Figure 1.5: Various OWT installation strategies.
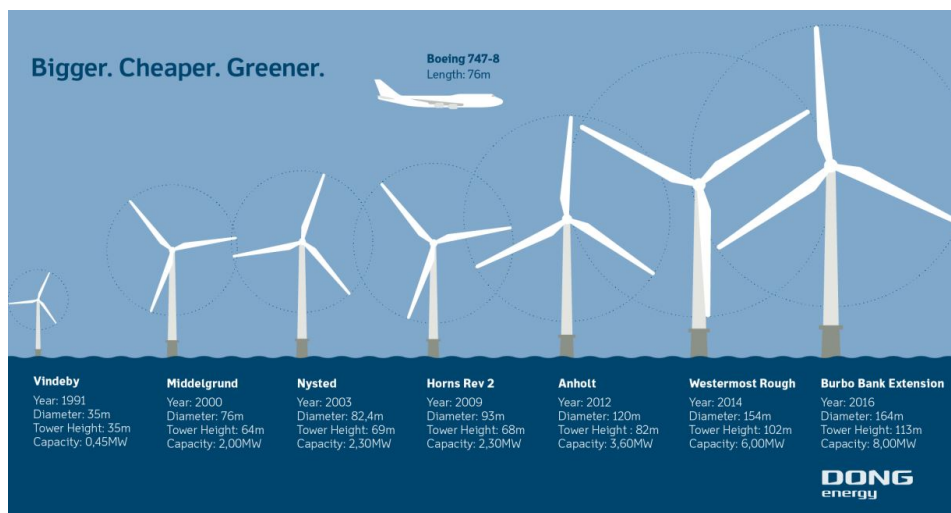
Figure 1.6: The trend of continued increasing in turbine size, source: Froese (2016).

offshore operation time is longer due to the increasing number of lifts and mating operations. Therefore, the level of preassembly is a tradeoff among deck usage, vessel selection, crane equipment, weather, etc.

At the current stage, the OWT installation heavily depends on the crew's experience and real-time weather. For example, the project is managed trough manual communication between the crane operator and the crew at the nacelle for connection. Straining by the crew is necessary in the final aligning and bolting process. Installation can only be conducted in calm seas. Therefore, automated installation procedures will help to increase the efficiency and to reduce the risk to the operators.

1.2   Problem description and objectives

The present work is a part of the Project 5 "OW: Installation of Offshore Wind Power Systems" in Center for Research-based Innovation on Marine Operations in Virtual Environment (SFI MOVE). The eight-year project started in 2016 and is funded by the Research Council of Norway. The aim of the project is to find innovative and cost-effective methods for installing and maintaining OWTs.

The target of the present thesis is to develop novel algorithms of real-time state estimation and control of the installation of bottom-fixed and float-

ing OWTs (including individual components like blades or pre-assembled subsystems), by state-of-the-art automatic control theories, aiming for improved efficiency, increased operation safety, and reduced installation cost. Two installation strategies are studied, i.e., single blade installation to a bottom-fixed OWT with a monopile foundation using a jackup vessel and tower-nacelle-rotor preassembly installation to a spar foundation using a catamaran. The major emphasis is on automated single blade installation. Since blade is the most complex structures among all components and its installation is the most time-consuming and expensive, the research on other components can be easily solved. Furthermore, part of the effort is put on improving the performance of the novel wind turbine installation concept using a catamaran proposed by SFI MOVE.

The research will focus on the following problems:

- Single blade installation to a bottom-fixed OWT with a monopile foundation using a jackup vessel:

  - Understand the challenges and dynamics during wind turbine installation.
  - Propose simplified state-space models for the operations.
  - Develop a high-fidelity simulation-verification model of the process.
  - Design automated control schemes for the blade installation, including the control laws and observers.
  - Real-time motion estimation based on GPS and IMU measurements.
  - Verify the controllers and observers through classic Lyapunov method, simulations, and sensitivity study.
  - Investigate the operational criteria during the mating operation.

- Tower-nacelle-rotor preassembly installation to a spar foundation using a catamaran installation vessel:

  - Develop control algorithm for the active roll reduction system.
  - Develop control algorithm for the hydraulic system lifting grippers.

The research methodologies in the thesis are theoretical calculation and numerical simulation. A numerical MATLAB/Simulink toolbox is developed

to simulate the OWT installation process for control design purpose, including the dynamics of different parts in the installation system, turbulent wind field, aerodynamic loads, and wave conditions. Code-to-code verification has been conducted to design controllers. Lyapunov's direct method and stability proves are applied in the control designs. Sensor fusion techniques are adopted to design state estimators.

From an overall perspective, the present thesis investigates novel automated wind turbine installation, which can accelerate the overall installation efficiency and broaden the application of wind energy.

1.3   List of publication and contributions

The thesis is based on a collection of several papers. The list and the main contributions of the work of the papers is given below.

Single blade installation to a bottom-fixed OWT with a monopile foundation using a jackup vessel

[**Paper A1**] Zhengru Ren, Zhiyu Jiang, Roger Skjetne, and Zhen Gao (2018). Development and application of a simulator for OWT blades installation. Ocean Engineering, 166:380–395.

Contribution: In this paper, the development of a modularized blade installation simulation toolbox for the purpose of control design in MATLAB/Simulink is presented. The toolbox can be used to simulate several blade installation configurations for both onshore and OWT installation. The key features and equations of the different modules, exemplified by a single blade installation operation. Code-to-code verification results are presented and discussed with both quasi-steady wind and three-dimensional turbulent wind field.

[**Paper A2**] Zhengru Ren, Roger Skjetne, and Zhen Gao (2019). A crane overload protection controller for blade lifting operation based on model predictive control. Energies, 12(1):50.

Contribution: In this paper, nonlinear model predictive control (NMPC) schemes are proposed to overcome the sudden peak tension and snap loads in the lifting wires caused by lifting speed changes in a lumped-mass payload lifting and a wind turbine blade lifting operation, respectively. A simplified three-dimensional crane-wire-payload model is adopted to design the optimal control algorithm. The direct multiple shooting approach is applied to

solve the nonlinear programming problem. High-fidelity simulations of the lifting operations are implemented based on a turbulent wind field with the MarIn and CaSADi toolkit in MATLAB. By well-tuned weighting matrices, the NMPC controller is capable of preventing snap loads and axial peak tension, while ensuring efficient lifting operation.

[**Paper A3**] Zhengru Ren, Zhiyu Jiang, Roger Skjetne, and Zhen Gao (2018). An active tugger line force control method for single blade installations. Wind Energy, 21:1344–1358.

Contribution: In this paper, an active control scheme is proposed to control the tugger line forces acting on a blade during the final installation stage before mating. A simplified 3 degree-of-freedom blade installation model is developed for the control design. An extended Kalman filter is used to estimate the blade motions and wind velocities. Feedback linearization and pole placement techniques are applied for the design of the controller. Simulations under turbulent wind conditions are conducted to verify the active control scheme, which effectively reduces the blade root motions in the wind direction.

[**Paper A4**] Zhengru Ren, Roger Skjetne, Zhiyu Jiang, Zhen Gao, and Amrit Shankar Verma (2019). Integrated GNSS/IMU hub motion estimator for offshore wind turbine blade installation. Mechanical Systems and Signal Processing, 123:222–243.

Contribution: In this paper, a hub motion estimation algorithm for the OWT with a bottom-fixed foundation using sensor fusion of a global navigation satellite system (GNSS) and an inertial measurement unit (IMU) is designed. Two schemes are proposed based on a moving horizon estimator, a multirate Kalman filter, an online smoother, and a predictor. The moving horizon estimator mitigates the slow GNSS sampling rate relative to the hub dynamics. The multirate Kalman filter estimates the position, velocity, and accelerometer bias with a constant GNSS measurement delay. The online smoothing algorithm filters the delayed estimated trajectory to remove sudden step changes. The predictor compensates the delayed estimate, resulting in real-time monitoring.

Tower-nacelle-rotor preassembly installation to a spar foundation using a catamaran vessel

[**Paper A5**] Jiafeng Xu, Zhengru Ren, Yue Li, Roger Skjetne, and Karl Henning Halse (2018). Dynamic simulation and control of an active roll reduction system using free-flooding tanks with vacuum pumps. Journal of Offshore Mechanics and Arctic Engineering, 140:061302.

Contribution: This paper demonstrates a dynamic simulation scheme of an active roll reduction system using free-flooding tanks controlled by vacuum pumps. Vacuum pumps and air valve stabilized the waveinduced roll motion by controlling the water levels in the tanks through a feedback controller. A simplified control plant model for the vacuum pumps is proposed where higher order behaviors are neglected and the external wave-induced load is unknown. A parameter-dependent observer and a backstepping controller are adopted to estimate the external load and to reduce the roll motion. The system stability is proved by Lyapunovs direct method. The performance of the entire system is evaluated in terms of roll reduction capability and power cost.

[**Paper A6**] Zhiyu Jiang, Zhengru Ren, Zhen Gao, Karl Henning Halse, and Peter Christian Sandvik (2018). Mating control of a wind turbine tower-nacelle-rotor assembly for a catamaran installation vessel. Proceedings of the 2018 International Ocean and Polar Engineering Conference, 584–593.

Contribution: In this paper, the mating control of a wind turbine tower-nacelle-rotor assembly for a catamaran installation vessel using an active heave compensator is studied. The installation of a rotor-tower-assembly onto a spar foundation is considered with a focus on the mating process of a tower-nacelle-rotor assembly. The spar foundation has been pre-installed at a representative site in the North Sea, and the catamaran has thrusters regulated by a dynamic positioning system. The active heave compensator can effectively reduce the relative heave velocity and the risks of structural damage during the mating process.

Other works

The following first-authored papers are not closely relevant to the thesis topic. Therefore, they are excluded from the present thesis. Additionally, the co-authored papers are also not included.

[**Paper B1**] Zhengru Ren, Roger Skjetne, and Øivind Kåre Kjerstad (2015). A tension-based position estimation approach for moored marine vessels. IFAC-PapersOnLine, 48(16):248–253.

[**Paper B2**] Zhengru Ren, Roger Skjetne, and Vahid Hassani (2015). Supervisory control of line breakage for thruster-assisted position mooring system. IFAC-PapersOnLine, 48(16):235–240.

[**Paper B3**] Zhengru Ren and Roger Skjetne (2016). An on-site current profile estimation algorithm for a moored floating structure. IFAC-PapersOnLine, 49(23):153–158.

[**Paper B4**] Zhengru Ren and Roger Skjetne (2016). A tension-based position estimation solution of a moored structure and its uncertain anchor positions. IFAC-PapersOnLine, 49(23):251–257.

[**Paper B5**] Zhengru Ren, Roger Skjetne, and Zhen Gao (2017). Modeling and control of crane overload protection during marine lifting operation based on model predictive control. ASME 2017 36th International Conference on Ocean, Offshore and Arctic Engineering, paper No. OMAE2017–62003.

[**Paper B6**] Zhengru Ren, Zhiyu Jiang, Roger Skjetne, and Zhen Gao (2018). Single blade installation using active control of three tugger lines. The 28th International Ocean and Polar Engineering Conference, pages 594–601.

[**Paper B7**] Zhengru Ren, Roger Skjetne, Zhiyu Jiang, and Zhen Gao (2018). Active single blade installation using tugger line tension control and optimal control allocation. International Journal of Offshore and Polar Engineering. Revision submitted.

[**Paper B8**] Zhiyu Jiang, Weifei Hu, Wenbin Dong, Zhen Gao, and Zhengru Ren (2017). Structural reliability analysis of wind turbines: a review. Energies, 10:2099.

[**Paper B9**] Zhiyu Jiang, Zhen Gao, Zhengru Ren, Ye Li, and Lei Duan (2018). A parametric study on the blade mating process formonopile wind turbine installations under rough environmental conditions. Engineering Structures, 172:1042–1056.

[**Paper B10**] Amrit Shankar Verma, Zhiyu Jiang, Nils Petter Vedvikc, Zhen Gao, and Zhengru Ren (2019). Impact assessment of blade root with a hub during the mating process of an offshore monopile-type wind turbine.

Engineering Structures, 180, 205–222.

[**Paper B11**] Amrit Shankar Verma, Zhiyu Jiang, Zhengru Ren, Zhen Gao, and Nils Petter Vedvik (2019). Response-based assessment of operational limits for mating blades on monopile-type offshore wind turbines. Energies, 12(10):1867.

[**Paper B12**] Amrit Shankar Verma, Zhiyu Jiang, Zhengru Ren, Zhen Gao, and Nils Petter Vedvikc (2019). Effects of wind-wave misalignment on a wind turbine blade mating process: impact velocities, blade root damages and structural safety assessment. Journal of Marine Science and Application. Revision submitted.

[**Paper B13**] Amrit Shankar Verma, Zhen Gao, Zhiyu Jiang, Zhengru Ren, and Nils Petter Vedvikc (2019). Structural safety assessment of marine operations from a long-term perspective a case study of offshore wind turbine blade installation. ASME 2017 36th International Conference on Ocean, Offshore and Arctic Engineering. American Society of Mechanical Engineers.

[**Paper B14**] Zhen Gao, Amrit Shankar Verma, Yuna Zhao, Zhiyu Jiang, and Zhengru Ren (2018). Probabilistic assessment of structural responses during installation of offshore wind turbine blades. ASME 2018 37th International Conference on Ocean, Offshore and Arctic Engineering, page V11AT12A044.

[**Paper B15**] Jingzhe Jin, Vatne Sigrid Ringdalen, Zhiyu Jiang, Zhengru Ren, Yuna Zhao, and Zhen Gao (2018). Installation of pre-assembled offshore wind turbines using a catamaran vessel and an active gripper motion control method. Grand Renewable Energy proceedings, Japan Council for Renewable Energy.

1.4   Thesis organization and overview

The thesis is written in the form of a collection of articles. Figure 1.7 shows how these papers interconnect in the scope of the present thesis. In the first part of the present thesis, the research background, research motivation, system modeling, control objectives, simulation results, and discussion are illustrated. The specific part of every paper is placed in the particular chapters.

The research is categorized into two main topics:

- The first topic is the single blade installation to a bottom-fixed OWT

using a jackup vessel. The research starts from the modeling processes, i.e., the model for control design in MATLAB/Simulink (Paper A1). According to the analysis results, control algorithms and state estimators are developed to improve the levels of automation (paper A2–A5). The algorithms are verified by numerical simulations and sensitivity studies.

- The second topic is the concept of floating OWT preassembly installation using a catamaran. The research procedures of the second topic are similar to those in the first topic. The roll-reduction system (Paper A6) and active heave compensator (Paper A7) are decoupled. A modeling and control design is proposed.
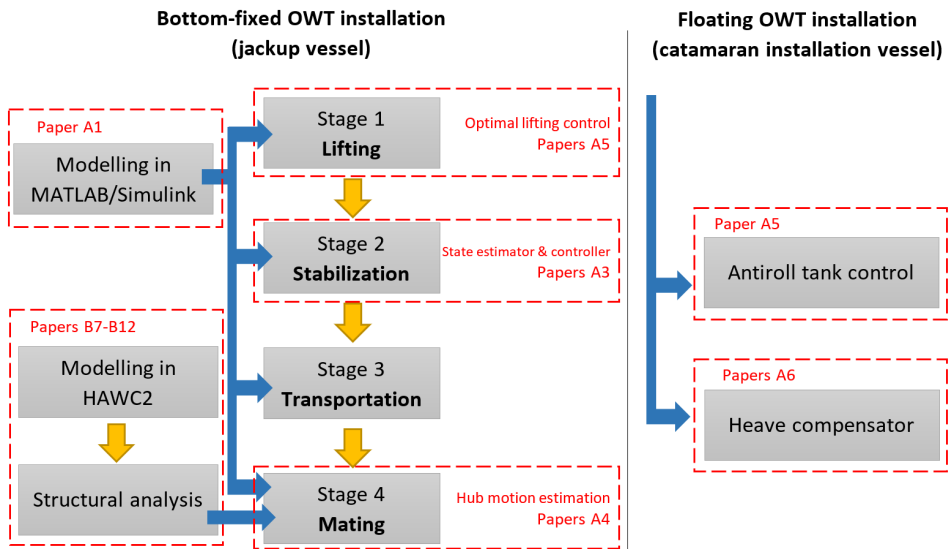
Figure 1.7: Interconnection of the papers in the thesis.

The summary part of this thesis consist of the following chapters:

Chapter 2 presents an overview of the wind turbine installation practices and illustrates the motivation of the research. The system configuration of both single blade installation system and catamaran installation concept are introduced. The operational criteria are discussed. The problem of single blade installation is categorized into four stages, including lifting, stabilizing, transporting, and mating. The actuators, sensors, and control objectives for each stage are presented. Moreover, the problem statement

of roll reduction tanks and active heave compensation for the catamaran vessel are shown.

Chapter 3 addresses the modeling of both systems. A comparison of state-of-art simulation tools is given. The single blade installation is firstly modeled in HAWC2. A simulation toolbox is proposed to provide high-fidelity simulation verification model for the purpose of control design. An overview of the proposed modeling toolbox is presented. The simplified control design models for single blade installation system, roll reduction system, and active heave compensator are then given.

Chapter 4 presents the simulation results to verify the proposed controllers and estimators. Aerodynamic loads of the proposed toolbox in steady wind are verified through code-to-code verification results. Both time-domain simulation and sensitivity studies are conducted to test the optimal lifting scheme using model predictive control, automatic single blade installation using active tugger line force control, hub motion estimator, roll-reduction tank control, and active heave compensator.

Chapter 5 summarizes the main contributions from this study, presents the major contributions, and discusses future research directions.

The second part contains the published conference and journal papers, that are included in the thesis.

Chapter 2

System description and problem statement

2.1 Problem 1: Single blade installation using automatic control

2.1.1 System description

A monopile-type wind turbine is selected as the example of the research. Monopile installation has been studied in Li et al. (2014), Li, Acero, Gao & Moan (2016), Li, Gao & Moan (2016). Consider a scenario that the monopile foundation has been driven into the seabed, gravel and rock materials are placed on the seabed at the foundation location to protect the supporting structure against scouring. Transition piece, tower, nacelle, hub, and blades are installed subsequently in several lifting operations. In the present stage, the installation vessels are commonly used jackup vessels; see Figure 2.1.

Single blade installation is a method of OWT blade installation, that allows for a broader range of installation vessels and lower crane capabilities. Specialized commercial products are developed to reduce the blade motion and to expand the operational limits, resulting in successful installations under higher wind speeds, such as LT575 Blade Dragon (Liftra 2018) and the Boom Lock technology (HighWind 2018).

The typical single blade installation procedure is shown in Figure 2.2. If the weather forecast satisfies the predefined conditions, the operation starts by rotating the hub to a horizontal position for wind turbines with a conven-

(a) Sideview (Espinoza 2016)

(b) Upward view (RWE Innogy GmbH 2014)
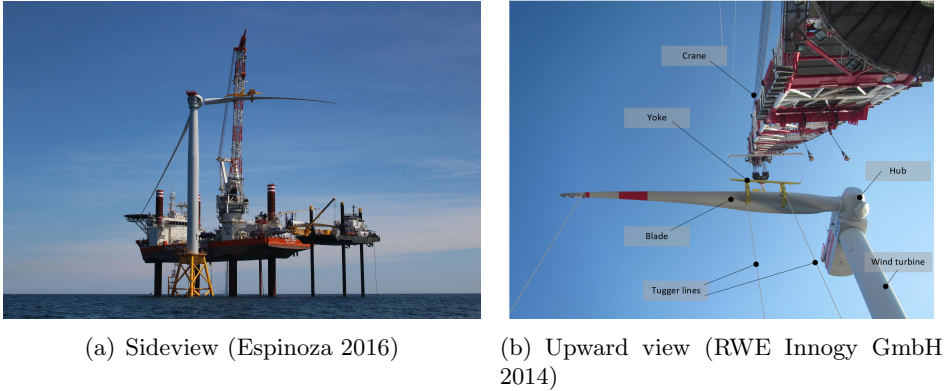
Figure 2.1: Single blade installation.

tional gear transmission. The blade is seized by a yoke at its center of mass and lifted to the hub height by the crane winch servo motor through the lift wire from the deck. The relative motions between the blade root and hub are closely monitored. If the motions are within the allowable predefined limits, then the mating process is executed. Tugger lines are used to constrain the blade motions. Typically, the tugger lines are passive without control. After the guide pins on the blade root enters the flange holes on the hub, the blade is bolted by the crew and the lifting gear is retracted. Then, the mating process is finished. If the conditions are not acceptable, the blade is lowered to the deck and the aforementioned steps are repeated when the weather is within allowable limits. In total, three lifts are involved for the three blades if the single blade installation technique is applied.

2.1.2   System configuration

The objective is to apply feedback control to the single blade installation to enhance the level of automation, operational efficiency, and safety. Before designing control algorithms, the installation process with the involvement of automatic control should be thoroughly understood. The entire single blade installation is categorized into four stages based on the various control objectives, i.e., (1) lifting the blade to the specified hub height, (2) stabilizing the blade in a turbulent wind field, (3) transporting the blade to the hub, and (4) mating the blade root to the hub; see Figure 2.3.

To simplify the problem, some states are neglected, resulting in different system configurations in specific stages, including the actuators and sensors, as summarized in Table 2.1.
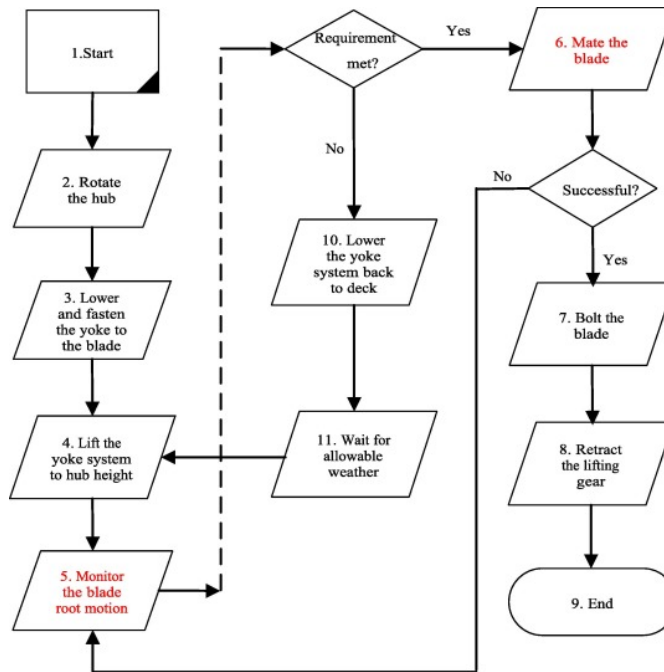
Figure 2.2: Flowcharts of the typical single blade installation (Jiang, Gao, Ren, Li & Duan 2018).

2.1.3   Operational criteria

The entire single blade installation procedure is divided into two problems, i.e., the lifting problem (Stage 1) and the mating problem (stages 2–4).

Stage 1: Lifting problem

The lifting operations are conducted according to pragmatic experiences and short-term weather forecast. In Stage 1, the vertical position of the blade and the axial tension on the lift wire are two important responses for the operation safety. A case study of the danger of lifting operation is shown in Figure 2.4. Sudden lowering and lifting-off operations are conducted to a suspended NREL 5MW reference wind turbine blade with constant speeds.

The large peak wire rope tension in the initial stages of the lifting and lowering of a payload is risky for safety hazards. The larger sudden tension occurs at the beginning of the lifting operation due to significant winch speed acceleration. Jerking occurs more easily at a higher lifting speed.
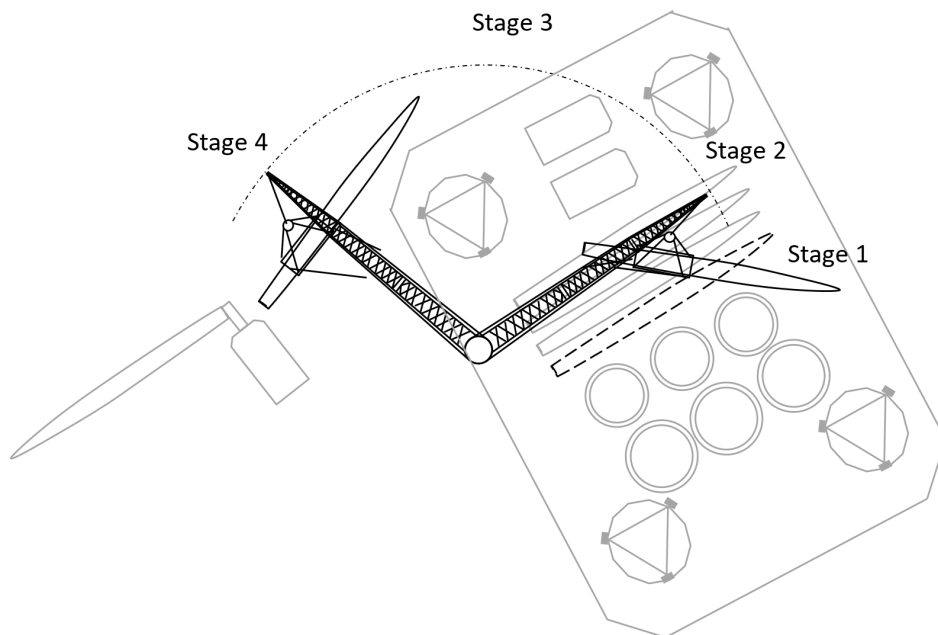
Figure 2.3: Diagram of the four stages during the single blade installation.

Snap loads, which occur when the axial tension decreases below zero, may cause the maximum tension exceed the lift wire strength. Furthermore, the magnitude of the blade motion is enlarged when snap loads occur, resulting in a potential impact damage between the blade and deck. Thus, optimal lifting control is desired to reduce the dynamic tension on the lift wire during the lifting-off and lowering operations.

Stages 2–4: Mating problem

In stages 2–4, the horizontal position and orientation of the suspended blade are critical. Specially, the mating operation in Stage 4 is determined by the relative motion between the blade root and hub. The influence is two-fold, i.e., the relative displacement and relative velocity. A successful mating operation can be executed if both the relative displacement and velocity satisfy the predetermined criteria. Additionally, the orientation of the blade root should be constrained to ensure the blade root face to the hub mating flange.

The relative displacement affects the success rate (Jiang, Gao, Ren, Li & Duan 2018). If the outcrossing rate is below the safe boundary, the mating

Table 2.1: Actuators and sensors in different stages of single blade installation.

Stage	Actuators	Sensors
1	Crane servo motor	Blade COG motion Lift wire length and changing rate
2	Tugger line force	Position and orientation of the blade Position of the crane tip
3	Tugger line force Crane boom rotation	Position and orientation of the blade Position of the crane tip
4	Tugger line force	Position and orientation of the blade Position of the crane tip Position and acceleration of the hub

operation is considered to a successful alignment; see Figure 2.5. The relative velocity influences the impact velocity, which may damage the guide pin (Verma et al. 2018, Verma, Vedvik, Haselbach, Gao & Jiang 2019). There are two sorts of impact damages, i.e., the sideways impact and head-on impact; see Figure 2.6. The potential consequence of sideways impact is bending the guide pin. With very large head-on impact speed, the guide pin can deform to an S-shape. Then, the blade should be lowered to the deck and repaired before the next mating attempt. Such failures reduce the overall operation efficiency. According to the finite element analysis results using Abaqus/explicit, the extreme values for the relative motion in specific axis over a period can be determined.

For a monopile wind turbine, the relative motion between the blade root and hub is mainly influenced by the wind and waves. Both the mean wind speed and turbulence intensity affect the motion of the suspended blade. The hub motion is influenced mainly by the wave-induced loads and partly by the wind field.

The number of the installed blades influences the hub motion. There are three mating conditions (MCs) for Stage 4, as illustrated in Figure 2.7.

- MC1: The nacelle and hub have been assembled on the tower. The wind turbine yaw system rotates the nacelle to the mating direction, and the rotor is rotated to an orientation such that the selected flange face on the hub opposes the suspended blade root horizontally.

- MC2: After successfully bolting the first blade, the rotor rotates 120
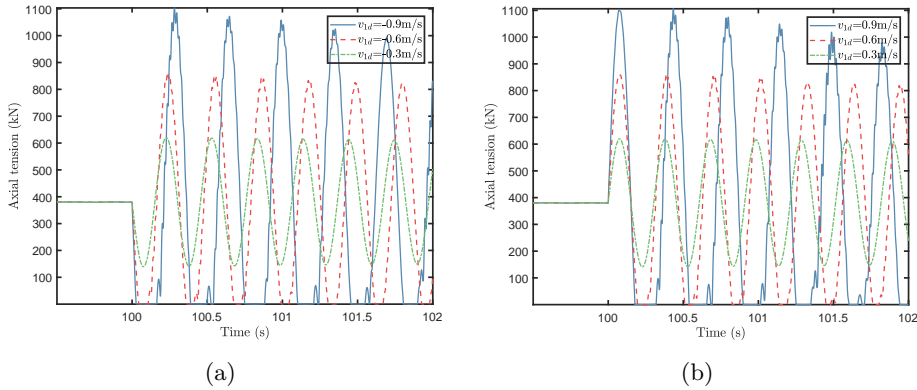
Figure 2.4: The lift wire tension history of a suspended blade with constant (a) lowering speeds, (b) lifting-off speeds. Source: Ren et al. (2019).

deg to let the second flange face the mating orientation. The second blade is ready to be mated.

- MC3: The rotor is rotated to horizontally align the third hub after bolting the second blade. The third blade is ready for the mating operation.

The influence of the installed blades is small. Taking a 5MW NREL reference wind turbine as example, the first fore-aft natural frequencies in MC1, MC2, and MC3 are 0.258, 0.249, and 0.239 Hz, respectively. The weight of each blade, approximately 17 tonnes, is much lower than the total mass of the structure without blades (1162 tonnes). Therefore, the total stiffness and the first fore-aft eigen-frequency are slightly reduced by the additional blades. Even though the eigenperiod moves towards the wave periods, the blades have a damping effect that increases with the number of installed blade and the blade pitch angle. The amplitude of the hub oscillation is enlarged with higher mean wind speed and the resulting aerodynamic loads. The pendulum motion of the blade has a dominant period of 10-12s.

2.1.4   Control objectives

The control objectives and performance criteria are summarized as follows.

In Stage 1, the crane servo motor is the actuator. The tugger lines are assumed to be released with the lifting operation. Therefore, tugger lines do not provide restoring forces unless wind-induced blade displacement is higher than expected. The blade orientation variance caused by the lifting
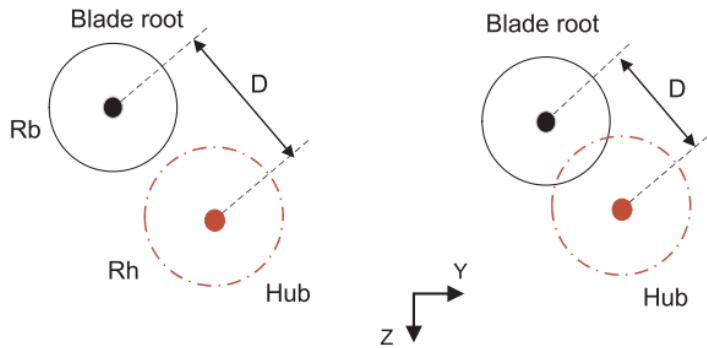
Figure 2.5: Schematic of the blade alignment plan, source: Jiang, Gao, Ren, Li & Duan (2018).

operation and the wind-induced loads are assumed to be insignificant, and the lifting or lowering operation is so short that wind-induced motion is not affected.

In stages 2–4, the blade horizontal motion is significant. Pendular motion is dominated by the wind-induced loads. Active tugger line force control is introduced to stabilize the blade motion and reduce the relative motion between the blade root and hub.

Stage 1: Lifting

- Operational objectives: Control the winch servo motor to lift the blade from deck to the hub height.

- Control objectives:

    1. Reach the desired setpoint lifting speed in the shortest time possible within the constraints;
    2. Protect overload tension and reduce dynamic tension by controlling the winch speed;
    3. Prevent winch servo motor burnout by limiting the winch acceleration;
    4. Prevent negative elongation and snap loads;
    5. Reduce the wire rope wear;
    6. Limit the maximum speed of the servo motor;
    7. Reach the desired wire rope length.
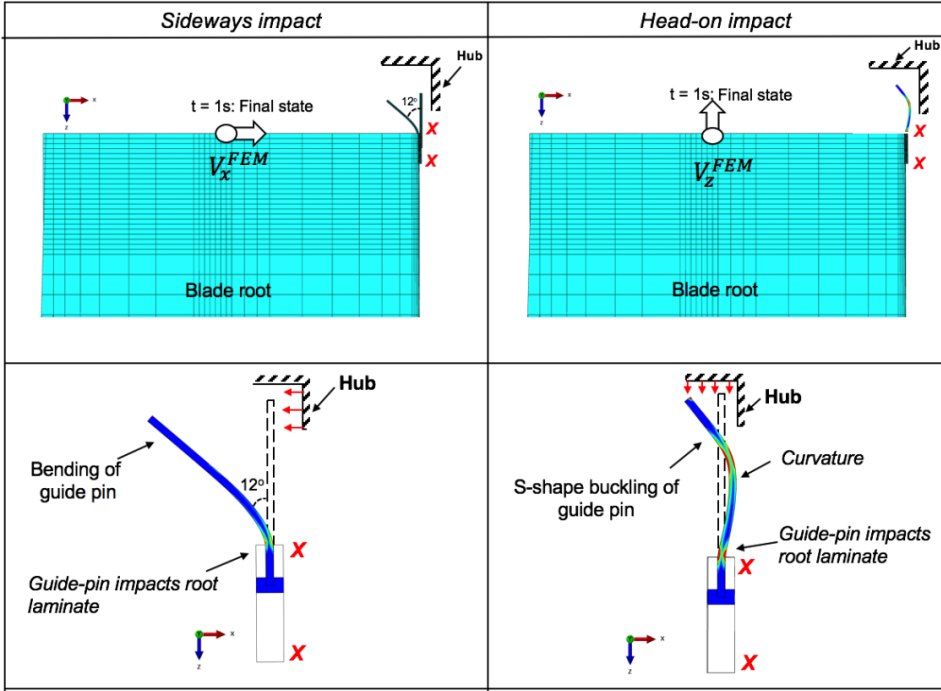
Figure 2.6: Impact damages to the guide pin, source: Verma, Jiang, Ren, Gao & Vedvik (2019).

- Performance criteria: The dynamic tension on the lift wire should be minimized; the lift wire elongation and winch servo motor acceleration and speed should be smaller than the operational limits.

Stage 2–4: Stabilizing

- Operation objectives: Stabilize the suspended blade in the air.

- Control objectives: Control the tension forces on the tugger lines to stabilize the suspended blade in the turbulent wind field.

- Performance criteria: The displacement of the blade COG in the mean wind direction and its orientation.

2.1.5   Hub motion estimation in Stage 4

To calculate the relative motion between the blade root and hub, the proposed controllers require highly accurate real-time estimates of the motion,
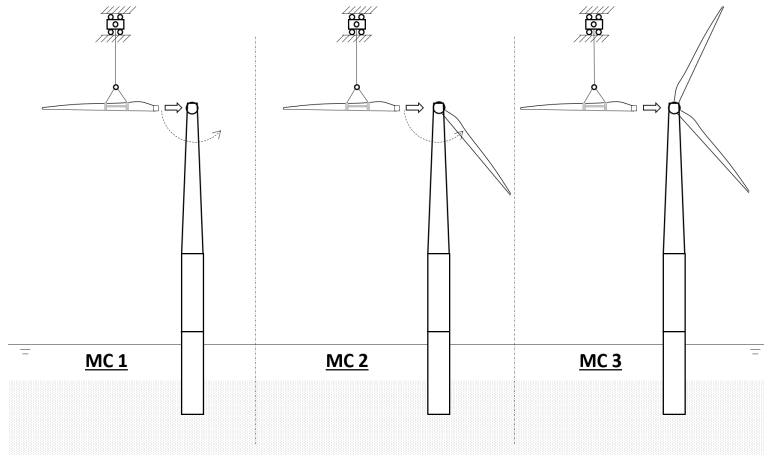
Figure 2.7: Three monopile configurations before single blade installation.

as studied in Maes et al. (2018). Real-time hub motion estimation is also important to achieve successful mating. An illustrating example for a 5MW NREL reference wind turbine hub motion in the water depth 30 m is presented in Figure 2.8.

From the simulation results, it is easy to notice that the vertical motion of the hub is negligible. Hence, only horizontal motion is of importance. GPS is the most commonly used sensor to measure the horizontal displacement. However, some shortages exist. Since the first fore-aft natural period of the structure is approximately 4 s, the GPS delay is significant for real-time estimation. Another issue is the sampling frequency of the GPS. The low sampling frequency, i.e. 1 Hz, is not sufficient to provide smooth and accurate hub displacement in a real-time motion estimator. The oscillation amplitude depends on the wave period and significant wave height. Resonance happens near the first fore-aft natural frequency, ranging from 0–1.5 m. Hence, the sensor noise of a low-cost GPS influences the measurement. An alternative to GPS for position measurement is the double integration of the acceleration measurements from an inertial measurement unit (IMU). However, the existence of sensor bias deteriorates the results. To overcome these shortages, sensor fusion approaches are adopted to provide accurate motion estimation with high sampling frequency. A study should be conducted to handle the GPS noise, GPS time delay, GPS low sampling rate, accelerometer noise, and accelerometer bias.
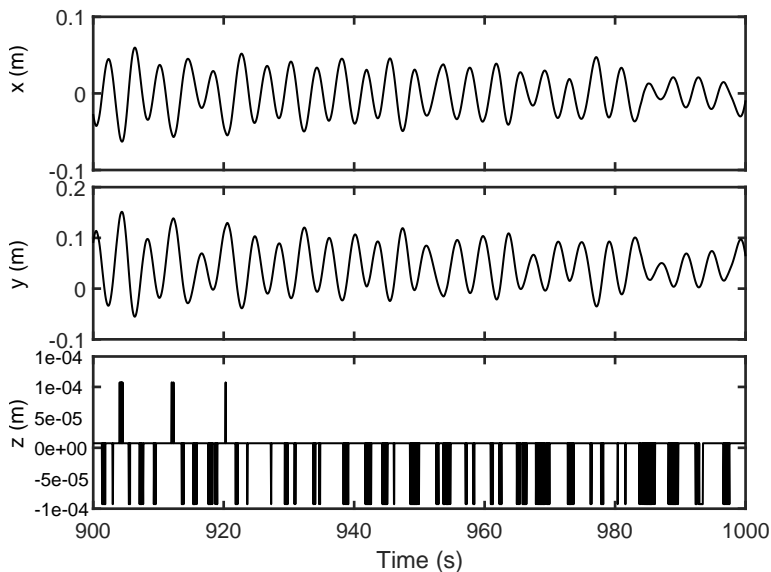
Figure 2.8: The history of the hub position for the proposed OWT with respect to the equilibrium, $H_s = 2$ m, $T_p = 8$ s, $\beta_{wave} = 30°$, $S_{wave} = 75$, $U_w = 8$ m/s, $TI = 0.146$, and $S_{TI} = 94$. Source: Ren, Skjetne, Jiang, Gao & Verma (2018).

2.2   Problem 2: Tower-nacelle-rotor assembly installation using a catamaran

2.2.1   System description

To shorten the offshore operation period, tower-nacelle-rotor assembly installation with only one lift is another possible solution. The tower, nacelle, and rotor have been assembled onshore and carried to the installation site by a catamaran. The installation can be accomplished with only one lift. The installation strategy is suitable for both bottom-fixed foundations and floating foundations. The device to compensate the relative motion between the lifted preassembly and foundation is still an open question. In the current stage, an innovative conceptual design proposed by SFI MOVE is studied in Jiang, Li, Gao, Halse & Sandvik (2018); see Figure 2.9.

A flowchart of the installation process is illustrated in Figure 2.10. When the operational weather condition is satisfied based on weather forecast, the installation starts. The catamaran gets connected to the floating foundation via the sliding grippers. A wind turbine assembly is first lifted up from the deck and then transported to the aft by the lifting grips. The relative motion
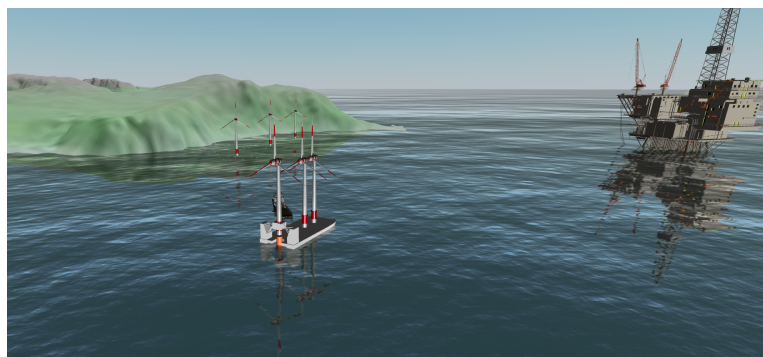
(a) Sideview
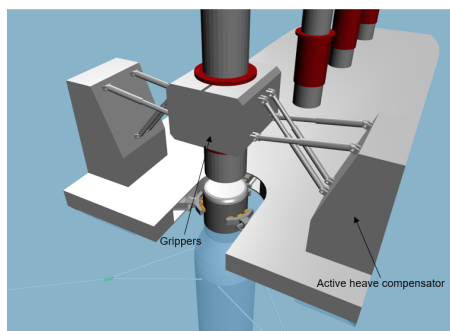
(b) Upward view
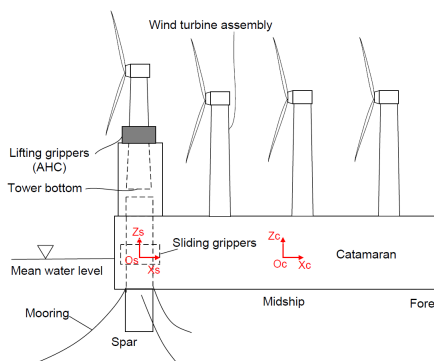
(c) Sideview

Figure 2.9: Tower-nacelle-rotor assembly concept, source: Jiang, Ren, Gao, Sandvik, Halse, Skjetne et al. (2018).

between the bottom of the tower bottom and the top of the foundation is monitored. If the relative motion satisfies the predefined criteria, the mating operation is executed. After successful mating on the floating foundation, the tower bottom is bolted on the foundation. At the end of the operation, the foundation is released. Only one lift is required for each OWT, resulting in a higher installation efficiency. The concept is suitable for both bottom-fixed and floating OWT installation. The gripper design has been studied in Rasekhi Nejad et al. (2018).

2.2.2 Operational criteria

Similar to the single blade installation approach, the relative motion at the mating point is critical, i.e., between the top of the floating foundation and bottom of the OWT assembly (Jiang, Li, Gao, Halse & Sandvik
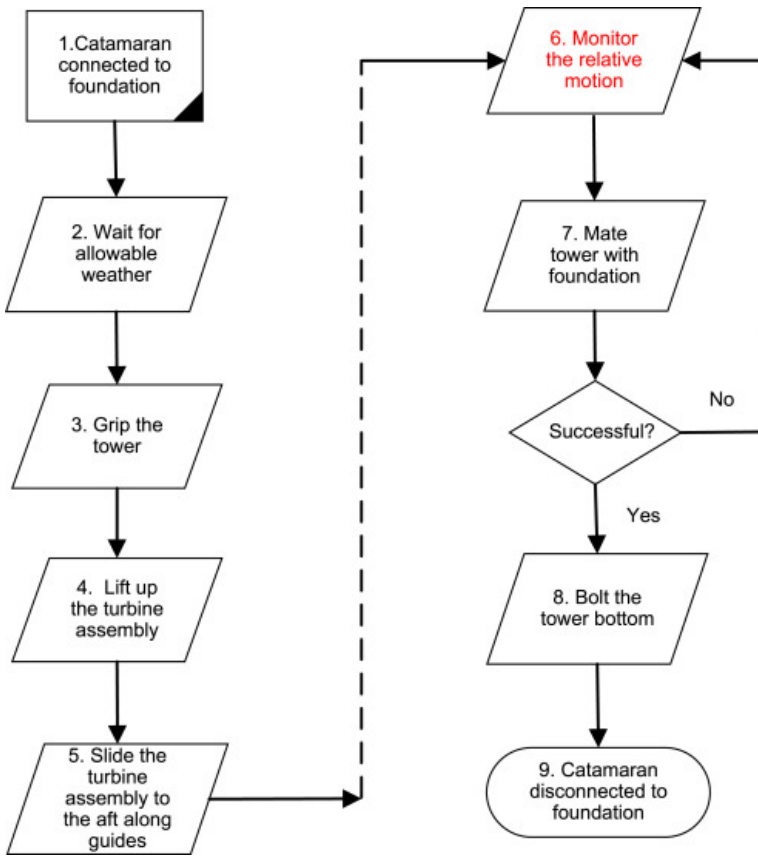
Figure 2.10: Flowcharts of the preassembly installation using a catamaran, source: Jiang, Li, Gao, Halse & Sandvik (2018).

2018). According to the proposed design, the gripper restrains the relative horizon motion between the foundation and installation. As the horizontal preassembly motion is fixed relative to the vessel, only the relative vertical motion between the tower bottom and foundation top is concerned.

The influences are two-fold. First, the relative velocity determines the impact velocity and impact force between the structures. The mating flange and guiding pins could be damaged when the impact velocity higher than the limits. Secondly, the operation successful rate is influenced by the relative displacement. The possibility of successful plugin enhances with reduced relative displacement. Meanwhile, the amplitude of the relative vertical displacement oscillation is proportional to that of the relative vertical velocity.

2.2.3   Control objectives

There are two stages in the operation, i.e., lowering and mating. The pre-assembly should be firstly lowered to the foundation slowly at required time instant to achieve the final mating operation. Additionally, the control objective of the mating operation is that the relative motion between the tower bottom and the spar top mating point in the vertical global axis should be remained with a constant distance by controlling the hydraulic cylinder motion. In the lowering stage, the heave compensator should not only cancel the relative motion between the spar top and preassembly bottom, but also slowly lower the preassembly to the spar foundation. In the mating stage, the heave compensator should be controlled to minimize the relative motion between the foundation top and preassembly bottom by controlling the height of the lifted assembly.

The design includes two subsystems, including (i) a roll reduction system and (ii) a hydraulic active heave compensator. Both systems cooperate to reduce the relative motion between the tower bottom and foundation top.

Offshore lifting operation is critically influenced by the ship roll motion. Hence, a roll-reduction system is designed, to its best, to reduce the motion of the payload. The typical U-shape tank is not applicable due to the special structure of a catamaran (Moaleji & Greig 2007). In addition, the relative vertical motion at bow is also the vessel heave and pitch motion, wind-induced loads, and environment-induced foundation motion. A hydraulic active heave compensator is then adopted to reduce the relative vertical motion between the foundation and preassembly.

Roll-reduction tanks

To reduce the roll motion in the phase of onsite installation, a free-flooding tank is installed on each side of the catamaran. The tanks are simplified as two symmetric cuboids with a constant cross section profile and a hatch opening on the bottom of each tank; see Figure 2.11. The tank hatches are opened downward into the water. The air duct on the top of the chamber is connected to a vacuum pump. The pump is a part of a larger control system, which controls the air flow to both tanks. The inlet flow from one side is not necessarily equal to the outlet flow to the other side due to the requirement of the pressure levels in both tanks.

- Control objectives: Regulate the roll angle caused by the wave loads to zero by actively controlling the tanks.

- Control input: Vacuum pump.

- Performance criteria: Vessel roll motion amplitude.
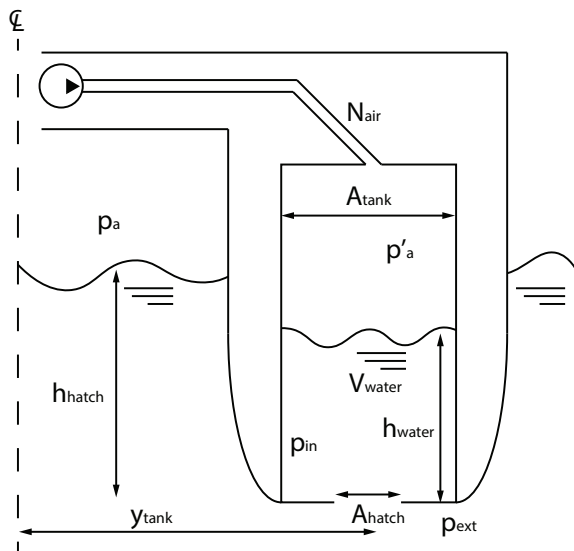
Figure 2.11: Diagram of the roll reduction system. Source: Xu et al. (2018).

Active heave compensator

A variable-displacement-controlled hydraulic cylinder is responsible to control the vertical motion of the preassembled wind turbine. The diagram of the concept is presented in Figure 2.12. A hydraulic system is considered for the AHC consisting of a motor, a pump, valves, hydraulic fluid, and a hydraulic cylinder. We assume that the real-time position and orientations of the catamaran and the spar has been well measured.

- Control objectives: Reduce the relative heave motion between the bottom center of the tower and top center of the floating foundation in the global z-axis when exposed to oscillatory wave motions.

- Control input: Pump displacement.

- Performance criteria: Relative heave motion between the bottom of the tower and the top of the foundation.

Figure 2.12: Diagram of the active heave compensator, modified from Jiang, Ren, Gao, Sandvik, Halse, Skjetne et al. (2018).

Chapter 3

System modeling

In this section, the modeling of the single blade installation system, roll-reduction tanks, and active heave compensator are presented.

3.1 Single blade installation system using a jackup vessel

Figure 2.1(b) illustrates the free-body diagrams of a typical lifting and mating phase of a single blade installation operation.

3.1.1 State-of-the-art simulation tools and their limitations

The modeling of a blade installation process under the wind and wave loads contains the hydrodynamics of jackup vessel, aerodynamics of lifted blade,

(a) Lifting model (b) Mating model
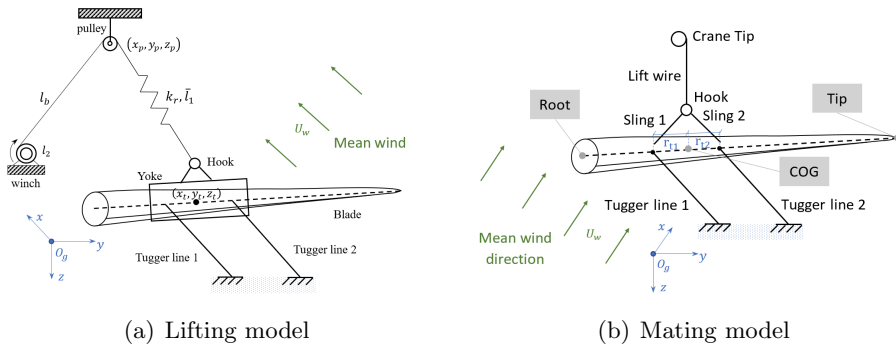
Figure 3.1: The free-body diagram of the single blade installation process.

multibody dynamics, necessary components, such as tugger lines. In addition, some features are preferred to design state estimation and control algorithms, i.e., (i) open-source, (ii) user-friendly interface, and (iii) easy implementation of control algorithms.

Currently, various aeroelastic codes are available to simulate the dynamics of offshore wind turbines during normal operation, not during the installation phase. For example, HAWC2 (Larsen & Hansen 2007), FAST (Jonkman & Buhl Jr 2005), and Bladed (Bossanyi 2009). To ensure the computational efficiency, most of them are developed based on blade element momentum (BEM) theory. The approach is limited to the homogeneous induction cases, which means uniform axial, stationary inflow, and radial independence. The basic assumptions are quasi-steady state and annuli independence. The rotor area is discretized into a finite number of annuli, which are assumed to be radially independent from each other. Engineering corrections due to blade tip loss, dynamic inflow, dynamic wake are applied. An alternative approach is the marine operation software according to multi-body dynamics, such as SIMA, DeepC, and Sesam from DNV GL. The advantages and shortages of these simulation tools are listed in Table 3.1.

Table 3.1: Comparison of existed simulation tools.

Item	Aeroelastic SW		Marine operation SW
	FAST	HAWC2	SIMA
Aerodynamic loads	Yes	Yes	No
Bottom-fixed OWT Instl.	No	Yes	Yes
Floating OWT Instl.	No	No	Yes
Open-source	Yes	No	No
Control algorithm	DLL/Simulink	DLL/Simulink	JavaScript

FAST and HAWC2 are designed for operational wind turbines, and not suitable for marine operation simulations. However, HAWC2 simulates the dynamic system with elements and connections between elements, resulting in the feasibility of modeling a steady-state installation process. The results are used to validate the proposed MATLAB/Simulink toolbox for aerodynamics.

The marine operation analysis software family from DNV-GL includes Sesam, Sima, and DeepC. Their core codes are SIMO and Riflex. Complex marine operations can be simulated. The aerodynamic module for SIMO is developed in Zhao et al. (2018). However, the control logarithms can be only implemented with external java script.

MATLAB/Simulink has been the most popular platform for control engineers and researchers. It is powerful due to the large amounts of available toolboxes, user-defined functions, and a great number of solvers. MSS toolbox (MSS. Marine Systems Simulator 2010) is widely used in the research on the dynamic positioning (DP) system. However, there still lack specific modules to simulate marine operations.

3.1.2   Modeling in HAWC2

The installation process is first modeled in HAWC2 as a basis in the code-to-code verification.

Suspended blade

The crane tip is modeled as a fixed point in space. The yoke is considered as a rigid-point mass fixed on the mass center of the suspended blade. The lift wire, slings, and tugger lines are modeled as wire ropes. Each wire rope is divided into a number of light-weight beam elements interconnected with bearings (Jiang, Gao, Ren, Li & Duan 2018). When the distance between the first and last beams is less than the length of all beams, the wire is loose due to gravity, and the axial tension on the wire is almost negligible. Otherwise, the rope is straight with axial elongation. Positive tension is achieved due to the Hooke's law. Hence, a tensile spring is modeled in HAWC2.

The Taylor's hypothesis of frozen turbulence is adopted and assumes that the advection of a field of turbulence past a fixed point can be taken to be entirely due to the mean flow, as the contribution from the turbulent circulation is small. A turbulence box is defined with evenly distributed points that moves along its length direction in the mean wind speed. The wind velocity at a point is interpolated based on the values of the neighborhood nodes. Mann's model is used to generated the turbulent wind field (Mann 1998). The parameters of the single blade installation system are tabulated in tables 3.2.

Monopile foundation

From low fidelity to high fidelity, the three most used soil-pile interaction models are the apparent fixity model, the coupled spring model, and the distributed spring model. Differences among the models are mainly from the modeling of the soil-pile interaction below the mudline. In our study,

Table 3.2: Parameters of the single blade installation system.

Parameters	Unit	Value
Position of the crane tip	m	$[0, 0, -110]^\top$
Hook maE)ss m_h	ton	1
Yoke mass m_y	ton	50
Blade mass m_b	ton	17.74
Blade moment of inertia about COG I_b	kg·m^2	4.31e6
Blade length	m	62.5
Blade root center POS $\{B\}$	m	$[-0.089, -20.51, 0.145]^\top$
Sling connection point POS $\{B\}$	m	$[0.089, \pm 4.5, 1.855]^\top$
Length of lift wire	m	9.2
Stiffness of lift wire	N/m	5.59e8
Length of slings	m	9.0
Stiffness of slings	N/m	1e8
Lift wire and spring damping ratio	-	1%
Tugger line connection point POS $\{B\}$	m	$[0.089, \pm 4.5, -0.145]^\top$
Tugger line length l_t	m	10
Stiffness of the tugger lines	N/m	1e8

the distributed spring model is adopted. The p-y model (Matlock & Reese 1960) is used in the simulation. The soil, modeled as elastic springs, is layered with different effective weights and angles of internal frictions. As defined by the American Petroleum Institute (2000), the soil resistance is a function of the pile displacement at a given point along the pile. Each layer is modeled as an uncoupled nonlinear spring with a layer-specific stiffness as shown in Figure 3.2. The soil has higher initial modulus of subgrade reaction with increasing depth. Timoshenko beams are used to model the pile, the transition piece, the tower, and the hub. The parameters of the wind turbine foundation is summarized in Table 3.3.

3.1.3   Simulation toolbox in MATLAB/Simulink

To overcome all shortages of presently existed tools, a modularized blade installation simulation toolbox for the purpose of control design is developed in MATLAB/Simulink, namely MarIn (**Mar**ine **In**stallation) (Ren, Jiang, Skjetne & Gao 2018b). The open-source toolbox contains all necessary modules and functions for bottom-fixed OWT installation. In addition, it is compatible with MSS toolbox for simulation of floating OWT installation. Various modules are contained in the toolbox. The functions
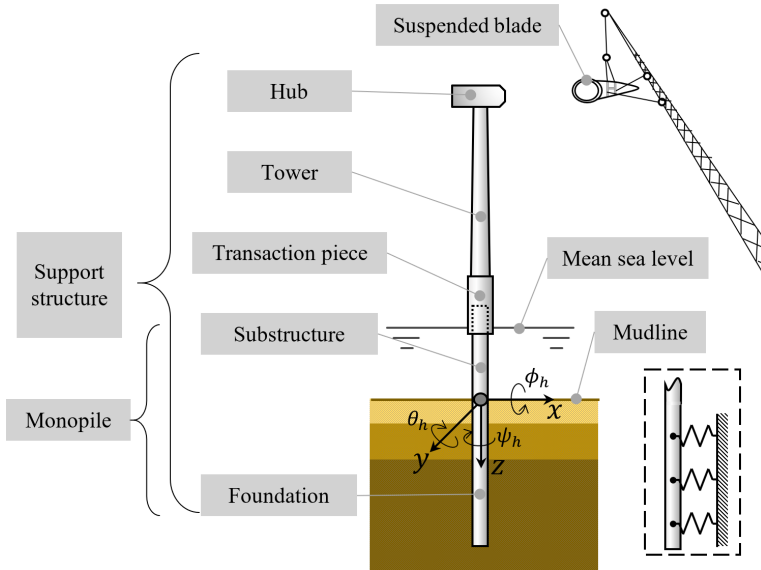
Figure 3.2: Diagram of the monopile foundation.

Table 3.3: Parameters of the wind turbine foundation.

Parameter	Unit	Value
Substructure length	m	36
Foundation length	m	30
Tower length	m	77.6
Monopile diameter	m	6
Monopile mass	tonnes	571.0
Tower mass	tonnes	347.5
Nacelle mass	tonnes	240.0

Figure 3.3: An overview of the proposed toolbox to simulate the blade installation process.

are modularized by subsystems in the MATLAB/Simulink environment. The specific parameters are given using the user interfaces. By connecting the modules with the relation shown in Figure 3.3, the complex simulation verification model is modeled. The toolbox is available on the website https://github.com/NTNU-MCS/MarIn .

Coordinate systems

To keep consistence with other research on marine control systems, the following 3-dimensional reference frames and 6 degrees of freedom (DOFs) motions are adopted in the toolbox.

Global north-east-down (NED) geographic reference frame $\{N\}$: The origin O_n is placed on the free sea surface with the x-axis pointing to the north, y-axis pointing to the east, and z-direction being downward. The orientations about the x-, y-, and z-axes are roll ( ), pitch ( ), and yaw ( ), respectively. The NED reference frame is assumed to be an inertial frame.

Vessel body-fixed frame $\{V\}$: The origin O_v coincides with the vessel center of gravity (COG). The positive directions of x^v-, y^v-, and z^v-axes, direct from aft to fore along the longitudinal axis of the vessel,

starboard, and downward. The orientation of the vessel are denoted by roll (ϕ_v), pitch (θ_v), and yaw (ψ_v), respectively.

- Crane-fixed reference frame $\{C\}$: The origin O_c is laid at the projection of the crane boom center on the free sea surface. The x^c-axis points from O_c to the projection of the crane tip on the free sea surface. The z^c- and z^v- axes are in the same direction. The reference frame $\{C\}$ is obtained by rotating $\{V\}$ with a crane boom angle β about the z^v-axis.

- Blade body-fixed frame $\{B\}$: The origin O_b is placed at the blade COG. The y^b-axis points from the root center to the tip center in the spanwise direction, and the x^b-axis is directed from the leading edge to the trailing edge in the chordwise direction. The angular velocities about the x^b-, y^b-, and z^b-axes are p, q, and r, respectively. Note that the y-axis is chosen as the longitudinal axis along the blade so that rotation about y results in a blade pitch angle, being consistent with the blade pitch during turbine operation.

- Aerodynamic frame at node $i \in \{0, 1, \cdots, n\}$ in the body-fixed frame $\{B_i\}$: The origin O_{bi} is at the geometric center of the blade i^{th} cross section. The y^{bi}-axis shares the same direction as the y^b-axis. The x^{bi}-axis and z^{bi}-axis are considered as a combination of a planar translation and a rotation about the y^b-axis. The aerodynamic twist, i.e., the angle between x^{bi} and x^b, is denoted by $\theta_{y,i}$.

- Mean-wind coordinate system $\{W\}$: The origin O_w is located at the lower-right corner of the wind turbulence box. O_w is placed at a preset point in $\{N\}$. The x^w-axis points in the wind inflow direction, i.e., the box's length, and z^w is directed downward, i.e., the box's height. The wind velocities in the x^w-, y^w-, and z^w-axes are u_w, v_w, and w_w, respectively. The box orientation about $\{N\}$ is constant, i.e., ϕ_w, θ_w, and ψ_w are constants.

Coordinate transformation

The following order is adopted to transform a vector from one frame to another:

$$\{W\} \leftrightarrow \{N\} \begin{cases} \leftrightarrow \{V\} \\ \leftrightarrow \{B\} \leftrightarrow \{B_i\} \end{cases}$$

The transformations are bidirectional. The position, orientation, and velocity vectors are defined in Table 3.4. The displacement vector of crane tip
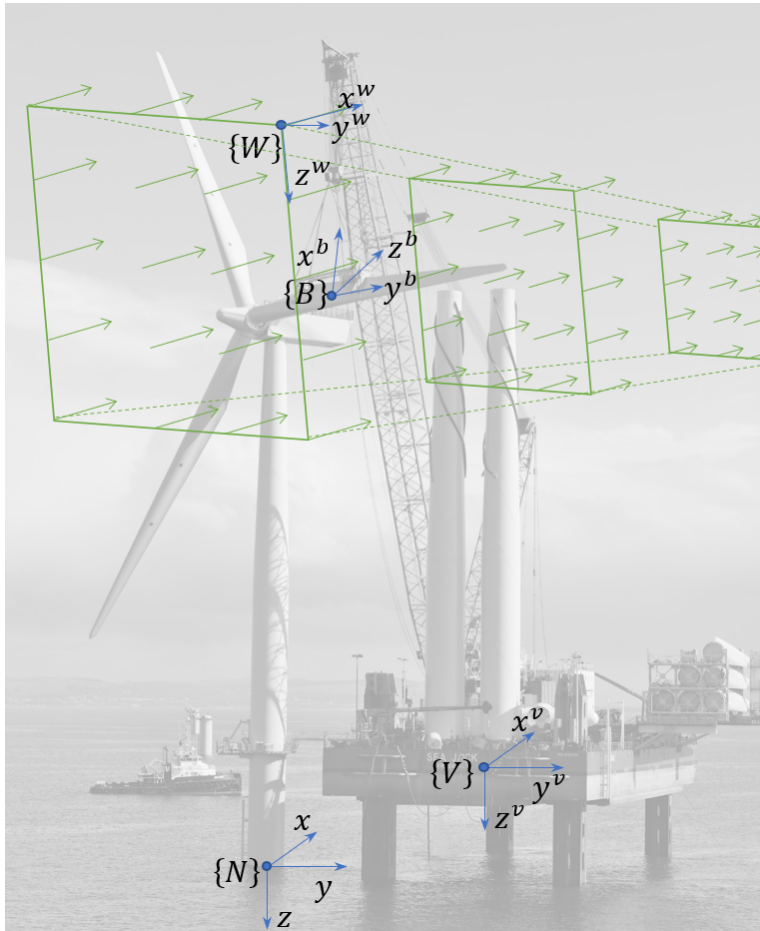
Figure 3.4: Reference frames used in the wind turbine installation.
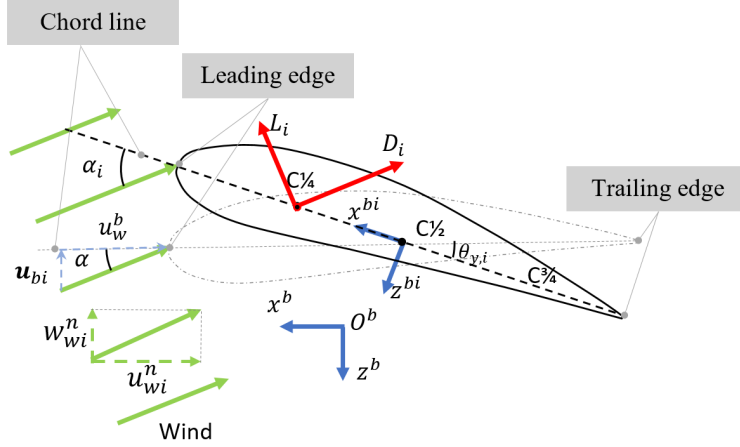
Figure 3.5: Body-fixed and aerodynamic coordinate systems. The solid line and the dashed line are the outline of the ith blade element with and without rotation $\theta_{y,i}$, respectively.

pulley relative to the crane base in $\{V\}$ is achieved by Denavit-Hartenberg (DH) matrix or direct calculation.

Table 3.4: Variables in the corresponding frame adopted in the MarIn toolbox.

	Position in	Rltv. orientation to $\{N\}$	Translational vel.	Angular vel.
$\{N\}$	$\boldsymbol{p} = [x, y, z]^\top$	-	$\boldsymbol{v}_n = [\dot{x}, \dot{y}, \dot{z}]^\top$	-
$\{B\}$	$\boldsymbol{p}^b = [x^b, y^b, z^b]^\top$	$\boldsymbol{\Theta}_{bn} = [\phi, \theta, \psi]^\top$	$\boldsymbol{v}_b = [u, v, w]^\top$	$\boldsymbol{\omega}_b = [p, q, r]^\top$
$\{W\}$	$\boldsymbol{p}^w = [x^w, y^w, z^w]^\top$	$\boldsymbol{\Theta}_{wn} = [\phi_w, \theta_w, \psi_w]^\top$	$\boldsymbol{v}_w = [u_w, v_w, w_w]^\top$	-

A vector, position or translational velocity, is transformed between the co-ordinate systems, from $\{B\}$ to $\{A\}$, by multiplying by the rotation matrix $\boldsymbol{R}_b^a$, i.e., the notation is similar to Fossen (2011)

$$\boldsymbol{v}^a = \boldsymbol{R}_b^a(\boldsymbol{\Theta}_{ab})\boldsymbol{v}^b, \tag{3.1}$$

where $\boldsymbol{v}^a$ and $\boldsymbol{v}^b \in \mathbb{R}^3$ are two vectors in $\{A\}$ and $\{B\}$, $\boldsymbol{\Theta}_{ab}$ denotes a vector of the Euler angles between $\{A\}$ and $\{B\}$, and the rotation matrix $\boldsymbol{R}_b^a$ rotates from the coordinate system $\{B\}$, expressed by the subscript, to the frame $\{A\}$, denoted by the superscript. The inverse transformation is given by the matrix $\boldsymbol{R}_b^a(\boldsymbol{\Theta}_{ab})^{-1} = \boldsymbol{R}_b^a(\boldsymbol{\Theta}_{ab})^\top = \boldsymbol{R}_a^b(\boldsymbol{\Theta}_{ab})$.

Dynamic equation

The module interaction and aerodynamic loads are according to the Newton's second law and the cross-low principle, respectively. The wire cables are modeled as tensile springs with specific damping coefficients, which only provide tension with positive elongations. The kinetics of the blade and yoke in $\{B\}$ about its COG is given by

$$\boldsymbol{M}_b\dot{\boldsymbol{\nu}}_b + \boldsymbol{C}_b(\boldsymbol{\nu}_b)\boldsymbol{\nu}_b = \boldsymbol{g}_b^b + \boldsymbol{\tau}_s^b + \boldsymbol{\tau}_t^b + \boldsymbol{\tau}_w^b, \tag{3.2}$$

where the mass matrix is $\boldsymbol{M}_b = \begin{bmatrix} (m_b + m_y)\boldsymbol{I}_3 & \boldsymbol{0}_3 \\ \boldsymbol{0}_3 & \boldsymbol{I}_b \end{bmatrix}$, m_b is the mass of the blade, m_y is the mass of the yoke, $\boldsymbol{I}_b \in \mathbb{R}^{3\times3}$ is the inertia matrix, and $\boldsymbol{g}_b^b \in \mathbb{R}^6$ is the gravity force and moment vector in $\{B\}$, i.e., $\boldsymbol{g}_b^b = \begin{bmatrix} \boldsymbol{R}_b^{n\top}[0, 0, (m_b + m_y)g]^\top \\ [0, 0, 0]^\top \end{bmatrix}$. The Coriolis matrix is then expressed as $\boldsymbol{C}_b = -\boldsymbol{C}_b^\top = \begin{bmatrix} (m_b + m_y)\boldsymbol{S}(\boldsymbol{\omega}_b) & \boldsymbol{0}_3 \\ \boldsymbol{0}_3 & -\boldsymbol{S}(\boldsymbol{I}_b\boldsymbol{\omega}_b) \end{bmatrix}$, where the skew-symmetric matrix $\boldsymbol{S}(\boldsymbol{\lambda})$ for a vector $\boldsymbol{\lambda} = [\lambda_1, \lambda_2, \lambda_3]^\top \in \mathbb{R}^3$ is defined as $\boldsymbol{S}(\boldsymbol{\lambda}) = \begin{bmatrix} 0 & -\lambda_3 & \lambda_2 \\ \lambda_3 & 0 & -\lambda_1 \\ -\lambda_2 & \lambda_1 & 0 \end{bmatrix}$.

The external load vectors from slings, tugger lines, and wind-induced loads in $\{B\}$ are denoted by $\boldsymbol{\tau}_s^b$, $\boldsymbol{\tau}_t^b$, and $\boldsymbol{\tau}_w^b \in \mathbb{R}^6$, respectively. They are

$$\boldsymbol{\tau}_s^b = \sum_{i=1}^{n_s} \begin{bmatrix} \boldsymbol{R}_b^{n\top}\boldsymbol{f}_{si_B} \\ \boldsymbol{S}(\boldsymbol{p}_{si}^b - \boldsymbol{p}_{COG}^b)\boldsymbol{R}_b^{n\top}\boldsymbol{f}_{si_B} \end{bmatrix}, \tag{3.3}$$

$$\boldsymbol{\tau}_t^b = \sum_{i=1}^{n_t} \begin{bmatrix} \boldsymbol{R}_b^{n\top}\boldsymbol{f}_{ti_B} \\ \boldsymbol{S}(\boldsymbol{p}_{ti}^b - \boldsymbol{p}_{COG}^b)\boldsymbol{R}_b^{n\top}\boldsymbol{f}_{ti_B} \end{bmatrix}, \tag{3.4}$$

where $\boldsymbol{p}_{si}^b$ and $\boldsymbol{p}_{ti}^b$ are the positions of the connecting points of the slings and tugger lines on the blade in $\{B\}$, respectively, $\boldsymbol{f}_{si_B}$ and $\boldsymbol{f}_{ti_B}$ are the restoring forces acting on the blade in $\{N\}$ acting on the specific sling and tugger line.

Aerodynamic loads

A single blade installation is a scenario with low inflow speed. The blade is separated into a number of segments along its longitude axis. When the yaw angle is small, the total loads are the integration of the loads acting on each segments and the force component in the y^b-axis is negligible according to

the cross-flow principle. The total wind-induced loads acting on the main-body COG are given by

$$\boldsymbol{\tau}_w^b = \begin{bmatrix} \sum_{i=0}^n \boldsymbol{f}_{w,i}^b \\ \sum_{i=0}^n \left[\boldsymbol{S}(\boldsymbol{p}_{C_{1/4},i}^b - \boldsymbol{p}_{COG}^b)\boldsymbol{f}_{w,i}^b + \boldsymbol{m}_{w,i}^b \right] \end{bmatrix}, \tag{3.5}$$

where the resulting force and moment vector acting at the ith node in the blade main-body frame $\{B\}$ are given by

$$\boldsymbol{f}_{w,i}^b = \boldsymbol{R}_b^{wi\top} \begin{bmatrix} -D_i \\ 0 \\ L_i \end{bmatrix}, \ \boldsymbol{m}_{w,i}^b = \boldsymbol{m}_{w,i}^{wi} = \begin{bmatrix} 0 \\ M_i \\ 0 \end{bmatrix}. \tag{3.6}$$

Based on the airfoil theory (Anderson Jr 2010), the lift force L_i, drag force D_i, and pitching moment M_i acting on the ith blade cross-section, are given by

$$L_i = \frac{1}{2}\rho_a C_l(\alpha_i, \text{T}/\text{C}_i)A_i V_i^2, \tag{3.7}$$

$$D_i = \frac{1}{2}\rho_a C_d(\alpha_i, \text{T}/\text{C}_i)A_i V_i^2, \tag{3.8}$$

$$M_i = \frac{1}{2}\rho_a C_m(\alpha_i, \text{T}/\text{C}_i)A_i V_i^2, \tag{3.9}$$

where the subscript i refers to the ith node, T/C denotes the thickness/chord ratio, ρ_a is the air density, A_i is the wing area which is the multiplication of the chord length and the length of the blade cross-section, and C_l, C_d, and C_m denote the lifting coefficient, the drag coefficient, and the pitching moment coefficient, respectively. The inflow speed is $V_i = |\boldsymbol{L}[\boldsymbol{R}_n^{bi}(\boldsymbol{v}_{wi} - \boldsymbol{v}_{C_{1/4},i})]|$, where $\boldsymbol{L} = \begin{bmatrix} 1 & 0 & 0 \\ 0 & 0 & 1 \end{bmatrix}$, and $\boldsymbol{v}_{C_{1/4},i}$ are the velocity vector of the ith center of pressure in $\{N\}$, respectively.

The angle of attack at the ith segment α_i is given by

$$\alpha_i = \alpha + \theta_{y,i}, \tag{3.10}$$

with $\alpha = f_a\left(\pi + \text{atan2}(w_{wi}^b - w_{C_{1/4}^b}, u_{wi}^b - u_{C_{1/4}}^b)\right)$, where f_a is a function that maps an angle to the range $[-\pi, \pi)$.

Turbulent wind field

The wind turbulence boxes are generated by importing and reshaping the binary files from TurbSim (Kelley & Jonkman 2006, Jonkman & Kilcher 2012),

with preset discrete points along the length, width, and height. TurbSim is a free stochastic turbulence simulator. Additionally, the binary turbulence file generated by HAWC2 is also supported. The position of a point in $\{N\}$ is transformed to the position in $\{W\}$. The box move forwards along its length in a speed same to the mean wind speed.

Hub motion

The hub is located on top of the monopile and its motion is mainly due to the monopile vibrations under the wave loads, while the blade motion is influenced by the wind loads. Since the wind-induced loads have minor effects to the monopile vibration and hub oscillation, the hub motion is assumed to be independent on the suspended blade motion. The hub motion is first generated by HAWC2 and imported to Simulink as a source.

3.1.4   Control design model

Before designing state estimation and control algorithms, simplified mathematics state-space models should be proposed to design control algorithms. The single blade installation process can be categorized into two models, i.e., the lifting model and the mating model.

Blade lifting model

In the blade lifting model (Ren et al. 2017, 2019), the blade vertical position should be considered. A reduced model is adopted for the optimization problem in a three-dimensional NED coordinate system. The crane is assumed to be rigidly fixed on the vessel. The masses of the hook, yoke, and blade are considered to be concentrated at the blade COG, i.e., the total mass is $m = m_h + m_y + m_b$, where m_h is the mass of the hook. Furthermore, the lift wire and slings are considered as one unit without the consideration of the lift wire control; it provides a restoring force on the moving blade. We assume that the ropes are replaced by a lightweight rope, i.e., its mass is assumed to be zero. The blade COG is suspended by the rope, which is connected to the winch through a pulley fixed at the crane tip. Hence, tensile springs are employed to model the wire ropes. The unstretched length of the spring $\bar{l}_1$ denotes the distance between the pulley and blade COG. Tugger lines are released at a speed such that only vertical lifting is allowed. Because the lifting operation is executed over a short period, the horizontal wind-induced load is assumed to be restrained by tugger lines and can be disregarded. A 3DOF lifting model, with an elastic wire rope and a controllable winch, is deduced based on the Newton–Euler method in the NED coordinate system.

To shorten the equations, four vectors are defined correspondingly: the position of the blade COG $\boldsymbol{r}_l = [x, y, z]^\top$, the position of the pulley $\boldsymbol{r}_p = [x_p, y_p, z_p]^\top$, the translational velocity of the blade COG $\boldsymbol{u}_l = [\dot{x}, \dot{y}, \dot{z}]^\top$, and the velocity of the pulley $\boldsymbol{u}_p = [\dot{x}_p, \dot{y}_p, \dot{z}_p]^\top$. Additional two vectors are defined to shorten the equations. The relative position vector from the pulley to payload $\boldsymbol{\Delta}_1$ and its time derivative $\boldsymbol{\Delta}_2$ are respectively defined as $\Delta_1 := r_l - r_p$ and $\boldsymbol{\Delta}_2 := u_l - u_p$. Disregarding wind-induced loads, the simplified control design model for the considered blade lifting operation is produced,

$$\dot{\boldsymbol{r}}_l = \boldsymbol{u}_l, \tag{3.11a}$$

$$\boldsymbol{M}_l \dot{\boldsymbol{u}}_l = -\boldsymbol{A}(\boldsymbol{r}_l, \boldsymbol{r}_p, l_1, v_1)\boldsymbol{\Delta}_1 + \boldsymbol{g}_l, \tag{3.11b}$$

$$\dot{l}_1 = v_1, \tag{3.11c}$$

$$\dot{v}_1 = u, \tag{3.11d}$$

where $\boldsymbol{M}_l = \mathrm{diag}(m,\ m,\ m)$, $\boldsymbol{A}(\boldsymbol{r}_l, \boldsymbol{r}_p, l_1, v_1) = a_l \boldsymbol{I}_{3\times3}$, with

$$a_l = \gamma E A_r \frac{|\Delta_1| - \bar{l}_1}{l_1 |\Delta_1|} + \frac{d_l}{|\Delta_1|}\left(\frac{\Delta_1^\top \Delta_2}{|\Delta_1|} - v_1\right),$$

γ is the modified coefficient of a stranded wire, E stands for the Young's modulus, A_r denotes the cross-sectional area of the rope, $l_1 = \bar{l}_1 + l_b$, l_b denotes the length of rope between the winch and pulley, $\delta = |\Delta_1| - \bar{l}_1$ is the elastic elongation, $\boldsymbol{g}_l = [0, 0, mg]^\top$ is gravity, $v_1 := \dot{l}_1$ denotes the wire length changing rate, and d_l is the damping coefficient.

Blade mating model

Since the pendular motions are of primary importance during the mating process, only the horizontal motion and orientation are considered in the mating model (Ren, Jiang, Skjetne & Gao 2018a, Ren, Jiang, Skjetne, Gao et al. 2018). The free-body diagram is presented in Figure 3.6.

The mating model is based on several assumptions as follows:

- The controller can stabilize the blade near the desired position and orientation, and the motion oscillation is small compared to the length of the tugger lines;

- The tugger lines are modeled as linear springs that provide positive restoring force in the direction from the blade yoke connecting point to the pulley on the boom;
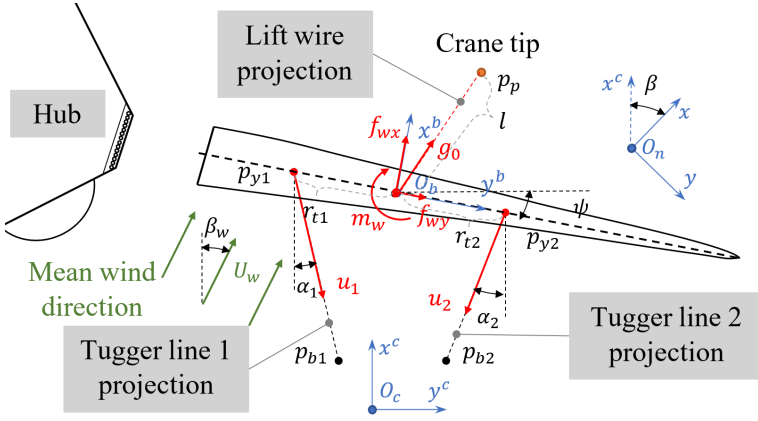
Figure 3.6: Free-body diagram of the mating model.

- The wind and wave directions do not significantly change during the installation.

A 3DOF simplified single blade installation model about the blade COG is given by

$$\dot{\boldsymbol{\eta}} = \boldsymbol{R}\boldsymbol{\nu}, \tag{3.12a}$$

$$\dot{\boldsymbol{b}} = -\frac{1}{\boldsymbol{T_b}}\boldsymbol{b} + \boldsymbol{w}_b, \tag{3.12b}$$

$$\boldsymbol{M}\dot{\boldsymbol{\nu}} = \boldsymbol{R}^\top(\boldsymbol{g_0} + \boldsymbol{b} + \boldsymbol{B}\boldsymbol{u_t}) + \boldsymbol{\tau}_w, \tag{3.12c}$$

where $\boldsymbol{\eta} = [x, y, \psi]^\top \in \mathbb{R}^2 \times \mathbb{S}$ denotes the position and orientation of the blade COG in the $\{N\}$, $\boldsymbol{\nu} = [u, v, r]^\top \in \mathbb{R}^3$ refers to the linear velocity and the updating rate of the Euler angle in $\{B\}$, $\boldsymbol{b} = [b_1, b_2, b_3]^\top \in \mathbb{R}^3$ is a state vector used to estimate the forces and moments resulting from the model uncertainty and environmental disturbance, and $\boldsymbol{T_b} = \text{diag}\{T_{b1}, T_{b2}, T_{b3}\}$ is a constant diagonal matrix. The transformation matrices $\boldsymbol{R}$ and $\boldsymbol{R}_1$ from $\{B\}$ to $\{N\}$ is given by

$$\boldsymbol{R}(\psi) = \begin{bmatrix} \cos\psi & -\sin\psi & 0 \\ \sin\psi & \cos\psi & 0 \\ 0 & 0 & 1 \end{bmatrix} \text{ and } \boldsymbol{R}_1(\psi) = \begin{bmatrix} \cos\psi & -\sin\psi \\ \sin\psi & \cos\psi \end{bmatrix}. \tag{3.13}$$

Note that the rotation matrix $\boldsymbol{R}$ in the horizontal plane satisfies

$$\boldsymbol{R}^{-1} = \boldsymbol{R}^\top, \ \dot{\boldsymbol{R}} = \boldsymbol{R}\boldsymbol{S}(r), \text{ where } \boldsymbol{S}(r) = \begin{bmatrix} 0 & -r & 0 \\ r & 0 & 0 \\ 0 & 0 & 0 \end{bmatrix}. \tag{3.14}$$

$\boldsymbol{M} = \mathrm{diag}(m, m, I_b) \in \mathbb{R}^{3 \times 3}$ denotes the mass matrix of the system where $m = m_b + m_h + m_y$ is the total mass of the blade, hook, and yoke, I_b is the blade's moment of inertia at COG about the yaw motion, $\boldsymbol{g_0} = [-\frac{mg}{l}(x-x_p), -\frac{mg}{l}(y-y_p), 0]^\top$ represents the gravity-induced restoring force where $l = \sqrt{(x-x_p)^2 + (y-y_p)^2}$ is the distance between the crane tip and the blade COG in xy-plane, and $\boldsymbol{u_t} = [u_1, \cdots, u_\sigma]^\top \in \mathbb{R}^\sigma$ is the control input vector, where σ is the total number of tugger lines, and $u_i \in \mathbb{R}$ is the ith tugger line horizontal force input, with $i = 1, \cdots, \sigma$.

By introducing pretension which is generated by gravity due to the blade initial displacement, u_i can be both positive and negative. Used to transfer the tugger line force inputs to the generalized control force and moment acting on the blade in $\{N\}$, a general form of control configuration matrix $\boldsymbol{B}$ is given by

$$\boldsymbol{B}(\alpha_1, \cdots, \alpha_\sigma) = \begin{bmatrix} \boldsymbol{B}_1(\alpha_1) & \cdots & \boldsymbol{B}_\sigma(\alpha_\sigma) \end{bmatrix}, \tag{3.15}$$

where $\boldsymbol{B}_i(\alpha_i) = [-\cos\alpha_i, -\sin\alpha_i, r_{ti}\cos\alpha_i\cos\psi]^\top$, r_{ti} is the moment arm of the tugger line force u_i with respect to the COG in y^b, and α_i is the tugger line inclination in the horizontal plane. In two-tugger-line configuration, $\sigma = 2$, $r_{t1} < 0$ and $r_{t2} > 0$. By Assumption 1, the angle α_i is considered to be unchanged in a short term, i.e., $\dot{\alpha}_1 = \dot{\alpha}_2 \cong 0$ and $\alpha_i = \sin^{-1}\left(\frac{y_{yi}-y_{bi}}{l_i}\right)$, $i = 1, 2$. The sign of α_i depends on r_{ti} and the diameter of the crane boom.

The wind-induced force in the body-fixed reference frame at an airfoil segment depends on the inflow velocity relative to the blade segment at y^b, given by $\boldsymbol{u}_{wr}^b(y^b) = \boldsymbol{u}_w^b - \boldsymbol{u}_b^b(y^b)$, where $\boldsymbol{u}_w^b = [U_w\cos(\psi - \beta_w), U_w\sin(\psi - \beta_w), 0]^\top \in \mathbb{R}^3$ is the wind velocity in $\{B\}$, $U_w \in \mathbb{R}$ and $\beta_w \in \mathbb{R}$ are the mean wind speed and direction, and $\boldsymbol{u}_b^b(y^b)$ is the velocity at the corresponding blade segment center of pressure at y^b. Assumption 3 meets the cross-flow principle. According to the cross-flow principle and neglecting the blade velocity, i.e., $\boldsymbol{u}_b^b(y^b) = 0$, the wind loads acting on the blade COG in $\{B\}$ is simplified to a following form

$$\boldsymbol{\tau}_w = \begin{bmatrix} f_{wx} \\ f_{wy} \\ m_w \end{bmatrix} = \begin{bmatrix} c_{wx}U_w^2\cos^2(\psi - \beta_w) \\ 0 \\ c_{w\psi}U_w^2\cos^2(\psi - \beta_w) \end{bmatrix}, \tag{3.16}$$

where c_{wx} and $c_{w\psi}$ are the generalized aerodynamic coefficients from the curve fitting of quasi-steady analysis results in surge and yaw respectively. For the sake of simplification, $\beta_w = 0$ is used in the following paper, i.e., the mean wind velocity vector is $\boldsymbol{u}_w = [U_w, 0, 0]^\top$ in $\{N\}$. The turbulent wind speed is considered as a zero-mean system disturbance.

The global positions of the tugger line connection points to the crane boom and yoke are $\boldsymbol{p}_{bi} = [x_{bi}, y_{bi}, z_{bi}]^\top$ and $\boldsymbol{p}_{yi} = [x_{yi}, y_{yi}, z_{yi}]^\top$, where $i \in \{1, 2\}$ is the index of the tugger lines. The position of the crane tip pulley is $\boldsymbol{p}_p = [x_p, y_p, z_p]^\top$. Due to the vertical displacement of the pulley, the positions of the tugger line base points are given by

$$\boldsymbol{p}_{bi} = \boldsymbol{p}_{O_b} + \left[\boldsymbol{R}_1(\psi) \begin{bmatrix} 0 \\ r_{ti} \\ 0 \end{bmatrix} + \boldsymbol{R}_1(\alpha_i) \begin{bmatrix} -l_{ti} \\ 0 \end{bmatrix} \right] + \begin{bmatrix} 0 \\ 0 \\ \Delta h_{bi} \end{bmatrix}, \qquad (3.17)$$

where p_{O_b} is the position of O_b in $\{N\}$, l_{ti} denotes the tugger line length, and Δh_{bi} is the pulley's vertical displacement.

Hub motion estimation model

The hub horizontal motion can be modeled in two approaches (Ren, Skjetne, Jiang, Gao & Verma 2018). One approach is to set acceleration as a state, and the estimate can output filtered acceleration. Hence, the state-space representation is then given by

$$\begin{bmatrix} \dot{\boldsymbol{x}}_1 \\ \dot{\boldsymbol{x}}_2 \\ \dot{\boldsymbol{x}}_3 \\ \dot{\boldsymbol{x}}_4 \end{bmatrix} (t - \tau_d) = \begin{bmatrix} \boldsymbol{0} & \boldsymbol{I} & \boldsymbol{0} & \boldsymbol{0} \\ \boldsymbol{0} & \boldsymbol{0} & \boldsymbol{I} & \boldsymbol{0} \\ \boldsymbol{0} & \boldsymbol{0} & \boldsymbol{0} & \boldsymbol{0} \\ \boldsymbol{0} & \boldsymbol{0} & \boldsymbol{0} & \boldsymbol{0} \end{bmatrix} \begin{bmatrix} \boldsymbol{x}_1 \\ \boldsymbol{x}_2 \\ \boldsymbol{x}_3 \\ \boldsymbol{x}_4 \end{bmatrix} (t - \tau_d) + \begin{bmatrix} \boldsymbol{0} & \boldsymbol{0} \\ \boldsymbol{0} & \boldsymbol{0} \\ \boldsymbol{I} & \boldsymbol{0} \\ \boldsymbol{0} & \boldsymbol{I} \end{bmatrix} \begin{bmatrix} \boldsymbol{w}_c(t - \tau_d) \\ \boldsymbol{w}_b(t - \tau_d) \end{bmatrix},$$

$$(3.18\text{a})$$

$$\begin{bmatrix} \boldsymbol{p}_{gps}(t) \\ \boldsymbol{f}_{imu}(t - \tau_d) \end{bmatrix} = \begin{bmatrix} \boldsymbol{I} & \boldsymbol{0} & \boldsymbol{0} & \boldsymbol{0} \\ \boldsymbol{0} & \boldsymbol{0} & \boldsymbol{R}^\top & -\boldsymbol{R}^\top \end{bmatrix} \begin{bmatrix} \boldsymbol{x}_1 \\ \boldsymbol{x}_2 \\ \boldsymbol{x}_3 \\ \boldsymbol{x}_4 \end{bmatrix} (t - \tau_d) + \begin{bmatrix} \boldsymbol{v}_g \\ \boldsymbol{v}_a \end{bmatrix} (t), \quad (3.18\text{b})$$

where τ_d is the delay of GPS signal due to communication and computation, $\boldsymbol{x}_1 = [x_h, y_h]^\top$ denotes the position vector indicating the location of the sensors at the hub, $\boldsymbol{x}_2 = [v_{hx}, v_{hy}]^\top = \dot{\boldsymbol{x}}_1$ is the velocity vector in $\{N\}$, $\boldsymbol{x}_3 = [a_{hx}, a_{hy}]^\top = \dot{\boldsymbol{x}}_2$ is the acceleration vector in $\{N\}$, $\boldsymbol{x}_4 = -\boldsymbol{b}_a + \boldsymbol{g} = [b_{ax}, b_{ay}]^\top$ with $\boldsymbol{b}_a = \boldsymbol{R}\boldsymbol{b}_a^b$ refers to the combined bias and gravity vector, $\boldsymbol{w}_c \sim (0, \boldsymbol{Q}_c)$ and $\boldsymbol{w}_b \sim (0, \boldsymbol{Q}_b)$ with $\boldsymbol{Q}_c$ and $\boldsymbol{Q}_b \in \mathbb{R}^{2 \times 2}$, $\boldsymbol{v}_a = \boldsymbol{R}\boldsymbol{v}_a^b \sim (0, \boldsymbol{Q}_a)$, and $\boldsymbol{v}_g \sim (0, \boldsymbol{Q}_g)$ with $\boldsymbol{Q}_g \in \mathbb{R}^{2 \times 2}$. The diagonal elements of $\boldsymbol{Q}_g \in \mathbb{R}^{2 \times 2}$ and $\boldsymbol{Q}_a \in \mathbb{R}^{2 \times 2}$ represent the covariances of the GPS noise and accelerometer noise, respectively. Two-dimensional GPS and IMU measurements are denoted by $\boldsymbol{p}_{gps}(t) \in \mathbb{R}^2$ and $\boldsymbol{f}_{imu} \in \mathbb{R}^2$.

Another approach is to let the acceleration be an input that drives the position/velocity dynamics. The aim of this model is to design the MHE.

Similar to Σ_1, the model is reduced according to

$$\begin{bmatrix} \dot{\boldsymbol{x}}_1 \\ \dot{\boldsymbol{x}}_2 \\ \dot{\boldsymbol{x}}_4 \end{bmatrix} (t - \tau_d) = \begin{bmatrix} \boldsymbol{0} & \boldsymbol{I} & \boldsymbol{0} \\ \boldsymbol{0} & \boldsymbol{0} & \boldsymbol{I} \\ \boldsymbol{0} & \boldsymbol{0} & \boldsymbol{0} \end{bmatrix} \begin{bmatrix} \boldsymbol{x}_1 \\ \boldsymbol{x}_2 \\ \boldsymbol{x}_4 \end{bmatrix} (t - \tau_d) + \begin{bmatrix} \boldsymbol{0} \\ \boldsymbol{I} \\ \boldsymbol{0} \end{bmatrix} \boldsymbol{R} \boldsymbol{f}_{imu}(t - \tau_d) \quad \text{(3.19a)}$$

$$+ \begin{bmatrix} \boldsymbol{0} & \boldsymbol{0} \\ \boldsymbol{I} & \boldsymbol{0} \\ \boldsymbol{0} & \boldsymbol{I} \end{bmatrix} \begin{bmatrix} \boldsymbol{w}_a \\ \boldsymbol{w}_b \end{bmatrix} (t - \tau_d),$$

$$\boldsymbol{z}(t) = \begin{bmatrix} \boldsymbol{I} & \boldsymbol{0} & \boldsymbol{0} \end{bmatrix} \begin{bmatrix} \boldsymbol{x}_1 \\ \boldsymbol{x}_2 \\ \boldsymbol{x}_4 \end{bmatrix} (t - \tau_d) + \boldsymbol{v}_g(t), \quad \text{(3.19b)}$$

where $\boldsymbol{x}_4 = -\boldsymbol{b}_a + \boldsymbol{R}\boldsymbol{g} = [b_{ax}, b_{ay}]^\top$, and $\boldsymbol{z}(t) = \boldsymbol{p}_{gps}(t)$.

3.2 Tower-nacelle-rotor assembly installation using a catamaran

Spar-type foundation is selected as the research objective. The wind turbine superstructures have been preassembled onshore. After carrying them to the installation site, the catamaran gets connected to the spar foundation via the sliding grippers. The hydraulic heave compensator lifts the tower-nacelle-rotor assembly in the body-fixed vertical axis.

The spar and installation vessel are simulated as rigid bodies with force response amplitude operators (RAOs) calculated by WAMIT. Both the catamaran and spar foundation are floating structures, which are exposed to complex environments, including, waves, current, and wind. The horizontal position of the catamaran vessel is maintained by the DP system. The spar is moored by three mooring lines, which are simulated with a finite element method (FEM) model. Current-induced loads are calculated by defining the current profile from the free sea surface to the seafloor. The spar and vessel are only influenced by the surface current. A sliding gripper is modeled as a pair of planar springs fixed on the vessel in the body-fixed frame; see Figure 3.7. The controllers of the roll reduction tanks and active heave compensator are developed independently. The parameters of the catamaran and spar foundation are summarized in tables 3.5–3.6. The rotor-nacelle-tower assembly is considered as a lumped mass which is rigidly connected to the catamaran vessel. In the study, a 10 MW wind turbine is adopted with the height of 115 meters and weight of 1200 tons.
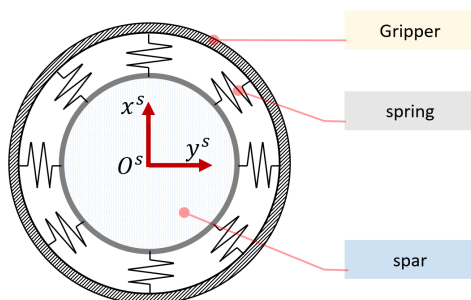
Figure 3.7: Diagram of the sling gripper at the interconnection height.

Table 3.5: Parameters of the catamaran.

Parameter	Symbol	Value
Length overall (m)	L_{OA}	144
Molded breadth (m)	B	60
Draft (m)	T_c	8.0
Displacement mass (tonnes)	Δ_c	18502.9
Vertical centre of gravity (COG) above baseline (m)	KG_c	28.6
Body origin in global coordinate system (m)	(X_c, Y_c, Z_c)	(64,0,0)
Number of wind turbines on board	N_w	4

Table 3.6: Parameters of the spar before mating.

Parameter	Symbol	Value
Diameter at top (m)	L_{bd1}	9.5
Diameter at waterline (m)	M_{bd1}	14
Draft (m)	T_{s1}	70
Vertical position of COG (m)	Zs_{COG1}	-51.8
Displacement mass (tonnes)	Δ_{s1}	11045
Vertical position of fairlead (m)	Z_{f1}	-15
Vertical position of mating point (m)	Z_m	20
Heave natural period (s)	T_{n3}	17.4

Table 3.7: Parameters of the roll-reduction tanks.

Parameter	Value
Tank length, width and height (m)	$(15-30) \times 8 \times 8$
Tank torque arm (m)	24
Hatch area (m^2)	15
Valve area (m^2)	1

3.2.1 Roll reduction tanks

The vacuum pump is modeled as a linear system without time-delay effects and with a maximum power output. The target catamaran is simplified as a single degree-of-freedom roll model.

The one-dimensional simplified model is given by

$$\dot{\phi} = p, \tag{3.20a}$$

$$\dot{p} = \frac{1}{I_t}(-T\phi - Dp + \tau_{tank} + d), \tag{3.20b}$$

$$\dot{V}_{water,1} = C_{v1}\text{sgn}(\Delta p_{h1})/\sqrt{|\Delta p_{h1}|}, \tag{3.20c}$$

$$\dot{V}_{water,2} = C_{v2}\text{sgn}(\Delta p_{h2})/\sqrt{|\Delta p_{h2}|}, \tag{3.20d}$$

$$\dot{N}_{air,1} = u_1, \tag{3.20e}$$

$$\dot{N}_{air,2} = u_2, \tag{3.20f}$$

where ϕ is the vessel roll angle, p denotes the roll velocity, I_t stands for the total moment of inertia of the catamaran, T indicates the linear restoring torque coefficient, D refers to the linear damping coefficient τ_{tank} is the torques exerted by the loss/gain of buoyancy from tanks on both sides, $V_{water,i}$ is the water volume in the ith tank, Δp_{hi} is pressure difference around hatch, $C_{vi} = C_{d,i}A_{hatch,i}\sqrt{2/\rho}$ indicates the combined discharge coefficient, $C_{d,i}$ is the discharge coefficient, $A_{hatch,i}$ refers to the opening area of the hatch, ρ denotes water density, $N_{air,i}$ is the air transfer, and u_i refers to the air transfer rate. The slowly-varying state d includes the wave-induced roll moment τ_{wave} and additional biases, such as the weightlessness effect, fluid-memory effect, and moment of inertia variation of the tanks. Coefficient C_d for the inlet and outlet flows are assumed to be two distinctive time-invariant average values of the steady states. The parameters used in the simulations are tabulated in Table 3.7.

3.2.2   Active heave compensator

A simplified variable-displacement controlled cylinder is considered for the hydraulic system. As illustrated in Figure 2.12, the cylinder will act as an equivalent of the actual system using a set of cylinders. The position of the cylinder is regulated by the oil pumped into and out of it. In the spar body-fixed reference frame $\{S\}$, the origin point O^s is located at the spar's COG with z^s-axis downwards, while the x^s- and y^s-axes are not of importance due to the axial symmetry around the longitudinal z^s-axis.

The main assumptions for the modelling are as follows:

- The reacting force from the hydraulic actuator does not influence the vessel motion;

- There is a rigid connection between the hydraulic cylinder and the wind turbine assembly. The vertical position of the wind turbine assembly in $\{V\}$ is lifted by the displacement of the hydraulic cylinder; see Figure 2.12;

- Hydraulic fluid density is constant;

- Pipeline distance is neglected;

- The effective bulk modulus of the hydraulic fluid is constant.

The position of the tower bottom in the global reference frame $\boldsymbol{p}_b$ becomes

$$\boldsymbol{p}_b = \boldsymbol{p}_v + \boldsymbol{R}(\boldsymbol{\Phi})(\boldsymbol{p}_h^b + \boldsymbol{d}_h), \tag{3.21}$$

where $\boldsymbol{p}_v$ stands for the position of the body origin of the catamaran in the global coordinate, $\boldsymbol{p}_h^b$ is the position of the hydraulic lifting device in the body-fixed frame, and $\boldsymbol{d}_h = [0, 0, -l_h]^\top$ with $l_h > 0$ refer to the moving distance of the lifting grippers.

The velocity $\boldsymbol{v}_b$ of the tower bottom in the global frame is given by

$$\boldsymbol{v}_b = \boldsymbol{v}_v + \boldsymbol{R}(\boldsymbol{\Phi})\boldsymbol{S}(\boldsymbol{\omega}_v)(\boldsymbol{p}_h^b + \boldsymbol{d}_h) + \boldsymbol{R}(\boldsymbol{\Phi})\boldsymbol{v}_h, \tag{3.22}$$

where $\boldsymbol{v}_v$ is the velocity of the body origin of the catamaran in the global coordinate, and $\boldsymbol{v}_h = [0, 0, -\dot{l}_h]^\top$. The load pressure P is defined as

$$P = \begin{cases} P_1 - P_r, & \text{if } P_1 > P_r \\ P_r - P_2, & \text{if } P_2 > P_r, \end{cases} \tag{3.23}$$

Table 3.8: Parameters of the hydraulic system.

Parameter	Symbol	Value
Cylinder cross-section area (m^2)	A	0.39
Bulk modulus (-)	β	2e9
Fluid leakage coefficient (-)	c_l	1e-7
Mass of the hydraulic piston (tonnes)	m_h	1
Friction coefficient (Ns/m)	f_c	1e5
Volume of fluid in the pipeline (m^3)	V_0	0.5

where P_r denotes the return pressure, considered constant, and P_1 and P_2 are the pressures on the two chambers of the cylinder.

The state-space equation of the one-degree variable displacement controlled cylinder system is

$$\dot{l}_h = v_h, \tag{3.24a}$$

$$\dot{v}_h = \frac{1}{m}(-f_c v_h + PA + F_{ext}), \tag{3.24b}$$

$$\frac{V}{\beta}\dot{P} = -Av_h - c_l P + u, \tag{3.24c}$$

where v_h denotes the moving velocity of the lifting grippers, m is the total mass including the mass of the hydraulic cylinder m_h and the mass of the turbine assembly m_t, f_c is the friction coefficient, A is the cross-section area of the cylinder, F_{ext} is the external force due to gravity of the turbine assembly, $V = V_0 + Al_h$ is the effective volume of the cylinder, V_0 is the fluid volume in the pipelines, β is bulk modulus of the hydraulic fluid, c_l is the fluid leakage coefficient, and u is equivalent to the axis rotating speed of the pump ω times pump displacement D_p.

Chapter 4

Main results and contributions

This chapter briefly reviews the main results in the thesis. Numerical simulation-verification models are first developed by using the proposed MarIn (**Mar**ine **In**stallation) toolbox in Section 4.1. The performance of the automated single blade installation system is then presented in sections 4.2.1–4.2.3. The results of the roll-reduction system and active heave compensator are shown in Section 4.3.1 and Section 4.3.2, respectively.

4.1 Numerical simulation toolbox for offshore operations

The MarIn toolbox is verified through code-to-code verification tests. The tests are conducted using the HAWC2 and MATLAB/Simulink with the NREL 5 MW reference wind turbine. Structural and aerodynamic coefficients are correctly read from the HAWC2 files, such as mass matrix, aerodynamic coefficient lookup tables, and COG position. Both steady wind fields and turbulent wind fields are simulated. The wind-induced loads are quadratic according to the wind speed, which agrees with the expectation.

Two illustrating examples of simulation verification models (SVMs) are given to present the applications of the proposed toolbox. The aforementioned single blade installation and preassembly installation are simulated in MATLAB/Simulink, respectively, shown in figures 4.1–4.2. For the catamaran scenario, the MSS toolbox (MSS. Marine Systems Simulator 2010) is combined with the MarIn toolbox.
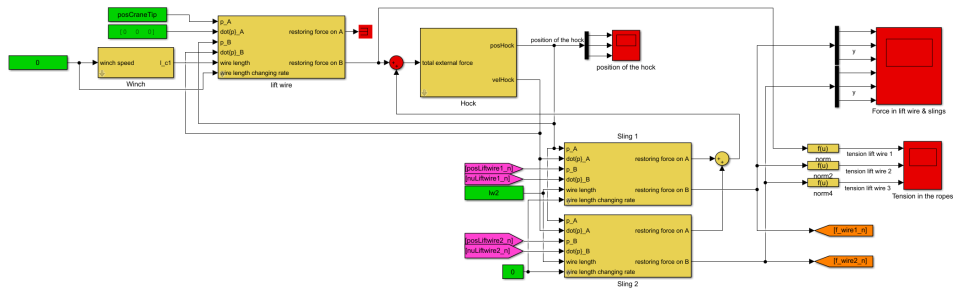
(a) Lift wire, hook, and slings.
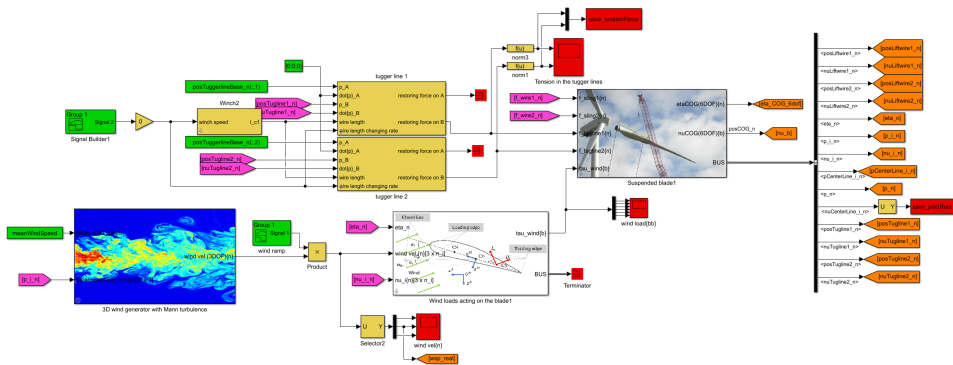
(b) Blade, tugger lines, turbulent wind field, and wind load.

Figure 4.1: Illustration of the single blade installation model. Source: Ren et al. (2017).
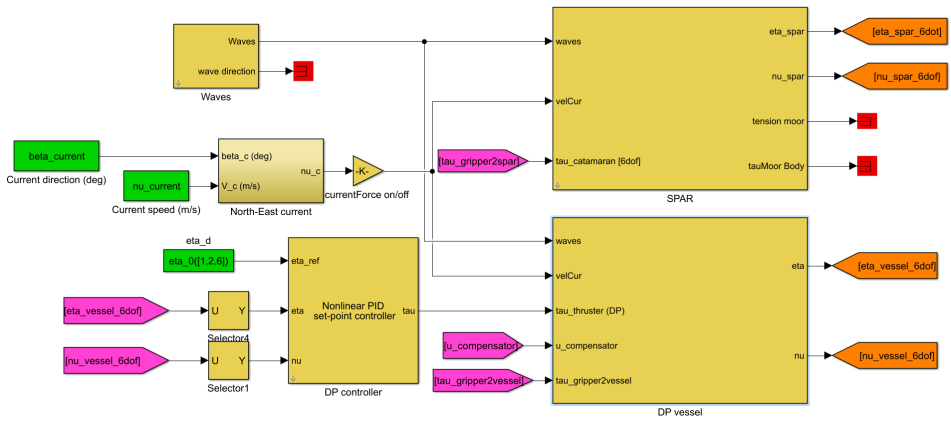
(a) Catamaran, spar, and dynamic positioning system.
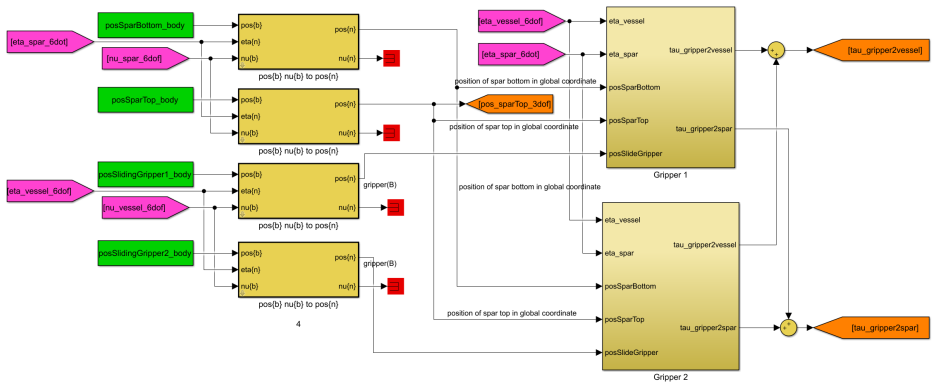
(b) Gripper.

Figure 4.2: Illustration of the preassembly installation model.

A series of code-to-code verification tests are conducted to verify that the proposed code models the blade with realistic parameters and coefficients. The tests are conducted using the HAWC2 and MATLAB/Simulink with the NREL 5 MW reference wind turbine blade.

The aerodynamic coefficients and wind-induced loads acting on the blade with respect to different wind speeds, roll angles, and yaw angles are presented in Figure 4.3. The pitch angle is set to 10, 30, 50, 60, and 90 degrees. The proposed model calculates the wind load quadratically according to the wind speed. In the figures, curves from the HAWC2 and the proposed Simulink model agree well. Therefore, the results confirm that the Simulink module calculates the aerodynamic coefficients and force correctly.
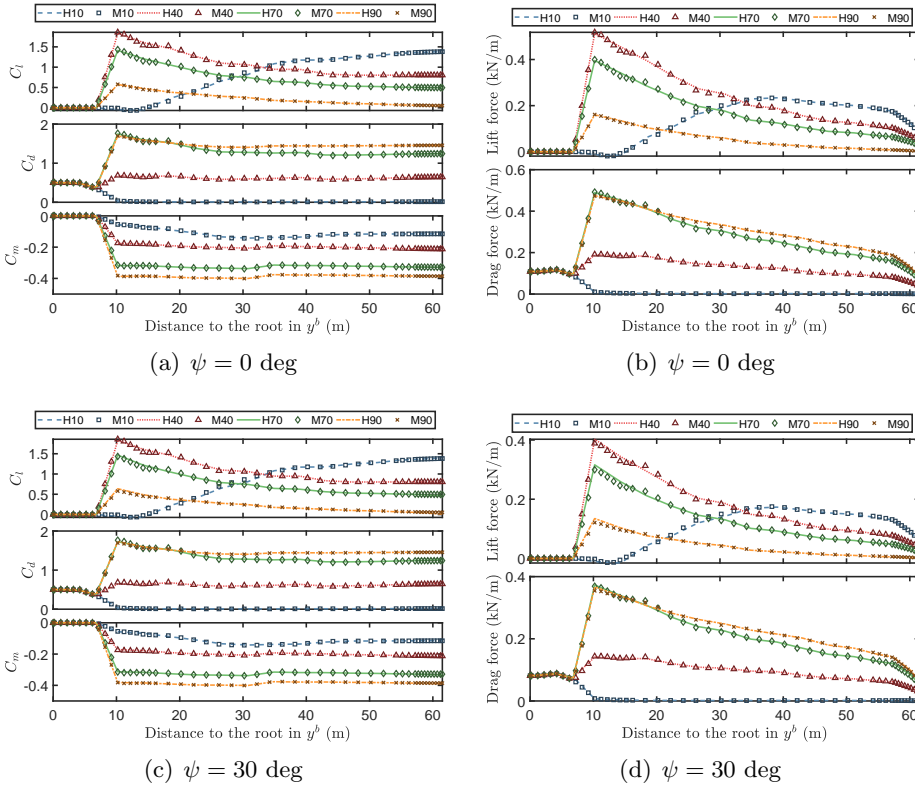
Figure 4.3: (Left) Aerodynamic coefficients C_l, C_d, C_m, w.r.t. θ and y^b; (Right) lift force and drag force per unit length. (In the legend, H and M denote the results from HAWC2 and the proposed toolbox, respectively. The numbers represent the pitch angles in deg.) Source: Ren et al. (2017).

The total loads acting on the blade are verified with respect to various wind speeds and blade pitch angles. The resulting forces at the steady states are presented in Figure 4.4. It is noticed that the wind-generated forces F_x and F_z are well-fitted and are proportional to the square of the mean wind speed. Deviations between the HAWC2 and proposed model occur in the subplot F_y. This is because of the different mechanics used in simulation, that is, Timoshenko beam elements in HAWC2 and the rigid body with assumed zero sway force in the proposed model. Comparing with the magnitudes of F_x and F_z, the deviation in F_y is very small and considered negligible for the intended use of our model.

(a) $\psi = 0$ deg   (b) $\psi = 30$ deg
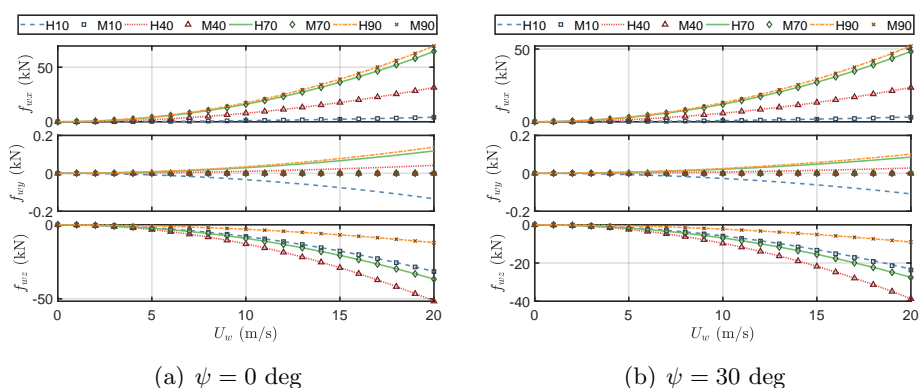
Figure 4.4: Total force acting on the blade in $\{B\}$. (In the legend, H and M denote the results from HAWC2 and the proposed toolbox, respectively. The numbers represent the pitch angles in deg.) Source: Ren et al. (2017).

4.2 Automated single blade installation using a jackup vessel

4.2.1 Optimal blade lifting control

The optimal lifting control is verified by a NREL 5 MW wind turbine blade. The system parameters has been introduced. Class C turbulent winds with corresponding turbulence intensity (TI) are adopted in the simulations. Applying nonlinear model predictive control (NMPC) technique, the dynamic tension on the lift wire is significantly reduced to almost less than 40% of those resulting from a conventional PD controller. The simulation results are shown in Figure 4.5.

The NMPC controller significantly reduces the dynamic tension at the start
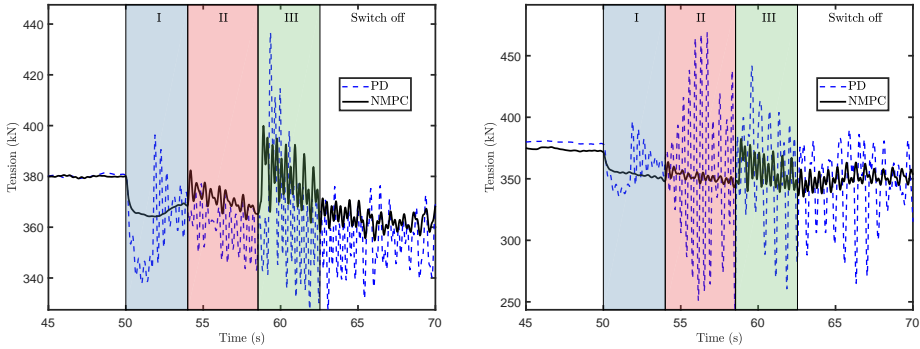
Figure 4.5: Comparison of the time-domain simulation results of the tension on the lift wire: (left) mean wind speed 8 m/s, $TI = 0.174$, (right) mean wind speed 12 m/s, $TI = 0.146$. Source: Ren et al. (2019).

and end of a lifting operation with or without system uncertainties, such as poorly estimated stiffness and mean wind speed. The statistic results in Figure 4.5 show that the system uncertainties do not significantly influence the controller's performance. The robustness of the proposed NMPC law is therefore satisfactory.
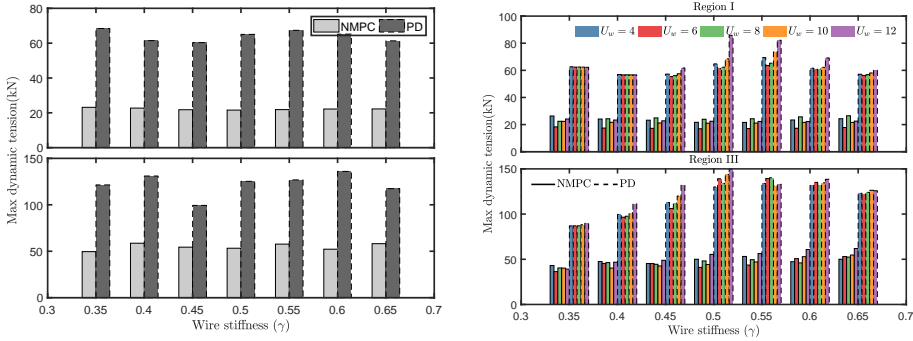
Figure 4.6: Comparison of the maximum dynamic tensions resulting from the NMPC and PD controllers: (left) mean wind speed = 0 m/s, (right) mean wind speed = 4-12 m/s (upper: startup, lower: slowdown). Source: Ren et al. (2019).

4.2.2 High-fidelity hub motion estimation

The monopile foundation is under the wave loads and induced large motions at the hub position. The hub motion estimators (HMEs) are developed based on the integration of GNSS and IMU. The time-domain estimation

performance are presented in Figure 4.7. Both HME1 and HME2 greatly improves the GPS measurement in terms of both the accuracy and sampling rate. The estimation algorithms provide high-frequency real-time hub motion state estimates of the installation process. The GPS delay is compensated.
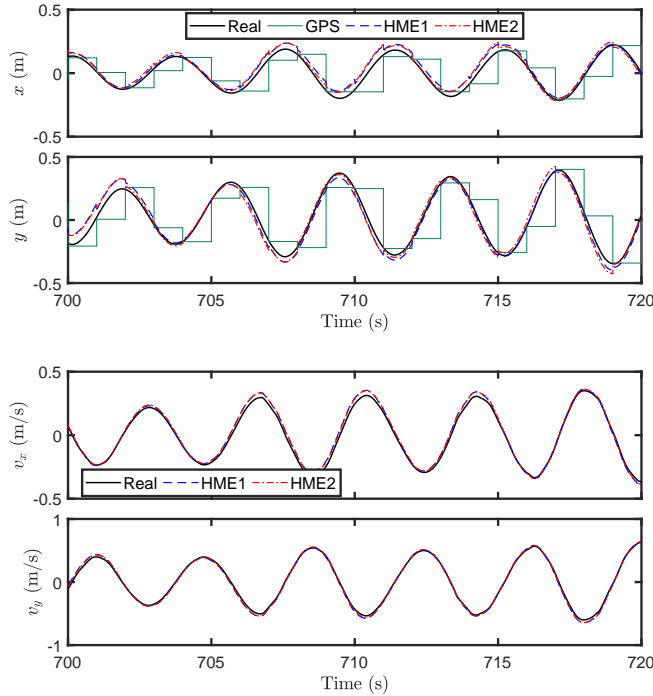
Figure 4.7: Estimation performance of the hub motion estimator: (upper) position estimate, (lower) velocity estimate, $H_s = 2$ m, $T_p = 6$ s, $\beta_{wave} = 30°$, $S_{wave} = 10$, $U_w = 8$ m/s, and $TI = 0.146$.

Taking the natural periods 4, 6, and 8 seconds as examples, the influence of the oscillation amplitudes on the various estimation schemes are shown in figures 4.8–4.10. It is easy to notice that the mean square errors (MSEs) of both position and velocity estimates increase with the motion amplitude. The extended Kalman filter (EKF) fails to accurately monitor the motion when $N_a \geq 0.1$. Use of only the multirate Kalman filter (MKF) without shift register yields medium performance results as compared with HME1 and HME2. With the correction by the predictor, the delay increases when the multirate Kalman filter (MKF) updates with the delayed IMU specific force measurement from shift register.

For an OWT with a first fore-aft natural period 4 s, HME2 estimates the position better when the oscillation amplitude is less than 0.3 m, whereas HME1 shows better performance when the amplitude is larger than 0.3 m; see Figure4.8. For an OWT with a 6-second natural period, the performance boundary is at an amplitude of 1 m; see Figure 4.9. Normally, the hub motion amplitude is located in the yellow envelope. Hence, both the HME1 and HME2 will improve the estimation performance over a single MKF.

4.2.3   Suspended blade stabilization

The time-domain results of the controller in Ren, Jiang, Skjetne & Gao (2018a) are presented in Figure 4.11. Compared with the passive scheme, the active control scheme significantly reduced the blade surge motion in the wind direction. Compared to the blade surge motion, the sway and heave motions in the y- and z-directions are small, with the absolute motion maxima below 0.2 m.

The statistic results of a series of 600-second simulations are illustrated in figures 4.12–4.13. The standard deviation and the motion maxima are used as the main criteria for evaluating the effect of active control. Considering the fact that the most critical motion is in the inflow direction x and the spanwise-direction motion y is relatively small, the active control scheme reduces the overall motion effectively. The controller greatly reduced the motion by more than 90% in the inflow direction, both at the COG and root center. The z-axis motion at the blade COG is also effectively reduced by the control scheme. However, the z motion at the blade root center is almost the same in the two cases. Therefore, it is concluded that the z motion depends on the blade roll motion, which is not controlled in this paper. Though the motion standard deviation and motion maxima is larger in the spanwise direction y, the active controller still provides beneficial performance improvement.

4.3   Tower-nacelle-rotor assembly installation using a catamaran

4.3.1   Roll reduction tanks

According to the internal model principle, reference signal or external disturbances can be asymptotically tracked if the external generator model is suitably reduplicated in the feedback path of the closed-loop control system. The control algorithm is developed with Lyapunov stability proof and an exosystem which is employed as a disturbance observer.
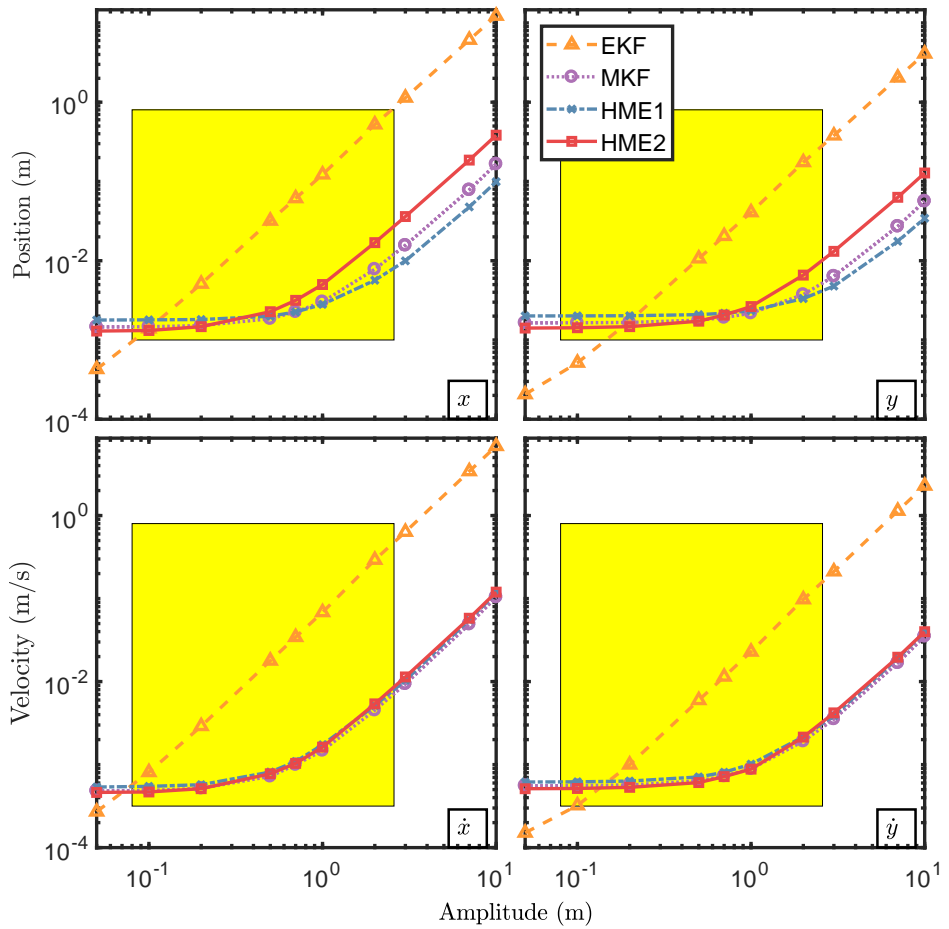
Figure 4.8: MSE of hub motion estimates using different methods in various hub motion amplitudes, natural period 4 seconds.
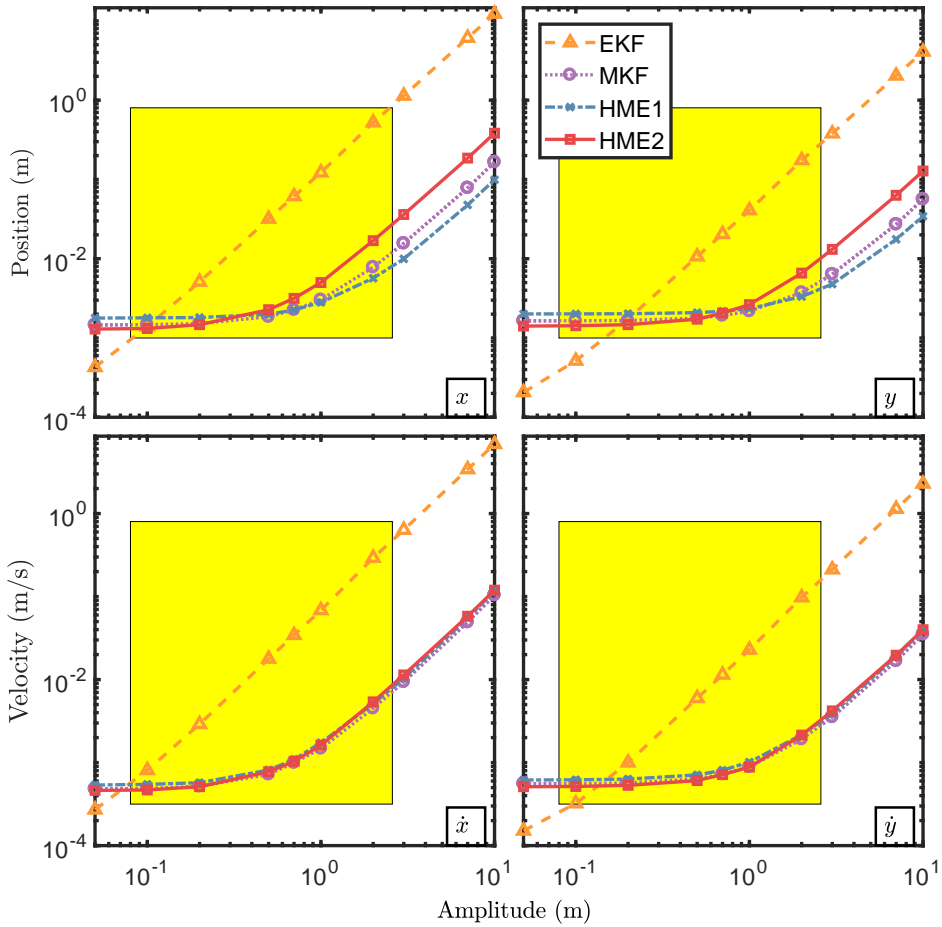
Figure 4.9: MSE of hub motion estimates using different methods in various hub motion amplitudes, natural period 6 seconds.
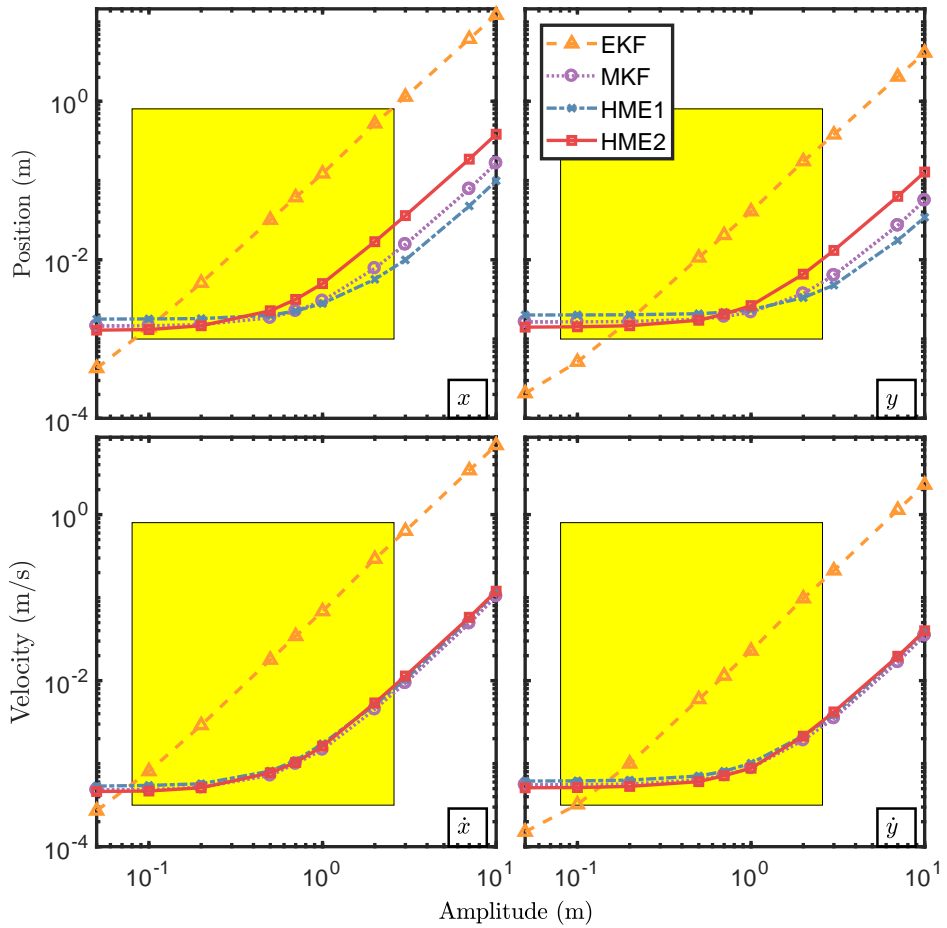
Figure 4.10: MSE of hub motion estimates using different methods in various hub motion amplitudes, natural period 8 seconds. Source: Ren, Skjetne, Jiang, Gao & Verma (2018).
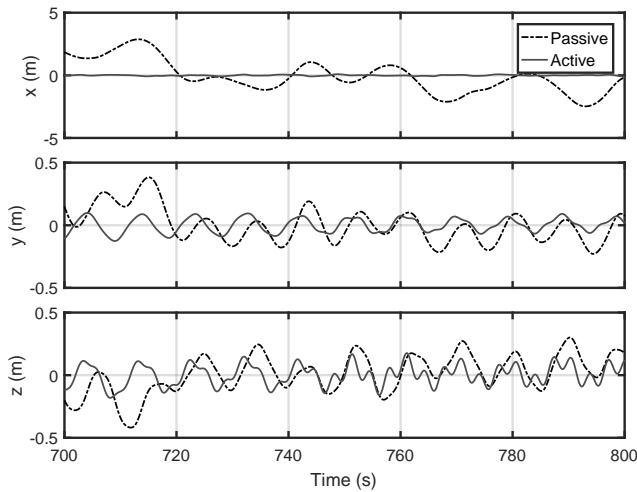
Figure 4.11: Time histories of the blade root center displacement relative to the mean position using the SVM, $U_w = 10$ m/s and TI=0.157. Source: Ren, Jiang, Skjetne & Gao (2018a).

The time-domain results are shown in Figure 4.14. The observer estimates the wave-induced disturbance well after the initialization period. An improved performance is achieved after the tank length is increased from 15 m to 20 m. The controller largely reduces the amplitude of the roll motion. The control performance is improved by increasing the control gains. However, the aggressive control also amplifies the energy input and challenges the physical capability of the actuators.

4.3.2   Active heave compensator

The time-domain simulation results of the relative displacement and velocity between the spar top and preassembly bottom are presented in Figure 4.15. Without AHC, responses of the tower bottom were derived from rigid body motions of the catamaran, and the catamaran's heave and pitch motions contribute to the tower-bottom heave responses. The spar-top motion is dominated by heave resonance of the spar, which is smaller than the tower bottom motion. The AHC minimizes the relative heave motion. After employing the AHC, the relative velocity is on the order of 0.2 m/s, which is expected to be handled by the protection system during the mating process.

(a) $U_w = 6$ m/s

(b) $U_w = 8$ m/s
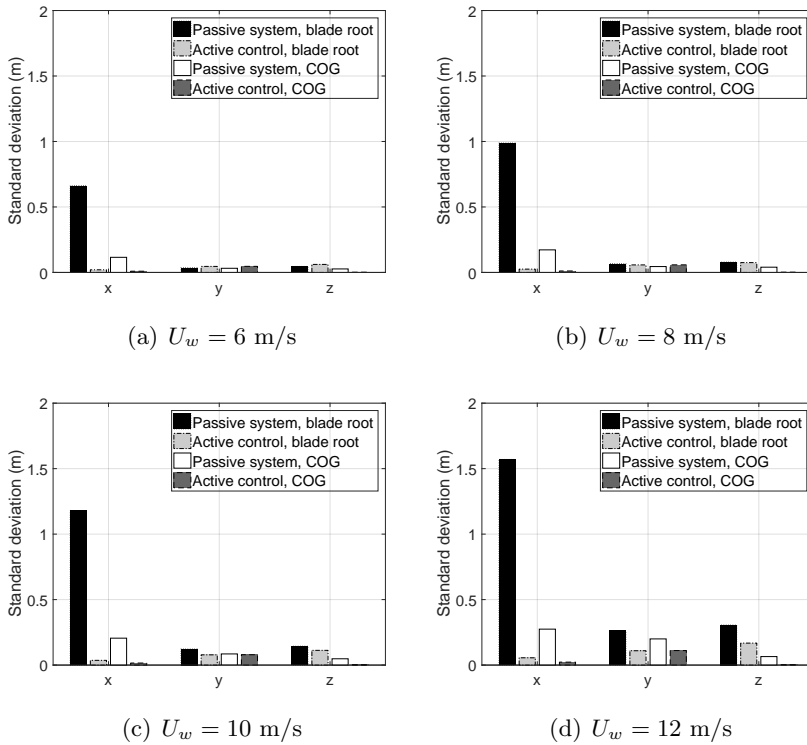
(c) $U_w = 10$ m/s

(d) $U_w = 12$ m/s

Figure 4.12: Standard deviation of the motions at the blade root center and the blade COG; $U_w = 6 - 12$ m/s, average of five 600-second simulations. Source: Ren, Jiang, Skjetne & Gao (2018a).

(a) U_w = 6 m/s

(b) U_w = 8 m/s

(c) U_w = 10 m/s

(d) U_w = 12 m/s

Figure 4.13: Motion maxima of the blade-root center and the blade COG; U_w = $6 - 12$ m/s, average of five 600-second simulations. Source: Ren, Jiang, Skjetne & Gao (2018a).

(a) H_s = 3.6 m, L_{tank} = 15m, and T_p = 12 s

(b) H_s = 3.6 m, L_{tank} = 20m, and T_p = 12 s

Figure 4.14: Controller performance of the anti-roll tanks. Source: Xu et al. (2018).

Figure 4.15: Time history of the relative heave displacement and velocity between the spar top and the tower bottom, H_s=2.0 m, T_p=10 s, $_{wave}$=0 deg (left) without AHC (right) with AHC. Source: Jiang, Ren, Gao, Sandvik, Halse, Skjetne et al. (2018).

Chapter 5

Conclusions and recommendations for future work

The thesis aims to improve the operational efficiency of OWT installation by introducing automated control. Two OWT installation strategies are studied, i.e., single blade installation to a bottom-fixed OWT with a monopile foundation using a jackup vessel and tower-nacelle-rotor preassembly installation to a spar foundation using a catamaran vessel. The operational criteria in all stages are analyzed and discussed. Several controllers and estimators have been developed. Various single blade installation models have been investigated. Time-domain simulations and sensitivity studies have been conducted to verify the performance of the proposed algorithms.

5.1   Contributions

Single blade installation to a bottom-fixed OWT with a monopile foundation using a jackup vessel

- The entire single blade installation process is categorized into four stages, i.e., the lifting (Stage 1), stabilization (Stage 2), transporting (Stage 3), and mating (Stage 4).

- A user-friendly numerical modeling framework for the OWT blade installation is developed for control design purposes. Necessary modules are included in the toolbox, such as crane, hook, blade, wire rope,

winch, several payloads, aerodynamic loads, and turbulent wind field. Being compatible with the widely used MSS toolbox, the proposed modeling framework can be adopted to simulate all sorts of onshore and offshore wind turbine installation processes.

- To facilitate the design of the observer algorithm and control law, the blade installation system was simplified as two 3DOF control design models for different stages and control objectives, the blade lifting model (Stage 1) and blade-hub mating model (Stages 2–4). In the lifting model, the hook, yoke, and blade are modeled as a 3DOF lumped-mass rigid-point payload. The lift wire and slings are modeled as a generalized tensile spring. In the mating model, the blade 3DOF horizontal model are considered. Tugger lines are involved to restrain the displacement.

- A nonlinear model predictive controller is adopted to optimize the lifting problem, by limiting the sudden overloads and avoiding snatch loads.

- A closed-loop scheme for active tugger line force control is developed to stabilize the pendular motion of the suspended blade in a turbulent wind field. An extended Kalman filter, a state feedback linearization and feedforward compensation algorithm, and pole placement techniques are utilized to design the controller. A third-order reference model was adopted to provide smooth position and velocity trajectories in real time.

- Two highly precise GNSS/IMU integration schemes are proposed to estimate the real-time OWT hub motion. The state observer filters the noise in the GPS and the IMU, overcomes the GPS delay, and achieves high-frequency displacement and velocity monitoring functionalities in real time. The systems include a multirate Kalman filter, an online RTS smoother, a moving horizon estimator, and a predictor.

Tower-nacelle-rotor preassembly installation to a spar foundation using a catamaran vessel

- The roll reduction tank and the hydraulic heave compensator are modeled for control design.

- The control algorithm of the roll-reduction control system is developed for the catamaran installation vessel. The wave-induced moment to the vessel in a feedback system is estimated by an exosystem.

- The active heave compensator is developed to reduce the relative vertical motion between the OWT preassembly and the spar foundation. Singular perturbation theory is used to handle the fast natural frequency of the hydraulic system.

5.2   Conclusion

Code-to-code verification studies with HAWC2 are conducted to prove the effectiveness and correctness of the proposed model. The proposed controller successfully prevents the sudden peak tension, tension dynamics, and the axial oscillation. The NMPC controller still performs well when the lift wire stiffness is poorly modeled or the suspended blade is exposed to a turbulent wind field. Time-domain simulation results, in turbulent wind conditions, show that the proposed automatic single blade installation scheme using active tugger line tension control worked well. The active control scheme can effectively reduce the blade-root surge motion standard and maxima deviations, resulting in an expediting mating operation. Sensitivity studies are conducted to shows that the hub motion estimates agree well with the real values for position, velocity, acceleration, and bias in various configurations and environmental conditions. The performance of the state estimators is affected by the oscillation amplitude and the natural period of the hub structure.

Vacuum pumps with active stabilization controller provide optimal filling in these tanks based on input from the ship movement. For vessels which operate mostly at low speed and a relatively calm sea state, the proposed roll reduction system provides great performance with minor cost. Bigger tank is required for severe sea state. The active heave compensator can effectively reduce the relative heave velocity and can potentially improve the safety of the mating process.

5.3   Recommendations for future work

To future improve the automation level of wind turbine installation, the following extensions of the topics treated in this thesis, are well suited for future work.

- The simulation verification model can be improved by including more complex models and functions. For example, complex aerodynamic effects can be integrated into the system, such as wake.

- To further improve the lifting system performance when exposed to

higher wind speeds and model uncertainties, the further research emphasis is on adaptive and robust optimal control schemes, e.g., tube-based model predictive control. In addition, NMPC applications to the blade lifting operation using a floating installation vessel for deep water installation is recommended to be investigated.

- The most critical horizontal relative motion has been greatly reduced by the proposed active tugger line control schemes. In future research, the vertical motion at the blade root should be reduced through more effective tugger line placement and corresponding controller.

- Hub oscillation is a periodic motion. Innovative observer design considering the periodic states can benefit the estimation performance.

- The acceleration is proportional to the external loads. Instead of position estimation, external load estimation using a system of IMUs is a promising topic. Additionally, the load and response estimates can be improved by placing a number of sensors at different places of the payload.

- Extreme motion and load prediction in short term is recommended to study for improved decision support during the operations. To ensure a sufficiently long reaction time for the operators, the warning should be based on prediction. Estimator design, prediction algorithms, and actuator control to ensure data robustness and satisfied performance are worthy to study.

The following topics are interesting for future more autonomous marine operations:

- Compared to today's autonomous systems, a human has superior judgment, higher flexibility, and better overview in complex scenarios. Though the development moves towards unmanned autonomous functions, meaningful human control and human-in-the-loop control will be interesting topics of research for many decades. though the topic is far outside the scope of this thesis, an interesting research question is how autonomous control functions and decision support functions can be integrated to ensure meaningful human control.

- The present marine operations are typically conducted by a single vessel. Alternatively, different (and possibly smaller) vessels can collaborate in some operations. Novel and efficient designs for wind turbine

installation can be developed. The bigger preassembled wind turbine can be installed with cooperation by several small vessels. A setup of multiple load-lifting systems (e.g., two vessels each with a crane) cooperating on lifting and moving a payload is recommenced for study.

- The cooperative marine operations typically require a maximized communication between the vessels. However, in some situations, the communication is reduced or becomes missing. In control theory there are many results on how cooperative dynamical systems can safely continue with reduced or intermittent communication. Interesting questions are therefore the modeling of the distributed system and intelligent control of the individual vessels to complete the overall operation with reduced communication.

Bibliography

American Petroleum Institute (2000), *API RP 2A-WSD Recommended Practice for Planning, Designing and Constructing Fixed Offshore Platforms: Working Stress Design*, American Petroleum Institute.

Anderson Jr, J. D. (2010), *Fundamentals of aerodynamics*, Tata McGraw-Hill Education.

Bossanyi, E. (2009), 'GH bladed user manual', *Garrad Hassan Bladed* .

Energinet (2018), Environmental report 2018, Technical report, Energinet, Fredericia, Denmark.

Espinoza, A. (2016), 'Block island wind farm enters final construction phase'. http://ripr.org/post/block-island-wind-farm-enters-final-construction-phase#stream/0, Accessed: November 19, 2017.

Fossen, T. I. (2011), *Handbook of marine craft hydrodynamics and motion control*, John Wiley & Sons.

Froese, M. (2016), 'Dong energy hits milestone with 1,000 wind turbines at sea', https://www.windpowerengineering.com/business-news-projects/dong-energy-hits-milestone-1000-wind-turbines-sea/. [Online; accessed 21-January-2019].

HighWind (2018), 'The boom lock', http://www.high-wind.eu/boomlock/. [Online; accessed 10-August-2017].

Jiang, Z., Gao, Z., Ren, Z., Li, Y. & Duan, L. (2018), 'A parametric study on the final blade installation process for monopile wind turbines under rough environmental conditions', *Engineering Structures* **172**, 1042–1056.

Jiang, Z., Hu, W., Dong, W., Gao, Z. & Ren, Z. (2017), 'Structural relia-
bility analysis of wind turbines: a review', *Energies* **10**(12), 2099.

Jiang, Z., Li, L., Gao, Z., Halse, K. H. & Sandvik, P. C. (2018), 'Dynamic
response analysis of a catamaran installation vessel during the positioning
of a wind turbine assembly onto a spar foundation', *Marine Structures*
61, 1–24.

Jiang, Z., Ren, Z., Gao, Z., Sandvik, P. C., Halse, K. H., Skjetne, R. et al.
(2018), Mating control of a wind turbine tower-nacelle-rotor assembly for
a catamaran installation vessel, *in* 'The 28th International Ocean and Po-
lar Engineering Conference', International Society of Offshore and Polar
Engineers.

Jonkman, B. J. & Kilcher, L. (2012), TurbSim user's guide: Version 1.06,
Technical report, National Renewable Energy Laboratory Colorado.

Jonkman, J. M. & Buhl Jr, M. L. (2005), FAST user's guide-updated august
2005, Technical report, National Renewable Energy Laboratory (NREL),
Golden, CO.

Kaiser, M. J. & Snyder, B. F. (2013), 'Modeling offshore wind installation
costs on the us outer continental shelf', *Renewable energy* **50**, 676–691.

Kelley, N. D. & Jonkman, B. J. (2006), Overview of the TurbSim stochas-
tic inflow turbulence simulator: Version 1.21, Technical report, National
Renewable Energy Laboratory (NREL), Golden, CO.

Lacal-Arántegui, R., Yusta, J. M. & Domínguez-Navarro, J. A. (2018), 'Off-
shore wind installation: Analysing the evidence behind improvements in
installation time', *Renewable and Sustainable Energy Reviews* **92**, 133–
145.

Larsen, T. J. & Hansen, A. M. (2007), How 2 HAWC2, the user's manual,
Technical report, Risø National Laboratory.

Li, L., Acero, W. G., Gao, Z. & Moan, T. (2016), 'Assessment of allowable
sea states during installation of offshore wind turbine monopiles with
shallow penetration in the seabed', *Journal of Offshore Mechanics and
Arctic Engineering* **138**(4), 041902.

Li, L., Gao, Z. & Moan, T. (2016), Operability analysis of monopile lowering
operation using different numerical approaches, ISOPE.

Li, L., Gao, Z., Moan, T. & Ormberg, H. (2014), 'Analysis of lifting operation of a monopile for an offshore wind turbine considering vessel shielding effects', *Marine structures* **39**, 287–314.

Liftra (2018), 'Lt575 blade dragon', `http://liftra.com/product/blade-dragon/`. [Online; accessed 10-August-2017].

Maes, K., De Roeck, G. & Lombaert, G. (2018), 'Motion tracking of a wind turbine blade during lifting using rtk-gps/ins', *Engineering Structures* **172**, 285–292.

Mann, J. (1998), 'Wind field simulation', *Probabilistic Engineering Mechanics* **13**(4), 269 – 282.

Matlock, H. & Reese, L. C. (1960), 'Generalized solutions for laterally loaded piles', *Journal of the Soil Mechanics and foundations Division* **86**(5), 63–94.

Moaleji, R. & Greig, A. R. (2007), 'On the development of ship anti-roll tanks', *Ocean Engineering* **34**(1), 103–121.

MSS. Marine Systems Simulator (2010), 'Viewed 30.10.2014'.
URL: *http://www.marinecontrol.org*

Rasekhi Nejad, A., Li, L., Acero, G., Ivan, W. & Moan, T. (2018), A systematic design approach of grippers hydraulic system utilized in offshore wind turbine monopile installation, *in* 'ASME 2018 37th International Conference on Ocean, Offshore and Arctic Engineering-Volume 11A: Honoring Symposium for Professor Carlos Guedes Soares on Marine Technology and Ocean Engineering', ASME.

Ren, Z., Jiang, Z., Skjetne, R. & Gao, Z. (2018*a*), 'An active tugger line force control method for single blade installations', *Wind Energy* **21**(12), 1344–1358.

Ren, Z., Jiang, Z., Skjetne, R. & Gao, Z. (2018*b*), 'Development and application of a simulator for offshore wind turbine blades installation', *Ocean Engineering* **166**, 380–395.

Ren, Z., Jiang, Z., Skjetne, R., Gao, Z. et al. (2018), Single blade installation using active control of three tugger lines, *in* 'The 28th International Ocean and Polar Engineering Conference', International Society of Offshore and Polar Engineers, pp. 594–601.

Ren, Z., Skjetne, R. & Gao, Z. (2017), Modeling and control of crane overload protection during marine lifting operation based on model predictive control, *in* 'ASME 2017 36th International Conference on Ocean, Offshore and Arctic Engineering', American Society of Mechanical Engineers, pp. OMAE2017–62003.

Ren, Z., Skjetne, R. & Gao, Z. (2019), 'A crane overload protection controller for blade lifting operation based on model predictive control', *Energies* **12**(1), 50.

Ren, Z., Skjetne, R., Jiang, Z., Gao, Z. & Verma, A. S. (2018), 'Integrated GNSS/IMU hub motion estimator for offshore wind turbine blade installation', *Mechanical Systems and Signal Processing* **123**, 222–243.

RWE Innogy GmbH (2014), 'Halfway through the turbine installation for the nordsee ost offshore wind farm'. [Online; accessed 16-July-2017].

Stehly, T., Heimiller, D. & Scott, G. (2017), *2016 Cost of wind energy review*.

Verma, A. S., Jiang, Z., Ren, Z., Gao, Z. & Vedvik, N. P. (2019), 'Effects of wind-wave misalignment on a wind turbine blade mating process: impact velocities, blade root damages and structural safety assessment', *Journal of Marine Science and Application* . Under review.

Verma, A. S., Jiang, Z., Vedvikc, N. P., Gao, Z. & Ren, Z. (2018), 'Impact assessment of blade root with a hub during the mating process of an offshore monopile-type wind turbine', *Engineering Structures* . In press.

Verma, A. S., Vedvik, N. P., Haselbach, P. U., Gao, Z. & Jiang, Z. (2019), 'Comparison of numerical modelling techniques for impact investigation on a wind turbine blade', *Composite Structures* **209**, 856–878.

Wind Europe (2017), 'Floating offshore wind vision statement'.

Wind Europe (2018), Wind in power 2017. annual combined onshore and offshore wind energy statistics, Technical report, International Electrotechnical Commission and others, Brussels, Belgium.

Xu, J., Ren, Z., Li, Y., Skjetne, R. & Halse, K. H. (2018), 'Dynamic simulation and control of an active roll reduction system using free-flooding tanks with vacuum pumps', *Journal of Offshore Mechanics and Arctic Engineering* **140**(6), 061302.

Zervos, A. & Kjaer, C. (n.d.), Pure power. wind energy scenarios up to 2030, Technical report.

Zhao, Y., Cheng, Z., Sandvik, P. C., Gao, Z. & Moan, T. (2018), 'An integrated dynamic analysis method for simulating installation of single blades for wind turbines', *Ocean engineering* **152**, 72–88.

Part II

Selected publications

Paper A1

Development and application of a simulator for OWT blades installation

Zhengru Ren, Zhiyu Jiang, Roger Skjetne, and Zhen Gao

Development and application of a simulator for offshore wind turbine blades installation

Zhengru Ren[a,b,c], Zhiyu Jiang[a,c,*], Roger Skjetne[a,b,c], Zhen Gao[a,b,c]

[a] Centre for Research-based Innovation of Marine Operations (SFI MOVE), Norwegian University of Science and Technology (NTNU), NO-7491 Trondheim, Norway
[b] Centre for Autonomous Marine Operations and Systems (AMOS), NTNU, NO-7491 Trondheim, Norway
[c] Department of Marine Technology, NTNU, NO-7491 Trondheim, Norway

ARTICLE INFO

ABSTRACT

In an offshore environment, offshore wind energy resources are more available and stable, but the investment cost is much higher than that of onshore wind. The installation cost is a crucial factor of the investment. With the increasing number of planned and approved offshore wind farms, offshore wind turbine installation and relevant operations have received tremendous attention. Therefore, expediting the turbine-structure mating operations through a higher level of automation in offshore wind turbine installations may provide important economic benefits. To achieve a higher automation level and reduce the weather waiting time during the installation of offshore wind turbines, a flexible simulation-verification framework with high fidelity is needed. However, state-of-the-art wind turbine numerical analysis code is neither convenient nor open enough for applications concerning the design and verification of control algorithms. MATLAB/Simulink is among the most widely utilized numerical platforms by control engineers and researchers. This paper describes the development of a modularized blade installation simulation toolbox for the purpose of control design in MATLAB/Simulink. The toolbox can be used to simulate several blade installation configurations, both onshore and offshore. The paper presents the key features and equations of the different modules, exemplified by a single blade installation operation. Code-to-code verification results are presented and discussed with both quasi-steady wind and three-dimensional turbulent wind field.

1. Introduction

With the growing interest and need for clean energy, wind energy has become increasingly popular in recent years. Wind turbines are categorized into onshore wind turbines and offshore wind turbines (OWTs) based on their installation locations. Because of their high initial installation and lifespan maintenance costs, the price of offshore wind energy remains more than three times higher than onshore wind energy (Moné et al., 2017). Installation expenses significantly influence the cost of offshore wind energy. Hence, techniques that can make the OWT installation more efficient are of great value.

For wind turbine blade installation, several approaches have been developed. For example, assembled rotor installation, bunny-ear configuration, and single blade installation are often used (Kaiser and Snyder, 2010; Zhao et al., 2018; Kuijken, 2015). The selection among these approaches is a trade-off among the equipment capacity, number of offshore lifting operations, weather, etc. All these factors influence the offshore operational time, deck usage, and the overall installation cost. As the example of this paper, single blade installation is a wind turbine blade installation method that is especially suitable for large-scale OWTs, as individual lifts of the blades are much easier than maneuvering of a full rotor-tower-nacelle assembly offshore. This method also facilitates deck usage and requires low crane capacity of the installation vessel. Blades are lifted and mated separately. When the weather conditions allow the operation, one blade is held by a yoke and lifted by a crane from the deck, with the blade root approaching the hub. After moving the blade to the mating position at the hub, the mating operation proceeds if the blade root motion is limited within a specified range. The single blade installation approach provides a more efficient deck utilization and reduces the transportation time, for instance, by allowing more turbine components to be carried in one trip. The disadvantage is that this installation approach typically requires more operation time. Using state-of-the-art lift equipment, the single blade installation approach is only allowed to be conducted up to a mean wind speed of approximately $8 - 12$ m/s at the hub height (Gaunaa et al., 2014). Hence, increasing the weather window for the installation work and making the lifting operation more time efficient will greatly reduce the installation costs.

Research on intelligent marine operations are seeing increasing attention (Johansen et al., 2003; Fang et al., 2014; Skaare and Egeland, 2006; Ren et al., 2018; Wang et al., 2018; Tian et al., 2018). The typical objectives are to enhance the overall efficiency, ensure safety, broaden the operating window, and, ultimately, gain economic benefits. Because single blade installation approach demands large amount of offshore working time, the installation cost can be reduced if the mating operations are accelerated by enhancing the automation level for the blade installation system. To the best of the authors' knowledge, no studies have looked into such issues. Therefore, there is an urgent need for highly efficient and user-friendly simulation tools for use during the controller design process for marine installations.

To start a control design for such a complex process as an OWT installation, a numerical model is surely needed. Open-source MATLAB/Simulink toolboxes, such as the MSS GNC and MSS Hydro toolboxes (Perez et al., 2006; MSS. Marine Systems Simulator, 2010) and MSS MarPowSim (Bø et al., 2015), are widely applied for marine control systems, e.g., the dynamic positioning of surface vessels and power management systems. However, these toolboxes lack modules to model wind turbine installations. Commercial software for marine operations, such as SIMA (MARINTEK, 2016; Jiang et al., 2015), are widely used during analysis and design. However, their closed-source policy and tedious customization of external dynamic-link libraries (DLLs) for the design of control systems weaken their applicability to control design and analysis. State-of-the-art aeroelastic codes for designing of wind turbines under normal operations, including HAWC2 (Larsen and Hansen, 2007), FAST (Jonkman and Buhl, 2005), and Bladed (Bossanyi, 2009), are based on blade element momentum (BEM) theory. Complex aerodynamic performances, such as blade tip flow, wake dynamic inflow, and dynamic stall, are modeled. Code-to-code comprehensive simulations (Jonkman et al., 2008), prove that these codes agree well with each other. Single blade installation has been studied using HAWC (Gaunaa et al., 2014; Jiang et al., 2018). Taking HAWC2 as an example, although they can interface with MATLAB/Simulink through TCP/IP or use some DLLs to implement simple control laws, there are disadvantages. First, setting up the interface and debugging the model are often time consuming. Furthermore, limitations of the supported modules restrict its flexibility and complexity, except for the blade, during modeling. Other limitations include fixed time steps and cumbersome user interfaces. In addition, numerous codes and toolboxes, for example, wind turbine gearbox (Haastrup et al., 2011), a wind turbine sub-model in an in-house computational fluid dynamics (CFD) code (Hallanger and Sand, 2013), and a computational aeroelastic tool with the Boundary Element Method (Calabretta et al., 2016), have been developed that are relevant to wind turbine simulations. None of these, however, is able to simulate blade installation.

This paper presents the development of an open-source object-oriented simulation-verification blade installation modeling toolbox targeting the design and analysis of automation and control functions. The code is developed primarily for wind turbine blade installation, but it can also be used in related fields with simple modifications. The resulting functions and modules are integrated in the **MarIn** (**Mar**ine **In**stallation) toolbox, which is under development within the SFI MOVE center at NTNU. The modularized code in MATLAB/Simulink can be used in place of commercial software with verified numerical correctness.

The main contributions of this paper are the development of an object-oriented MATLAB/Simulink-based simulation verification toolbox for the blade installation of OWTs and a verification of the model against the mainstream commercial software HAWC2.

The paper is structured as follows. In Section 2, the problem formulation and development guidelines are proposed. In Section 3, relevant coordinate systems and coordinate transformations are introduced. The models of the wire ropes, winches, and hook are presented in Section 4. The blade dynamics, wind velocity with turbulence model, and wind-induced loads are presented in Section 5.

Code-to-code verification with steady wind is conducted in Section 6 to confirm that the code calculates the correct aerodynamic loads acting on the blade. In Section 7, a single blade installation process is modeled as an example, and time-domain simulations are conducted to verify the model. Finally, the conclusion summarizes the paper.

Notations: In this paper, scalars, vectors, and matrices are denoted with normal lowercase letters, bold lowercase letters, and bold capital letters, respectively. $|x|$ stands for the Euclidean norm, i.e., $|x|^2 = x^\top x$. The overline $\bar{a}$ denotes the upper bound of a variable a, and I_n and 0_n are the identity matrix and the zero matrix of size, respectively. A nomenclature is given Appendix A.

Color codes in figures: To avoid confusion, the colors in the following diagrams have the following meanings:

- Blue: Coordinate frame
- Red: Load (force/moment)
- Green: Wind velocity

Superscripts and subscripts: Normally, the superscripts denote the coordinate systems. To simplify the expression, the global reference frame is adopted without any superscripts. The subscripts below have the following corresponding meanings:

- b Blade
- h Hook
- l Lift wire
- m Winch motor
- p Pulley (crane tip)
- r Wire rope
- s Slings
- t Tugger line
- TI Turbulence intensity
- w Wind
- y Yoke

2. Blade installation framework

2.1. Description of single blade installation

In this section, a commonly used single blade installation configuration is introduced to help the reader understand the necessary components in the toolbox and the basic ideas utilized during the modeling of such a process. The configuration of a single blade lifting operation is depicted in Fig. 1. In this example, a monopile foundation
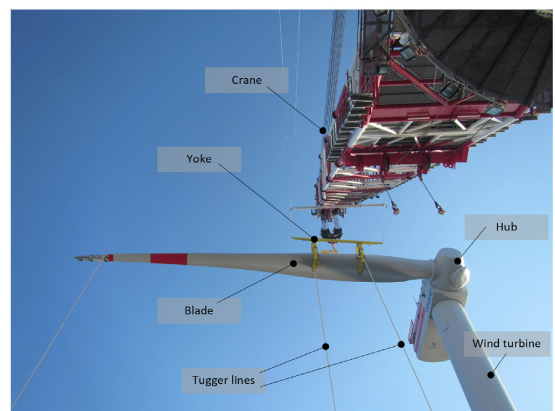

Fig. 1. The mating phase during a single blade installation (Image source: RWE GmbH (RWE Innogy GmbH, 2014)).

is considered, which has been hammered into the seabed. The supporting structures, including the transition piece, tower, and hub, were assembled subsequently. A jackup installation vessel is assumed to be conducting the single blade installation operation. The vessel-mounted crane is responsible for lifting a blade by wire ropes. A lift wire connects the crane tip and the hook, and the hook connects to a yoke with slings. A turbine blade is held by the yoke and suspended in the air. Tugger lines connecting the crane boom to the yoke are used to reduce the blade's pendulum motion. The crane-wire-hook-blade system is exposed to a windy environment with both a mean wind load and dynamic wind loads.

When the weather window allows the installation to be conducted, the hub is first rotated to the desired orientation such that the flange holes on the hub are ready to mate with the guide pins on the blade root, normally horizontally. Then, the blade is lifted from the deck to the hub elevation by controlling the boom winch and corresponding lift wire length. Afterward, the crane is rotated to move the blade horizontally to a position near the final mating point while the blade's motion is monitored. If the motion stays within the allowable range, the final mating operation is executed by manually inserting the guide pins into the flange holes. After bolting the blade and the hub, the installation is finished.

During the mating process, if the relative motions between the blade root and hub are too large, guide pins can be damaged which causes unnecessary delays. Visual guidance is needed, and banksmen are often used to give orders to the crane operator and to assist the final mating process. The need for banksmen poses potential risks in such activities. If sensorial or automated guidance can be used to automate the process, such risks can be lowered substantially.

2.2. Model assumptions

From the above description, the main components of the blade installation process are

- Physical components: vessel, crane, winch, lift wires, slings, tugger lines, hook, yoke, blade;
- Environmental components: wind turbulence simulator, and wind-induced loads.

The proposed toolbox can be applied to simulation of blade installation using either a jackup or a floating vessel. To install blades with a jackup is a simplified scenario, and the crane boom is fixed in space. The simplified configuration is illustrated in Fig. 2. For a floating installation vessel, the real-time crane tip position can be calculated by a coordinate transformation of the vessel's position and orientations and the crane configuration. Because the wind-induced loads acting on a blade are substantially smaller than the vessel's inertial and gravity

Fig. 2. Single blade installation setup.

loads, the influence of the crane on the vessel is neglected. Given the light weight of the blade system (less than 100 tonnes), it is acceptable to assume that the load and load effects on the crane caused by its payload can be disregarded. The crane flexibility can be modeled which affects the stiffness of the rigging system and hence the wire tension. Normally, an equivalent stiffness of the wire rope can be used to model the crane flexibility, in which the crane flexibility can be considered together with the actual flexibility of the rope.

Remark 1. Note that for high-fidelity numerical models for engineering design and risk assessment, such effects should not be neglected and instead should be considered. However, for the purpose of control design, one can typically reduce the fidelity of the model by disregarding fast stable dynamics to produce a simplified model capturing the most important dynamics. The control system, with its actuators, will typically dominate the loads on the plant and make it behave according to the specified control objective. That is also why it is very important to include a realistic model of the control functions when performing detailed analysis of loads and load effects.

The length of the lift wire is a sum of the wire between the crane winch drum and the crane tip and the wire between the crane tip and the hook. Two slings connect the hook to the yoke. We assume that the crane, hook, and blade are all rigid bodies and that the yoke mass is located at the blade COG. The primary objectives for active turbine installation operations are to stabilize the payloads and to move the payloads with desired trajectories. Global loads and motion analysis are of importance, while the local structural analysis with attention on structural flexibility is disregarded. Therefore, the rigid-body dynamics are the focus instead of the BEM technique adopted by operational wind turbines.

The hook dynamics is modeled in 3 degrees of freedom (DOFs), and the blade motion is simulated in 6 DOFs. The NREL 5 MW reference turbine blade is taken as an example hereafter in this paper (Jonkman et al., 2009). The mass of the yoke is concentrated at the COG of the blade. Two tugger lines are placed symmetrically about the blade COG on the yoke. The other ends of the tugger lines are fixed to the vessel, which moves with the vessel. Lift wires, slings, and tugger lines are modeled as tensile springs with specific damping coefficients, therein merely providing tension with a positive elongation.

2.3. Toolbox overview

With the simplified assumptions, the main modules in this toolbox correspond to the vessel, crane, wire rope, hook, blade, wind generator, and wind-induced loads. The proposed toolbox consists of a framework to simulate the blade installation with a relatively high fidelity for control design purposes. The modeling procedure is object oriented, therein interconnecting blocks with Newton-Euler mechanics. All components should be easy to assemble to achieve different configurations. The inputs/outputs (I/O) are tabulated in Tables A.5-A.10; see Appendix C for more details.

The configuration of an example system is presented in Fig. 3. The vessel is an optional component for offshore wind turbine blade installation. For an installation operation conducted with a floating vessel, the position of the crane tip and the ends of the tugger lines are movable. For simulating an installation using a jackup vessel rigidly fixed to the seabed, the vessel model is skipped, and the boundary conditions of the crane tip and the tugger lines are imposed. The crane tip and the hook are the ends of a lift wire. The restoring force can be calculated based on the elongation and stiffness. The same calculations are applied to the slings and the tugger lines. The total force acting on the hook is the restoring force from the lift wire and slings by disregarding the wind-induced loads. The external loads acting on the blade are the wind-induced loads and restoring forces from the corresponding connected wires.

The proposed toolbox is able to model not only single blade
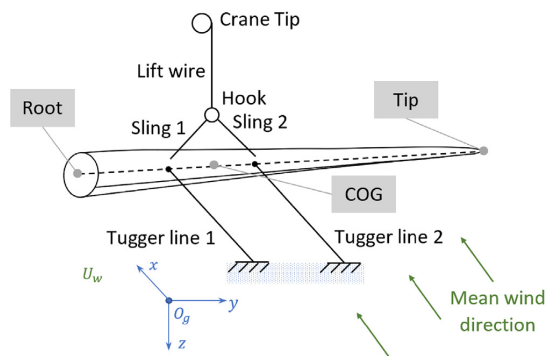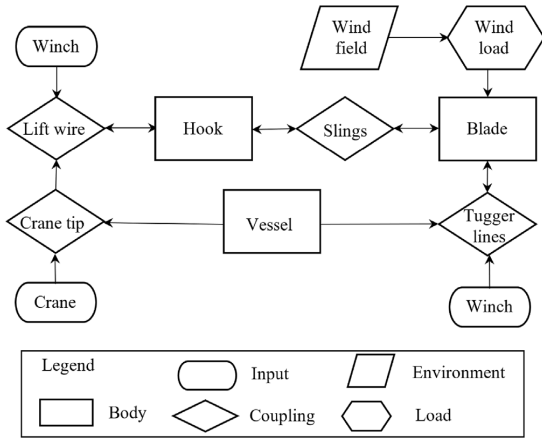
Fig. 3. Model overview.

installation but also other complex installation configurations. With the combination of individual blade modules, bunny-ear configuration and assembled rotor configurations are realizable by fixing the root end to a hub or rotor, which is modeled as a point mass. The external wind-induced loads acting on the entire payload can then be calculated.

The latest version of the proposed toolbox can be download as a .zip file at https://github.com/NTNU-MCS/MarIn.

3. Coordinate systems and coordinate transformation

3.1. Coordinate systems

We use the convention that all the coordinate systems follow the right-hand rule. To sum up the wind-induced load, the blade is divided into n segments with $n + 1$ nodes along the span. The blade root and tip are nodes numbered with 0 and n, respectively. The wind turbulence data are pre-calculated information in a box-shape structure, where the wind box runs in its length direction.

Four coordinate systems are briefly defined as follows:

- Global north-east-down (NED) geographic coordinate system $\{N\}$: The origin O_n is placed on the free sea surface with the x-axis pointing to the north, y-axis pointing to the east, and z-direction being downward. The orientations about the x-, y-, and z-axes are roll (ϕ), pitch (θ), and yaw (ψ), respectively. NED is assumed to be an inertia frame.
- Blade body-fixed frame $\{B\}$: The origin O_b is placed at the blade COG. The y^b-axis points from the root center to the tip center in the spanwise direction, and the x^b-axis is directed from the leading edge to the trailing edge in the chordwise direction. The angular velocities about the x^b-, y^b-, and z^b-axes are p, q, and r, respectively. Note that the y-axis is chosen as the longitudinal axis along the blade so that rotation about y results in a blade pitch angle, being consistent with the blade pitch during turbine operation.
- Aerodynamic frame at node $i \in \{0, 1, \cdots, n\}$ in the body-fixed frame: The origin O_{bi} is at the geometric center of the blade i^{th} cross section. The y^{bi}-axis shares the same direction as the y^b-axis. The x^b-axis and z^b-axis are considered as a combination of a planar translation and a rotation about the y^b-axis. The aerodynamic twist, i.e., the angle between x^{bi} and x^b, is denoted by $\theta_{y,i}$.
- Mean-wind coordinate system $\{W\}$: The origin O_w is located at the lower-right corner of the wind turbulence box. O_w is placed at a preset point in $\{N\}$. The x^w-axis points in the wind inflow direction, i.e., the box's length, and z^w is directed downward, i.e., the box's height. The wind velocities in the x^w-, y^w-, and z^w-axes are u_w, v_w,

Fig. 4. Global, body-fixed, and mean-wind coordinate systems for the blade installation model (Image source: HeavyLiftNews).

and w_w, respectively. The box orientation about $\{N\}$ is constant, i.e., ϕ_w, θ_w, and ψ_w are constants.

The NED reference frame is a widely used coordinate system in ocean engineering, such as, the control of dynamic positioning vessels, moored vessels, autonomous underwater vehicles (AUVs), and remotely operated vehicles (ROVs). The blade body-fixed frame is also called the main-body coordinate system. The configuration is shown in Figs. 4–5. The wind shear is not considered. For the single blade horizontally positioned, the vertical variation in wind speed due to wind profile is not important, since the blade vertical movement is limited.

Remark 2. The reference frames $\{B_i\}$ are only used to compute the aerodynamic loads; these frames otherwise do not enter the calculation loop.

Remark 3. Euler angles are used to show the rotation relation between
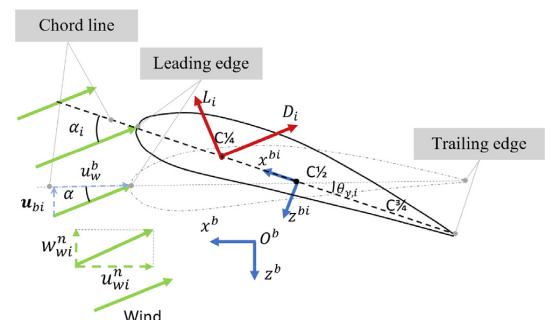
Fig. 5. Body-fixed and aerodynamic coordinate systems. The solid line and the dashed line are the outline of the ith blade element with and without rotation $\theta_{y,i}$, respectively.

Table 1
Variables in the corresponding frame.

	Position in	Relative orientation to {n}	Translational velocity	Angular velocity
{N}	$\boldsymbol{p} = [x, y, z]^\top$	–	$\boldsymbol{v}_n = [\dot{x}, \dot{y}, \dot{z}]^\top$	–
{B}	$\boldsymbol{p}^b = [x^b, y^b, z^b]^\top$	$\boldsymbol{\Theta}_{bn} = [\phi, \theta, \psi]^\top$	$\boldsymbol{v}_b = [u, v, w]^\top$	$\boldsymbol{\omega}_b = [p, q, r]^\top$
{W}	$\boldsymbol{p}^w = [x^w, y^w, z^w]^\top$	$\boldsymbol{\Theta}_{wn} = [\phi_w, \theta_w, \psi_w]^\top$	$\boldsymbol{v}_w = [u_w, v_w, w_w]^\top$	–

the coordinate frames. Rotations about the fixed x-, y-, and z-axes are named roll, pitch, and yaw. For the sake of consistency and clarity, the roll, pitch, and yaw are denoted by ϕ, θ, and ψ, respectively, regardless of the coordinate systems. The variables in the above-mentioned reference frames are tabulated in Table 1.

3.2. Transformation between coordinate systems

A vector, position or translational velocity is transformed between the coordinate systems, from {B} to {A}, by multiplying by the rotation matrix $\boldsymbol{R}_b^a$, i.e.,

$$\boldsymbol{v}^a = \boldsymbol{R}_b^a(\boldsymbol{\Theta}_{ab})\boldsymbol{v}^b, \tag{1}$$

where $\boldsymbol{v}^a$ and $\boldsymbol{v}^b \in \mathbb{R}^3$ are two vectors in {A} and {B}, $\boldsymbol{\Theta}_{ab}$ denotes a vector of the Euler angles between {A} and {B}, and the rotation matrix $\boldsymbol{R}_b^a$ rotates from the coordinate system {B}, expressed by the subscript, to the frame {A}, denoted by the superscript. The inverse transformation is given by the matrix $\boldsymbol{R}_b^a(\boldsymbol{\Theta}_{ab})^{-1} = \boldsymbol{R}_b^a(\boldsymbol{\Theta}_{ab})^\top = \boldsymbol{R}_a^b(\boldsymbol{\Theta}_{ab})$.

In this paper, the following order is adopted to transform a vector from one frame to another: $\{W\} \leftrightarrow \{N\} \leftrightarrow \{B\} \leftrightarrow \{B_i\}$. The transformations are bidirectional. Therefore, the wind velocity is transformed to the aerodynamic frame to represent the realistic wind-induced loads by three transformations, i.e., first from {W} to {N}, then from {N} to {B}, and finally from {B} to {B$_i$}. The relations between the vectors in the above-mentioned coordinate systems are tabulated in Table 2. The variables $\boldsymbol{R}_b^n$ and $\boldsymbol{R}_w^n$ are short for $\boldsymbol{R}_b^n(\boldsymbol{\Theta}_{bn})$ and $\boldsymbol{R}_w^n(\boldsymbol{\Theta}_{wn})$, respectively.

Additionally, position transformations between the coordinate systems are expressed by

$$\{B\} \rightarrow \{N\}: \qquad \boldsymbol{p} = \boldsymbol{R}_b^n \boldsymbol{p}^b + \boldsymbol{d}_b^n, \tag{2}$$

$$\{W\} \rightarrow \{N\}: \qquad \boldsymbol{p} = \boldsymbol{R}_w^n \boldsymbol{p}^w + \boldsymbol{d}_w^n, \tag{3}$$

where the distance vectors between the coordinate origins are

$$\boldsymbol{d}_b^n = -\boldsymbol{d}_n^b = \boldsymbol{p}_{O_n} - \boldsymbol{p}_{O_b}, \tag{4}$$

$$\boldsymbol{d}_w^n = -\boldsymbol{d}_n^w = \boldsymbol{p}_{O_n} - \boldsymbol{p}_{O_w}, \tag{5}$$

with $\boldsymbol{p}_{O_n} = [x_{O_n}, y_{O_n}, z_{O_n}]^\top$, $\boldsymbol{p}_{O_b} = [x_{O_b}, y_{O_b}, z_{O_b}]^\top$, and $\boldsymbol{p}_{O_w}$

$$= [x_{O_w}, y_{O_w}, z_{O_w}]^\top. \tag{6}$$

4. Ropes, winches, and hook

4.1. Wire rope, sling, and tugger line

The lift wires, slings, and tugger lines are modeled as tensile springs,

Table 2
Vector transformation among the above-mentioned coordinate systems. In the table, $\boldsymbol{a} = (\cdot)\boldsymbol{b}$.

a \ b	$\boldsymbol{v}^n$	$\boldsymbol{v}^b$	$\boldsymbol{v}^w$
$\boldsymbol{v}^n =$	$\boldsymbol{I}_3$	$\boldsymbol{R}_b^n$	$\boldsymbol{R}_w^n$
$\boldsymbol{v}^b =$	$\boldsymbol{R}_b^{n\top}$	$\boldsymbol{I}_3$	$\boldsymbol{R}_b^{n\top} \boldsymbol{R}_w^n$
$\boldsymbol{v}^w =$	$\boldsymbol{R}_w^{n\top}$	$\boldsymbol{R}_w^{n\top} \boldsymbol{R}_b^n$	$\boldsymbol{I}_3$

which only provide tension when the axial elongation is positive. The self weight of the rope is disregarded. Without loss of generality, a tensile spring between points A and B, with an initial length $\bar{l}_{AB}$ between points A and B, is presented as an example. Define $\boldsymbol{l}_{AB} = \boldsymbol{p}_A - \boldsymbol{p}_B$, where $\boldsymbol{p}_A$ and $\boldsymbol{p}_B \in \mathbb{R}^3$ are the positions of the ends of the wire. If the mass of the wire rope is negligible, the restoring force (Ren et al., 2017) in the global frame, $\boldsymbol{f}_A \in \mathbb{R}^3$, is modeled as

$$\boldsymbol{f}_A = -\left(\kappa(\delta_{AB})k_r\delta_{AB} - d_r\frac{d\,\delta_{AB}}{d\,t}\right)\frac{\boldsymbol{l}_{AB}}{|\boldsymbol{l}_{AB}|}, \tag{7}$$

where $\frac{\boldsymbol{l}_{AB}}{|\boldsymbol{l}_{AB}|}$ decomposes the total force into three components in the NED frame. The restoring acting coefficient κ is

$$\kappa(\delta_{AB}) = \begin{cases} 1 & \delta_{AB} \geq 0, \\ 0 & \text{otherwise.} \end{cases} \tag{8}$$

The axial elongation is

$$\delta_{AB} = |\boldsymbol{l}_{AB}| - \bar{l}_{AB}. \tag{9}$$

The elastic stiffness of the wire rope k_r is a function of its length, as well as the characteristics of the wire rope, e.g., material, diameter, and strand construction, given by (Ren et al., 2017)

$$k_r = \gamma_r \frac{EA_r}{l_1}, \tag{10}$$

where E denotes the Young's modulus, A_r refers to the cross-sectional area of the rope, and l_1 is the overall initial length of the rope. For a lift wire or a tugger line, the initial overall length is $l_1 = l_l(\text{or } l_t) = \bar{l}_{AB} + l_0$, where l_0 is the length of the rope between the corresponding winch and pulley, which is assumed to be a constant. For a sling, there is no connected winch, i.e., $l_1 = l_s = \bar{l}_{AB}$. To sum up,

$$l_1 = \begin{cases} \bar{l}_{AB} + l_0 & \text{lift wire/tugger line,} \\ \bar{l}_{AB} & \text{sling.} \end{cases} \tag{11}$$

A general form of the modified coefficient for a stranded wire γ_r is deduced in (Feyrer, 2007), given by

$$\gamma_r = \sum_{i=0}^{n_r} \frac{z_{ri}\cos^3\alpha_{ri}}{1 + v_{ri}\sin^2\alpha_{ri}} E_{ri}A_{ri}, \tag{12}$$

where n_r is the number of wire layers counted from the inside, with $i = 0$ for the center wire, and z_{ri}, E_{ri}, A_{ri}, α_{ri}, and v_{ri} are the number of wires in layer i, the Young's modulus, the cross-sectional area, the lay angle, and the Poisson ratio of a wire in the ith wire layer, respectively. A specific example of Eqn. (12) is $\gamma_r = \frac{\cos^3\alpha_r}{1 + v_r\sin^2\alpha_r}$ when all the strands share the same lay angle and Poisson ratio.

The tension on the rope is $f_r = |\boldsymbol{f}_A|$. According to Newton's third law, the reaction force at the other end of the rope is

$$\boldsymbol{f}_B = -\boldsymbol{f}_A. \tag{13}$$

This rope model is implemented in the MarIn module called Lifting equipment/Wire rope.

4.2. Winch

A winch is connected at the end of a lift wire or a tugger line. The winch rotational acceleration is based on the friction, external load
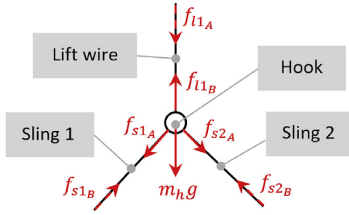
Fig. 6. Free-body diagram of the lift wire and hook.

acting on the wire, and the torque input acting on the winch (Egeland and Gravdahl, 2002). The external load is positive or zero. The winch model is given by

$$\dot{l}_1 = r_m \omega_m, \tag{14a}$$

$$\dot{\omega}_m = \frac{1}{J_m}(-d_m \omega_m + f_r r_m + T_m), \tag{14b}$$

where ω_m denotes the angular velocity of the winch motor, r_m is the radius of the winch motor, J_m represents the moment of inertia of the winch, d_m refers to the damping coefficient of the torsional damper, and T_m is the torque acting on the winch by the motor (usually viewed as the control input to the winch).

This winch dynamics is implemented in the MarIn module called Lifting equipment/Winch.

4.3. Hook

The hook is modeled as a 3-DOF rigid-body point. All the forces act on the COG. The gravity is not negligible; therefore, the mass of the hook, m_h, should be considered. Air resistance is negligible. The kinetic model of the hook, presented in Fig. 6, is given by Newton's second law according to

$$\dot{p}_h = v_h, \tag{15a}$$

$$M_h \dot{v}_h = g_h + \sum_{i=1}^{n_l} f_{li_B} + \sum_{i=1}^{n_s} f_{si_A}, \tag{15b}$$

where p_h and are the position and velocity vectors of the hook mass center in the global reference $\{N\}$, $M_h = \text{diag}\{m_h, m_h, m_h\}$ is the hook mass matrix, $g_h = [0,0, m_h g]^\top$ is the hook gravity vector, n_l and n_s are the numbers of the connected lift wires and slings, and f_{li_B} and f_{si_A} are the restoring forces acting on the hook from the lift wires and slings in $\{N\}$, respectively. The subscripts A and B are used to distinguish the pair of reacting forces at both ends of a rope. To remain consistent, the higher points are labeled A, and the lower points are labeled B. See Fig. 6 for an illustration.

This hook dynamics is implemented in the MarIn module called Lifting equipment/Hook.

5. Blade dynamics

It is assumed that the mass of the yoke concentrates on the COG of the blade, and the moment of inertia of yoke is disregarded. Hence, the blade and the yoke are considered as one body. Hereafter, the blade dynamics is the dynamic of the entire blade-yoke system.

5.1. Blade 6DOF kinematics

The kinematic dynamics for the blade (Fossen, 2011) is given by

$$\dot{\eta}_b = J(\Theta_{bn}) v_b, \tag{16}$$

$$J(\Theta_{bn}) = \begin{bmatrix} R_b^n(\Theta_{bn}) & 0_{3\times3} \\ 0_{3\times3} & T(\Theta_{bn}) \end{bmatrix}, \tag{17}$$

where $J \in \mathbb{R}^{6\times6}$ is a transformation matrix and

$$\eta_b = \begin{bmatrix} p_n \\ \Theta_{bn} \end{bmatrix}, \ v_b = \begin{bmatrix} v_b \\ \omega_b \end{bmatrix}. \tag{18}$$

This rotation matrix is implemented in the MarIn module called Basic functions/Euler angles to rotation matrix (z-y-x).

5.1.1. Blade rotation matrix

Three Euler angles are sufficient to represent an arbitrary rotation in 3D space. There are 12 sequences to do this. However, the rotation matrix is singular when the second orientation equals $\pm 90°$, namely, the gamble lock. Instead of the widely applied roll-pitch-yaw sequence (Diebel, 2006), the rotation sequence is modified in case of a singularity of the rotation matrix. For a blade installation process, the yaw angle and pitch angle may practically become $\pm 90°$. In addition, it is reasonable to assume that the blade span would not be assembled vertically, i.e., the roll angle would not reach $\pm 90°$. Therefore, the rotation matrix for the blade is based on a pitch-roll-yaw sequence, and the rotation matrix from the body-fixed frame $\{B\}$ to the global frame $\{N\}$ becomes

$$R_b^n(\Theta_{bn}) = R_{z,\psi} R_{x,\phi} R_{y,\theta} \tag{19}$$

$$= \begin{bmatrix} c\psi & -s\psi & 0 \\ s\psi & c\psi & 0 \\ 0 & 0 & 1 \end{bmatrix} \begin{bmatrix} 1 & 0 & 0 \\ 0 & c\phi & -s\phi \\ 0 & s\phi & c\phi \end{bmatrix} \begin{bmatrix} c\theta & 0 & s\theta \\ 0 & 1 & 0 \\ -s\theta & 0 & c\theta \end{bmatrix}$$

$$= \begin{bmatrix} c\psi c\theta - s\psi s\phi s\theta & -s\psi c\phi & c\psi s\theta + s\psi s\phi c\theta \\ s\psi c\theta + c\psi s\phi s\theta & c\psi c\phi & s\psi s\theta - c\psi s\phi c\theta \\ -c\phi s\theta & s\phi & c\phi c\theta \end{bmatrix}.$$

Moreover, the wind-induced load transformation from $\{B\}$ to $\{B_i\}$ is defined by

$$R_b^{wi} = R([0, \alpha, 0]^\top), \tag{20}$$

where α is the angle of attack (AOA) of the dashed airfoil outline without aerodynamic twist $\theta_{y,i}$ shown in Fig. 5. The details will be presented in the following.

Remark 4. Note that the rotation matrix R_b^{wi} here is not for a coordinate transformation. It is responsible for transforming the wind-induced forces, i.e., the drag force and the lift force, to the body-fixed frame $\{B\}$. The superscript wi here is another coordinate used to express the lift force and drag force. Because it only appears once, the formal definition is omitted to keep the paper clear and short.

5.1.2. Angular updating rate

The matrix $T(\Theta_{bn})$ transforms the body-fixed angular velocity to the Euler angle update rate, given by

$$T(\Theta_{bn})^{-1} \dot{\Theta}_{bn} = \begin{bmatrix} 0 \\ \dot{\theta} \\ 0 \end{bmatrix} + R_{y,\theta}^\top \begin{bmatrix} \dot{\phi} \\ 0 \\ 0 \end{bmatrix} + R_{y,\theta}^\top R_{x,\phi}^\top \begin{bmatrix} 0 \\ 0 \\ \dot{\psi} \end{bmatrix}. \tag{21}$$

Removing $\dot{\Theta}_{bn}$ from both sides yields

$$T(\Theta_{bn})^{-1} = \begin{bmatrix} c\theta & 0 & -c\phi s\theta \\ 0 & 1 & s\phi \\ s\theta & 0 & c\phi c\theta \end{bmatrix}. \tag{22}$$

Hence,

$$T(\Theta_{bn}) = \begin{bmatrix} c\theta & 0 & s\theta \\ t\phi s\theta & 1 & -c\theta t\phi \\ -s\theta/c\phi & 0 & c\theta/c\phi \end{bmatrix}. \tag{23}$$

Remark 5. Note that this update law will cause drift because $T(\Theta_{bn})$ is only a first-order approximation (Diebel, 2006). However, the drift is

small with restoring forces acting on the payload. Hence, this simplification is suitable for control design.

5.2. Blade kinetics

A turbine blade is free to move in 6 DOFs. Assume that the yoke and the blade are rigidly fixed to each other. The yoke COG coincides with the blade COG as a single body. We disregard the moment of inertia of the yoke, while the air resistance is included in the relative motion of the wind load. The overall kinetics of the blade and yoke in $\{B\}$ about its COG is given by

$$\boldsymbol{M}_b \dot{\boldsymbol{v}}_b + \boldsymbol{C}_b(\boldsymbol{v}_b)\boldsymbol{v}_b = \boldsymbol{g}_b^b + \boldsymbol{\tau}_s^b + \boldsymbol{\tau}_t^b + \boldsymbol{\tau}_w^b, \tag{24}$$

where $\boldsymbol{g}_b^b \in \mathbb{R}^6$ is the gravity force and moment vector in $\{B\}$, i.e.,

$$\boldsymbol{g}_b^b = \begin{bmatrix} \boldsymbol{R}_b^{n\top}[0,0,(m_b+m_y)g]^\top \\ \top \end{bmatrix}, \tag{25}$$

$\boldsymbol{\tau}_s^b$, $\boldsymbol{\tau}_t^b$, and $\boldsymbol{\tau}_w^b \in \mathbb{R}^6$ are the external load vectors from slings and tugger lines and wind-induced loads in $\{B\}$, i.e.,

$$\boldsymbol{\tau}_s^b = \sum_{i=1}^{n_s} \begin{bmatrix} \boldsymbol{R}_b^{n\top}\boldsymbol{f}_{s_{iB}} \\ \boldsymbol{S}(\boldsymbol{p}_{si}^b - \boldsymbol{p}_{COG}^b)\boldsymbol{R}_b^{n\top}\boldsymbol{f}_{s_{iB}} \end{bmatrix}, \tag{26}$$

$$\boldsymbol{\tau}_t^b = \sum_{i=1}^{n_t} \begin{bmatrix} \boldsymbol{R}_b^{n\top}\boldsymbol{f}_{t_{iB}} \\ \boldsymbol{S}(\boldsymbol{p}_{ti}^b - \boldsymbol{p}_{COG}^b)\boldsymbol{R}_b^{n\top}\boldsymbol{f}_{t_{iB}} \end{bmatrix}, \tag{27}$$

where $\boldsymbol{p}_{si}^b$ and $\boldsymbol{p}_{ti}^b$ are the positions of the connecting points of the slings and tugger lines, respectively. The mass matrix is

$$\boldsymbol{M}_b = \begin{bmatrix} (m_b+m_y)\boldsymbol{I}_3 & \boldsymbol{0}_3 \\ \boldsymbol{0}_3 & \boldsymbol{I}_b \end{bmatrix}, \tag{28}$$

where m_b is the mass of the blade, m_y is the mass of the yoke, and $\boldsymbol{I}_b \in \mathbb{R}^{3\times3}$ is the inertia matrix. The mass of the blade m_b is given by

$$m_b = \sum_{i=0}^{n} m_{bi} = \sum_{i=0}^{n} \rho_{bi}\Delta l_{bi}, \tag{29}$$

where ρ_{bi} is the mass per unit length at the ith node,

$$\Delta l_{bi} = \begin{cases} \frac{1}{2}(r_{b,1} - r_{b,0}), & i = 0, \\ \frac{1}{2}(r_{b,i+1} - r_{b,i-1}), & i = 1, \cdots, n-1, \\ \frac{1}{2}(r_{b,n} - r_{b,n-1}), & i = n. \end{cases} \tag{30}$$

in which $r_{b,i}$ with $i = 0, \cdots, n$ denotes the axial distance from the position of the ith node to the blade root center.

For a vector $\boldsymbol{\lambda} = [\lambda_1, \lambda_2, \lambda_3]^\top \in \mathbb{R}^3$, the matrix $\boldsymbol{S}(\boldsymbol{\lambda})$ (Fossen, 2011) in Eqns. (26) and (27) is given by

$$\boldsymbol{S}(\boldsymbol{\lambda}) = \begin{bmatrix} 0 & -\lambda_3 & \lambda_2 \\ \lambda_3 & 0 & -\lambda_1 \\ -\lambda_2 & \lambda_1 & 0 \end{bmatrix}. \tag{31}$$

The Coriolis matrix (Fossen, 2011) then becomes

$$\boldsymbol{C}_b = -\boldsymbol{C}_b^\top = \begin{bmatrix} (m_b+m_y)\boldsymbol{S}(\boldsymbol{\omega}_b) & \boldsymbol{0}_3 \\ \boldsymbol{0}_3 & -\boldsymbol{S}(\boldsymbol{I}_b\boldsymbol{\omega}_b) \end{bmatrix}. \tag{32}$$

The blade dynamics is implemented in the MarIn module called Payload/Suspended blade.

5.3. Wind field

Unlike an operational turbine, the wind-induced motion to the different sections of the blade is small. When calculating the aerodynamic loads, the blade is assumed to be divided into a group of n small segments with $n+1$ nodes, enumerated from 0 to n. The total

wind-induced load to the blade is basically the integration of local two-dimensional elemental loads acting along the span according to the cross-flow principle.

During a single blade installation, the wind-induced loads are the main external disturbance. Because the lengths of the blade are often greater than 60 m for a 5 MW turbine, a time-varying wind velocity should be considered. The wind load limits the weather window; therefore, uniform wind is not sufficient to calculate the wind-induced load in this case. The wind velocity at a point in space (x, y, z) at time t, denoted by $\boldsymbol{v}_w(x, y, z, t)$, is the sum of the mean wind speed and the turbulence, i.e.,

$$\boldsymbol{v}_w(x, y, z, t) = \bar{\boldsymbol{v}}_w(\boldsymbol{R}_w^n, t) + \boldsymbol{v}_{TI}(x, y, z, t), \tag{33}$$

where $\bar{\boldsymbol{v}}_w(t) = \boldsymbol{R}_w^n[U_w(t), 0, 0]^\top$ is the mean wind velocity vector in $\{N\}$, U_w is the mean wind speed, and $\boldsymbol{v}_{TI}(x, y, z, t)$ is the spatio-temporal turbulence velocity at (x, y, z).

5.3.1. Wind turbulence

The Taylor's hypothesis of frozen turbulence is adopted and assumes that the advection of a field of turbulence past a fixed point can be taken to be entirely due to the mean flow, as the contribution from the turbulent circulation is small. This only holds if the relative turbulence intensity (TI) is small, that is, $\frac{U_e}{U_w} \ll 1$, where U_e refers to the eddy velocity.

A turbulence box is assumed in a space with evenly distributed points inside that moves with the mean wind speed U_w in the length direction, i.e., x^w-axis. The size of the turbulence box is $N_{wx} \times N_{wy} \times N_{wz}$ with intervals D_{wx}, D_{wy}, and D_{wz} along the corresponding axes, where N_{wx}, N_{wy} and N_{wz} are the numbers of points in the x^w-, y^w-, and z^w-axes, respectively (Mann, 1998). The wind turbulence boxes are generated by importing and reshaping the binary files from TurbSim (Kelley and Jonkman, 2006; Jonkman and Kilcher, 2012), with preset discrete points along the length, width, and height. TurbSim is a free stochastic turbulence simulator (Turbsim, 2017). Additionally, the binary turbulence file generated by HAWC2 is also supported. According to a rule of thumb in aeroelastic simulations, the grid sizes are chosen to be smaller than the blade root diameter in order to capture the effects of wind speed variation of the turbulent wind field on the blade loads.

A blade is a smooth interpolation of a number of cross sections. The position of a point in $\{N\}$ is transformed to the position in $\{W\}$. To remain consistent, the wind force is considered to act on the center of pressure $C_{1/4}$ based on the wind velocity at $C_{1/4}$. The position of $C_{1/4}$ at the ith cross section in $\{N\}$ is defined by $\boldsymbol{p}_{C_{1/4},i} = [x_{C_{1/4},i}, y_{C_{1/4},i}, z_{C_{1/4},i}]^\top$. The wind velocity vector at the ith node in $\{N\}$, $\boldsymbol{v}_{wi}(\boldsymbol{p}_{C_{1/4},i}, t) = [u_{wi}, v_{wi}, w_{wi}]^\top$, is interpolated by a 3D lookup table with the following relation:

$$\boldsymbol{v}_{wi} = \boldsymbol{R}_w^n \left(\begin{bmatrix} U_w \\ 0 \\ 0 \end{bmatrix} + \begin{bmatrix} \boldsymbol{\Omega}_{x,mann}^w(\boldsymbol{p}_{C_{1/4},i}^w, t) \\ \boldsymbol{\Omega}_{y,mann}^w(\boldsymbol{p}_{C_{1/4},i}^w, t) \\ \boldsymbol{\Omega}_{z,mann}^w(\boldsymbol{p}_{C_{1/4},i}^w, t) \end{bmatrix} \right) \tag{34}$$

with

$$\boldsymbol{p}_{C_{1/4},i}^w = \begin{bmatrix} x_{C_{1/4},i}(t) + \int_0^t U_w(\tau)d\tau - x_{O_w} \\ y_{C_{1/4},i}(t) - y_{O_w} \\ z_{C_{1/4},i}(t) - z_{O_w} \end{bmatrix}, \tag{35}$$

where $\boldsymbol{\Omega}_{x,mann}^w$, $\boldsymbol{\Omega}_{y,mann}^w$, and $\boldsymbol{\Omega}_{z,mann}^w$ are the generated turbulence boxes for the x^w-, y^w-, and z^w-directions, respectively.

This turbulence is implemented in the MarIn module called Environment/3D wind generator with turbulence.

5.3.2. Wind-induced loads acting on a blade

A centerline is defined in the main-body coordinate system. Because the NREL 5 MW reference wind turbine blade does not have a prebend, the centerline is almost a straight line. The aerodynamic center $C^1/_2$ of a cross section lays on the centerline with a rotation $\theta_{y,i}$ about the y^b-axis in the main-body x^b-z^b coordinate plane. The centerline connects all $C^1/_2$ from the blade root to the blade tip. The root is defined using a circular shape. The shape of the main blade body is a series of airfoils with various chord lengths, geometric centers, and thickness/chord ratios (T/C). Define $T/C_i = \frac{t_i}{C_i}$, where C_i and are the chord length and the maximum thickness of the ith airfoil section. In a quasi-steady analysis, the aerodynamic coefficients are a function of the AOA and T/C. The structural parameters and aerodynamic coefficients can be obtained by interpolation though data from the reference turbine. The aerodynamic load calculation is based on the following assumptions:

- Rigid structure: blade vibration is negligible.
- Vertex shedding or dynamic stall can be ignored.

The lift force, drag force, and pitching moment acting on the ith node, denoted by L_i, D_i, and M_i, are calculated with airfoil theory (Anderson, 2010) and an integration along the span. This gives

$$L_i = \frac{1}{2}\rho_a C_l(\alpha_i, \text{T/C}_i) A_i V_i^2, \tag{36}$$

$$D_i = \frac{1}{2}\rho_a C_d(\alpha_i, \text{T/C}_i) A_i V_i^2, \tag{37}$$

$$M_i = \frac{1}{2}\rho_a C_m(\alpha_i, \text{T/C}_i) A_i V_i^2, \tag{38}$$

where the subscript i refers to the ith node, ρ_a is the air density, and C_l, C_d, and C_m denote the lifting coefficient, the drag coefficient, and the pitching moment coefficient, respectively. The inflow speed is $V_i = |\boldsymbol{L}[\boldsymbol{R}_n^{bi}(\boldsymbol{v}_{wi} - \boldsymbol{v}_{C1/4,i})]|$, where $\boldsymbol{L} = \begin{bmatrix} 1 & 0 & 0 \\ 0 & 0 & 1 \end{bmatrix}$, and $\boldsymbol{v}_{C1/4,i}$ are the velocity vector of the ith center of pressure in $\{N\}$, respectively. Note that the relative velocity here contributes to the air resistance. The wing area is

$$A_i = \begin{cases} \frac{(r_{b,1} - r_{b,0})C_1}{2} & \text{if } i = 0, \\ \frac{(r_{b,i} - r_{b,n-1})C_n}{2} & \text{if } i = n, \\ \frac{(r_{b,i} - r_{b,i-1})C_i}{2} + \frac{(r_{b,i+1} - r_{b,i})C_{i+1}}{2} & \text{otherwise.} \end{cases} \tag{39}$$

The AOA at the ith segment α_i is given by

$$\alpha_i = \alpha + \theta_{y,i}, \tag{40}$$

with

$$\alpha = f_a\left(\pi + \text{atan2}\left(w_{wi}^b - w_{C1/4}^b, u_{wi}^b - u_{C1/4}^b\right)\right), \tag{41}$$

where f_a is a function that converts an angle to the range $[-\pi, \pi)$, $\text{atan2}(y, x)$ is the multi-valued inverse tangent function, and $w_{wi}^b - w_{C1/4}^b$ and $u_{wi}^b - u_{C1/4}^b$ denote the relative wind velocity at the ith blade segment center in $\{B\}$. For small α_i in the range [-45,45] deg, a series of aerodynamic coefficients w.r.t. the AOA has been calculated and stored in a lookup table. For high α_i, in the ranges [-180,-45] and [45,180] deg, the aerodynamic coefficients are calculated as flat plates, which are given by

$$C_l(\alpha_i, \text{T/C}_i) = 2\cos(\alpha_i)\sin(\alpha_i), \tag{42a}$$

$$C_d(\alpha_i, \text{T/C}_i) = \overline{C}_d(\text{T/C}_i)\sin^2(\alpha_i), \tag{42b}$$

$$C_m(\alpha_i, \text{T/C}_i) = -\sin(\alpha_i)/4, \tag{42c}$$

where $\overline{C}_d$(T/C) is the maximum value for C_d with respect to T/C (Bak

et al., 2013). The coefficients for an arbitrary AOA are then found by interpolation.

When the yaw angle is small, the force component in the y^b-axis is negligible according to the cross-flow principle. Consequently, the resulting force and moment vector acting at the ith node in the blade main-body frame $\{B\}$ are given by

$$\boldsymbol{f}_{w,i}^b = \boldsymbol{R}_b^{wi\top} \begin{bmatrix} -D_i \\ 0 \\ L_i \end{bmatrix}, \tag{43}$$

$$\boldsymbol{m}_{w,i}^b = \boldsymbol{m}_{w,i}^{wi} = \begin{bmatrix} 0 \\ M_i \\ 0 \end{bmatrix}. \tag{44}$$

Therefore, the total wind-induced force and moment acting on the main-body COG are given by

$$\boldsymbol{\tau}_w^b = \begin{bmatrix} \sum_{i=0}^n \boldsymbol{f}_{w,i}^b \\ \sum_{i=0}^n \left[\boldsymbol{S}\left(\boldsymbol{p}_{C1/4,i}^b - \boldsymbol{p}_{COG}^b\right)\boldsymbol{f}_{w,i}^b + \boldsymbol{m}_{w,i}^b \right] \end{bmatrix}. \tag{45}$$

These wind-induced loads are implemented in the MarIn module called Payload/Wind-induced load acting on the blade.

6. Code-to-code verification of the blade model with quasi-static analysis

In this section, a series of code-to-code verification tests are conducted to verify that the proposed code models the blade with realistic parameters and coefficients. The tests are conducted using the HAWC2 and MATLAB/Simulink with the NREL 5 MW reference wind turbine. The aerodynamic coefficients are read from the HAWC2. dat file, to obtain the same wind loads and perform a fair comparison study. A brief summary of the blade is tabulated in Table 3. In the simulations of this section, the wind velocity is constant without turbulence. In the next section, we will introduce turbulence and conduct testing with more realistic wind loads.

6.1. Test 1. mass and moment of inertia

The mass, the moment of inertia, and the COG position are

Table 3
Basic parameters of a single blade installation configuration with the NREL 5 MW turbine blade.

Parameter	Symbol	Unit	Value
Mass of blade	m_b	ton	17.74
Length of blade	l_b	m	61.5
Mass of yoke	m_y	ton	20
Mass of hook	m_h	ton	1
Length of lift wire 1	l_l	m	10
Stiffness of lift wire 1	k_l	N/m	1e8
Damping of lift wire 1	d_l	N.m/s	1e4
Length of sling 1	l_{s1}	M	9.2
Stiffness of sling 1	k_{s1}	k/m	1e8
Damping of sling 1	d_{s1}	N.m/s	1e4
Length of sling 2	l_{s2}	M	9.2
Stiffness of sling 2	k_{s2}	N/m	1e8
Damping of sling 2	d_{s2}	N.m/s	1e8
Length of tugger line 1	l_{t1}	m	9.17
Stiffness of tugger line 1	k_{t1}	k/m	1e7
Damping of tugger line 1	d_{t1}	N.m/s	0
Length of tugger line 2	l_{t2}	M	9.17
Stiffness of tugger line 2	k_{t2}	N/m	1e7
Damping of tugger line 2	d_{t2}	N.m/s	0
Length, width, and height of the turbulence box	N_{wx}, N_{wy}, N_{wz}	–	65536, 32, 16
Grid size of the turbulence box	D_{wx}, D_{wy}, D_{wz}	m	4, 4, 4

Table 4
Mass and moment of inertia verify the NREL 5 MW blade.

Parameters	HAWC2 outputs	Proposed user-defined function
Mass (kg)	17704	17740
Position of COG in {B} (m)	[0.145 0.022 20.561]	[−0.1454 0.089 20.507]
Inertia at the root center in {B} (kg.m²) $[I_{xx}, I_{yy}, I_{zz}; I_{xy}I_{xz}, I_{yz}]$	$\begin{bmatrix} 1.1808e7 & 2.6714e4 & 1.1817e7 \\ -6.556e4 & -1.417e3 & -7.166e3 \end{bmatrix}$	$\begin{bmatrix} 1.1776e7 & 2.6837e4 & 1.1776e7 \\ -6.515e4 & -1.491e3 & -7.097e3 \end{bmatrix}$

calculated by a user-defined function init_blade_hawc2. The function reads the structural coefficients from HAWC2 files. This test attempts to verify that the function init_blade_hawc2 reads the correct parameters from the HAWC2 data files and calculates the correct mass matrix and COG position. The results are tabulated in Table 4. From the results, the init_blade_hawc2 function outputs are close to those from HAWC2.

6.2. Test 2. Aerodynamic-coefficient lookup tables

Due to the rotation of the centerline and axial-varying thickness, the aerodynamic coefficients along the blade span are also varied. The init_blade_hawc2 function reads the aerodynamic coefficients to construct lookup tables for the aerodynamic force modules. For the NREL 5 MW reference turbine blade, the resulting aerodynamic coefficients w.r.t. blade AOA and T/C are shown in Figs. 7–9. The curves agree with the results in Ref. (Jonkman et al., 2009). Therefore, the init_blade_hawc2 function is accepted to correctly read the aerodynamic coefficients from the HAWC2 data files.

6.3. Test 3. Aerodynamic coefficients and force along the blade axis

We conducted tests to verify the wind-induced load acting on the blade with respect to different wind speeds, roll angles, and yaw angles, i.e., the algorithm proposed in Section 5.3.2. The blade is fixed at 90 m above the sea surface with $\psi = 0$ deg and $\psi = 30$ deg, respectively. The horizontal wind speed at the height of 90 m is 10 m/s in the global negative x-direction. The pitch angle is set to 10, 30, 50, 60, and 90°. The wind speeds up during the first 20 s, and the results are the corresponding values at 100 s. For the HAWC2 model, the wind-induced load quadratically increases with a slight delay at the later stage. After the wind speed reaches a steady value, the wind-induced load is constant. The proposed model calculates the wind load quadratically according to the wind speed. The aerodynamic coefficients and forces are illustrated at various spanwise cross-planes as shown in Figs. 10–13. In

Fig. 8. C_d lookup table w.r.t. airfoil thickness/chord ratio and AOA for the NREL 5 MW wind turbine blade.
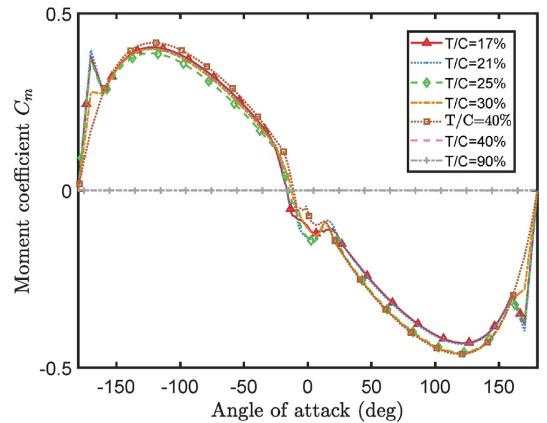
Fig. 9. C_m lookup table w.r.t. airfoil thickness/chord ratio and AOA for the NREL 5 MW wind turbine blade.

the figures, curves from the HAWC2 and the proposed Simulink model agree well. Therefore, the results confirm that the Simulink module calculates the aerodynamic coefficients and force correctly.

6.4. Test 4. Total wind-induced load acting on the blade

The total load acting on the blade is tested with respect to various wind speeds and blade pitch angles. The wind speed is from 0 to 20 m/s with a 1 m/s interval. The pitch angle is from 10° to 90° with a 10 deg interval. The blade yaw is 0°, i.e., the wind loads are at their maxima in this situation. The resulting forces at the steady states are presented in Fig. 14. From the results, it is noticed that the wind-generated forces F_x
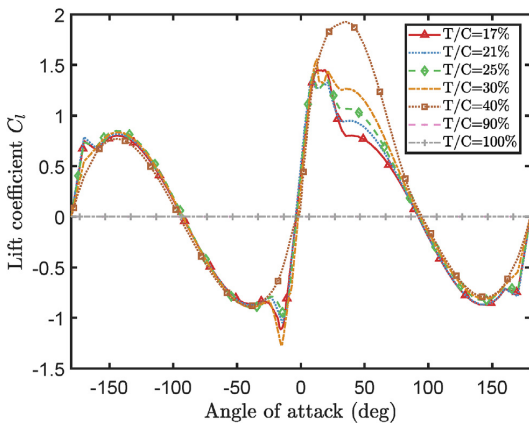

Fig. 7. C_l lookup table w.r.t. airfoil thickness/chord ratio and AOA for the NREL 5 MW wind turbine blade.
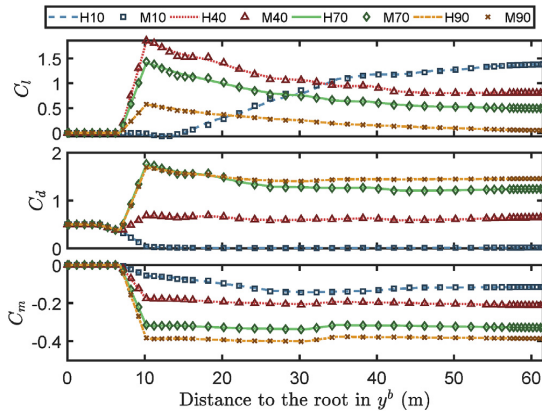
Fig. 10. Aerodynamic coefficients C_l, C_d, C_m, $\psi = 0$ deg, w.r.t. θ and y^b. (In the legend, H and M denote the results from HAWC2 and the proposed toolbox, respectively. The numbers represent the pitch angles in deg.)

Fig. 11. Lift force and drag force per unit length $\psi = 0$ deg, w.r.t. θ and y^b, wind speed = 10 m/s. (In the legend, H and M denote the results from HAWC2 and the proposed toolbox, respectively. The numbers represent the pitch angles in deg.)

Fig. 12. Aerodynamic coefficients, $\psi = 30$ deg, C_l, C_d, C_m w.r.t. θ and y^b. (In the legend, H and M denote the results from HAWC2 and the proposed toolbox, respectively. The numbers represent the pitch angles in deg.)
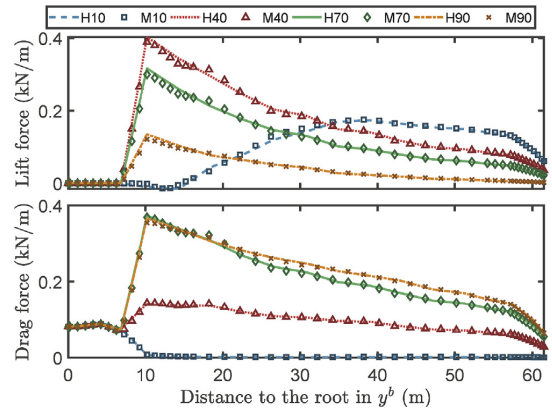
Fig. 13. Lift force and drag force per unit length, $\psi = 30$ deg, w.r.t. θ and y^b, wind speed = 10 m/s. (In the legend, H and M denote the results from HAWC2 and the proposed toolbox, respectively. The numbers represent the pitch angles in deg.)
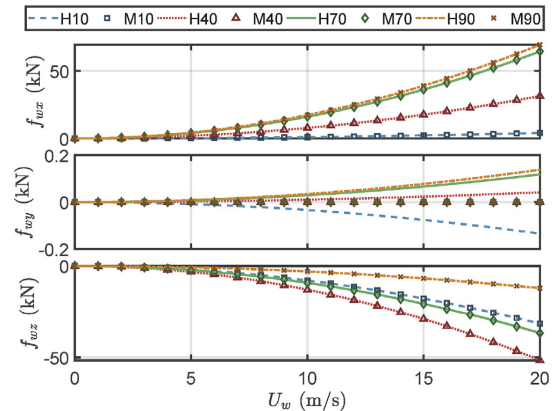
Fig. 14. Total force acting on the blade in {B}, $\psi = 0$ deg. (In the legend, H and M denote the results from HAWC2 and the proposed toolbox, respectively. The numbers represent the pitch angles in deg.)

and F_z are well-fitted and are proportional to the square of the mean wind speed. This observation corresponds well with (Gaunaa et al., 2014). Deviations between the HAWC2 and the proposed model occur in the subplot F_y. This is because of the different mechanics used in simulation, that is, Timoshenko beam elements in HAWC2 and the rigid body with assumed zero sway force in the proposed model. Comparing with the magnitudes of F_x and F_z, the deviation in F_y is very small and considered negligible for the intended use of our model.

The same issue appears in simulations with $\psi = 30°$, whose results are presented in Fig. 15.

7. Case study: single blade installation model

After confirming the performance of each module individually, the overall single blade installation model is built. A single blade installation is performed with a yoke that grabs and holds the blade around the center of gravity. The yoke is lifted by lift wires from a crane and stabilized by tugger lines symmetrically arranged around the COG on the blade axis.

The model is, to a certain degree, of low fidelity due to the lack of
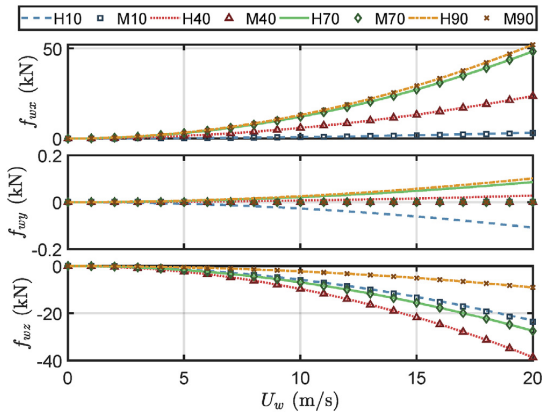
Fig. 15. Total force acting on the blade in {B}, ψ = 30 deg. (In the legend, H and M denote the results from HAWC2 and the proposed toolbox, respectively. The numbers represent the pitch angles in deg.)

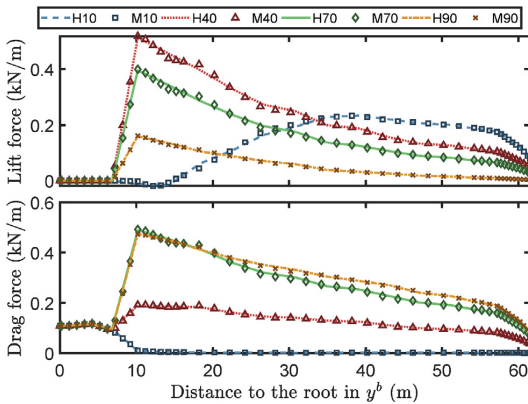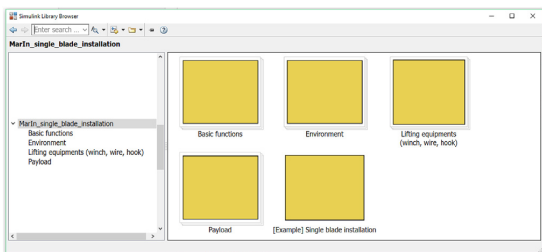**Fig. 16.** Interface of the toolbox in Simulink library browser.
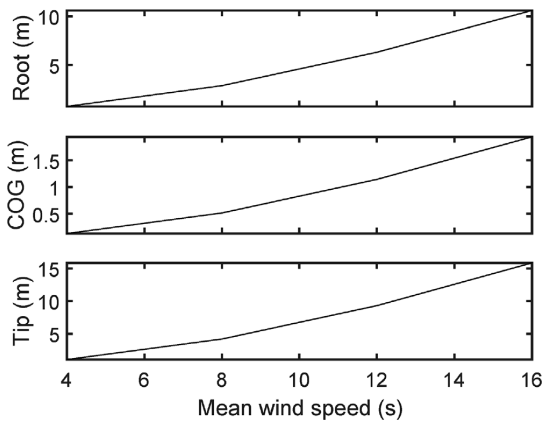
Fig. 17. Displacements of the equilibrium point of the root center, the tip center, and the COG, under various mean wind speeds without turbulence.

complex aerodynamic effects. This increases the run-time performance of the model while maintaining the most important dynamic effects for the purposes of control design and analysis.
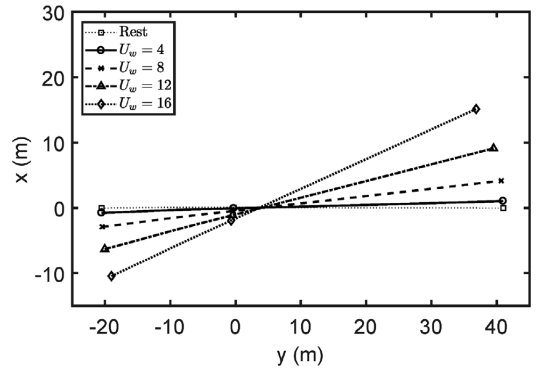
Fig. 18. Equilibrium positions of the blade centerline in the x-y horizontal plane under constant mean wind speeds without turbulence.
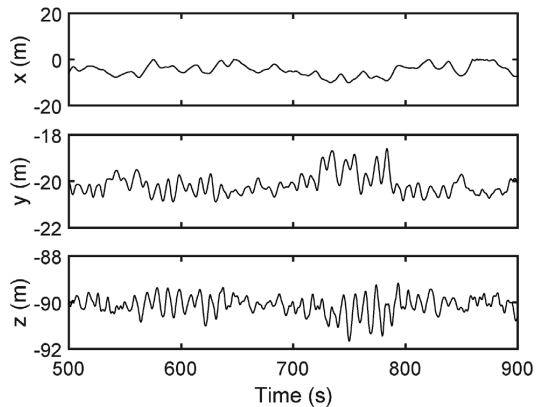
Fig. 19. Position of the blade root center, U_w = 12 m/s, TI = 0.146.

7.1. Modeling procedure

All modules and basic functions are packaged as an individual package of MarIn toolbox, which will be integrated into MarIn in the future; see Fig. 16. The single blade installation model, presented in Figs. B.22-B.23, is given as an example of the use of this toolbox. Newton-Euler mechanics is used to connect the modules in the inflow direction.

7.2. Test 5. Equilibrium point in steady wind

First, tests concerning the equilibrium points in an environment with constant wind speed are conducted. For the nonrotating blade studied under a constant wind speed, the displacements of the root center, the COG, and the tip center around their equilibrium positions approximately follow a quadratic relation with the wind speed. This observation is aligned with (Gaunaa et al., 2014; Jiang et al., 2018). The position of the crane and the lengths of all the wire ropes are fixed. The blade leading edge is downward, i.e., the pitch angle is equal to $-90°$ and $\Theta_{bn}(0) = [0, -\pi/2, 0]^\top$. The mean wind direction is in the x-axis, i.e., $\Theta_{wn} = [0,0,0]^\top$.

A constant wind speed starts acting on the blade with a 5-s ramp increasing. The results are presented in Figs. 17 and 18. The
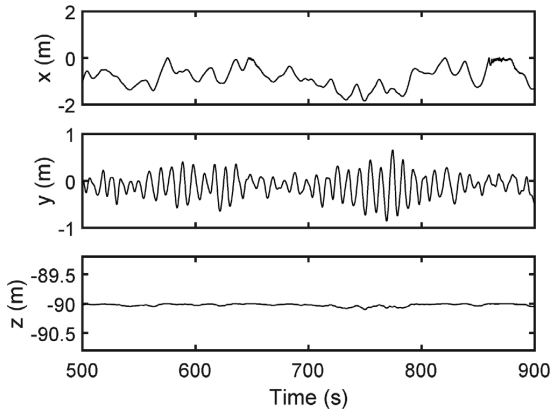
Fig. 20. Position of the blade COG, U_w = 12 m/s, TI = 0.146.
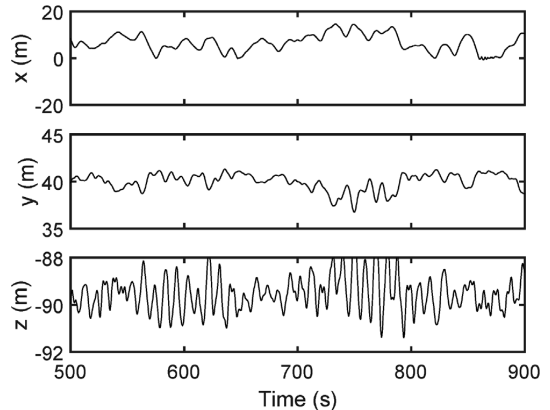
Fig. 21. Position of the blade tip center, U_w = 12 m/s, TI = 0.146.

displacements of the root center, COG, and tip center all satisfy quadratic relations.

7.3. Test 6. Time-domain simulation with wind turbulence

In practical situations, the wind speed is not constant. Therefore, a complex turbulent wind field is used in the simulation. The external loads are caused by the wind field with spatio-temporal turbulence; see Jiang et al. (2018) for more details. The mean wind speed is set to 12 m/s, and TI = 0.146. The seed number is set to 94.

The simulations are conducted with a personal computer with an Intel Core i7 3.6 GHz CPU using MATLAB version R2017b. The solver in Simulink is more powerful and flexible than aerodynamic software. A variable step size and the maximum step size can be set to ensure both accuracy and efficiency. For a 1000-s simulation, the average computation time is 710 s. Therefore, the proposed simulation model is fast enough for the simulation. The histories of the blade root position, COG position, and tip position are presented in Figs. 19–21. As shown, the motions in the x-direction are dominant, and the pendulum mode (0.1 Hz) of the blade system is visible in the time series of the blade root. Under the turbulent wind condition, the blade root and the blade tip experience significantly larger motions compared to the blade COG. For the blade root, the displacement has a 553.6% increase in x, 152.0 %increase in y, and 2482.2% increase in z. The motion at the blade tip is even larger, whose displacement experiences a 823.3% increase in x, 303.1 %increase in y, 4701.1% increase in z.

8. Conclusion and future research

In this paper, a numerical modeling framework for blade installation for wind turbine is presented. A single blade installation model is given along with an example. The model is based on the Newton-Euler method. The hook, blade, lift wire, sling, tugger line, winch, and wind are modeled. Code-to-code verification studies are conducted to prove the effectiveness and correctness of the proposed model. This model presents a starting point for future research on OWT installation and related control and monitoring functions.

The model will be integrated with other modules to verify controllers for various scenarios of single blade installation as well as other marine operations with emphasis on crane operation. In the future, a structured and more comprehensive MarIn toolbox will be proposed specifically for marine operations.

Acknowledgment

Appendix A. The I/O and parameter description

Table A.5
I/O and important parameters for the winch module.

Module name	Winch	Symbol	Dimension
Inputs	Wire length changing rate (m/s)	$\dot{l}_1$	[1]
Outputs	Wire length (m)	l_1	[1]
Parameters	Initial wire length (m)	$l_1(0)$	[1]

Table A.6

I/O and important parameters for the wire rope module.

Module name	Wire rope	Symbol	Dimension
Inputs	Positions of both ends (m)	$\boldsymbol{p}_A, \boldsymbol{p}_B$	[3 × 1]
	Wire length (m)	l_1	[1]
	Wire length changing rate (m/s)	$\dot{l}_1$	[1]
Outputs	Forces at both ends (N)	$\boldsymbol{f}_A, \boldsymbol{f}_B$	[3 × 1]
Parameters	Wire stiffness (N/s)	d_r	[1]
	Wire damping (N.s/m)	k_r	[1]

Table A.7

I/O and important parameters for the hook module.

Module name	Hook	Symbol	Dimension
Inputs	Force input from the connected wires (N)	$\boldsymbol{f}_{li_B}, \boldsymbol{f}_{si_A}$	[3 × 1]
Outputs	Position of the hook (m)	$\boldsymbol{p}_h$	[3 × 1]
Parameters	Initial position of the hook(m)	$\boldsymbol{p}_h(0)$	[3 × 1]
	Initial velocity of the hook(m)	$\boldsymbol{v}_h(0)$	[3 × 1]
	Hook mass (kg)	m_h	[3 × 1]

Table A.8

I/O and important parameters for the wind generator module.

Module name	3D wind generator with turbulence	Symbol	Dimension
Inputs	Mean wind speed (m/s)	U_w	[1]
	Position of the given point(m)	$\boldsymbol{p}_{C_{1/4},i}$	[3 × n]
Outputs	Wind velocity at the given points (m/s)	$\boldsymbol{v}_{wi}$	[3 × n]
Parameters	Position of the turbulence box center (m)	$\boldsymbol{p}_{O_w}$	[3]
	Orientations of the turbulence box (rad)	$\boldsymbol{\Theta}_{wn}$	[3]
	Turbulence data structure	–	structure

Table A.9

I/O and important parameters for the wind-induce loads.

Module name	Wind-induced loads	Symbol	Dimension
Inputs	Position and orientations of the blade (m,rad)	$\boldsymbol{\eta}_b$	[6]
	Wind velocity at the centers of pressure of the airfoil segments (m/s)	$\boldsymbol{v}_{wi}$	[3 × n]
	Velocity at the centers of pressure of the airfoil segments (m/s)	$\boldsymbol{v}_{C_{1/4}}$	[3 × n]
Outputs	Wind-induced load in the body-fixed frame (N,N·m)	$\boldsymbol{\tau}_w^b$	[6]
Parameters	Blade aerodynamic coefficient structure	–	–

Table A.10
I/O and important parameters for the suspended blade module.

Module name	Suspended blade	Symbol	Dimension
Inputs	Force input from the connected wires (N)	$\boldsymbol{f}_{siB}, \boldsymbol{f}_{tiB}$	$[3 \times n]$
	Wind-induced load (N·m)	τ_w^b	$[6]$
Outputs	Position and orientations of the blade (m,rad)	$\boldsymbol{\eta}_b$	$[6]$
	Position of the positions of the connecting points of the connected wires (m)	$\boldsymbol{p}_{si}, \boldsymbol{p}_{ti}$	$[3 \times n_s], [3 \times n_t]$
	Position of the centers of pressure of the airfoil segments (m)	$\boldsymbol{p}_{C_{1/4,i}}$	$[3 \times n]$
	Position of the blade aerodynamic centers (m)	$\boldsymbol{p}_{C_{1/2,i}}$	
Parameters	Initial position and velocity of the blade	$\boldsymbol{\eta}_b(0)$	$[6]$
	Yoke mass	m_y	$[1]$
	Blade data structure	–	–
	Positions of the connected points to the slings and tugger lines in $\{B\}$	$\boldsymbol{p}_{si}^b, \boldsymbol{p}_{ti}^b$	$[3 \times n_s], [3 \times n_t]$

Appendix B. Modeling of single blade installation in Simulink

The blue labels in Figs. B.22-B.23 are the section numbers in which the specific modules use equations.
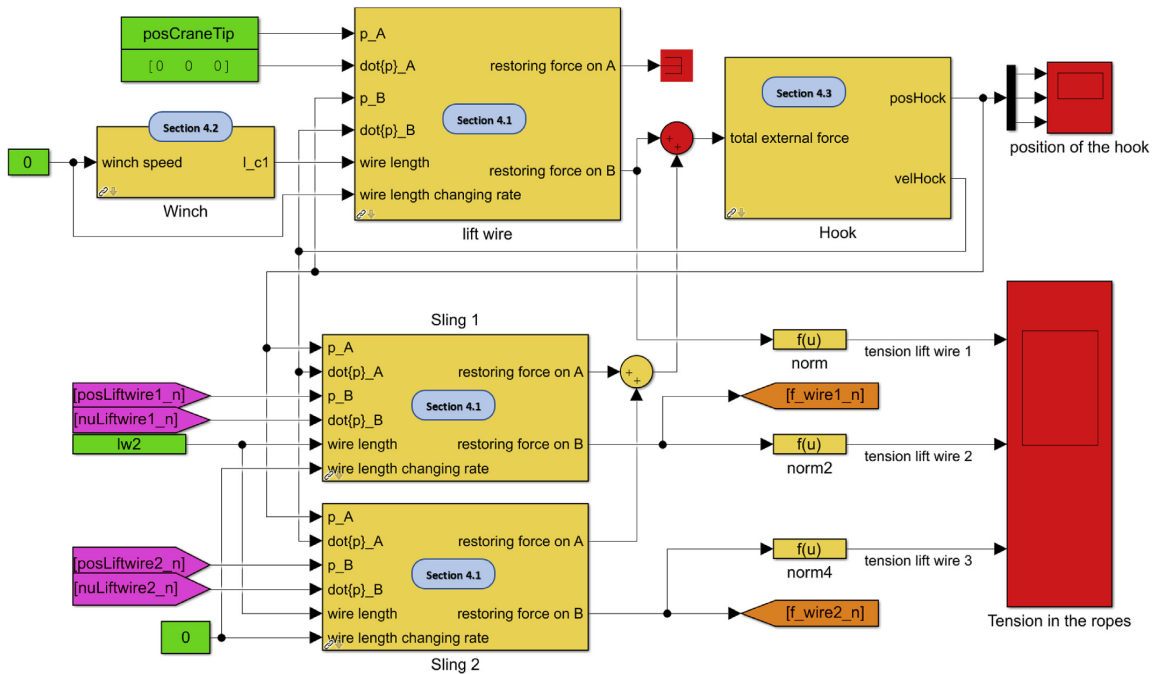

Figure B.22. Illustration of the single blade installation model - Part I: lift wire, hook, and slings.
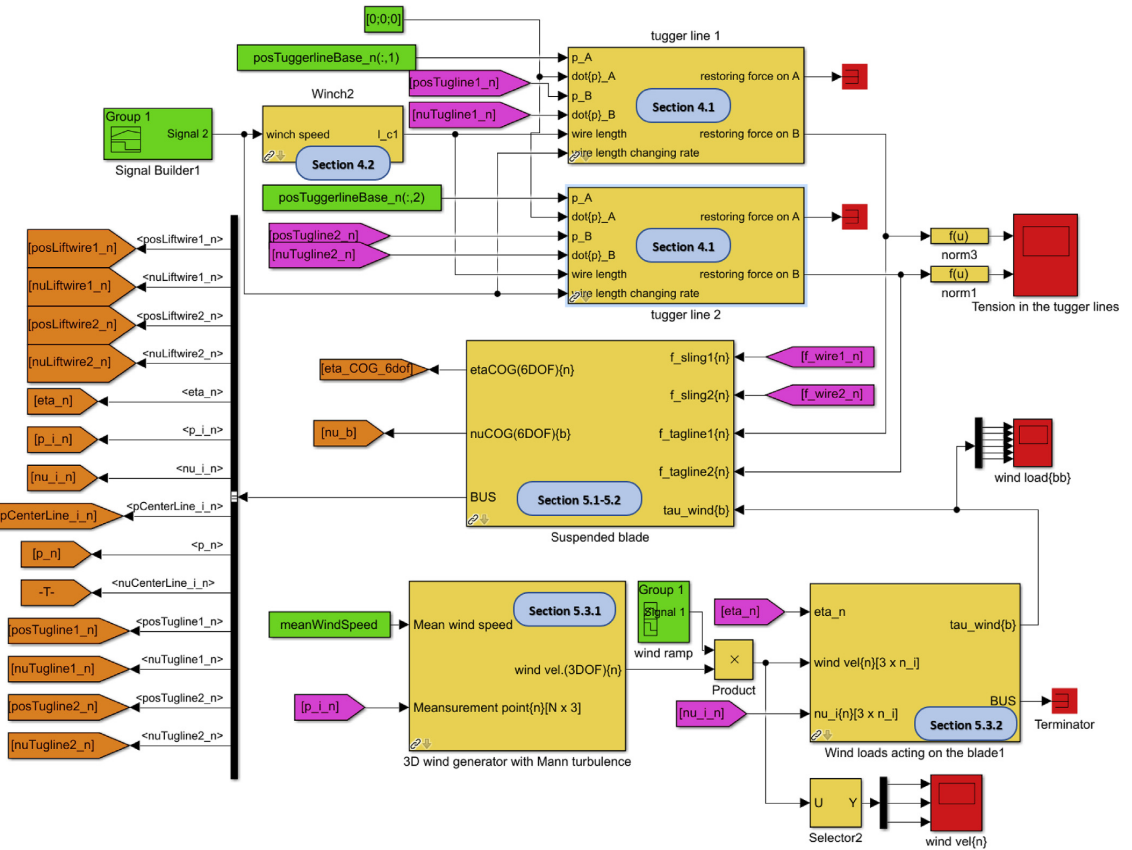
Figure B.23. Illustration of the single blade installation model - Part II: blade, tugger lines, and wind load.

References

Anderson Jr., J.D., 2010. Fundamentals of Aerodynamics. Tata McGraw-Hill Education.

Bak, C., Zahle, F., Bitsche, R., Kim, T., Yde, A., Henriksen, L., Andersen, P., Natarajan, A., Hansen, M., 2013. Description of the DTU 10 Mw Reference Wind Turbine. DTU wind energy report-i-0092. Technical University of Denmark, Fredericia (Denmark).

Bø, T.I., Dahl, A.R., Johansen, T.A., Mathiesen, E., Miyazaki, M.R., Pedersen, E., Skjetne, R., Sørensen, A.J., Thorat, L., Yum, K.K., 2015. Marine vessel and power plant system simulator. IEEE Access 3, 2065–2079.

Bossanyi, E., 2009. GH Bladed User Manual. Garrad Hassan Bladed.

Calabretta, A., Molica Colella, M., Greco, L., Gennaretti, M., 2016. Assessment of a comprehensive aeroelastic tool for horizontal-axis wind turbine rotor analysis. Wind Energy 19 (12), 2301–2319.

Diebel, J., 2006. Representing attitude: Euler angles, unit quaternions, and rotation vectors. Matrix 58 (15–16), 1–35.

Egeland, O., Gravdahl, J.T., 2002. Modeling and Simulation for Automatic Control, vol.76 Marine Cybernetics Trondheim, Norway.

Fang, Y., Wang, P., Sun, N., Zhang, Y., 2014. Dynamics analysis and nonlinear control of an offshore boom crane. IEEE Trans. Industrial Electron. 61 (1), 414–427.

Feyrer, K., 2007. Wire Ropes, Springer.

Fossen, T.I., 2011. Handbook of marine Craft Hydrodynamics and Motion Control. John Wiley & Sons.

Gaunaa, M., Bergami, L., Guntur, S., Zahle, F., 2014. First-order aerodynamic and aero-elastic behavior of a single-blade installation setup. In: Journal of Physics: Conference Series, vol.524. IOP Publishing, pp. 012073.

Haastrup, M., Hansen, M.R., Ebbesen, M.K., 2011. Modeling of wind turbine gearbox mounting, Modeling. Identif. Control 32 (4), 141.

Hallanger, A., Sand, I.Ø., 2013. CFD wake modelling with a BEM wind turbine sub-model, Modeling. Identif. Control 34 (1), 19.

Jiang, Z., Moan, T., Gao, Z., 2015. A comparative study of shutdown procedures on the dynamic responses of wind turbines. J. Offshore Mech. Arct. Eng. 137 (1), 011904.

Jiang, Z., Gao, Z., Ren, Z., Li, Y., Duan, L., 2018. A parametric study on the blade mating process for monopile wind turbine installations under rough environmental conditions. Eng. Struct (accepted).

Johansen, T.A., Fossen, T.I., Sagatun, S.I., Nielsen, F.G., 2003. Wave synchronizing crane control during water entry in offshore moonpool operations-experimental results. IEEE J. Ocean. Eng. 28 (4), 720–728.

Jonkman, J.M., Buhl Jr., M.L., 2005. FAST user's guide-updated august 2005. Tech. Rep. Natl. Renew. Energy Lab. (NREL) Golden, CO.

Jonkman, B.J., Kilcher, L., 2012. TurbSim user's guide: version 1.06. Tech. Rep. Natl. Renew. Energy Lab. Colo.

Jonkman, J., Butterfield, S., Passon, P., Larsen, T., Camp, T., Nichols, J., Azcona, J., Martinez, A., 2008. Offshore code comparison collaboration within iea wind annex xxiii: phase II results regarding monopile foundation modeling. Tech. Rep. Natl. Renew. Energy Lab. (NREL) Golden, CO.

Jonkman, J., Butterfield, S., Musial, W., Scott, G., 2009. Definition of a 5-MW reference wind turbine for offshore system development. Tech. Rep. Natl. Renew. Energy Lab Golden, CO, Technical Report No. NREL/TP-500–38060.

Kaiser, M.J., Snyder, B., 2010. Offshore Wind Energy Installation and Decommissioning Cost Estimation in the US Outer Continental Shelf. US Bureau of Ocean Energy Management, Enforcement and Regulation.

Kelley, N.D., Jonkman, B.J., 2006. Overview of the TurbSim stochastic inflow turbulence simulator: version 1.21. Tech. Rep. Natl. Renew. Energy Lab. (NREL) Golden, CO.

Kuijken, L., 2015. Single Blade Installation for Large Wind Turbines in Extreme Wind Conditions. Master's thesis. Technical University of Denmark & TU Delft.

Larsen, T.J., Hansen, A.M., 2007. How 2 HAWC2, the user's manual. Tech. Rep. Risø Natl. Lab.

Mann, J., 1998. Wind field simulation. Probabilistic Eng. Mech. 13 (4), 269–282. https://doi.org/10.1016/S0266-8920(97)00036-2.

MARINTEK, 2016. SIMO - Theory Manual Version 4.8.4.

Moné, C., Hand, M., Bolinger, M., Rand, J., Heimiller, D., Ho, J., 2017. 2015 Cost of Wind Energy Review. Tech. rep.. National Renewable Energy Laboratory.

MSS. Marine Systems Simulator, 2010. Viewed 30.10. 2014. http://www.marinecontrol.org.

Perez, T., Smogeli, Ø.N., Fossen, T.I., Sørensen, A.J., 2006. An overview of the marine systems simulator (MSS): a simulink® toolbox for marine control systems, Modeling. Identif. Control 27 (4), 259–275.

Ren, Z., Skjetne, R., Gao, Z., 2017. Modeling and control of crane overload protection during marine lifting operation based on model predictive control. In: ASME 2017

36th International Conference on Ocean, Offshore and Arctic Engineering. American Society of Mechanical Engineers OMAE2017–62003.

Ren, Z., Jiang, Z., Skjetne, R., Gao, Z., 2018. Active tugger line force control for single blade installation. Wind Energy (under review).

RWE Innogy GmbH, 2014. Halfway through the turbine installation for the nordsee ost offshore wind farm. https://www.rwe.com/web/cms/en/113648/rwe/press-news/press-release/?pmid=4012024, Accessed date: 16 July 2017.

Skaare, B., Egeland, O., 2006. Parallel force/position crane control in marine operations. IEEE J. Ocean. Eng. 31 (3), 599–613.

Tian, X., Wang, P., Li, X., Wu, X., Lu, W., Wu, C., Hu, Z., Rong, H., Sun, H., Wang, A., et al., 2018. Design and application of a monitoring system for the floatover installation. Ocean. Eng. 150, 194–208.

Turbsim, https://nwtc.nrel.gov/TurbSim, accessed: 2017-09-17.

Wang, P., Tian, X., Peng, T., Luo, Y., 2018. A review of the state-of-the-art developments in the field monitoring of offshore structures. Ocean. Eng. 147, 148–164.

Zhao, Y., Cheng, Z., Sandvik, P.C., Gao, Z., Moan, T., 2018. An integrated dynamic analysis method for simulating installation of single blades for wind turbines. Ocean. Eng. 152, 72–88. https://doi.org/10.1016/j.oceaneng.2018.01.046.

Paper A2

A crane overload protection controller for blade lifting operation based on model predictive control

Zhengru Ren, Roger Skjetne, and Zhen Gao

A Crane Overload Protection Controller for Blade Lifting Operation Based on Model Predictive Control

Zhengru Ren [1,2,3,*] , **Roger Skjetne** [1,2,3] **and Zhen Gao** [1,2,3]

1   Centre for Research-based Innovation on Marine Operations (SFI MOVE), NO-7491 Trondheim, Norway; roger.skjetne@ntnu.no (R.S.); zhen.gao@ntnu.no (Z.G.)
2   Centre for Autonomous Marine Operations and Systems (AMOS), NO-7491 Trondheim, Norway
3   Department of Marine Technology, Norwegian University of Science and Technology, NO-7491 Trondheim, Norway
*   Correspondence: zhengru.ren@ntnu.no; Tel.: +47-474-422-832

Abstract: Lifting is a frequently used offshore operation. In this paper, a nonlinear model predictive control (NMPC) scheme is proposed to overcome the sudden peak tension and snap loads in the lifting wires caused by lifting speed changes in a wind turbine blade lifting operation. The objectives are to improve installation efficiency and ensure operational safety. A simplified three-dimensional crane-wire-blade model is adopted to design the optimal control algorithm. A crane winch servo motor is controlled by the NMPC controller. The direct multiple shooting approach is applied to solve the nonlinear programming problem. High-fidelity simulations of the lifting operations are implemented based on a turbulent wind field with the MarIn and CaSADi toolkit in MATLAB. By well-tuned weighting matrices, the NMPC controller is capable of preventing snap loads and axial peak tension, while ensuring efficient lifting operation. The performance is verified through a sensitivity study, compared with a typical PD controller.

1. Introduction

The rapid development of offshore wind farms has been noticed with a trend of continued increasing in turbine size. The favor of larger offshore wind turbines (OWTs) results in decreasing costs of installation and grid connection per unit energy produced [1]. This comes with new challenges in offshore OWT installation. Single blade installation is a method of OWT blade installation, which allows for a broader range of installation vessels and lower crane capabilities. One blade is lifted in one lifting operation. Passive and active single blade installation methods have been studied [2–7].

Typically, the lifting operations are conducted according to pragmatic experiences and short-term weather forecast. The large peak wire rope tension in the initial stages of the lifting and lowering of a payload is risky for safety hazards. Extensive research has been conducted on effective crane and winch control. Various simplified models have been developed to model the crane and payload systems, e.g., Lagrangian models [8,9], Newton–Euler equations [10], and partial differential Equation [11]. Normally, the axial wire rope elongation is disregarded due to the its high stiffness. The ship-mounted crane systems have more complicated dynamic characteristics, with a higher number of degrees of freedom (DOFs) in the control system. A high-fidelity simulation-verification OWT blade installation model for the control purpose is developed in [4]. However, the model is unnecessarily complex for design of control laws. The ordinary studied payloads are lumped mass [12,13] and distributed

mass [14]. Though wire rope elongation is always neglected in transportation mode, it is an important issue in e.g., heave compensation through a wave zone during moonpool operations [15–19].

Model predictive control (MPC) is a widely applied optimal control technology. The MPC controller provides real-time feedback by optimizing the future plant behavior in a finite horizon. Considerable effort has been devoted to improving its robustness and performance [20–25]. The performance of the nonlinear model predictive controller (NMPC) depends on the computation interval, initial guess, programming algorithms, etc. The stability can be ensured through a careful selection of designed parameters [26]. Direct methods transform a continuous system of infinite dimension into a discrete nonlinear programming system of finite dimension. The direct methods can be categorized into sequential and parallel-in-time approaches. Direct single shooting is a sequential approach, with a strong requirement to the initial guess, especially for highly nonlinear systems. However, the shortages of the parallel-in-time approach are the unnecessarily strong nonlinearity of the optimization problem and the poor convergence behaviors to the desired reference trajectory [27,28]. Optimization theories have been widely used in marine research [29–31]. To effectively solve the programming problem using embedded platforms, automatic code generation is a widely discussed issue. A number of user-friendly codes have been developed, where C++ codes for embedded systems can be generated automatically by several published quadratic programming solvers [32–34].

Though efforts have been made to improve the level of automation for blade mating operations [3,5,18,35,36], studies are lacking on constrained optimal blade lifting operations from the deck to improve safety and performance. An NMPC framework for lifting a lumped-mass payload was presented by the authors in [37]. In this paper, we extend the NMPC scheme for a winch servo to reduce the abrupt wire tension load increase and to avoid snap loads resulting from a suspended blade at the initial stages of lift-off (and also lowering) operation. This makes the transfer to the next phase, moving the blade towards the hub safer and more efficient. The main advantages of NMPC are that an optimal control action is achieved, where the performance and efficiency can be targeted by proper tuning of an objective function, while at the same time adhering to constraints that for other methods must be handled through implementation of logics. The lifted blade should reach the desired height in a specified speed abstaining from possible dangers. An optimal control problem is formulated for the lifting process of a blade, with implementation in a well-proven optimization solver. The performance and properties of the method, compared to a standard proportional-derivation (PD) crane lifting control law, are then demonstrated in a simulation study with a high-fidelity numerical model. In [37], only a simplified lifting system was considered, with a lumped-mass payload and known parameters, whereas wind-induced loads, motor dynamics, hook, and slings were neglected in the simulations. The extensions made in this paper therefore consist of deriving a reduced model for a more realistic blade payload in a lifting control design. Based on this, we design an NMPC controller to solve the formulated constrained optimal lifting problem in a turbulent wind field. Compared to a lumped-mass payload, a blade has more complex dynamics and aerodynamic characteristics. Simulations are finally conducted in turbulent wind fields with different mean wind speeds, as well as varying parametric uncertainties, and the simulation results are discussed.

The paper is structured as follows. In Section 2, the problem formulation is proposed with a description of the system and an illustrative example. A simplified model of the NMPC controller is introduced in Section 3. Basic concepts and theories concerning the direct multiple shooting approach are introduced in Section 4. Simulation results and comparative studies with a proportional-derivative (PD) controller are presented in Section 5. Finally, conclusions are drawn.

Notation: $|x|$ and $|x|_A$, respectively, denote the Euclidean vector norm and weighted Euclidean vector norm, i.e., $|x|^2 = x^\top x$ and $|x|_A^2 = x^\top A x$ with $A = A^\top > 0$. The vector inequality of $b \in \mathbb{R}^n$ is denoted by $\underline{b} \preceq b \preceq \bar{b}$, i.e., component-wise inequalities $\underline{b}_i \leq b_i \leq \bar{b}_i$ hold for $i = 1, \cdots, n$.

Overlines and underlines, $\underline{b}, \overline{b} \in \mathbb{R}^n$, stand for vectors containing all the lower and upper limits of the elements in b, respectively. The saturation operator sat : $\mathbb{R} \to \mathbb{R}$ is denoted by

$$\text{sat}(a) = \begin{cases} \overline{a} & \text{if } a \geq \overline{a}, \\ a & \text{if } \underline{a} < a < \overline{a}, \\ \underline{a} & \text{if } a \leq \underline{a}. \end{cases} \tag{1}$$

2. Problem Formulation

2.1. System Description

A jackup vessel is considered hereafter for the single blade installation operation. The legs have been lowered into the seafloor and the jack-up vessel has been lifted out of water, which provides a stable platform for lifting operations. The blade lifting operation is conducted by a rigidly fixed boom crane on the vessel. The blade is seized by a yoke through a lift wire and two slings; the configuration is shown in Figures 1 and 2. A hook connects the lift wire and two slings. The yoke and crane boom are fastened by two horizontal tugger lines, constraining the blade motion within the horizontal plane due to the wind-induced loads. The lengths of the tugger lines are adjusted with the blade. Active tension force control on the tugger lines, such as [3], is not considered. The blade is first lifted up from the deck of the jackup or a barge, in which the lift wire gradually takes the gravity of the blade and the wind-induced dynamic loads. The blade is then lifted from a low position up to the hub height. During this phase, the main dynamic loads are the wind loads acting on the blades. If the lifting speed changes, the lift wire experiences the inertial loads on the blade. There are always gravity loads acting on the blade. When the blade is close to the hub height, one may reduce the lifting speed and adjust the position of the blade root for the final connection.

In this paper, we consider a scenario in which the blade starts in the air with a zero lifting speed. The supporting force from the deck is not considered. The lifting speed is increased to the target value and then reduced to zero when it reaches the specific hub height. The payload motion can be estimated by various methods, e.g., GPS and inertial measurement unit (IMU) sensor fusion algorithm and motion capture systems.

Figure 1. Single blade installation (Image source: RIPR [38]).
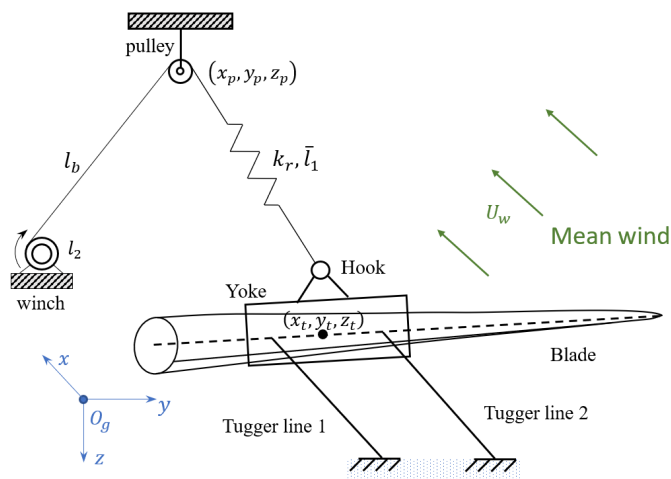
Figure 2. Free body diagram of the blade lifting operation.

2.2. System Modeling

The blade installation simulation framework used is developed in MATLAB and Simulink [4], in which necessary modules for blade installation are included, e.g., wire rope, suspended blade, hook, winch, and wind turbulence. This approach has been applied to analyze and verify active single blade installation methods [3].

The hook and blade are modeled in 3DOF and 6DOF, respectively. Lift wires function as single-direction tensile springs that can only provide tension when the axial elongation is greater than zero. A turbulent wind field is generated by the Mann model in HAWC2. Because of the geometric complexity, the wind-induced loads are calculated according to the cross-flow principle. The total wind loads acting on the entire blade are the sum of the lift and drag forces measured at each airfoil segment.

An National Renewable Energy Laboratory (NREL) 5MW wind turbine blade is selected as the payload for a case study [39]. Due to physical limitations, the winch cannot reach a reference speed infinitely fast, nor exceed the designated safe speed. Hence, we assume the occurrence of saturation for both winch acceleration and winch speed. The main system parameters used are tabulated in Table 1.

Table 1. Parameters of the single blade installation system.

Parameter	Symbol	Unit	Value
Mass of the blade	m_t	ton	17.74
Mass of the yoke	m_t	ton	20
Mass of the hook	m_h	ton	1
Initial length of the lift wire	$\bar{l}_1(0)$	m	40
Length of the rope positioned in front of the pulley	l_b	m	60
Length of the slings	l_s	m	9.17
Elastic module	EA	N	2.375×10^9
Modified coefficient	γ	-	0.5
Initial lifting speed	$l_2(0)$	$\frac{m}{s}$	0
Desired lifting speed	v_{1d}	$\frac{m}{s}$	±1.2
Winch speed boundary	$[\underline{v}_1, \overline{v}_1]$	$\frac{m}{s}$	$[-1.2, 1.2]$
Winch acceleration boundary	$[\underline{u}, \overline{u}]$	$\frac{m}{s^2}$	$[-2, 2]$

A local Earth-fixed, assumed inertial, reference frame is adopted with the *x*-, *y*-, and *z*-axes pointing in northern, eastern, and downward (NED) directions, respectively. Translational velocities

measured along the axes are denoted $\dot{x}$, $\dot{y}$, and $\dot{z}$. The orientations about the fixed axes are given by roll, pitch, and yaw angles, denoted ϕ, θ, and ψ, respectively.

2.3. Case Study

Since the blade is lifted off at a low level where the wind speed is low and the lift-off operation happens in a short duration of a few seconds, we consider a blade lift without aerodynamic loads. At the start of the simulation, the suspended blade is stabilized at an equilibrium point by the lift wire, slings, and tugger lines without oscillation in the lift wire. When a sudden lifting or lowering action is executed at 100 s, the lifting speed is changed to the constant desired speed v_{1d} in a very short time. The wire tension history is shown in Figures 3 and 4 for lifting and lowering, respectively.
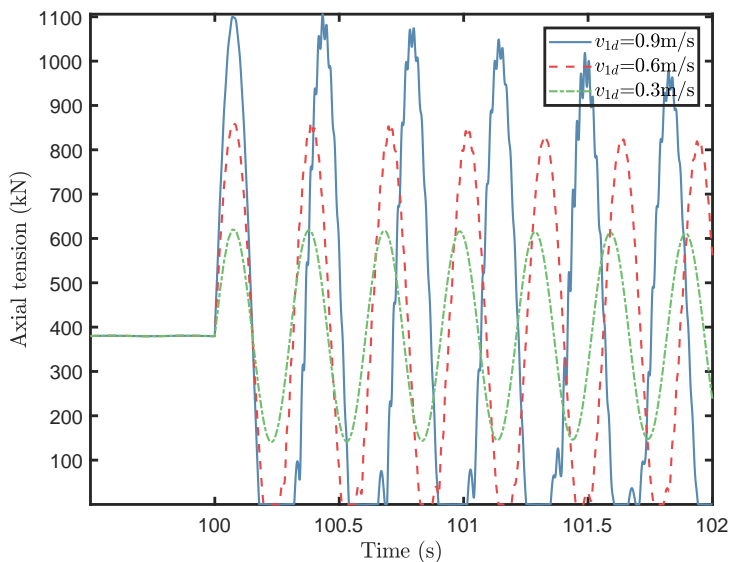
Figure 3. The lift wire tension history of a suspended blade with constant lifting-off speeds.

In the figures, the only changing parameter is the setpoint lifting speed. It is observed that snap loads or sudden peak tensions are excited in the first 0.5 s, followed by the occurrence of damped oscillations due to the axial damping. The larger sudden tension occurs at the beginning of the lifting operation due to significant winch speed acceleration. The magnitude of the dynamic tension increases with the lifting speed.

In the tension history curves, there are some high-frequency peaks of minor amplitude, which are induced by the slings. The tension deviation caused by the blade's motion in the horizontal plane is very small compared to the peak values. The amplitude of the oscillation decreases slowly.

Jerking occurs more easily at a higher lifting speed. A sudden tension maximum is dangerous. Snap loads, which occur when the axial tension decreases to below zero, are induced during this lifting operation. The maximum tension, on the other hand, may exceed the lift wire strength. Thus, the minimum value for the axial elongation of the wire should always be non-negative. The restoring force does not act on the payload due to the negative axial elongation when snap occurs. Furthermore, the magnitude of the blade motion is enlarged when snap loads occur, resulting in a potential impact damage between the blade and deck.
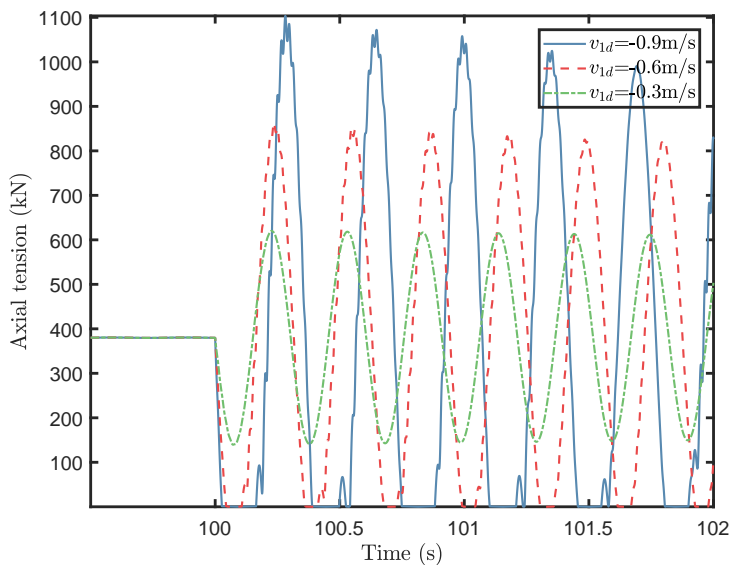
Figure 4. The lift wire tension history of a suspended blade with constant lowering speeds.

In practice, the lifting speed should be changed gradually from 0 to the setpoint speed to prevent the zero tension in the lift wire. In this paper, we show how constrained optimization conveniently can be designed to achieve this while simultaneously satisfying relevant constraints in the control system.

2.4. Problem Statement

The objective is to design a safe and efficient lifting scheme using constrained optimal control to achieve the necessary lifting performance. In more detail, there are seven optimal targets:

(a)　Reach the desired setpoint lifting speed v_{1d} from zero speed in the shortest time possible within the constraints,

(b)　Protect overload tension and reduce dynamic tension by controlling the winch speed,

(c)　Prevent winch servo motor burnout by limiting the winch acceleration,

(d)　Prevent negative elongation and snap loads,

(e)　Reduce the wire rope wear,

(f)　Limit the maximum speed of the servo motor,

(g)　Reach the desired wire rope length.

The tugger lines are assumed to be released with the lifting operation. Therefore, tugger lines do not provide restoring forces unless wind-induced blade displacement is higher than expected. We assume that the blade orientation variance caused by the lifting operation and the wind-induced load is insignificant, and the lifting or lowering operation is so short that wind-induced motion is not affected.

A lifting process is divided into three phases: the startup region, the steady region, and the slowdown region; see Figure 5. The control objective of each region is tabulated in Table 2. Region I denotes the startup stage, wherein the payload speeds up to the desired lifting speed v_{1d} from initial winch speed $v_1(0) = 0$. Sudden overloads or snap loads mainly occur at the beginning of Region I. In Region II, spanning from the end of the startup stage to the outset of the slowdown stage, a steady motion is performed. The purpose of this stage is to ensure the desired lifting speed, i.e., $v_1(t) = v_{1d}$. The controller should be deactivated during this stage due to the low dynamic tension. Instead, a simple proportional controller is used in this phase for its simplicity. Region III is the slowdown stage,

where the controller is again activated. The lifting speed should be reduced to zero. Dynamic tension mainly occurs in the initial period. In addition to all requirements for Region I, the desired wire rope length should be achieved. The controller is switched off at the end of Region III.
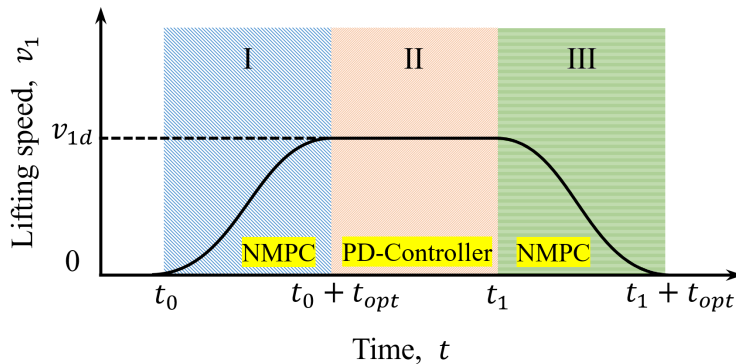
Figure 5. Example of the lifting problem in different regions.

Table 2. Objectives for Regions I and III.

Objective No.	Region I	Region III
(a)	✓	✓
(b)	✓	✓
(d)	✓	✓
(d)	✓	✓
(e)	✓	✓
(f)	✓	✓
(g)		✓

3. Reduced Model for Control Design

A reduced model is adopted for the optimization problem in a three-dimensional north–east–down (NED) coordinate system [40]. The crane is assumed to be rigidly fixed on the vessel. The masses of the hook, yoke, and blade are m_h, m_y, and m_b, respectively. We assume that the overall payload mass m_t is concentrated at the blade center of gravity (COG), where $m_t = m_h + m_y + m_b$. Furthermore, the lift wire and slings are considered as one unit without the consideration of the lift wire control; it provides a restoring force on the moving blade. We assume that the ropes are replaced by a lightweight rope, i.e., its mass is assumed to be zero. The blade COG is suspended by the rope, which is connected to the winch through a pulley fixed at the crane tip. Hence, a tensile spring is employed to model the wire rope. The unstretched length of the spring $\bar{l}_1$ denotes the distance between the pulley and blade COG. Tugger lines are released at a speed such that only vertical lifting is allowed. Because the lifting operation is executed over a short period, the horizontal wind-induced load is assumed to be restrained by tugger lines and can be disregarded. A 3DOF lifting model, with an elastic wire rope and a controllable winch, is deduced based on the Newton–Euler method in the NED coordinate system. Four vectors are defined correspondingly:

the position of the blade COG: $r_t = [x_t, y_t, z_t]^\top$,

the position of the pulley: $r_p = [x_p, y_p, z_p]^\top$,

the translational velocity of the blade COG: $u_t = [\dot{x}_t, \dot{y}_t, \dot{z}_t]^\top$,

the velocity of the pulley: $u_p = [\dot{x}_p, \dot{y}_p, \dot{z}_p]^\top$.

The total force acting on the payload is given by

$$M_t \dot{u}_t = G + \tau_{tr} + \tau_{td}, \tag{2}$$

where the mass matrix is written as $M_t = \mathrm{diag}(m_t, m_t, m_t)$, G, τ_{tr}, τ_{td} are the gravity, restoring force, and damping force, respectively. If the lifting speed changes quickly, the main reason for the large dynamic tension is from the lifting wire. Then, the blade wind loads could be considered as quasi-static loads. Hence, the controller is not developed to compensate the dynamic tension due to the disturbance in wind.

3.1. Restoring Force

Additional two vectors are defined to shorten the equations. The relative position vector from the pulley to payload Δ_1 and its time derivative Δ_2 are respectively defined as

$$\Delta_1 := r_t - r_p, \tag{3a}$$

$$\Delta_2 := u_t - u_p. \tag{3b}$$

The restoring force of the lift wire τ_{tr} reacts with positive wire rope axial elongation, i.e.,

$$\tau_{tr} = -\kappa(\delta)k_r\delta\frac{\Delta_1}{|\Delta_1|}, \quad \kappa(\delta) = \begin{cases} 1, & \delta \geq 0, \\ 0, & \text{otherwise}, \end{cases} \tag{4}$$

where κ denotes the restoring action coefficient, $\delta = |\Delta_1| - \bar{l}_1$ is the elastic elongation, and k_r is the stiffness. Determined by the material, diameter, and strand construction, the generalized stiffness of the rope is modeled as

$$k_r = \gamma\frac{EA_r}{l_1}, \tag{5}$$

where γ is the modified coefficient of a stranded wire, E stands for the Young's modulus, A_r denotes the cross-sectional area of the rope, and $l_1 = \bar{l}_1 + l_b$, where we assume that the length of rope between the winch and pulley l_b is constant.

3.2. Damping

The wire rope has a small damping ratio, generally selected as 0.1–0.5% of the critical damping value [41]. Hence, the damping force τ_{td} is given by

$$\tau_{td} = -d_l\dot{\delta}\frac{\Delta_1}{|\Delta_1|} = -\frac{d_l}{|\Delta_1|}\left(\frac{\Delta_1^\top\Delta_2}{|\Delta_1|} - v_1\right)\Delta_1, \tag{6}$$

where $v_1 := \dot{l}_1$ denotes the wire length changing rate, d_l is the damping coefficient, and the elongation changing rate $\dot{\delta}$ is given by

$$\dot{\delta} = \frac{\Delta_1^\top}{|\Delta_1|}\Delta_2 - v_1. \tag{7}$$

3.3. Winch Servo Motor

A variable-speed DC motor with motion feedback control is used as the winch servo motor to follow the specific motion trajectory. The field voltage is employed as an input for the DC motor. The produced magnetic torque T_m is proportional to the armature current i_f, given by

$$T_m = k_m i_f = T_l + T_d, \tag{8}$$

where k_m is the motor constant, T_l is the load torque, and T_d is the disturbance torque. The transfer function between i_f and the field voltage V_f is given by

$$\frac{i_f}{V_f}(s) = \frac{1}{R_f + L_f s}, \tag{9}$$

where R_f and L_f are the armature resistance and inductance. The transfer function between the winch servo motor acceleration, $u = \dot{v}_1$, and T_l is given by

$$\frac{u}{T_l}(s) = \frac{s/r_m}{J_m s + B_m}, \tag{10}$$

where r_m is the radius of the winch, J_m is the moment of inertial, and B_m denotes the viscous friction coefficient. The low-level servo motor speed and torque control is not discussed in this paper. We assume that the field-current-controlled motor can effectively track the signal u generated from the proposed controller.

3.4. Model Summary

Under the aforementioned assumptions, disregarding wind-induced loads and substituting Equations (4) and (6) into Newton's second law (2), the simplified control design model for the considered blade lifting operation is produced,

$$\dot{r}_t = u_t, \tag{11a}$$
$$M_t \dot{u}_t = -A(r_t, r_p, l_1, v_1)\Delta_1 + G, \tag{11b}$$
$$\dot{l}_1 = v_1, \tag{11c}$$
$$\dot{v}_1 = u, \tag{11d}$$

where $A(r_t, r_p, l_1, v_1) = a_t I_{3\times3}$, with $a_t = \gamma EA \frac{|\Delta_1| - \bar{l}_1}{l_1 |\Delta_1|} + \frac{d_l}{|\Delta_1|}(\frac{\Delta_1^\top \Delta_2}{|\Delta_1|} - v_1)$, and $G = [0, 0, m_t g]^\top$ is gravity. The nonlinearity of the differential Equation (11) mainly derives from the function a_t.

4. Design of the Optimal Control

NMPC is adopted to solve the proposed constrained optimization problem. Numerical nonlinear optimization involves finding suitable inputs for a complex nonlinear system that minimizes a specified performance objective within system constraints. The direct multiple shooting approach is adopted hereafter for discretization, and the ODE (11) is used for prediction.

4.1. Direct Multiple Shooting Method

A continuous optimal control problem is transformed into a nonlinear programming (NLP) problem through a direct multiple shooting approach. According to the discretization of the state variables and control inputs for finite dimensional parameterization of the path constraints, shooting nodes and piecewise functions are adopted to approximate the variables. Then, a quasi-Newton method is employed to solve it.

A time grid $t_0 < t_1 < \cdots < t_N$ is generated over a time horizon $[t_0, t_0 + T]$ by dividing the period into N subintervals with a constant time step equal to the sampling time, i.e., $\delta t = T/N$. To simplify the expression, $x(t_k)$ is denoted by x_k, where $t_k = t_0 + k\delta t$. For a subinterval $[t_k, t_{k+1}]$, the state numerically updates with the explicit integrator F and approximates the solution mapping, i.e., $x_{k+1} = F(x_k, u_k)$. Two additional variables, s_i and q_i, are introduced as discrete representations of x and u, respectively, i.e., $s_{k+1} = F_k(s_k, q_k)$. Zero-order hold is used as the feedback signal input from a finite-dimensional NLP problem during subinterval $[t_k, t_{k+1}]$. The notations of the above processes are presented in Figure 6.
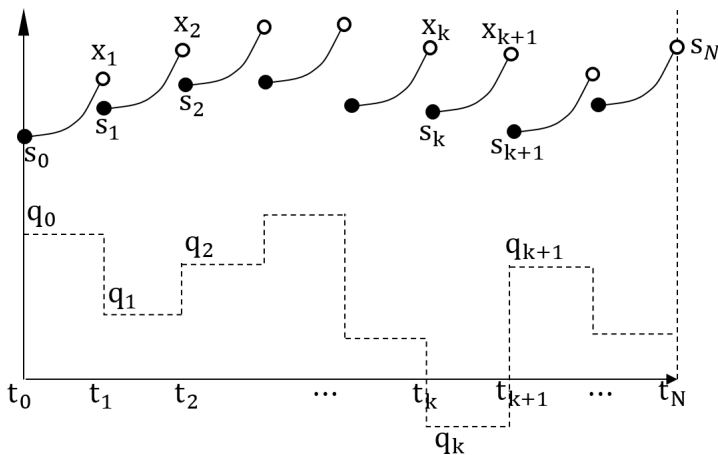
Figure 6. Illustration of direct multiple shooting.

A dynamic optimization problem with constraints can be solved using a multiple shooting approach, which is formulated as

$$\min_{S,Q} \frac{1}{2} \sum_{k=0}^{N-1} l_k(s_k, q_k) + E_N(s_N), \tag{12a}$$

$$\text{s.t. } x_0 - s_0 = 0, \tag{12b}$$

$$F(t_{k+1}; t_k, s_k, q_k) - s_{k+1} = 0, \qquad k = 0, \cdots, N-1, \tag{12c}$$

$$h(s_k, q_k) \preceq 0, \qquad k = 0, \cdots, N, \tag{12d}$$

$$r(s_N) \preceq 0, \tag{12e}$$

where $S = [s_1, \cdots, s_N]$ denotes the state trajectory containing all the the state vector at the kth time interval x_k, $Q = [q_1, \cdots, q_{N-1}]$ refers to the control trajectory, equations (12b–12e) denote the initial value, continuity condition, path constraints, and terminal constraints, respectively. The objective function, which consists of an integral cost contribution (or Lagrange term) l_k and an end time cost contribution (or Mayer term) E_N, can be chosen as, e.g.,

$$l_k(s_k, q_k) = |s_k - x_k^{ref}|_Q^2 + |q_k - u_k^{ref}|_R^2,$$
$$E_N(s_N) = |s_N - x_N^{ref}|_P^2,$$

where Q, R, and P denote positive-definite diagonal weighting matrices.

An example of the path is given by

$$\underline{u} \preceq u_k \preceq \overline{u}, \qquad k = 0, \cdots, N-1,$$
$$\underline{s} \preceq s_k \preceq \overline{s}, \qquad k = 0, \cdots, N-1,$$

where $\underline{s}$, $\overline{s}$, $\underline{u}$, and $\overline{u}$ are the lower and upper limits for state s and input u. The limits can be chosen according to the critical operational conditions and physical actuator constraints. The desired trajectory for s_k and q_k are denoted by x_k^{ref} and u_k^{ref}. Several established methods can be used to solve the NLP problem, e.g., interior point methods [42–44] and genetic algorithms [45,46].

4.2. NMPC Design

For the blade lifting problem, the NLP problems in Regions I and III are summarized in Table 3.

Table 3. Summary of the control algorithm for different regions.

Region	Control Law	
I	$\displaystyle \min_{S,Q} \sum_{k=0}^{N}[k_\delta(\frac{d}{dt}|\Delta_1|-v_1)^2+k_d(v_1-v_{1d})^2]+\sum_{k=0}^{N-1}k_u u^2,$	(13a)
	s.t. $\underline{u}\le u\le\overline{u}, \qquad k=0,\cdots,N-1,$	(13b)
	$|\Delta_1|-\bar{l}_1\ge 0, \qquad k=0,\cdots,N,$	(13c)
	$|\dot{\Delta}|_1-v_{1d}=0, \qquad k=N;$	(13d)
II	$u=-k_p(v_1-v_{1d});$	(14)
III	$\displaystyle \min_{S,Q} \sum_{k=0}^{N}[k_\delta(\frac{d}{dt}|\Delta_1|-v_1)^2+k_d(v_1-v_{1d})^2+k_l(\bar{l}_1-\bar{l}_{1d})^2]+\sum_{k=0}^{N-1}k_u u^2,$	(15a)
	s.t. $\underline{u}\le u\le\overline{u}, \qquad k=0,\cdots,N-1,$	(15b)
	$|\Delta_1|-\bar{l}_1\ge 0, \qquad k=0,\cdots,N,$	(15c)
	$|\dot{\Delta}|_1-v_{1d}=0, \qquad k=N,$	(15d)
	$\bar{l}_1-\bar{l}_{1d}=0, \qquad k=N;$	(15e)

In Table 3, $k_p>0$ is the gain of the P controller, and k_u, k_δ, and k_d are the weights for different components in the cost function. Quadratic objective functions are adopted. The physical meaning of different equations are explained as follows: in equations (13a) and (15a), $(\frac{d}{dt}|\Delta_1|-v_1)^2$, $(v_1-v_{1d})^2$, $(\bar{l}_1-\bar{l}_{1d})^2$, and u^2 penalize the relative speed between the payload and winch, the deviation between the real-time winch speed and the desired final winch speed, the difference between the real-time lift wire length and the desired final length, and the winch input, respectively. The corresponding targets of these terms in Section 2.4 are (b,e), (a,f), (g), and (c), respectively. The objectives of the inequality constraints (13b) and (13c) are (c) by limiting the control input and (d) by ensuring that elongation is always non-negative. The selection of the boundary values $\underline{u}$ and $\overline{u}$ depends on characteristics and configuration of the winch. The equality constraints (13d) and (15e) ensure that the lifting speed and lift wire length reach their specified values at the final time.

For the proposed model in (11), there are eight states and one control input. The initial prediction is significant for the computational efficiency and stability. Figures 7 and 8 show an example of the weight selection with respect to the time interval t_k, $k=0,\cdots,N-1$. Sudden tension peaks occur at the beginning of the start up and slowdown phases. Hence, high weights are selected for k_δ at the beginning period to prevent significant sudden overload, and similarly high weights are needed for k_d at the end of the period to achieve desired lifting speed.
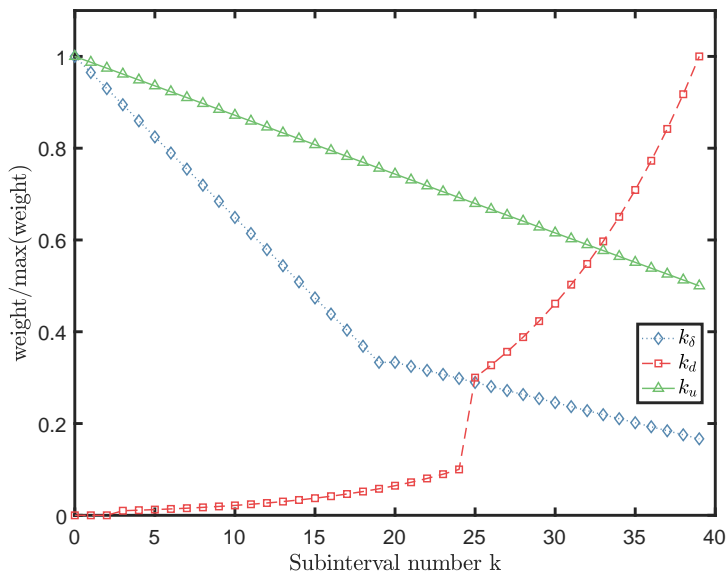
Figure 7. An example of the normalizing weights for Region I with respect to the subinterval number.
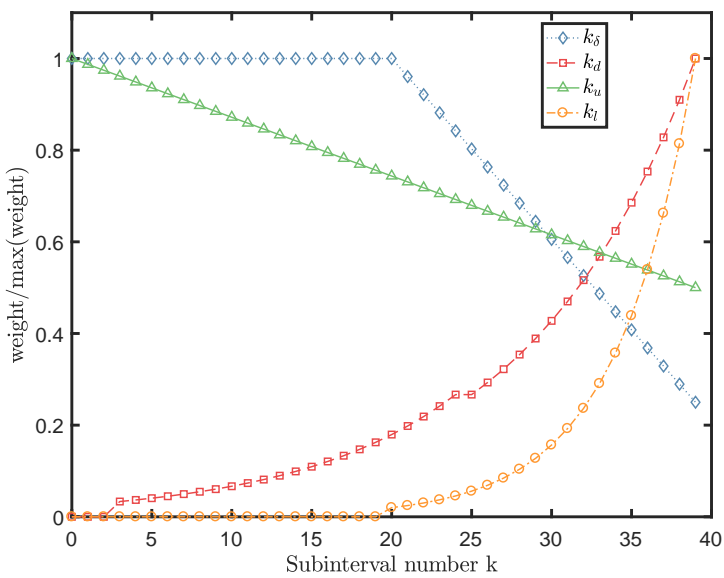
Figure 8. An example of the normalizing weights for Region III with respect to the subinterval number.

4.3. Stability Considerations

Define new states as $x_1 = |\Delta_1| - \bar{l}_1 - \frac{mgl_1}{\gamma EA}$, $x_2 = \dot{x}_1 = \frac{d}{dt}|\Delta_1| - (1 + \frac{mg}{\gamma EA})v_1$ with $\frac{d}{dt}|\Delta_1| = \frac{\Delta_1^\top \Delta_2}{|\Delta_1|}$, $x_3 = l_1 - l_{1d}$, and $x_4 = \dot{x}_3 = v_1 - v_{1d}$. The dynamics are given by

$$\dot{x}_1 = x_2, \tag{16a}$$

$$\dot{x}_2 = -\frac{1}{|\Delta_1|^3}(\Delta_1^\top \Delta_2)^2 + \frac{1}{|\Delta_1|}\Delta_2^\top \Delta_2 + \frac{1}{|\Delta_1|}\Delta_1^\top \dot{\Delta}_2 - (1 + \frac{mg}{\gamma EA})u, \tag{16b}$$

$$\dot{x}_3 = x_4, \tag{16c}$$

$$\dot{x}_4 = u - \dot{v}_{1d}(t). \tag{16d}$$

The vector form is

$$\dot{x} = f(t, x, u), \ x(t_0) = x_0, \ t \geq t_0 \geq 0, \tag{17}$$

where $x = [x_1, x_2, x_3, x_4]^\top$ and u is constrained, i.e., $u \in U$.

Function f is twice continuously differentiable. For $x = 0$, we have that $|\Delta_1| = \bar{l}_1 + \frac{mgl_1}{\gamma EA}$ is a constant, $l_1 = l_{1d}$, and $v_1 = v_{1d}$. Hence, $\frac{d}{dt}|\Delta_1| = 0$, $\Delta_1^\top \Delta_2 = 0$, $|\Delta_2|^2 = 0$. When the crane pulley is fixed, $\dot{\Delta}_2 = \dot{u}_t = 0$. In addition, if $u = 0$, we get $f(t, 0, 0) = 0$ for all $t \geq t_0$. From (13b) and (15b), $u = 0$ is included in U, and U is a compact and convex set. Hence, system (16) has a unique solution for any initial condition x_0 and piecewise continuous input $u(t)$, $t \geq 0$. Furthermore, the Jacobian linearization of the nonlinear system (16) is stabilizable. In our case, starting in Region I at zero velocity and Region III from a constant desired speed, a feasible solution is a matter of accelerating slowly enough. Hence, feasibility solutions always exist so that there exists at least one input profile Q for which all the constraints are satisfied. Therefore, according to the Theorem 1 in [47], the closed-loop system (16) with optimal control problem (13) and (15) is asymptotically stable, if a sufficiently small sampling time δt is adopted and there exist no disturbances.

4.4. Overview of the Control System

A block diagram of the control scheme is presented in Figure 9. As several controllers are proposed in Table 3, a switching logic outputs a signal σ to determine the working controller used for a specific period. The switching rule is given in Algorithm 1, where $\sigma = 0$ denotes that all controllers are switched off and $\sigma \in \{1, 2, 3\}$ is the index of the corresponding controller; $\mu \in (0, 1)$ is a coefficient setting the boundary of Controller I. The feedback to the controller I is the position and velocity of the payload, length of lift wire, and winch servo motor speed. The feedback to the PD controller is the length of lift wire and winch servo motor speed.
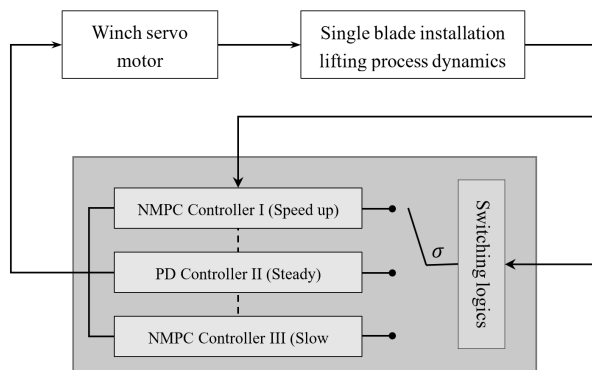
Figure 9. Block diagram of the hybrid control scheme.

In addition, an observer is needed to filter the sensor noise and estimate unmeasured states in practical applications [48]. Observer design is not the emphasis of this paper and therefore not considered.

Algorithm 1 Switching rule.

Data: $(l_1, v_1, \mu, l_{1d}, v_{1d}, l_s)$
Initialize: $\sigma = 0$,
if operation starts
    if ($\sigma = 0$ or 1) and $v_1 < \mu v_{1d}$
        $\sigma = 1$
    elseif ($\sigma = 1$ or 2) and $v_1 \geq \mu v_{1d}$
        $\sigma = 2$
    elseif ($\sigma = 2$ or 3) and $0 \leq |l_1 - l_{1d}| \leq l_s$
        $\sigma = 3$
    end
else
    $\sigma = 0$
end
Return: σ

---

5. Simulations and Results

5.1. Simulation Overview

The simulations are conducted in MATLAB. The structural parameters used are tabulated in Table 1. The limits of the winch loads are considered to be expressed by the maximum acceleration. The wind field with turbulence starts acting on the blade with a ramp over the first five seconds. Class C turbulent winds with corresponding turbulence intensity (TI) are adopted in the simulations [49]. CaSADi and MarIn toolboxes are used to solve the NLP problems. The *ipopt* solver is adopted.

The simulation scenario involves lowering a suspended NREL 5 MW wind turbine blade 10 m. The initial wire length is $\bar{l}_1 = 40$ m, the final desired length is $\bar{l}_1 = 50$ m, and the final desired lifting speed is $v_{1d} = 1.2$ m/s. The control horizon is $t_{opt} = 4$ s with 40 subintervals. The following parameters are used for the different regions:

(a) Region I: Start a lifting with an initial wire length and initial speed, and reach a desired speed in t_{opt}:

- $\bar{l}_1(t_0) = 40$ m,
- $v_1(t_0) = 0$ m/s,
- $v_1(t_0 + t_{opt}) = v_{1d} = 1.2$ m/s.

(b) Region II: Stabilize the lifting speed to the desired value:

- $v_1(t) = v_{1d} = 1.2$ m/s.

(c) Region III: Stop the lifting operation with the following initial speed, and reach the desired lift wire length in t_{opt}:

- $v_1(t_1) = 1.2$ m/s,
- $v_1(t_1 + t_{opt}) = 0$ m/s,
- $\bar{l}_1(t_1 + t_{opt}) = 50$ m.

Tugger lines are released with a speed of v_{tug}, i.e.,

$$v_{tug,i} = \frac{z_t - z_{tug,i}}{l_{tug,i}} v_1, \tag{18}$$

where subscript *i* is the index of the tugger line, z_{tug} is the vertical position of the tugger line connection point to the crane boom, and l_{tug} is the length of the tugger line.

5.2. Basic PD Controller

To compare the NMPC controller performance, PD controllers are used. These open-loop controllers accelerate the winch servo motor to the desired speed. Due to physical limitations of the actuator (winch servo motor), saturation modules are applied to bound the lifting acceleration and velocity. A lowpass filter is used as a reference model. In summary, the combination of the lowpass filter and PD controller is given by

$$\dot{l}_d = -\omega_{v1}(l_d - l_{ref}), \tag{19a}$$

$$\dot{\bar{l}}_1 = \text{sat}(v_1), \tag{19b}$$

$$u = \begin{cases} \text{sat}\left(-\omega_{v1}^2(\bar{l}_1 - l_d) - 2\zeta_{v1}\omega_{v1}v_1\right), & \text{Reg. I, III,} \\ \text{sat}\left(-k_{v1}(v_1 - v_{1d})\right), & \text{Reg. II,} \end{cases} \tag{19c}$$

where l_{ref} and l_d denote the final reference and desired trajectory for the lift wire length, ζ_{v1} is the relative damping ratio, and ω_{v1} is the natural frequency. Select $\zeta_{v1} = 1$ to ensure critical damping. Different ω_{v1} values are assigned to different regions. In Region II, ω_{v1} can be smaller than ω_{v1} in Regions I and III. In the simulation, $\omega_{v1} = 0.57$ in Region I and III and $k_p = 0.5$ in Region II.

5.3. Comparative Simulation Results

By well-tuned weighting matrices, the simulation results are illustrated in Figures 10–14. In the simulations, $\gamma = 0.5$ is used in the NMPC controller. Each bar presents the mean value of five simulations with different turbulence seeds.
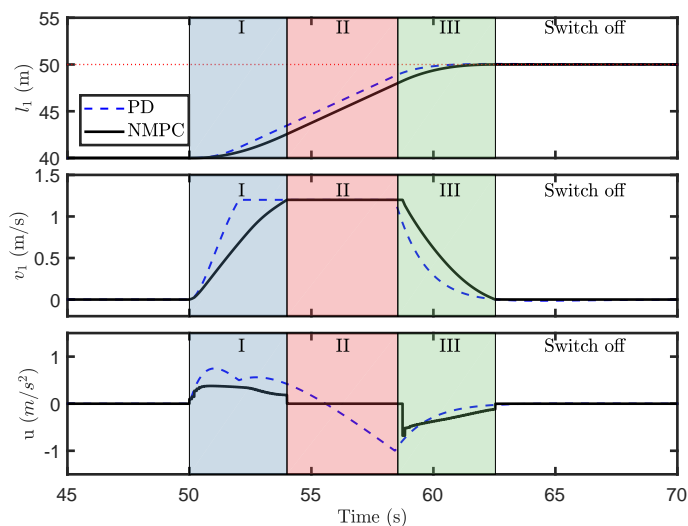
Figure 10. Performance of the PD controller with saturating elements and NMPC controller.
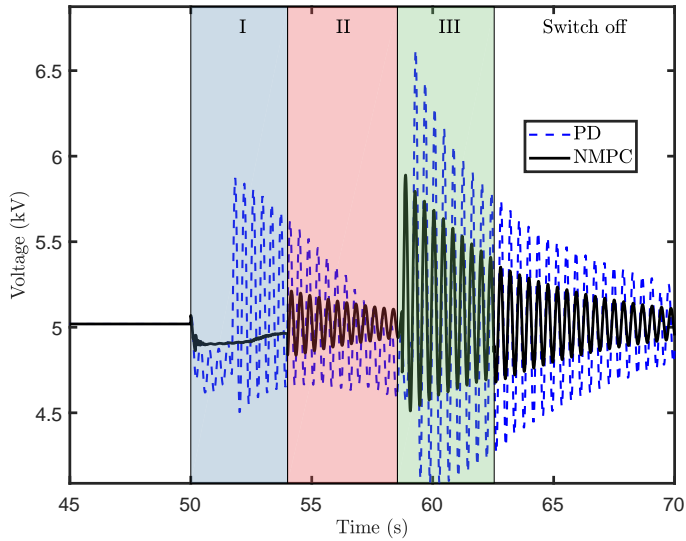
Figure 11. The field voltage, $\gamma = 0.5$, mean wind speed 0 m/s, $TI = 0$.

Note that this is not an accurate value because the overall stiffness is influenced by the slings. The simulations feature a difficult scenario with a short Region II. Typically, the Region II operation can be much longer than five seconds, so that the transient effect in the lifting wire tension may die out. Hence, the maximum dynamic tension in the results simulated here may be higher than those with a longer Region II. The controller is switched off at the end of Region III.
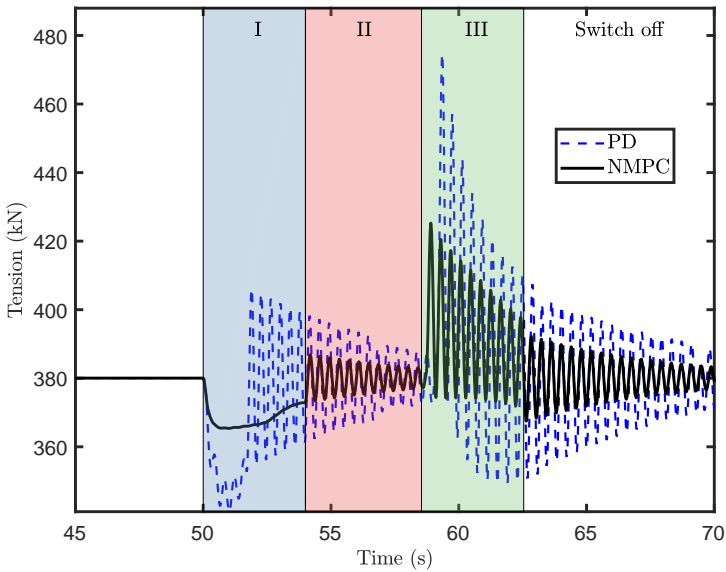
Figure 12. Comparison of the time-domain simulation results of the tension on the lift wire, $\gamma = 0.5$, mean wind speed 0 m/s, $TI = 0$.
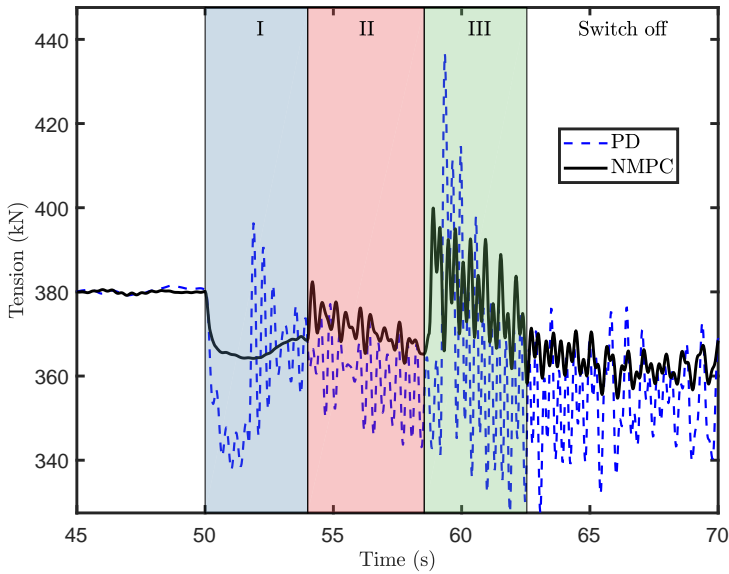
Figure 13. Comparison of the time-domain simulation results of the tension on the lift wire, $\gamma = 0.5$, mean wind speed 8 m/s, $TI = 0.174$.

Both the PD controller and NMPC controller are successful at lifting the payload to the desired position at the required speed. However, much less dynamic tension is generated by the NMPC controller than by the PD controller. The PD controller generates a smoother control input profile that is unable to cancel out the axial oscillation. The lift natural frequency of the wire tension is the same for both simulations. Because the NMPC controller significantly reduces the tension on the lift wire, the amplitude oscillation of the servo motor field voltage input is much lower for the NMPC scheme.
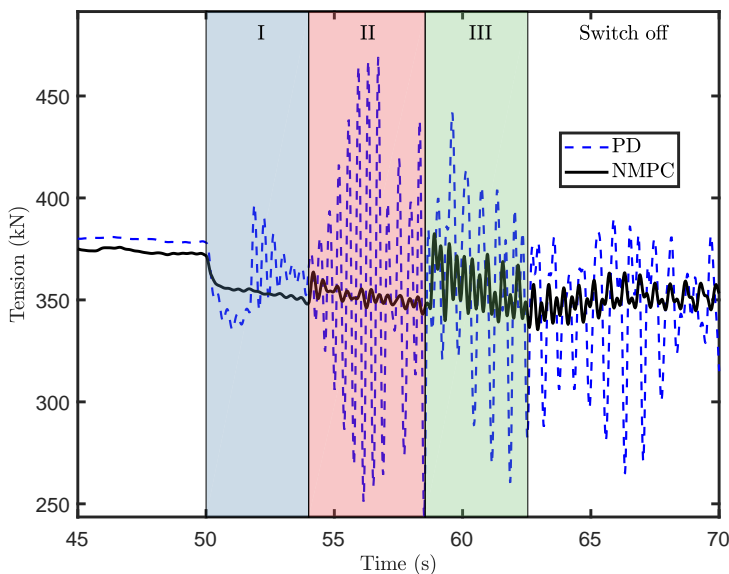
Figure 14. Comparison of the time-domain simulation results of the tension on the lift wire, $\gamma = 0.5$, mean wind speed 12 m/s, $TI = 0.146$.

Before the start of the lifting operation, the blade is stabilized by the tugger lines, and the tension oscillation is not remarkable. In Region I, the NMPC controller eliminates most of the oscillation. In Region II, the tension oscillation is caused by interactions between the wind-induced load and the tugger lines. However, the tension oscillation is acceptable in this region. Although the axial tension is not perfectly canceled out in Region III, the NMPC controller performs better than the PD controller. Due to the small wire rope damping ratio, the dynamic tension continues to oscillate after reaching the desired lifting speed. Additionally, because of the higher wind loads, the magnitude of the tension oscillation after the end of the lifting operation increases with higher mean wind speed. It is evident that the amplitude of oscillation is effectively reduced by the proposed NMPC scheme.

The NMPC approach exhibits a superior capacity to regulate the dynamic oscillation, compared to the PD controller. Thus, the NMPC algorithm succeeds to limit winch wear. However, its performance can be further improved, as shown in [37] owing to the simplification of the reduced model.

5.4. Robustness Test of the Algorithm

The performance of an NMPC controller is determined by the fidelity of the selected control design model. In our case, the most uncertain parameters are the lift wire stiffness and the neglected wind speed. The effects of model uncertainty matter, as the lift wire stiffness is estimated. Hence, a series of simulations are conducted to test their influence to the controller performance. The wire stiffness is changed by $\gamma = \{0.35, 0.4, 0.45, 0.5, 0.55, 0.6, 0.65\}$, while the γ of the NMPC controller remains set at $\gamma = 0.5$. The mean wind speed is used as a variable in the simulation, ranges from 4–12 m/s. The corresponding results are presented in Figures 15 and 16.
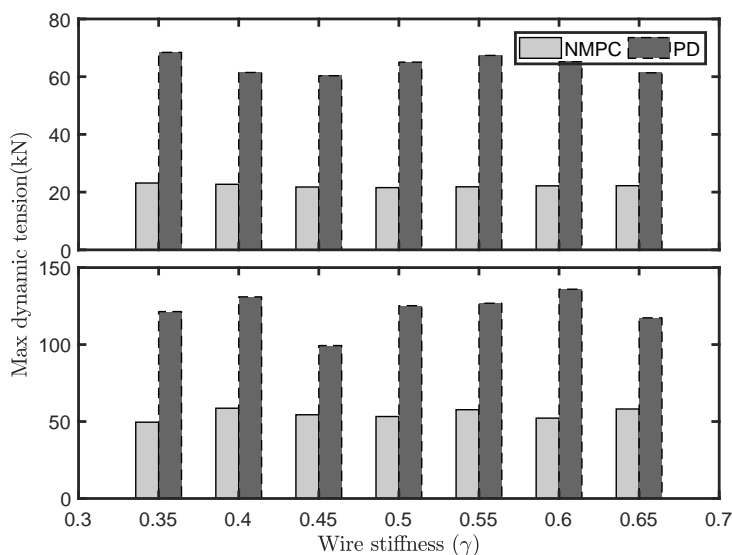
Figure 15. Comparison of the maximum dynamic tensions resulted by the NMPC and PD controllers, mean wind speed = 0 m/s (upper: Region I, lower: Region III).

In Figure 15, we see that the dynamic tension caused by the NMPC controller is almost less than 40% of those resulting from the PD controller. The NMPC controller significantly reduces the dynamic tension at the start and end of a lifting operation, even when the stiffness is not well known. In Figure 16, the performance variation of the PD controller resulted from the increasing stiffness uncertainty increasing significantly, while the performance variation of the NMPC controller is small under the same uncertainties. The mean wind speed does not weaken the NMPC performance,

since the mean wind speed does not seem to influence the wire tension considerably. Wind loads are compensated by the tugger lines. Therefore, the robustness of the proposed NMPC law is satisfactory.
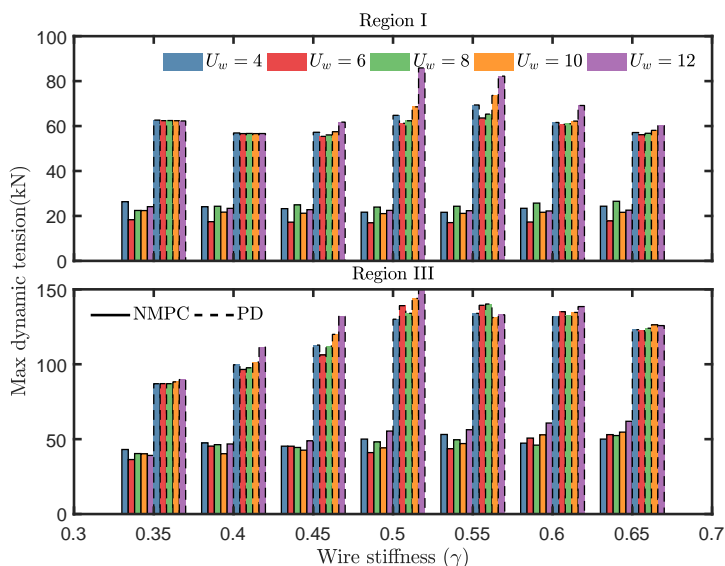
Figure 16. Comparison of the maximum dynamic tensions resulted by the NMPC and PD controllers in a turbulent wind field, mean wind speed = 4–12 m/s (upper: Region I, lower: Region III).

5.5. Discussion

We found that the NMPC performance deteriorates with a large sampling interval. In this case, the sampling rate does not satisfy the Nyquist–Shannon sampling theorem if the interval is greater than twice the natural period of the axial oscillation (approximately 0.4 s), i.e., discrete measurements do not approximate the underlying continuous responses. Using shorter sampling and control intervals, not surprisingly, the performance of the control scheme is significantly improved, resulting in more subtle control. Nonetheless, the computation speed depends on the computational capabilities of the measurement and embedded systems. Hence, a trade-off must be made between hardware capabilities and control performance. In the simulation results, we have chosen the sampling period as 0.1 s for this trade-off. The variance in results observed at various lengths of time horizons is limited, as several axial oscillation periods exist in the selected optimal horizon. Therefore, several tension oscillation periods occur over an optimization horizon.

The control effort is determined by the weight matrices in the cost functions. The weights in the Mayer term is more important than the weight values for the end step, since the latter only determines one value among $N + 1$ values of the sum operator. The final performance could be prioritized by enhancing it. The running time for the direct multiple shooting approach is longer than that of the direct single shooting approach due to much fewer Karush–Kuhn–Tucker (KKT) conditions involved in the single shooting approach [50]. On the other hand, its application is limited by the strong dependence on the initial guess.

6. Conclusions

An NMPC algorithm is proposed as a mean for efficient and safe lifting operations of a wind turbine blade, by limiting sudden overloads and snatch loads. The simplified model for control design is derived using the Newton–Euler approach. The proposed algorithm has a simple structure. According to the comparative study results, the proposed controller successfully prevents the sudden peak tension, tension dynamics, and the axial oscillation. The NMPC controller still performs well

when the lift wire stiffness is poorly estimated or the suspended blade is exposed to a turbulent wind field.

To further improve the system performance when exposed to higher wind speed and model uncertainties, the further research emphasis is on adaptive and robust optimal control schemes, e.g., tube-based model predictive control. In addition, NMPC applications to the blade lifting operation using a floating installation vessel for deep water installation will be investigated.

Conflicts of Interest: The authors declare no conflict of interest.

References

1. Jiang, Z.; Hu, W.; Dong, W.; Gao, Z.; Ren, Z. Structural Reliability Analysis of Wind Turbines: A Review. *Energies* **2017**, *10*, 2099. [CrossRef]
2. Jiang, Z.; Gao, Z.; Ren, Z.; Li, Y.; Duan, L. A parametric study on the final blade installation process for monopile wind turbines under rough environmental conditions. *Eng. Struct.* **2018**, *172*, 1042–1056. [CrossRef]
3. Ren, Z.; Jiang, Z.; Skjetne, R.; Gao, Z. An active tugger line force control method for single blade installations. *Wind Energy* **2018**, *21*, 1344–1358. [CrossRef]
4. Ren, Z.; Jiang, Z.; Skjetne, R.; Gao, Z. Development and application of a simulator for Offshore Wind Turbine Blades Installation. *Ocean Eng.* **2018**, *166*, 380–395. [CrossRef]
5. Maes, K.; De Roeck, G.; Lombaert, G. Motion tracking of a wind turbine blade during lifting using RTK-GPS/INS. *Eng. Struct.* **2018**, *172*, 285–292. [CrossRef]
6. Verma, A.S.; Jiang, Z.; Vedvikc, N.P.; Gao, Z.; Ren, Z. Impact assessment of blade root with a hub during the mating process of an offshore monopile-type wind turbine. *Eng. Struct.* **2018**, in press.
7. Verma, A.S.; Vedvik, N.P.; Haselbach, P.U.; Gao, Z.; Jiang, Z. Comparison of numerical modelling techniques for impact investigation on a wind turbine blade. *Compos. Struct.* **2019**, *209*, 856–878. [CrossRef]
8. Abdel-Rahman, E.M.; Nayfeh, A.H.; Masoud, Z.N. Dynamics and control of cranes: A review. *J. Vib. Control* **2003**, *9*, 863–908. [CrossRef]
9. Spathopoulos, M.; Fragopoulos, D. Pendulation control of an offshore crane. *Int. J. Control* **2004**, *77*, 654–670. [CrossRef]
10. Schaub, H. Rate-based ship-mounted crane payload pendulation control system. *Control Eng. Pract.* **2008**, *16*, 132–145. [CrossRef]
11. He, W.; Zhang, S.; Ge, S.S. Adaptive control of a flexible crane system with the boundary output constraint. *IEEE Trans. Ind. Electron.* **2014**, *61*, 4126–4133. [CrossRef]
12. d'Andréa Novel, B.; Coron, J.M. Exponential stabilization of an overhead crane with flexible cable via a back-stepping approach. *Automatica* **2000**, *36*, 587–593. [CrossRef]
13. Sun, N.; Fang, Y.; Zhang, X. Energy coupling output feedback control of 4-DOF underactuated cranes with saturated inputs. *Automatica* **2013**, *49*, 1318–1325. [CrossRef]
14. Tang, R.; Huang, J. Control of bridge cranes with distributed-mass payloads under windy conditions. *Mech. Syst. Signal Process.* **2016**, *72*, 409–419. [CrossRef]
15. Johansen, T.A.; Fossen, T.I.; Sagatun, S.I.; Nielsen, F.G. Wave synchronizing crane control during water entry in offshore moonpool operations-experimental results. *IEEE J. Ocean. Eng.* **2003**, *28*, 720–728. [CrossRef]
16. Skaare, B.; Egeland, O. Parallel force/position crane control in marine operations. *IEEE J. Ocean. Eng.* **2006**, *31*, 599–613. [CrossRef]
17. Messineo, S.; Serrani, A. Offshore crane control based on adaptive external models. *Automatica* **2009**, *45*, 2546–2556. [CrossRef]

18. Jiang, Z.; Ren, Z.; Gao, Z.; Sandvik, P.C.; Halse, K.H.; Skjetne, R. Mating Control of a Wind Turbine Tower-Nacelle-Rotor Assembly for a Catamaran Installation Vessel. In Proceedings of the 28th International Ocean and Polar Engineering Conference, Sapporo, Japan, 10–15 June 2018; pp. 584–593.

19. Yang, T.; Yang, X.; Chen, F.; Fang, B. Nonlinear parametric resonance of a fractional damped axially moving string. *J. Vib. and Acoustics* **2013**, *133*, 064507. [CrossRef]

20. Bemporad, A.; Morari, M. Robust model predictive control: A survey. In *Robustness in Identification and Control*; Springer: London, UK, 1999; pp. 207–226.

21. Kellett, C.M.; Teel, A.R. Smooth Lyapunov functions and robustness of stability for difference inclusions. *Syst. Control Lett.* **2004**, *52*, 395–405. [CrossRef]

22. Adetola, V.; DeHaan, D.; Guay, M. Adaptive model predictive control for constrained nonlinear systems. *Syst. Control Lett.* **2009**, *58*, 320–326. [CrossRef]

23. Mayne, D.Q.; Kerrigan, E.C.; Van Wyk, E.; Falugi, P. Tube-based robust nonlinear model predictive control. *Int. J. Robust Nonlinear Control* **2011**, *21*, 1341–1353. [CrossRef]

24. Mayne, D.Q. Model predictive control: Recent developments and future promise. *Automatica* **2014**, *50*, 2967–2986. [CrossRef]

25. Deng, W.; Yao, R.; Zhao, H.; Yang, X.; Li, G. A novel intelligent diagnosis method using optimal LS-SVM with improved PSO algorithm. *Soft Comput.* **2017**, *161*, 1–18. [CrossRef]

26. Mayne, D.Q.; Rawlings, J.B.; Rao, C.V.; Scokaert, P.O. Constrained model predictive control: Stability and optimality. *Automatica* **2000**, *36*, 789–814. [CrossRef]

27. Diehl, M.; Findeisen, R.; Allgöwer, F.; Bock, H.G.; Schlöder, J.P. Nominal stability of real-time iteration scheme for nonlinear model predictive control. *IEE Proc. Control Theory Appl.* **2005**, *152*, 296–308. [CrossRef]

28. Diehl, M.; Bock, H.G.; Schlöder, J.P. A real-time iteration scheme for nonlinear optimization in optimal feedback control. *SIAM J. Control Optim.* **2005**, *43*, 1714–1736. [CrossRef]

29. Zhu, M.; Hahn, A.; Wen, Y.; Bolles, A. Identification-based simplified model of large container ships using support vector machines and artificial bee colony algorithm. *Appl. Ocean Res.* **2017**, *68*, 249–261. [CrossRef]

30. Zhu, M.; Hahn, A.; Wen, Y. Identification-based controller design using cloud model for course-keeping of ships in waves. *Eng. Applic. Artific. Intell.* **2018**, *75*, 22–35. [CrossRef]

31. Niu, H.; Lu, Y.; Savvaris, A.; Tsourdos, A. An energy-efficient path planning algorithm for unmanned surface vehicles. *Ocean Eng.* **2018**, *161*, 308–321. [CrossRef]

32. Andersson, J. A General-Purpose Software Framework for Dynamic Optimization. Ph.D. Thesis, Arenberg Doctoral School, KU Leuven, Department of Electrical Engineering (ESAT/SCD) and Optimization in Engineering Center, Heverlee, Belgium, 2013.

33. Ariens, D.; Houska, B.; Ferreau, H.; Logist, F. *ACADO for Matlab User's Manual*; Optimization in Engineering Center (OPTEC): Wetzikon, Switzerland, 2010. Available online: http://www.acadotoolkit.org (accessed on 19 November 2017).

34. Mattingley, J.; Boyd, S. CVXGEN: A code generator for embedded convex optimization. *Optim. Eng.* **2012**, *13*, 1–27. [CrossRef]

35. Ren, Z.; Jiang, Z.; Skjetne, R.; Gao, Z. Single blade installation using active control of three tugger lines. In Proceedings of the 28th International Ocean and Polar Engineering Conference, Sapporo, Japan, 10–15 June 2018; pp. 594–601.

36. Ren, Z.; Skjetne, R.; Jiang, Z.; Gao, Z.; Verma, A.S. Integrated GNSS/IMU Hub Motion Estimator for Offshore Wind Turbine Blade Installation. *Mech. Syst. Signal Process.* **2019**. Revision.

37. Ren, Z.; Skjetne, R.; Gao, Z. Modeling and Control of Crane Overload Protection during Marine Lifting Operation Based on Model Predictive Control. In Proceedings of the ASME 2017 36th International Conference on Ocean, Offshore and Arctic Engineering, Trondheim, Norway, 25–30 June 2017; p. V009T12A027.

38. Espinoza, A. Block Island Wind Farm Enters Final Construction Phase. 2016. Available online: http://ripr.org/post/block-island-wind-farm-enters-final-construction-phase#stream/0 (accessed on 19 November 2017).

39. Jonkman, J.; Butterfield, S.; Musial, W.; Scott, G. *Definition of a 5-MW Reference Wind Turbine for Offshore System Development*; Technical Report No. NREL/TP-500-38060; National Renewable Energy Laboratory: Golden, CO, USA, 2009.

40. Fossen, T.I. *Handbook of Marine Craft Hydrodynamics and Motion Control*; John Wiley & Sons: Hoboken, NJ, USA, 2011.

41. Todd, M.; Vohra, S.; Leban, F. Dynamical measurements of ship crane load pendulation. In Proceedings of the OCEANS'97, MTS/IEEE Conference Proceedings, Halifax, NS, Canada, 6–9 October 1997; Volume 2, pp. 1230–1236.

42. Wächter, A. *Short Tutorial: Getting Started with Ipopt in 90 Minutes*; Dagstuhl Seminar Proceedings, Schloss Dagstuhl-Leibniz-Zentrum für Informatik: Wadern, Germany, 2009.

43. Johansen, T.A. Introduction to nonlinear model predictive control and moving horizon estimation. *Sel. Top. Constrained Nonlinear Control* **2011**, 1–53. [CrossRef]

44. Vukov, M.; Domahidi, A.; Ferreau, H.J.; Morari, M.; Diehl, M. Auto-generated algorithms for nonlinear model predictive control on long and on short horizons. In Proceedings of the 52nd IEEE Conference on Decision and Control, Florence, Italy, 10–13 December 2013; pp. 5113–5118.

45. Deng, W.; Zhao, H.; Zou, L.; Li, G.; Yang, X.; Wu, D. A novel collaborative optimization algorithm in solving complex optimization problems. *Soft Comput.* **2017**, *21*, 4387–4398. [CrossRef]

46. Deng, W.; Zhao, H.; Yang, X.; Xiong, J.; Sun, M.; Li, B. Study on an improved adaptive PSO algorithm for solving multi-objective gate assignment. *Appl. Soft Comput.* **2017**, *59*, 288–302. [CrossRef]

47. Chen, H.; Allgower, F. A Quasi-infinite Horizon nonlinear model predictive control scheme with guaranteed stability. In Proceedings of the IEEE European Control Conference, Brussels, Belgium, 1–7 July 1997; pp. 1421–1426.

48. Zhou, L.; Moan, T.; Riska, K.; Su, B. Heading control for turret-moored vessel in level ice based on Kalman filter with thrust allocation. *J. Mar. Sci. Technol.* **2013**, *18*, 460–470. [CrossRef]

49. *Wind Turbine Generator Systems-Part 1: Safety Requirements*; Standard, International Electrotechnical Commission: Geneva, Switzerland, 2005.

50. Luo, Z.Q.; Yu, W. An introduction to convex optimization for communications and signal processing. *IEEE J. Sel. Areas Commun.* **2006**, *24*, 1426–1438.

Paper A3

An active tugger line force control method for single blade installations

Zhengru Ren, Zhiyu Jiang, Roger Skjetne, and Zhen Gao

WILEY

Active tugger line force control for single blade installation

Zhengru Ren[1,2,3] | Zhiyu Jiang[1,3] | Zhen Gao[1,2,3] | Roger Skjetne[1,2,3]

[1]Centre for Research-based Innovation of Marine Operations (SFI MOVE), Norwegian University of Science and Technology (NTNU), NO-7491 Trondheim, Norway

[2]Centre for Autonomous Marine Operations and Systems (AMOS), NTNU, NO-7491 Trondheim, Norway

[3]Department of Marine Technology, NTNU, NO-7491 Trondheim, Norway

Correspondence

Zhiyu Jiang, Centre for Research-based Innovation of Marine Operations, Norwegian University of Science and Technology, NO-7491 Trondheim, Norway.
Email: zhiyu.jiang@ntnu.no

Funding information

Research Council of Norway RCN, Grant/Award Number: CRI MOVE, RCN-project 237929; Centre of Excellence on Autonomous Marine Operations and Systems, Grant/Award Number: NTNU AMOS, RCN-project 223254

Abstract

Single blade installation is one of the methods for installing large wind turbine blades at an off-shore site. During this installation, each blade is lifted by the main crane from the deck of an installation vessel or a transportation barge with blade root approaching the hub. The blade root is then bolted to the hub. The final mating phase is critical and requires high precision. Tugger lines from the crane boom are connected to the suspended blade to reduce pendulum motions. The entire process is typically completed without active tugger line force control. Due to wind-induced blade loads, strict requirement on installation precision, and the limitations imposed by the lifting equipment, the single blade installation operations are subject to weather constraints. Therefore, developing techniques to reduce the blade motions and consequently shorten the installation time is desired. In this paper, an active control scheme is proposed to control the tugger line forces acting on a blade during the final installation stage before mating. A simplified three degree-of-freedom blade installation model is developed for the control design. An extended Kalman filter is used to estimate the blade motions and wind velocities. Feedback linearization and pole placement techniques are applied for the design of the controller. Simulations under turbulent wind conditions are conducted to verify the active control scheme, which effectively reduces the blade root motions in the wind direction.

KEYWORDS

extended kalman filter, feedback linearization, force control, pole placement, single blade installation, wind turbine

1 | INTRODUCTION

With increasing energy consumption and environmental concerns, renewable wind energy has received substantial scientific, societal, and industrial attention in recent years. Many countries plan to enlarge the share of wind energy in their national energy portfolio.[1] In 2016, wind energy accounted for 51% of all new energy installed capacity in the European Union.[2]

Because of land resource limitations and better wind quality, offshore wind turbines (OWTs) are becoming increasingly popular. At present, most offshore wind farms consist of wind turbines supported by monopiles, which are the most cost-effective type of support structure for shallow water.[3-7] However, the price of electricity from offshore wind can be approximately three to four times greater than electricity from onshore wind.[8] For an offshore wind farm project, capital expenditures (CapEx) and operational expenditures (OpEx) are the two main categories of the expenses. The assembly and installation cost is the third largest element in CapEx, accounting for 11.6%.[8] Offshore installations, including lifting and mating operations, are expensive. Because of the limitations of lifting and monitoring equipment, spending time waiting for the right weather window is not uncommon.

Selecting the suitable installation method for OWTs is often a trade-off among several aspects, such as onshore and offshore assembly costs, crane capacity, and deck usage of the transportation vessel. Different installation strategies exist, with varying numbers of pre-assembled components and offshore lifts. For example, if the rotor and all three blades are assembled onshore, then only one offshore lift is required for the rotor assembly, without the need for individual blade lifts.[9] As the rotor diameters of the biggest wind turbines begin to reach 180 m, lifting an entire rotor assembly offshore may face more challenges in addition to transportation issues. Large and high cranes have to be used.

Single blade installation is one of the alternatives for installing wind turbine blades at an offshore site. In this approach, one blade is lifted by the main crane from the deck of an installation vessel or a transportation barge and attached to the nacelle on the top of the tower. Tugger lines are used

to connect the suspended blade to the crane boom to reduce pendulum motions, typically without any active control. Single blade installation allows for the selection of a wider range of installation vessels with lower crane capacity. The deck space is more efficiently used, and a crane vessel can carry more turbine components in a single trip. Nevertheless, single blade installation requires more offshore lifts than the assembled rotor approach, and it is limited to a mean wind speed[10] of 8 to 12 m/s. Recently, both the research community and industry have made efforts to understand the physics of and to make improvements to the state-of-the-art single blade installations. The aerodynamics and aeroelastic behavior of a single blade at standstill are studied in other studies.[10-13] In Jiang et al,[14] the motion characteristics of a blade installation model are identified, and the critical parameters that influence the final blade installation stage are investigated. Meanwhile, specialized commercial products, such as LT575 Blade Dragon,[15] allow single blade installations to be conducted under higher wind speeds. Another example is the Boom Lock technology,[16] which reduces the blade motion and expands the operational limits.

In addition to the aforementioned tools, using automatic control to assist single blade installation is of interest. Successful applications of automatic control are familiar in the fields of marine operations and wind turbine operations. Traditionally, marine operations are heavily dependent on human interactions. With the advancements in automatic control, many operations can be performed with increased efficiency and reliability. In the field of ship-mounted crane operations alone, various control strategies have been applied to reduce the motions of suspended cargoes,[17-20] to reduce the roll motion,[21] and to facilitate moonpool operations.[22,23] For wind turbines, studies have primarily focused on the operating conditions. Control strategies are developed concerning voltage control,[24] generator speed regulation,[25] and load reduction.[26] However, to the authors' knowledge, no active control scheme has been applied to regulate the tugger line forces for blade installation purposes.

In this paper, a closed-loop control scheme for single blade installation is proposed, which includes an extended Kalman filter (EKF) and a feedback linearization proportional-integral-derivative (PID) controller. The active controller reduces the blade motions in the assumed scenarios and can potentially be used to expedite the installation process. The remainder of this paper is structured as follows. The system description and problem formulation are presented in Section 2. Additionally, a simplified control design model (CDM) with the blade motion described by three degrees of freedom (DOFs) is introduced for designing the observer and the controller. A simulation verification model (SVM) with a 6DOF blade is also introduced to verify the closed-loop performance. In Section 3, an EKF is designed to filter the measurement noise and to estimate the unknown states, while the feedback linearization and pole placement techniques are applied in the control design. Section 4 presents the verification of the control scheme using both the CDM and the SVM. A set of comparative studies are conducted to prove the active controller performance. Section 5 presents conclusions and recommendations for future studies.

Notations: In this paper, scalars, vectors, and matrices are denoted with normal lowercase letters, bold lowercase letters, and bold capital letters, respectively.

2 | PROBLEM FORMULATION

2.1 | Description of the installation procedure

The installation of an offshore monopile-type wind turbine can be divided into several stages. The monopile is first hammered into the seabed, followed by assembly of the transition piece, tower, nacelle, and blades. Three lifts are involved for the blades if the single blade installation technique is applied. Before the blade installation begins, the hub is rotated to a horizontal position for wind turbines with a conventional gear transmission. Then, the blade is seized by a yoke at its center of mass and lifted to the hub height by a crane vessel from the deck. At the final installation stage, the blade root motions are closely monitored using an onboard motion capture device.[27] If the motions are within the allowable limits, then the mating process follows. Figure 1 illustrates a typical mating phase between the blade and hub. Tugger lines are used to constrain the blade motions. When the guide pins on the blade root have entered the flange holes on the hub, the mating process is finished. Then, manual work is involved to bolt the blade onto the hub, followed by retraction of the lifting gear. A detailed description of the procedure can be found in Jiang et al.[14]

The main wind direction is supposed to be constant. Two reference frames with right-hand coordinates are defined in the following:

- Global frame $\{G\}$: The origin O_g is placed at the mean water level with the x-axis pointing in the constant main wind direction, the z-axis pointing downward, and the y-axis according to the right hand rule. The rotations about the x-, y-, and z-axes are named roll (ϕ), pitch (θ), and yaw (ψ), respectively.
- Blade body-fixed frame $\{B\}$: The origin O_b is located at the blade center of gravity (COG). The y^b-axis points in the spanwise direction, from the root to the tip. The z^b-axis points downward. The planar translational velocity in the body-fixed frame and the rotational velocity in yaw are denoted by u, v, and r, respectively.

2.2 | Control design model

To facilitate the design of an observer algorithm and a control law, we use a simplified CDM to describe the blade installation system. The following fundamental assumptions are made in the analysis:

1. The position of the crane tip $[x_p, y_p, z_p]^\top$ remains constant. Without loss of generality, we assume that $[x_p, y_p]^\top = [0, 0]^\top$.
2. Only the three planar motions are considered, ie, surge (x), sway (y), and yaw (ψ).
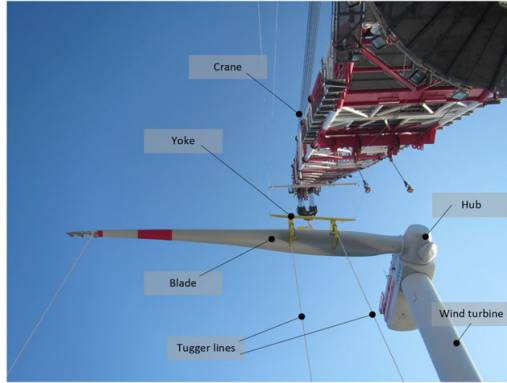
FIGURE 1   Illustration of the mating phase during a single blade installation. (Image source: RWE GmbH[28]) [Colour figure can be viewed at wileyonlinelibrary.com]

3. The blade yaw angular velocity $\dot{\psi}$ is small.
4. The blade motions in different DOFs at COG are independent, but the resulting translational motions at the blade root are also dependent on the yaw motion.

Based on these assumptions, a decoupled 3DOF single blade installation model can be expressed as follows:

$$\dot{\eta} = R\nu, \tag{1a}$$

$$\dot{b} = -\frac{1}{T_b}b + w_b, \tag{1b}$$

$$M\dot{\nu} = R^\top(g + b + Bu) + \tau_w, \tag{1c}$$

$$\dot{U}_w = -\frac{1}{T_w}U_w + w_w, \tag{1d}$$

where $\eta = [x, y, \psi]^\top \in \mathbb{R}^2 \times \mathbb{S}$ denotes the position and orientation of the blade COG in the global frame, $\nu = [u, v, r]^\top \in \mathbb{R}^3$ includes the linear velocity and the updating rate of the Euler angle in the body-fixed frame, and $U_w \in \mathbb{R}$ is the mean wind speed. R is the transformation matrix from the body-fixed frame to the global frame, and it is given by the following:

$$R(\psi) = \begin{bmatrix} \cos\psi & -\sin\psi & 0 \\ \sin\psi & \cos\psi & 0 \\ 0 & 0 & 1 \end{bmatrix}. \tag{2}$$

Note that the rotation matrix R in the horizontal plane satisfies

$$R^{-1} = R^\top, \quad \dot{R} = RS(r), \quad \text{where} \quad S(r) = \begin{bmatrix} 0 & -r & 0 \\ r & 0 & 0 \\ 0 & 0 & 0 \end{bmatrix}. \tag{3}$$

$M = \text{diag}(m, m, I_b)$ denotes the mass matrix of the system where $m = m_b + m_h + m_y$ is the total mass combining the blade, hook, and yoke masses and I_b is the blade's moment of inertia.

In Equation 1c, $g = [-\frac{mg}{l}(x - x_p), -\frac{mg}{l}(y - y_p), 0]^\top$ represents the gravity-induced restoring force where l is the distance between the crane tip and the blade COG. $u = [u_1, u_2]^\top \in \mathbb{R}^2$ is the control input vector, where u_1 and u_2 are the tugger line horizontal force inputs. These can be both positive and negative because of pretension. The pretension is generated by gravity due to the initial displacement of the blade. The control allocation matrix B is used to transfer the tugger line force inputs to the generalized control force in the global frame. It is given by

$$B = \begin{bmatrix} -1 & -1 \\ 0 & 0 \\ -r_{t1}\cos\psi & r_{t2}\cos\psi \end{bmatrix}, \tag{4}$$

where $r_{t1} > 0$ and $r_{t2} > 0$ are the moment arms of the tugger line forces u_1 and u_2 with respect to the COG.

τ_w represents the wind load acting on the blade COG in the body-fixed frame. The mean wind velocity in the global frame is assumed to be $\boldsymbol{u}_w = [U_w, 0, 0]^\top$. After coordinate transformation by the yaw angle ψ, the wind velocity in the body-fixed frame is $\boldsymbol{u}_w^b = [U_w \cos \psi, -U_w \sin \psi, 0]^\top$. The wind induced-force in the body-fixed frame at an airfoil segment depends on the inflow velocity relative to the blade segment at y^b, given by $\boldsymbol{u}_{wr}^b(y^b) = \boldsymbol{u}_w^b - \boldsymbol{u}_b^b(y^b)$, where $\boldsymbol{u}_b^b(y^b)$ is the velocity at the blade segment center of pressure at y^b. It is practical to assume that the blade motion is small and negligible compared with the mean wind speed. Hence, $\boldsymbol{u}_w^b$ is instead used directly to calculate the induced wind force. It should also be noted that the wind-induced force in the y^b-direction is negligible compared with the force in x^b-direction and the moment in yaw. Thus, we assume that the wind-induced load in sway (y^b-axis) is zero, according to the cross-flow principle. To sum up, the simplified wind-induced load for the CDM is then given by

$$\tau_w = \begin{bmatrix} f_{wx} \\ f_{wy} \\ m_w \end{bmatrix} = \begin{bmatrix} aU_w^2\cos^2\psi \\ 0 \\ bU_w^2\cos^2\psi \end{bmatrix}, \tag{5}$$

where $a = \sum_i a_i = \sum_i \frac{1}{2}\rho_{air}\bar{C}_d(t_i)\sin^2(\alpha_i)A_i$ and $b = \sum_i a_i r_i$ according to a segmentation of the blade into n elements. Here, ρ_{air} refers to the air density, $\bar{C}_d(t_i)$ is the aerodynamic drag coefficient with respect to the relative thickness t_i of the ith segment center, and α_i is the angle of attack that depends on the pitch θ and aerodynamic twist. $A_i = (r_{i+1} - r_i)C_i$ is the wing area, where C_i is the chord length, and r_i is the distance from the center of the ith segment to the COG. The cross-flow principle[10] is applied to calculate the wind loads on the blade, and interested readers are referred to Ren et al[29] for a verification using the HAWC2[30] numerical model. Simulation results in Ren et al[29] has also proven the feasibility of the assumptions for Equation 5.

A state vector $\boldsymbol{b} = [b_1, b_2, b_3]^\top \in \mathbb{R}^3$ is used in the observer to estimate the forces and moments biases in $\{B\}$ caused by the pretension, model uncertainty, environmental disturbance, etc. Elements in vector $\boldsymbol{b}$ are assumed to be primarily due to the variation in the blade pitch, as illustrated in Figure 2. After exerting the pretension on the tugger lines, the blade moves in the opposite direction of the incoming wind and becomes inclined with respect to its original position. The inclination affects the blade pitch angle and the airfoil angle of attack along the blade. In addition, the model uncertainty also has an impact on $\boldsymbol{b}$. For example, the wind-induced load τ_w in Equation 5 is a simplified approximation since the blade aerodynamics is very complex in a turbulent wind field.[31,32] Therefore, the deviation of the total wind-induced loads in different DOFs is modeled as a slowly varying Markov model in a vector form, Equation 1b, where $\boldsymbol{T}_b = \text{diag}\{T_{b1}, T_{b2}, T_{b3}\}$ is a constant diagonal matrix, with parameters $T_{b1}, T_{b2}, T_{b3} > 0$ to be tuned during the observer design stage. The process disturbance $\boldsymbol{w}_b = [w_{b1}, w_{b2}, w_{b3}]^\top \in \mathbb{R}^3$ and the wind speed disturbance $w_w \in \mathbb{R}$ are Gaussian white noise processes. The wind speed disturbance is used to account for the location-dependent wind since an anemometer is generally installed on the yoke; it is only able to measure the wind speed of one location.

The measurement equation is given by

$$\boldsymbol{y} = \boldsymbol{H}\boldsymbol{x} + \boldsymbol{v}, \tag{6}$$

where $\boldsymbol{x} = [\boldsymbol{\eta}^\top, \boldsymbol{b}^\top, \boldsymbol{v}^\top, U_w]^\top \in \mathbb{R}^{10}$ is the state vector, $\boldsymbol{y} = [x, y, \psi, U_w]^\top \in \mathbb{R}^4$ is the sensor measurement vector containing the position of the blade COG and wind speed measurement from the anemometer, and $\boldsymbol{v} = [v_x, v_y, v_\psi, v_{U_w}]^\top \in \mathbb{R}^4$ is the Gaussian sensor white noise vector. The output matrix $\boldsymbol{H}$ is given in Appendix A.

2.3 | Simulation verification model

Rather than the simplified CDM that addresses the horizontal problem, an SVM in full 6DOF should be used to verify the controller performance. The SVM considers the coupling of DOFs within a body and captures more physics of the system. Table 1 highlights the differences between the SVM and the CDM. In the SVM, the blade is modeled as a 6DOF rigid body, and the lift wire, slings, and tugger lines are all modeled as linear tensile
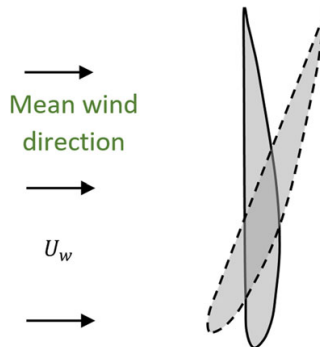
FIGURE 2 Illustration of the variation in the blade pitch angle (solid line represents the assumed orientation, and dashed line represents a possible orientation) [Colour figure can be viewed at wileyonlinelibrary.com]

springs. The hook is modeled as a rigid point with three DOFs. Moreover, the lift wire and tugger lines are assumed to be rigidly fixed to the crane tip and crane boom, respectively.

Ignoring the blade flexibility, the present blade model in SVM does not fully represent the aerodynamic loads acting on the blade. Figure 3 gives a comparison of the numerical models on the aerodynamic force and moment distribution along the length of the NREL 5-MW blade. For the rigid-blade case, there is a good agreement between the SVM model and the HAWC2 model; refer to Ren et al.[29] For the flexible-blade case, only HAWC2 is used, and the distributed lift forces experience harmonic oscillations; the deviations from the rigid-blade results become greater at the blade tip which has more flexibility. Unlike a blade on an operating wind turbine, a blade during offshore installations experiences no cyclic motions and has low moving speed, and usually the inboard part of the blade (radius<20 m) is more heavily loaded. Hence, the blade flexibility is expected to have less impact on the integrated aerodynamic forces and moments. As the focus of this paper is on the development of control methods, we use the rigid-blade model in estimation of the aerodynamic loading for the sake of simplification, ie, Equation 5.

2.3.1 | Actuator dynamics

In the SVM, a sophisticated actuator model depends on industrial winch products[33] suitable for such an operation, but this is beyond the scope of this work. The ability of the tugger lines to supply the desired forces fast enough, dependent on the actuator characteristics. Due to the dynamic responses and physical limitations of the winches, the control signal cannot reach any desired values or change at any desired rate. Additionally, the

TABLE 1 Components of the simulation verification model and the control design model

Components	Simulation verification model	Control design model
Lift wire	Yes	Yes
Hook	3DOF	No
Slings	Yes	No
Blade	6DOF	3DOF
Tugger lines	Yes	Yes
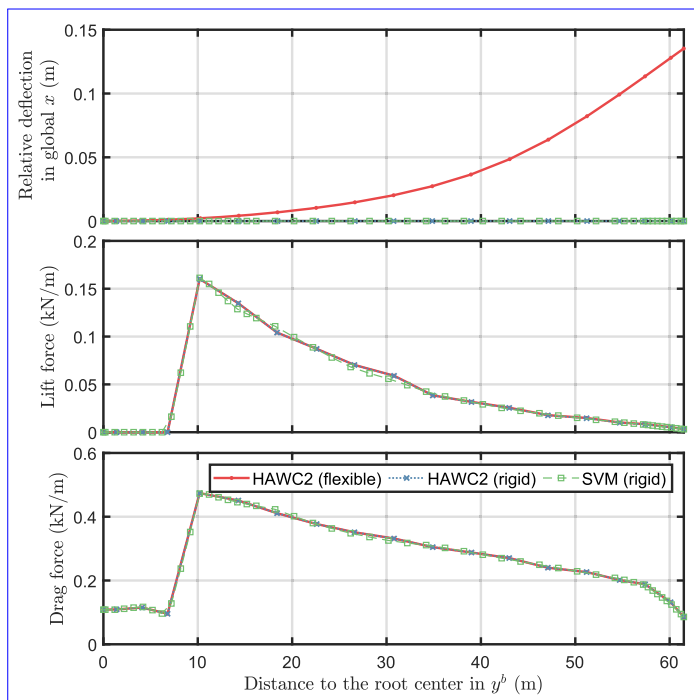
FIGURE 3 Comparison of the aerodynamic load distribution on a blade fixed at the root ($\theta = 90$ deg and $U_w = 10$ m/s) [Colour figure can be viewed at wileyonlinelibrary.com]
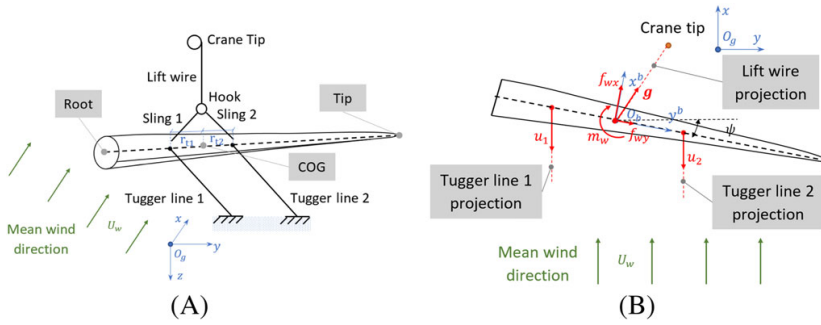
FIGURE 4 Scenario of the final installation stage of a blade prior to mating. A, 3-D view and B, 2-D projection in the horizontal plane. The red arrows stand for forces and moment; the blue lines denote the coordinate systems [Colour figure can be viewed at wileyonlinelibrary.com]

other ends of the ropes move with the connecting points on the yoke-blade structure, which makes the tension control process more complex. In this study, the actuator process is simplified as a stable first-order dynamics,[34] expressed in the frequency domain by

$$\frac{u_i(s)}{u_{cmd,i}(s)} = \frac{T_{iu}}{s + T_{iu}}, \quad i \in \{1, 2\}, \tag{7}$$

where $1/T_{iu}$ is the time constant of the lowpass filter which influences the speed of convergence, and $u_{cmd,i}$ is the control input command signal from the proposed controller described in Section 3.3.

2.4 | Problem statement

Figure 4A illustrates a typical scenario prior to the mating phase. The leading edge of the blade faces downward with a 90-deg pitch angle. This blade orientation does not have minimal loading, but it is often adopted in practice due to the concerns for transportation and loading predictability when wind direction changes.[13] One lift wire is used to rigidly connect the hook and crane tip, and two slings are used to connect the hook and yoke. Two horizontal tugger lines are connected to the blade with arm lengths of r_{t1} and r_{t2} relative to the blade COG.

Figure 4B presents a top view of the scenario. In the figure, $\boldsymbol{g}$ is the restoring force caused by the blade gravity, u_1 and u_2 are the horizontal components of the tugger line forces. The global x-direction is critical for this configuration because large loads are exerted on the blade system. The turbulent wind continuously affects the motion of the blade. The control objective is therefore to stabilize the blade in the main wind direction, in particular the blade root position, by controlling the force inputs, u_1 and u_2, assuming these are control inputs (and disregarding the actuator dynamics, which afterwords are individually controlled through a control allocation method).

To achieve this in practice, there is a need to apply a pretension by moving the blade with an initial offset before the mating operation. To move the blade to a desired setpoint $\boldsymbol{r}_d$ with required pretension, a reference filter should be used to generate a smooth trajectory to avoid a sudden step change of the setpoint $\boldsymbol{r}_d$. After reaching $\boldsymbol{r}_d$ and desired orientation, these are kept constant and the blade should be kept stable. The control objective is thus to control the blade COG to track the desired position and orientation given by the reference filter. The ultimate goal is to reduce the motion of the root center in order to ensure a successful mating operation.

3 | DEVELOPMENT OF THE CONTROL ALGORITHM

3.1 | System overview

In this work, the observer and the controller are designed independently by assuming the separation principle.[35] The block diagram of the control scheme is presented in Figure 5. At each time instant, an EKF receives the noisy measurements $\boldsymbol{y}$ from sensors to estimate the blade position and orientation $\hat{\boldsymbol{\eta}}$, the blade velocity $\hat{\boldsymbol{v}}$, the wind velocity $\hat{U}_w$, and the bias compensation term $\hat{\boldsymbol{b}}$. When the controller is turned on at time t_0, the EKF provides the initial value for the reference model and controller. A reference module is applied to generate smooth trajectories of the real-time desired position and velocity, denoted by $\boldsymbol{\eta}_d$ and $\boldsymbol{v}_d$, to the preset setpoint where the blade is stabilized. All estimates and reference signal are fed back into the feedback controller. The controller calculates the corresponding tension input $\boldsymbol{u}$ to the two tugger lines according to the error between the estimated values and the desired trajectory, as well as some feedforward compensation of the estimated wind and bias loads.

3.2 | Extended Kalman filter

Because the sensors only measure the noisy blade COG position and wind velocity, the blade velocity at the COG is obtained from an observer. A model-based observer not only filters the measurement noise but also estimates the unmeasured states, ideally with no phase lag. An EKF with
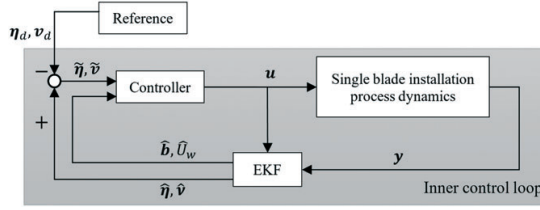
FIGURE 5 Block diagram of the active control scheme for single blade installation. The hat operator (ˆ) denotes the estimation. The tilde (˜) indicates the error between the estimated and desired value (eg, $\tilde{\eta} = \hat{\eta} - \eta_d$)

discrete measurements is used to estimate the states of the simplified system modeled by Equation 1. A continuous model evaluated and measured at discrete time instants is expressed as follows:

$$\dot{x}(t_k) = f(x(t_k), u(t_k)) + Ew(t_k), \tag{8a}$$

$$z_k = Hx(t_k) + v(t_k), \tag{8b}$$

where x is the state variables to be estimated, u is the force input vector, z_k refers to the sampled measurement vector at time t_k, w is the white-noise process presenting system disturbances, v is the Gaussian white noise of the sensor measurements, and f and H correspond to the state equation vector and the output matrix, respectively. The subscript k refers to the kth time step t_k. The time step length is $h = t_k - t_{k-1}$, and the vector elements are $x = [x, y, \psi, b_1, b_2, b_3, u, v, r, U_w]^\top$, $u = [u_1, u_2]^\top$, $w = [w_{b1}, w_{b2}, w_{b3}, w_w]^\top$, and $v = [v_x, v_y, v_\psi, v_{U_w}]^\top$. The discrete extended Kalman filter is briefly described here, while a detailed description can be found in Brown and Hwang.[36] At every time step, the prediction, correction, and propagation processes are executed.

- **Initialization**:

$$\hat{x}_{0|0} = \hat{x}_0, \qquad P_{0|0} = \hat{P}_0, \tag{9}$$

where $\hat{x}_0$ and $\hat{P}_0$ are initial guesses of $x(t_0)$ and the covariance matrix var($x(t_0)$), with $\hat{P}_0$ normally chosen as a symmetric, positive definite matrix. The hat (ˆ) denotes the estimate.

- **Prediction**:

$$\hat{x}_{k|k-1} = f(\hat{x}_{k-1|k-1}, u(t_{k-1})), \tag{10}$$

$$P_{k|k-1} = F_{k-1}P_{k-1|k-1}F_{k-1}^\top + Q, \tag{11}$$

- **Correction**:

$$K_k = P_{k|k-1}H^\top(HP_{k|k-1}H^\top + \Upsilon)^{-1}, \tag{12}$$

$$\hat{x}_{k|k} = \hat{x}_{k|k-1} + K_k(z_k - H\hat{x}_{k|k-1}), \tag{13}$$

$$P_{k|k} = (I - K_kH)P_{k|k-1}(I - K_kH)^\top + K_k\Upsilon K_k^\top, \tag{14}$$

- **Propagation**:

$$\hat{x}_{k+1|k} = \hat{x}_{k|k-1} + hf(\hat{x}_{k|k}, u(t_k)) \tag{15}$$

$$P_{k+1|k} = \Phi_k P_{k|k}\Phi_k^\top + \Gamma Q\Gamma^\top, \tag{16}$$

where $Q \in \mathbb{R}^{3\times3}$ and $\Upsilon \in \mathbb{R}^{4\times4}$ are constant diagonal tuning matrices, corresponding to w and v, and

$$F_k = \frac{\partial f}{\partial x}\bigg|_{x=\hat{x}_{k|k}, u=u(t_k)}, \qquad \Phi_k = I + h\frac{\partial f}{\partial x}\bigg|_{x=\hat{x}_{k|k}, u=u(t_k)}, \qquad \Gamma = hE. \tag{17}$$

The Jacobian matrix $\partial f/\partial x$ used to handle the nonlinearities that exist in the process dynamics and the measurements is given in Appendix A.

3.3 | State feedback control

The nonlinear system is transformed into a linear system through feedback linearization. The nonlinearity in the model is canceled, and classical PID control algorithms can be applied. The simplified system possesses three decoupled DOFs and two control inputs, and it is hence an underactuated system. In other words, fewer DOFs than those of interest (surge, sway, and yaw) can be controlled independently.

The error vector between the current and desired position and orientation is defined as $\bar{\eta} = \eta - \eta_d$, where $\eta_d \in \mathbb{R}^3$ is the desired position and orientation. To overcome the underactation problem, we consider to control the blade root motion in the inflow direction and the yaw angle. Hence, the error vector of the considered states is $L\bar{\eta}$, where the projection matrix is $L = \begin{bmatrix} 1 & 0 & 0 \\ 0 & 0 & 1 \end{bmatrix}$. The relative degree for the system proposed in Equation 1 is 2. Time derivative of $\bar{\eta}$ is $\dot{\bar{\eta}} = R\mathbf{v} - \dot{\eta}_d$. The model is further transformed into the reduced form with only the controlled states by multiplying by L on both sides of $\ddot{\bar{\eta}}$, that is,

$$L\ddot{\bar{\eta}} = L\left[\dot{R}\mathbf{v} + RM^{-1}(R^{\top}(g + b) + \tau_w) - \ddot{\eta}_d\right] + LRM^{-1}R^{\top}B\mathbf{u}. \tag{18}$$

When Equation 3 is substituted into (18), the control input can be simplified as

$$\mathbf{u} = -(LM^{-1}B)^{-1}\left[L\left(RS(r)\mathbf{v} + M^{-1}(g + b) + RM^{-1}\tau_w - \ddot{\eta}_d\right) - \mathbf{u}_{pid}\right], \tag{19}$$

where $\mathbf{u}_{pid} = -K_p L\bar{\eta} - K_d L\dot{\bar{\eta}} - K_i \int L\bar{\eta}dt$.

Furthermore, substituting the feedback linearization control law (19) into (18) gives

$$L\ddot{\bar{\eta}} = -K_p L\bar{\eta} - K_d L\dot{\bar{\eta}} - K_i \int L\bar{\eta}dt. \tag{20}$$

Defining $\zeta = \int L\bar{\eta}dt$, applying a Laplace transformation to Equation 20, and using the pole placement technique yields

$$(s^3 + K_d s^2 + K_p s + K_i)\zeta(s) = (s + \Lambda)^3\zeta(s) = 0, \tag{21}$$

where $\Lambda = \text{diag}(\lambda_x, \lambda_\psi)$. When the eigenvalues $-\lambda_x < 0$ and $-\lambda_\psi < 0$, the system achieves global exponential stability. By placing the poles on the negative real axis, the system is exponentially decaying without oscillation. For a second-order system with integration, placing both the two poles at the same point on negative real axis ensure a critical damping characteristic. All the three poles are selected with the same value. Hence, the PID gain matrices are found by

$$K_p = \text{diag}\left(3\lambda_x, 3\lambda_\psi\right), \tag{22}$$

$$K_d = \text{diag}\left(3\lambda_x^2, 3\lambda_\psi^2\right), \tag{23}$$

$$K_i = \text{diag}\left(\lambda_x^3, \lambda_\psi^3\right). \tag{24}$$

The eigenvalues $(-\lambda_x, -\lambda_\psi)$ should be selected based on hardware capacity and the desired reaction speed. With increasing $|\lambda_x|$ and $|\lambda_\psi|$, the reaction speeds become higher, and the maximum error is smaller, but more powerful actuators are needed. Also, noise/uncertainties in the feedforward and cancellation terms in Equation 19 may be significantly amplified, severely reducing the closed-loop performance at high gains. According to the control law, the feedforward terms in Equation 19 compensating g, τ_w, and b, accelerate the integral controller and improve the overall performance.

3.4 | Reference model

The reference model is used to generate real-time trajectories $\eta_d(t)$ and $\mathbf{v}_d(t) = \dot{\eta}_d(t)$ to the controller, including the blade COG position, orientation, and velocity. In this paper, the final setpoint position is where the blade is stabilized and the orientation vector is denoted by $r_d \in \mathbb{R}^2 \times \mathbb{S}$. Continuous and smooth trajectories are planned between the initial and final values to achieve a smooth control toward the final desired position and orientation. A third-order filter is adopted as the reference model, which is given by

$$\eta_d^{(3)} + (2\Delta + I)\Omega\ddot{\eta}_d + (2\Delta + I)\Omega^2\dot{\eta}_d + \Omega^3\eta_d = \Omega^3 r_d, \tag{25}$$

where $\Delta = \text{diag}\{\zeta_1, \zeta_2\} = \text{diag}\{1, 1\}$ and $\Omega = \text{diag}\{\omega_{n1}, \omega_{n2}\}$ are the matrices of relative damping ratios and natural frequencies, respectively. The parameters ω_{n1} and ω_{n2} should be tuned feasibly to the dynamic model.

4 | SIMULATION RESULTS

4.1 | Overview

Numerical simulations were conducted in the MATLAB/Simulink environment. First, the 3DOF CDM was used to tune the parameters for the observer and controller. Then, the SVM was used to verify the control scheme in detail. Selected properties of the blade installation model and the controller parameters are summarized in Table 2. The blade of the NREL 5 megawatt (MW) reference wind turbine[37] is used.

Table 3 lists the four load cases considered, with the turbulence intensities (TIs) calculated according to the IEC standard.[38] HAWC2 was used to generate the wind turbulence box according to Mann's turbulence model.[39] From the start of the simulations in MATLAB/Simulink, the wind

TABLE 2 Parameters used for numerical simulations

Parameters	Unit	Value
Position of the crane tip	m	$[0, 0, -110]^T$
Hook mass m_h	ton	1
Yoke mass m_y	ton	50
Blade mass m_b	ton	17.74
Blade moment of inertia about COG I_b	kg/m	4.31e6
Blade length	m	62.5
Blade root center position in the body-fixed frame $\{B\}$	m	$[-0.089, -20.51, 0.145]^T$
Position of the sling connection points in $\{B\}$	m	$[0.089, \pm 4.5, 1.855]^T$
Length of lift wire	m	9.2
Stiffness of lift wire	N/m	5.59e8
Length of slings	m	9.0
Stiffness of slings	N/m	1e8
Lift wire and spring damping ratio	-	1%
Position of the tugger line connection points in $\{B\}$	m	$[0.089, \pm 4.5, -0.145]^T$
Tugger line length l_t	m	10
Stiffness of the tugger lines	N/m	1e8
Noise power in the position and orientation	W/Hz	1e-8
Noise power in the wind speed sensor	W/Hz	0.005
Sensor sampling rate	Hz	100
Gain of the lowpass filter T_{iu}	-	5
Diagonal matrix $\mathbf{T_b}$	-	diag([5e6, 1e5, 2e5])
Constant T_w	-	100
Tuning matrix $\mathbf{Q}$	-	diag([1, 1, 1, 1])
Tuning matrix Υ	-	diag([1e-9,1e-10,1e-12,0.005])
Eigenvalues of the PID controller $[\lambda_x, \lambda_\psi]$	-	[1,1]

TABLE 3 Load cases under turbulent wind conditions (Wind Turbine Class C)[38]

Load Case	1	2	3	4
Mean wind speed (U_w) (m/s)	6	8	10	12
Turbulence intensity (TI)	0.202	0.174	0.157	0.146

turbulence box moves in the positive global x-direction, and it passes the blade installation model. For each wind speed, five simulations were conducted using different random seed numbers to reduce statistical uncertainties. The seed numbers are 25, 48, 94, 242, and 596. Each simulation lasted 1000 seconds. In the response statistics, the first 400 seconds were removed during postprocessing to avoid the start-up transient effect. In the figures presented in Section 4.2, the legend "Real" denotes the simulated values without any sensor noises, the legend "Measured" stands for the simulated values with sensor noises considered, and the legend "Estimated" refers to the values estimated by the observer which filters the sensor noises.

4.2 | Observer and controller performance

4.2.1 | Control design model

The CDM is first adopted to verify the control scheme. The load case with $U_w = 10$ m/s and $TI = 0.157$ is selected as a representative case. The observer and controller performance are presented in Figure 6A-D. The results show that the controller and the observer work well for the CDM, as expected. The EKF is able to provide satisfactory estimates of the blade velocities and the wind velocity. The noise in the wind speed measurement has been filtered. Because of the effect of the tugger line force control, the range of the blade motion in the x-direction remains below 0.01 m, and the angular oscillation of the yaw motion is less than 10^{-3} deg. The tugger line force inputs u_1 and u_2 from the controller are positive, and their change rates (time derivatives) are acceptable (<20.2 kN/s). Although the blade motion in the spanwise direction is not controlled, the v-displacement is limited. This observation is consistent with the cross-flow principle, which neglects the wind speed component in the y^b-direction during the wind load calculation.
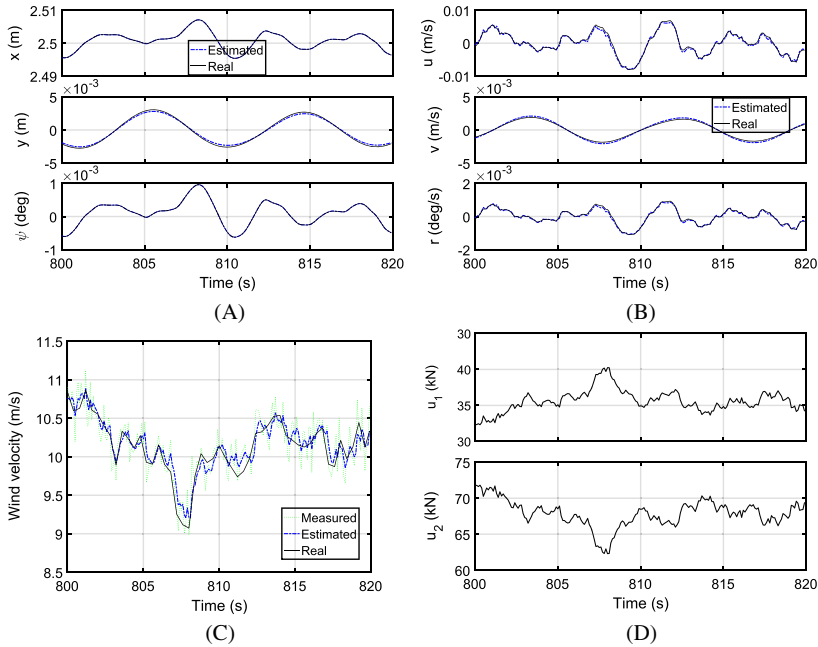
FIGURE 6 Performance of the EKF estimation for the simplified blade model, U_w=10 m/s, TI=0.157. A, Blade COG position and orientation estimation in the global frame; B, velocity estimation at the blade COG in the body-fixed frame; C, wind speed estimation in the global x-direction; and D, control inputs to the tugger lines [Colour figure can be viewed at wileyonlinelibrary.com]

4.2.2 | Simulation verification model

The SVM is used to test more realistically the performance of the proposed control and observer algorithms. The simulation results for the load case with U_w ramp up from 0 to 12 m/s in 100-300 seconds are presented in Figure 7. For the SVM, the discrepancies between the estimated and real blade motions and velocities are, as expected, greater than those for the CDM; see Figure 7A,B. However, the dynamic part of the blade oscillations in the global x-axis has been effectively maintained at less than 0.1 m because of the active force control. For the estimated wind speed, there is also a noticeable difference compared with the real wind speed, as shown in Figure 7C. Due to the spatial variation of the wind field, measurements from one location of the anemometer are not adequate for fully describing the wind speed variation along the blade, and the wind speed estimate therefore deviates. It is also seen to be somewhat noisy. Although the wind speed estimate is not accurate, it can still be used to accelerate the disturbance rejection part of the controller and reduce the initial drift, since the mean estimated wind speed approximately tracks the actual wind speed. Similar to the observation of the CDM, the tugger line forces are always positive during the simulations, and the change rates are still within reasonable ranges (<7.25 kN/s). The change rates is smaller than those in Section 4.2.1 because of the actuator lowpass dynamics.

4.3 | Comparison of active and passive schemes

4.3.1 | Time histories

A set of comparative studies of the active control scheme with a typical passive single blade installation system were conducted to evaluate the performance the proposed controller under various wind conditions. The passive system has the same structural properties as the SVM, but the tugger lines are not actively controlled.

The time-domain results are compared in Figure 8 for the selected load case. For the passive system (dash-dot line in the figure), the blade surge motion in the x-direction is dominant, and the motion maxima is within 2 m in this case, where motion maxima is defined by the difference between the motion response maxima and its mean value. Compared with the blade surge motion, the sway and heave motions in the y- and z-directions are small, with the absolute motion maxima below 0.2 m.

In contrast, when the active scheme is applied, the blade surge motion in the x-direction has a significant reduction. For the blade sway and heave motions in the y- and z-directions, the response magnitudes are slightly reduced compared with those of the passive system. This result is reasonable because the y- and z- motions are not controlled. In addition, the blade root sway motion is also affected by the controlled yaw motion, which is further related to the controlled surge motion. Although the active control scheme is mainly effective in the x-direction, it thus also reduces the motions of the other DOFs.
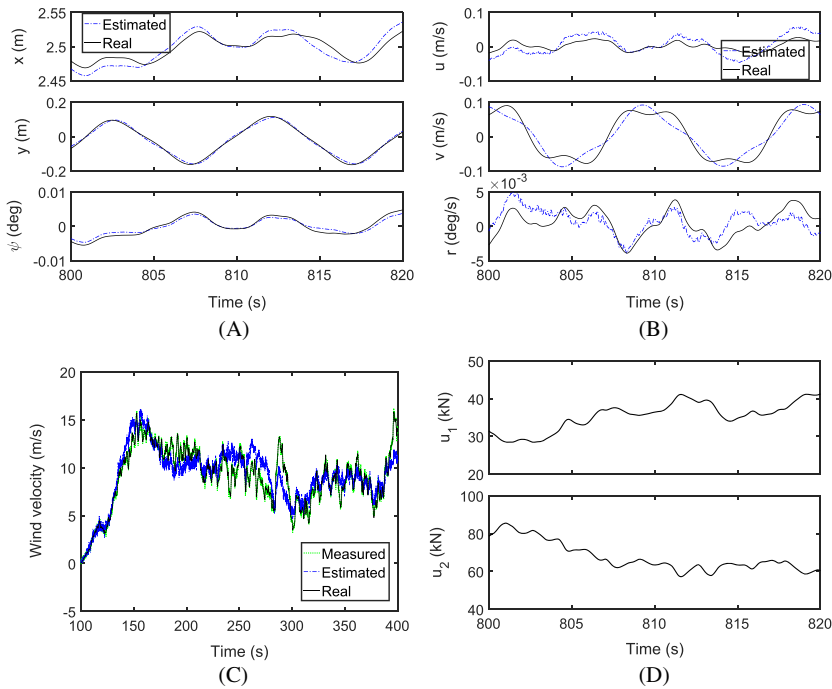
FIGURE 7 Performance of the EKF estimation at the blade COG for the SVM, U_w=10 m/s and TI=0.157. A, Blade COG position and orientation estimation in the global frame; B, velocity estimation at the blade COG in the body-fixed frame; C, wind speed estimation in the global x-direction; and D, control inputs to the tugger lines [Colour figure can be viewed at wileyonlinelibrary.com]
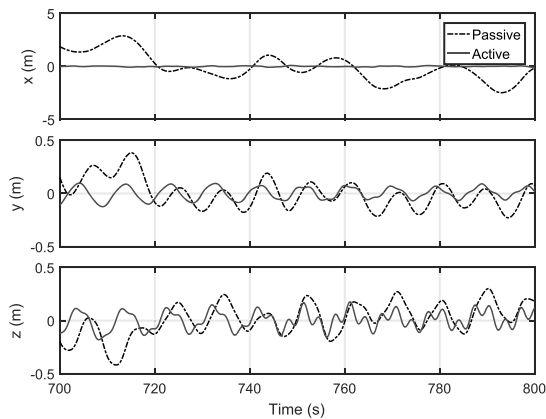
FIGURE 8 Time histories of the blade root center displacement relative to the mean position using the SVM, $U_w = 10$ m/s and $TI = 0.157$

4.3.2 | Statistical results

The statistics were obtained by averaging the results of five 600-second simulations. The standard deviation and the motion maxima are used as the main criteria for evaluating the effect of active control. The mean value is always controlled accurately to the constant reference value.

As shown in Figure 9, the motion maxima in the x-direction is dominant, and the use of active control causes a significant reduction for both the blade COG and root center. Under the investigated mean wind speeds from 6 to 12 m/s, the maximum reduction exceeds 90%. Reductions are also observed in the y- and z-directions, albeit less prominent because of coupling with other DOFs. When the blade yaws about the z-axis, the rotational center is close to the COG. Hence, the motion in one DOF of the blade root is more affected by other DOFs because of rigid body motions. For example, the sway motion of the blade root center is more influenced than the blade COG by the yaw motion.
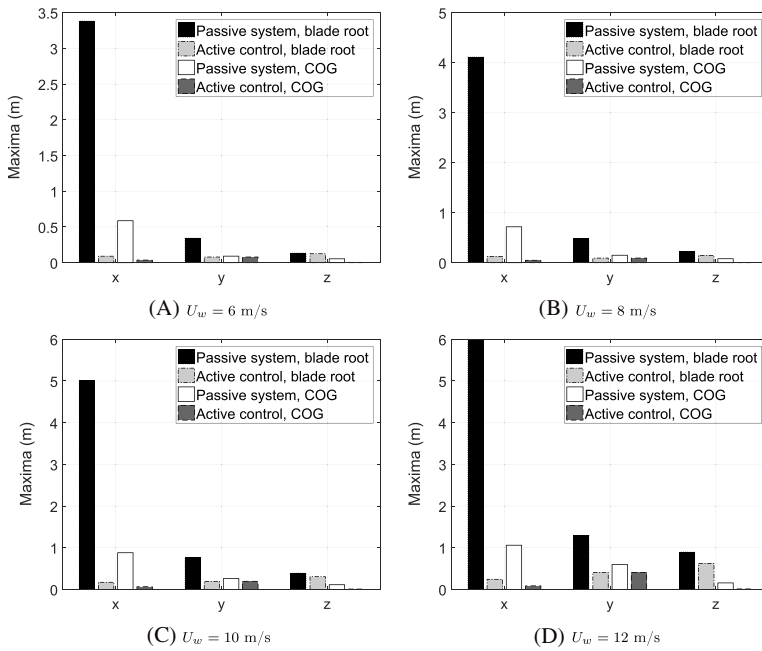
FIGURE 9 Motion maxima of the blade-root center and the blade COG using the SVM; $U_w = 6 - 12$ m/s, average of five 600-second simulations
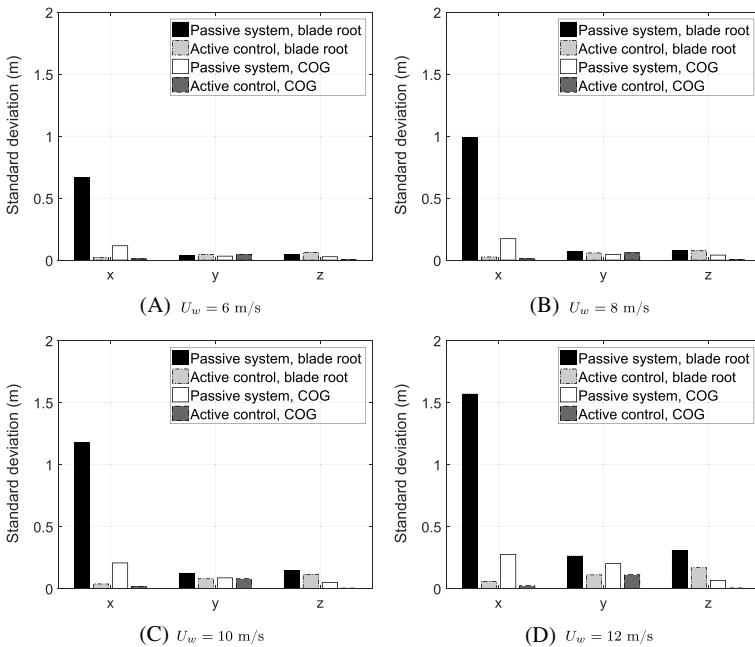
FIGURE 10 Standard deviation of the motions at the blade root center and the blade COG using the SVM; $U_w = 6 - 12$ m/s, average of five 600-second simulations

Figure 10 compares the standard deviations of the response for the passive and the active schemes. Similar to the motion maxima, the standard deviation has the greatest reduction in the x-direction at all wind speeds, but reductions are also observed in the y- and z-directions.

Overall, the statistical results are consistent with the time series of blade root motions. In the blade mating process, the blade root will be docked into the hub, and the blade root motions in the xz-plane are closely associated with the success rate of the mating process. The proposed control system considerably reduces the motion variations in the x-direction and indicates a potential for improved mating efficiency.

5 | CONCLUSIONS AND FUTURE WORK

This paper proposes a closed-loop scheme for active tugger line force control for single blade installation. To facilitate the design of the observer algorithm and control law, the blade installation system was simplified as a 3DOF control design model. Based on the reduced model, an extended Kalman filter, a state feedback linearization and feedforward compensation algorithm, and pole placement techniques were applied to design the proportional-integral-derivative controller. A third-order reference model was adopted to provide smooth position and velocity trajectories in real time. In addition to the control design model, a simulation verification model that includes a 6DOF blade, other lifting components, and more real-istic environmental load models was also developed. To verify the performance of the control system, time-domain simulations were conducted in turbulent wind conditions.

It was found that the proposed actively-controlled tugger line system works well as tested with the simulation verification model. A comparison with a passive system without control shows that the active control scheme can effectively reduce the blade-root surge motion standard and maxima deviations. This observation indicates that the active tugger line control method can potentially expedite the blade mating process.

In future work, other scenarios of single blade installation is planned to be addressed. For example, flexibility of the crane tip should be considered for the boundary condition of the lift wire, and other possible directions of the tension provided by the tugger lines should also be considered. In addition to the blade-root motions, the monopile vibrations may also cause concern during the blade mating process. Thus, real-time measurement of the monopile vibrations from available sensors, such as inertial measurement units (which steadily become better and cheaper), may be used by the controller. For accurate representation of the aerodynamic loading on large wind turbine blades during installation, structural flexibility and advanced computational methods such as the computational fluid dynamics method can be considered.

ORCID

Zhengru Ren [iD] http://orcid.org/0000-0001-5522-8094
Zhiyu Jiang [iD] http://orcid.org/0000-0002-8778-0999
Roger Skjetne [iD] http://orcid.org/0000-0001-9289-1450

REFERENCES

1. Commission of the European Communities. *Communication From the Commission to the European Parliament, the Council, the European Economic and Social Committee and the Committee of the Regions—offshore wind energy: Action Needed to Deliver on the Energy Policy Objectives for 2020 and Beyond.* The European Commission; 2008.
2. WindEurope. Wind in power: 2016 European statistics; 2017.
3. Soyoz S, Aydin C. Effects of higher wave harmonics on the response of monopile type offshore wind turbines. *Wind Energy*. 2013;16(8):1277-1286.
4. Pahn T, Rolfes R, Jonkman J. Inverse load calculation procedure for offshore wind turbines and application to a 5-mw wind turbine support structure. *Wind Energy*. 2017;20(7):1171-1186.
5. Shirzadeh R, Weijtjens W, Guillaume P, Devriendt C. The dynamics of an offshore wind turbine in parked conditions: a comparison between simulations and measurements. *Wind Energy*. 2015;18(10):1685-1702.
6. Zhang D, Yue Q. Major challenges of offshore platforms design for shallow water oil and gas field in moderate ice conditions. *Ocean Eng*. 2011;38(10):1220-1224.
7. Shi W, Park HC, Na S, Song J, Ma S, Kim CW. Dynamic analysis of three-dimensional drivetrain system of wind turbine. *Int J Precis Eng Manuf*. 2014;15(7):1351-1357.
8. Moné C, Hand M, Bolinger M, Rand J, Heimiller D, Ho J. 2015 cost of wind energy review; 2017.
9. Kaiser MJ, Snyder B. Offshore wind energy installation and decommissioning cost estimation in the U.S. outer continental shelf. In: Energy Research Group LLC. Louisiana, Baton Rouge; 2010.
10. Gaunaa M, Bergami L, Guntur S, Zahle F. First-order aerodynamic and aeroelastic behavior of a single-blade installation setup. *J Phys: Conf Ser*. 2014;524(1):012073.
11. Gaunaa M, Heinz J, Skrzypiński W. Toward an engineering model for the aerodynamic forces acting on wind turbine blades in quasisteady standstill and blade installation situations. *J Phys Conf Ser*. 2016;753(2):022007.

12. Skrzypiński W, Gaunaa M, Heinz J. Modelling of vortex-induced loading on a single-blade installation setup. *J Phys: Conf Ser*. 2016;753(8):082037.

13. Kuijken L. Single blade installation for large wind turbines in extreme wind conditions. *Master's Thesis*; 2015.

14. Jiang Z, Gao Z, Ren Z, Li Y, Duan L. A parametric study on the blade mating process for monopile wind turbine installations under rough environmental conditions. *Eng Struct*. 2018;172:1042-1056.

15. Liftra. LT575 Blade Dragon. http://liftra.com/product/blade-dragon/. Accessed August 10, 2017.

16. HighWind. The boom lock. http://www.high-wind.eu/boomlock/. Accessed August 10, 2017.

17. Fang Y, Wang P, Sun N, Zhang Y. Dynamics analysis and nonlinear control of an offshore boom crane. *IEEE Trans Ind Electron*. 2014;61(1):414-427.

18. Ngo QH, Hong K-S. Sliding-mode antisway control of an offshore container crane. *IEEE/ASME Trans Mechatron*. 2012;17(2):201-209.

19. Masoud ZN, Nayfeh AH, Mook DT. Cargo pendulation reduction of ship-mounted cranes. *Nonlinear Dyn*. 2004;35(3):299-311.

20. Abdel-Rahman EM, Nayfeh AH, Masoud ZN. Dynamics and control of cranes: a review. *Modal Anal*. 2003;9(7):863-908.

21. Xu J, Ren Z, Li Y, Skjetne R, Halse KH. Dynamic simulation and control of an active roll reduction system using free-flooding tanks with vacuum pumps. *J Offshore Mech Arct Eng*. 2018;140(6):061302.

22. Johansen TA, Fossen TI, Sagatun SI, Nielsen FG. Wave synchronizing crane control during water entry in offshore moonpool operations-experimental results. *IEEE J Oceanic Eng*. 2003;28(4):720-728.

23. Messineo S, Celani F, Egeland O. Crane feedback control in offshore moonpool operations. *Control Eng Pract*. 2008;16(3):356-364.

24. Martínez J, Rodriguez P, Kjær PC, Teodorescu R. Design and coordination of a capacitor and on-load tap changer system for voltage control in a wind power plant of doubly fed induction generator wind turbines. *Wind Energy*. 2012;15(4):507-523.

25. Díaz de Corcuera A, Pujana-Arrese A, Ezquerra JM, Milo A, Landaluze J. Linear models-based LPV modelling and control for wind turbines. *Wind Energy*. 2015;18(7):1151-1168.

26. Lu Q, Bowyer R, Jones BL. Analysis and design of coleman transform-based individual pitch controllers for wind-turbine load reduction. *Wind Energy*. 2015;18(8):1451-1468.

27. Skjetne R, Fossen TI, Kokotović PV. Adaptive maneuvering, with experiments, for a model ship in a marine control laboratory. *Automatica*. 2005;41(2):289-298.

28. RWE Innogy GmbH. Halfway through the turbine installation for the nordsee ost offshore wind farm. 2014. [Online; Accessed July 16, 2017].

29. Ren Z, Jiang Z, Skjetne R, Gao Z. Development of a numerical simulator for offshore wind turbine blades installation. *Ocean Eng*. 2018. https://doi.org/10.1016/j.oceaneng.2018.05.011

30. Larsen TJ, Hansen AM. How 2 hawc2, the user's manual; 2007.

31. Hu W, Choi KK, Zhupanska O, Buchholz JH. Integrating variable wind load, aerodynamic, and structural analyses towards accurate fatigue life prediction in composite wind turbine blades. *Struct Multi Optim*. 2016;53(3):375-394.

32. Liang H, Chen X. A new multi-domain method based on an analytical control surface for linear and second-order mean drift wave loads on floating bodies. *J Comput Phys*. 2017;347:506-532.

33. Egeland O, Gravdahl JT. *Modeling and Simulation for Automatic Control*. Norway: Marine Cybernetics Trondheim; 2002.

34. Bø TI, Dahl AR, Johansen TA, et al. Marine vessel and power plant system simulator. *IEEE Access*. 2015;3:2065-2079.

35. Loria A, Fossen TI, Panteley E. A separation principle for dynamic positioning of ships: Theoretical and experimental results. *IEEE Trans Control Syst Technol*. 2000;8(2):332-343.

36. Brown RG, Hwang P. YC. *Introduction to Random Signals and Applied Kalman Filtering with MATLAB Exercises*, 4th ed. Wiley; 2012.

37. Jonkman J, Butterfield S, Musial W, Scott G. Definition of a 5-mw reference wind turbine for offshore system development. Technical Report No. NREL/TP-500-38060, National Renewable Energy Laboratory, Golden, CO; 2009.

38. IEC 61400-1. *Wind Turbine Generator Systems-Part 1: Safety Requirements*. Geneva, Switzerland: International Electrotechnical Commission and others; Standard; 2005.

39. Jonkman BJ, Kilcher L. Turbsim user's guide: version 1.06; 2012.

APPENDIX A: LIST OF MATRICES

$$
H = \begin{bmatrix} 1 & 0 & 0 & 0 & 0 & 0 & 0 & 0 & 0 \\ 0 & 1 & 0 & 0 & 0 & 0 & 0 & 0 & 0 \\ 0 & 0 & 1 & 0 & 0 & 0 & 0 & 0 & 0 \\ 0 & 0 & 0 & 0 & 0 & 0 & 0 & 0 & 1 \end{bmatrix}
\tag{A1}
$$

$$
E = \begin{bmatrix} 0 & 0 & 0 & 1 & 0 & 0 & 0 & 0 & 0 \\ 0 & 0 & 0 & 0 & 1 & 0 & 0 & 0 & 0 \\ 0 & 0 & 0 & 0 & 0 & 1 & 0 & 0 & 0 \\ 0 & 0 & 0 & 0 & 0 & 0 & 0 & 0 & 1 \end{bmatrix}
\tag{A2}
$$

$$\frac{\partial \boldsymbol{f}}{\partial \boldsymbol{x}} = \begin{bmatrix} 0 & 0 & -S_\psi u - C_\psi v & 0 & 0 & 0 & C_\psi & -S_\psi & 0 & 0 \\ 0 & 0 & C_\psi u - S_\psi v & 0 & 0 & 0 & S_\psi & C_\psi & 0 & 0 \\ 0 & 0 & 0 & 0 & 0 & 0 & 0 & 0 & 1 & 0 \\ 0 & 0 & 0 & -\frac{1}{T_{b1}} & 0 & 0 & 0 & 0 & 0 & 0 \\ 0 & 0 & 0 & 0 & -\frac{1}{T_{b2}} & 0 & 0 & 0 & 0 & 0 \\ 0 & 0 & 0 & 0 & 0 & -\frac{1}{T_{b3}} & 0 & 0 & 0 & 0 \\ -\frac{g}{l}C_\psi & -\frac{g}{l}S_\psi & \frac{g}{l}(S_\psi x - C_\psi y) - \frac{2a}{m}U_w^2 C_\psi S_\psi + \frac{1}{m}(-b_1 S_\psi + b_2 C_\psi) + \frac{S_\psi}{m}(u_1 + u_2) & \frac{C_\psi}{m} & \frac{S_\psi}{m} & 0 & 0 & 0 & 0 & \frac{2a}{m}U_w C_\psi^2 \\ \frac{g}{l}S_\psi & -\frac{g}{l}C_\psi & \frac{g}{l}(-C_\psi x + S_\psi y) + \frac{1}{m}(-b_1 S_\psi - b_2 C_\psi) + \frac{C_\psi}{m}(u_1 + u_2) & -\frac{S_\psi}{m} & \frac{C_\psi}{m} & 0 & 0 & 0 & 0 & 0 \\ 0 & 0 & -\frac{2b}{l}U_w^2 C_\psi S_\psi + \frac{S_\psi}{l}(r_{t1}u_1 - r_{t2}u_2) & 0 & 0 & \frac{1}{l} & 0 & 0 & 0 & \frac{2b}{l}U_w C_\psi^2 \\ 0 & 0 & 0 & 0 & 0 & 0 & 0 & 0 & 0 & -\frac{1}{T_w} \end{bmatrix} \tag{A3}$$

Paper A4

Integrated GNSS/IMU hub motion estimator for offshore wind turbine blade installation

Zhengru Ren, Roger Skjetne, Zhiyu Jiang, Zhen Gao, and Amrit Shankar Verma

Integrated GNSS/IMU hub motion estimator for offshore wind turbine blade installation

Zhengru Ren [a,b,c,*], Roger Skjetne [a,b,c], Zhiyu Jiang [d], Zhen Gao [a,b,c], Amrit Shankar Verma [a,c]

[a] Centre for Research-based Innovation on Marine Operations (SFI MOVE), Norwegian University of Science and Technology (NTNU), Norway
[b] Centre for Autonomous Marine Operations and Systems (AMOS), NTNU, Norway
[c] Department of Marine Technology, NTNU, NO-7491 Trondheim, Norway
[d] Department of Engineering Sciences, University of Agder, 4879 Grimstad, Norway

ARTICLE INFO

ABSTRACT

Offshore wind turbines (OWTs) have become increasingly popular for their ability to harvest clean offshore wind energy. Bottom-fixed foundations are the most used foundation type. Because of its large diameter, the foundation is sensitive to wave loads. For typical manually assisted blade-mating operations, the decision to perform the mating operation is based on the relative distance and velocity between the blade root center and the hub, and in accordance with the weather window. Hence, monitoring the hub real-time position and velocity is necessary, whether the blade installation is conducted manually or automatically. In this study, we design a hub motion estimation algorithm for the OWT with a bottom-fixed foundation using sensor fusion of a global navigation satellite system (GNSS) and an inertial measurement unit (IMU). Two schemes are proposed based on a moving horizon estimator, a multirate Kalman filter, an online smoother, and a predictor. The moving horizon estimator mitigates the slow GNSS sampling rate relative to the hub dynamics. The multirate Kalman filter estimates the position, velocity, and accelerometer bias with a constant GNSS measurement delay. The online smoothing algorithm filters the delayed estimated trajectory to remove sudden step changes. The predictor compensates the delayed estimate, resulting in real-time monitoring. HAWC2 and MATLAB are used to verify the performance of the estimation algorithms, showing that a sufficiently accurate real-time position and velocity estimate with a high sampling rate is achieved. A sensitivity study compares the accuracy of different algorithms applied in various conditions. By combining both proposed algorithms, a sufficiently accurate estimation can be achieved for a wider scope of practical applications.

© 2019 Elsevier Ltd. All rights reserved.

1. Introduction

Offshore wind turbines (OWTs) have become increasingly popular because of their high energy production and quality. Though sensitive to wave loads, bottom-fixed monopile foundations are the most common type, because of their simple shape, their large diameter, and a structural design driven mainly by fatigue loads [1]. Several publications focus on passive and active approaches to reduce the fatigue damages by, e.g., adding a tuned mass damper [2,3], controlling the blade pitch for operating OWTs [4], and using a ball vibration absorber [5].

---

* Corresponding author.
  E-mail address: zhengru.ren@ntnu.no (Z. Ren).

Nonetheless, the price of the electricity from offshore wind energy was three times higher than that from onshore wind energy in 2016 [6]. Large expenses for installation and maintenance are primary reasons for the high price. Two important approaches to reduce the cost of OWT installation are to improve the installation efficiency and to decrease the offshore waiting time between successive operations. Fifteen million euros is currently the extra cost of waiting for lower wind speed windows for the construction of a middle-sized wind farm in Europe [7]. Hence, several studies have been conducted with an emphasis on installation in high wind scenarios, thereby improving the installation efficiency. Studies on the critical allowable weather conditions for wind turbine installations are found in the literature [8–10]. In other studies [11,12], a closed-loop controller has been proposed to stabilize a suspended single blade. To achieve an effective mating performance, the blade root should follow the hub motion to reduce their relative displacement and relative velocity, consequently reducing the resulting impact force. Therefore, a method to monitor the hub displacement in real time is acutely necessary. The advantages and disadvantages of more than 20 commercial wind turbine condition monitoring systems, as well as their main functions, have been compared in the literature [13]. On-site acceleration data are recorded by the wind turbine condition monitoring systems; however, hub displacement monitoring is lacking [14].

To estimate a position trajectory, the most used strategies are the direct measurement from a global navigation satellite system (GNSS) and the double integration of the acceleration measurement, after a coordinate transformation, using an inertial measurement unit (IMU) [15,16]. However, neither method is sufficient to handle the positioning problem for a dynamic system with high frequency. In this study, a global positioning system (GPS) is used as a representation of the GNSS, illustrating that vital shortages exist in the direct GPS measurement. A GPS receiver operates at a low sampling rate with inferior accuracy and with a time delay from the communication and computation. For a slow dynamic system, the low sampling rate and the time delay effects are insignificant, e.g., in the case of a dynamic positioning system of an offshore vessel. However, the wave-induced motion on the wind turbine foundation is not a slow dynamic system [17]. The delay of the GPS receiver can be several hundred milliseconds, such that the intersample motion becomes significant. Therefore, a motion estimator must consider the time delay. The challenge of using measurements from an IMU is that the bias in the acceleration measurement results in a drift when integrated twice. The bias results from assembly flaws and the ambient conditions, such as temperature and humidity [18].

Integration of displacement and acceleration using a navigation filter has been widely applied in various areas. Normally, the estimation approaches are categorized into extended stochastic linear estimation techniques, deterministic complementary filter and nonlinear observer design techniques, and combinations of these techniques [19]. Linearized Kalman filters, such as the extended Kalman filter (EKF) and the unscented Kalman filter, are widely used in practice, even though global stability is typically not guaranteed [20,21]. Nonlinear observers with stronger stability properties, however, are case-specific and lack generic design methodologies. An exogenous Kalman filter is a combination of a linearized Kalman filter and a nonlinear observer, which ensures both global stability and low variance in the estimates [22]. Examples of the application of these approaches are building deformation and earthquake monitoring [23–25], pedestrian navigation systems [26], dead reckoning [27], dynamic positioning systems [16,28], and aerial applications [29,30].

In this study, two hub motion estimation algorithms based on a GNSS/IMU fusion are customized to monitor the hub's real-time displacement and velocity for an OWT with a bottom-fixed monopile foundation. Combining both algorithms ensures sufficient accurate estimations for most practical applications.

This paper is structured as follows. In Section 2, the problem statement is proposed with foundation modeling and a motivational example. The characteristics of the hub motion are analyzed, and the complexity of the estimation scheme is reduced to ensure operational feasibility. In Section 3, the estimation model is proposed. In Section 4, two algorithms are developed based on a moving horizon estimator (MHE), a multirate Kalman filter (MKF), an online smoother, and a predictor. The algorithms monitor the OWT hub displacement and velocity in real time. In Section 5, HAWC2 and MATLAB are used to verify the performance of the monitoring algorithms. Sensitivity studies are conducted to evaluate the estimation performance. The conclusions are presented in Section 6.

Notation: Scalars, vectors, and matrices are expressed with normal letters, bold lowercase letters, and bold uppercase letters, respectively. The hat notation, $\hat{x}$, denotes the estimate of a state x. $\boldsymbol{I}$ and $\boldsymbol{0}$ are a 2×2 identity matrix and a zero matrix, i.e., $\boldsymbol{I} = \begin{bmatrix} 1 & 0 \\ 0 & 1 \end{bmatrix}$ and $\boldsymbol{0} = \begin{bmatrix} 0 & 0 \\ 0 & 0 \end{bmatrix}$.

2. Problem formulation

An OWT with a monopile foundation without blades is simulated in HAWC2 to illustrate the problem. HAWC2 is an aeroelastic code designed to calculate the wind turbine response in the time domain [31]. In this study, the north-east-down coordinate system $\{n\}$ and body-fixed reference frame $\{b\}$ are adopted and assumed inertial (see Figs. 1,2). Both the frames follow the right-hand rule. The origin $\{n\}$ is located at the projection on the free water surface by the center of the cross-section of the substructure at rest. The x-axis points to the north, the y-axis points the east, and z-axis points downward. The origin of $\{b\}$ is placed at the location of the IMU, with the x^b- and z^b-axes are pointing to the hub and downward, respectively. The relative roll, pitch, and yaw orientation of $\{b\}$ in $\{n\}$ are denoted as ϕ_h, θ_h, and ψ_h, respectively.
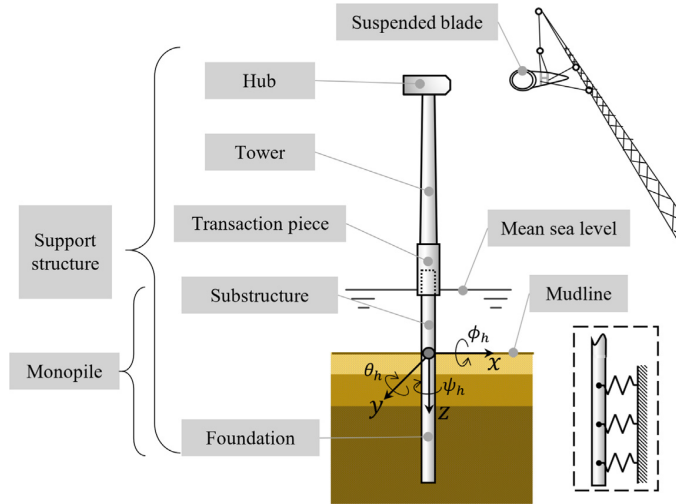
Fig. 1. The single blade installation scenario with monopile foundation, tower, pre-assembled hub, suspended blade, and the distributed spring model.
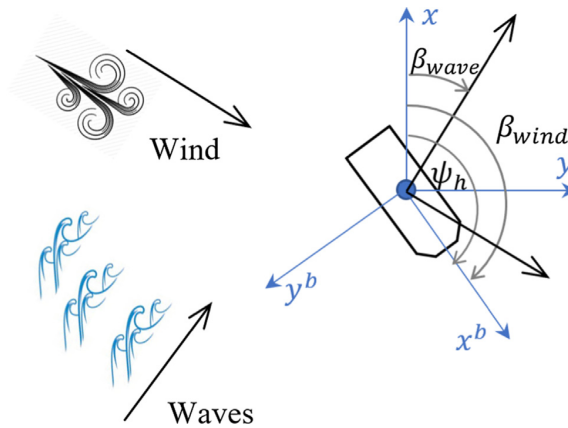

Fig. 2. Proposed model in the horizontal plane.

2.1. Modeling of the monopile foundation and support structures

From low fidelity to high fidelity, the three most used monopile models are the apparent fixity model, the coupled spring model, and the distributed spring model. Differences among the models are mainly from the modeling of the soil-pile interaction below the mudline. In this study, the distributed spring model is adopted [32,33]. The p-y model [34] is used in the simulation. The soil, modeled as elastic springs, is layered with different effective weights and angles of internal frictions. As defined by the American Petroleum Institute [35], the soil resistance is a function of the pile displacement at a given point along the pile. Each layer is modeled as an uncoupled nonlinear spring with a layer-specific stiffness as shown in Fig. 1. The soil parameters can be found in Table 1. The soil has higher initial modulus of subgrade reaction with increasing depth. Timoshenko beams are used to model the pile, the transaction piece, the tower, and the hub [36–38].

In the following, the environmental parameters are the mean wind speed U_w, the turbulence intensity TI, the wind turbulence seed S_{TI}, the main wind direction β_{wind}, the significant wave height H_s, the wave period T_p, the wave seed S_{wave}, and the wave heading β_{wave}. Normally, wave conditions for offshore operations are selected as $H_s \leqslant 3$ m and 4 s $\leqslant T_p \leqslant 10$ s. The IEC Class C wind turbulence model is chosen [41]. Structure parameters could be identified by various optimization approaches [42–44].

Table 1
Soil profile [39,40].

Depth under mudline (m)	Effective weight (kN/m³)	Angle of internal friction (deg)
0–5	10.0	33.0
5–14	10.0	35.0
14–36	10.0	38.5

2.2. Illustrating example

An OWT with a 66-meter monopile foundation has been hammered into the seafloor to a depth of 36 m. The water depth is 30 m. All support structures have been assembled except the blades. The damping ratio of the foundation is tuned to be 1%. The hub is rotated to a fixed yaw $\psi_h = 0°$, ready for further installation operations. The foundation structure is exposed to a JONSWAP wave spectrum. The structural and environmental parameters are tabulated in Table 2. The waves spread to 30 deg north of east. The measurements are ideal, without sensor noise, bias, or delay. The simulation is conducted for 2000 s. The time domain simulation results of the hub displacement and its fast Fourier transform (FFT) results are presented in Figs. 3 and 4. Since no blade is considered in the proposed simulation, the main responses of the monopile and tower mainly result from the wave loads. The resonant responses at the first eigenmode at 3–4 s due to wave loads are dominated. Furthermore, the relative velocity between the hub and blade root is important when dealing with the final connection of the blade to hub. The velocity of the hub might be large due to the high resonant frequency.

The influence of the installed blades to the first fore-aft natural frequencies is presented in Table 3. As the total mass on top of the tower increases when more blades are installed, it slightly decreases the natural frequencies of the fore-aft modes. However, for the studied 5-MW wind turbine, the influences on the natural frequencies are very small, since the blades are lightweight (17 tonnes each) compared with total mass without blade (1158.5 tonnes), which includes the nacelle (240 tonnes), the tower (347.5 tonnes) and the monopile (571 tonnes).

Since the hub displacement spectra agree well with narrow-band spectra, a second-order wave-induced motion spectrum is used to fit the spectra, with the following form:

$$S(f) = \frac{af}{f^2 + bf + c},$$

(1)

where a, b, and c are the coefficients. The derivative is

$$\frac{dS(f)}{df} = \frac{-a\left(f^2 - c\right)}{\left(f^2 + bf + c\right)^2},$$

(2)

which implies a maximum value $S(f^*) = \frac{a}{2\sqrt{c}+b}$ at $f^* = \sqrt{c}$. In Section 5.3, the time series generated by Eq. (1) are used to test the estimation performance. Moving the FFT results in Fig. 4 leftward and rightward on the x-axis, the coefficients of the fitted resulting spectra are tabulated in Table 4. The oscillation amplitude, spectrum bandwidth, and structural first fore-aft natural frequency are determined by a, b, and c, respectively.

The key observations from the simulation results are as follows:

- The displacement of the hub is limited to a range in which the GPS noise is not negligible. Therefore, sensor noise from a GPS receiver of poor quality will be a problem.

Table 2
OWT structural and environmental parameters.

Parameter	Unit	Value
Sub-structure length	m	36
Foundation length	m	30
Tower length	m	77.6
Monopile diameter	m	6
Wave spectrum type	–	JONSWAP
Water depth	m	30
Significant wave height	m	2.87
Wave period	s	6.03
Monopile mass	tonnes	571.0
Tower mass	tonnes	347.5
Nacelle mass	tonnes	240.0
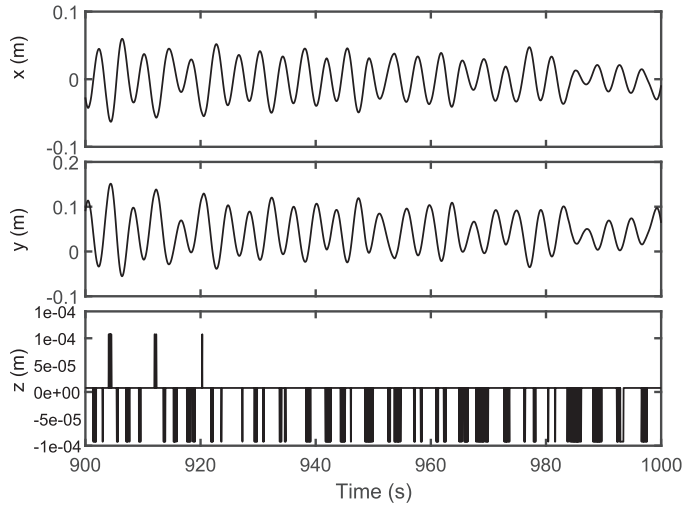
Fig. 3. The history of the hub position for the proposed OWT w.r.t. the equilibrium, $H_s = 2$ m, $T_p = 8$ s, $\beta_{wave} = 30°$, $S_{wave} = 75$, $U_w = 8$ m/s, $TI = 0.146$, and $S_{TI} = 94$.
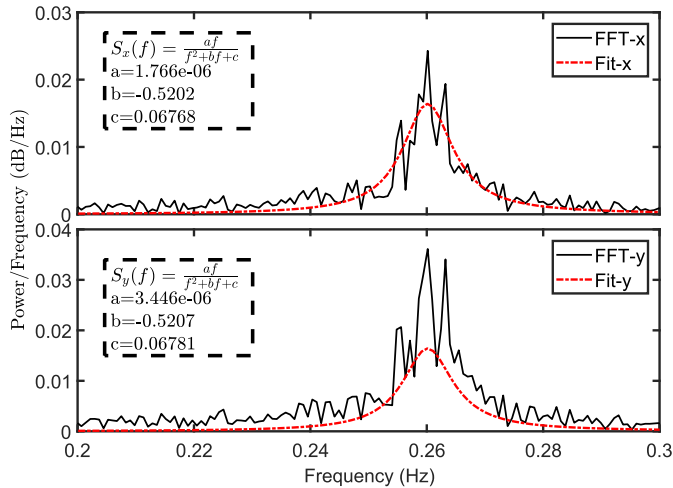
Fig. 4. The hub displacement spectra of measurement from Fig. 3 after an FFT, $H_s = 2$ m, $T_p = 8$ s, $\beta_{wave} = 30°$, $S_{wave} = 75$, $U_w = 8$ m/s, $TI = 0.146$, and $S_{TI} = 94$.

Table 3
First fore-aft natural frequencies with different number of installed blades.

Number of installed blades	First fore-aft natural frequency (Hz)
0	0.258
1	0.249
2	0.239

- It is noted that the motion in the z-axis is small; hence, only the displacement in the horizontal plane, i.e., the x- and y-directions, are of interest.
- From the eigenvalue analysis results, the first fore-aft natural period of the structure is approximately 4 s. Consequently, the monopile wave-induced motion is not a slow dynamic process. Thus, the GPS update frequency may be too slow to capture the motion well. This situation means that the intersample motion between the GPS updates must be considered.

Table 4
Coefficients that determine the fitted spectra of the hub horizontal motion at different natural periods.

Natural period (s)	a	b	c
3	1.37e−06	−0.67	0.11
4	1.83e−06	−0.50	0.062
5	2.32e−06	−0.40	0.040
6	2.81e−06	−0.33	0.028
7	3.23e−06	−0.28	0.020
8	3.67e−06	−0.25	0.016

In summary, neither a GPS nor an accelerometer is independently able to measure the OWT hub displacement adequately. The GPS noise, GPS time delay, GPS low sampling rate, accelerometer noise, and accelerometer bias are significant factors that influence the hub displacement in a real-time motion estimator.

2.3. Problem statement

The objective of this study is to develop an integrated motion estimator using sensor fusion of the GPS and IMU measurements. It should provide real-time estimates of the position, velocity, and acceleration of an oscillating OWT hub at the mating height. For a single blade installation operation, the relative distance between the hub and the blade root affects the successful mating rate, and the relative velocity influences the impact force [11]. Therefore, real-time hub position and velocity estimates with a sufficient accuracy and high sampling rate are necessary.

We assume the availability of a DGPS receiver and an IMU that are assembled as a sensor suite near the hub attachment; the sample time steps for them are T_g and T_a, respectively, with $T_g \gg T_a$. The GPS operates at a lower sampling rate with a delay τ_d. It is assumed that the time delay of the GPS signal varies as a function of the number of connected satellites, which is a known constant during a given period. Define an integer $N_d \coloneqq \frac{\tau_d}{T_a}$. The sampling interval of the GPS is assumed to be an integer multiple of the IMU sampling interval, i.e., $T_g/T_a = M$ where $M \geqslant 2$ is an integer. The IMU provides a real-time noisy and biased specific force measurement at a high sampling rate [16,18]. The IMU data are received in a sensor-fixed reference frame at a fixed location in $\{b\}$. Zero-order hold (ZOH) sampling is used to simulate the discrete measurements, i.e., each measurement remains constant until the next sampling instant. The assumptions are as follows:

1. The hub has been rotated to a fixed known yaw ψ_h and ψ_h is measured by a compass, where the wave- and wind-induced motions have a negligible influence on ψ_h.
2. The variation in rotation of the IMU about the x- and y-axes caused by the monopile motion is negligible, i.e., $\phi_h \approx 0$ and $\theta_h \approx 0$.
3. The gravity vector is assumed constant in the NED coordinates.
4. The NED frame is assumed inertial, which implies the effect of the rotation of the earth is negligible.
5. The uncertain sensor parameters, i.e., unknown sensor bias and time delay, are constant during a given short period.
6. The GPS bias is negligible.

The first fore-aft natural frequency of the hub and the first-order natural frequency of the pendulum motion of the blade are close to 0.26 Hz and 0.09 Hz, respectively. To accurately replicate both the shape and amplitude of a periodic motion, a fast sampling is essential. Hence, 10 Hz is a suitable sampling frequency. Moreover, since the diameter of the guide pins are only a few centimeters, a centimeter level accuracy positioning is necessary.

The IMU specific force measurement is transferred to $\boldsymbol{f}_{imu}$ in $\{b\}$ by a constant coordinate transformation. A simplified horizontal-plane measurement model is given by

$$\boldsymbol{f}_{imu}(t) = \boldsymbol{R}^\top (\dot{\boldsymbol{v}}(t) - \boldsymbol{g}(t)) + \boldsymbol{b}_a^b(t) + \boldsymbol{w}_a^b(t), \tag{3}$$

$$\boldsymbol{p}_{gps}(t) = \boldsymbol{p}(t - \tau_d) + \boldsymbol{v}_g(t), \tag{4}$$

where $\boldsymbol{f}_{imu}$ and $\boldsymbol{p}_{gps} \in \mathbb{R}^2$ are the specific force and position measurements from the IMU in $\{b\}$ and the GPS in $\{n\}$, respectively, $\boldsymbol{p} \in \mathbb{R}^2$ is the real GPS receiver position, $\boldsymbol{v} \in \mathbb{R}^2$ is the velocity in $\{b\}$, $\dot{\boldsymbol{v}}$ is the acceleration at the IMU mounting location, $\boldsymbol{g} \in \mathbb{R}^2$ is the acceleration caused by the gravity in $\{n\}$, $\boldsymbol{b}_a^b \in \mathbb{R}^2$ is the bias in the specific force measurements, $\boldsymbol{w}_a^b$ and $\boldsymbol{v}_g \in \mathbb{R}^2$ denote the zero-mean measurement noise from the IMU and GPS, t refers to the time, τ_d is the delayed time caused by the GPS position estimate and the data communication time, and the rotation matrix is

$$\boldsymbol{R} = \begin{bmatrix} \cos\psi_h & -\sin\psi_h \\ \sin\psi_h & \cos\psi_h \end{bmatrix}, \tag{5}$$

where ψ_h is received from compass measurements.

The motions on the top of a floating wind turbine, e.g., a floating spar, is easier to estimate, since the wave-frequency and low-frequency motions are dominate, instead of the resonant frequency of the tower vibration. Therefore, the motion estimation for a bottom-fixed wind turbine is more critical.

3. Observer design

The state estimate problem is modeled as a Wiener process. Because of Assumptions 1 and 4, the terms $\boldsymbol{R}$ and $\boldsymbol{g}$ are assumed to be known constants.

We propose a hub motion estimator that consists of a multirate Kalman filter to estimate the state trajectories with optimal filtering of the measurements, a smoothing filter for the step changes that occur due to the slower GNSS updates, and a state predictor to compensate for the delays of the GNSS and the smoothing filter. To ensure good filtering of the IMU measurements, we define the acceleration as a state driven by white noise in the process model used in the MKF, as shown in model (6). In this way, the issue of the acceleration estimate being a direct feedthrough of the IMU measurements is avoided. In the moving horizon estimator and predictor function, however, it is convenient to define the IMU acceleration measurement as an input driving the position/velocity dynamics. Accordingly, we use a reduced model with only position and velocity as states for the predictor, as shown in model (8).

3.1. Process model for the Kalman filter

One approach is to set acceleration as a state, and the estimate can output filtered acceleration. Hence, the state-space representation is then given by

$$
\begin{bmatrix} \dot{\boldsymbol{x}}_1 \\ \dot{\boldsymbol{x}}_2 \\ \dot{\boldsymbol{x}}_3 \\ \dot{\boldsymbol{x}}_4 \end{bmatrix}(t - \tau_d) = \begin{bmatrix} \boldsymbol{0} & \boldsymbol{I} & \boldsymbol{0} & \boldsymbol{0} \\ \boldsymbol{0} & \boldsymbol{0} & \boldsymbol{I} & \boldsymbol{0} \\ \boldsymbol{0} & \boldsymbol{0} & \boldsymbol{0} & \boldsymbol{0} \\ \boldsymbol{0} & \boldsymbol{0} & \boldsymbol{0} & \boldsymbol{0} \end{bmatrix} \begin{bmatrix} \boldsymbol{x}_1 \\ \boldsymbol{x}_2 \\ \boldsymbol{x}_3 \\ \boldsymbol{x}_4 \end{bmatrix}(t - \tau_d) + \begin{bmatrix} \boldsymbol{0} \\ \boldsymbol{0} \\ \boldsymbol{0} \\ \boldsymbol{I} \end{bmatrix} \boldsymbol{w}_b(t - \tau_d), \tag{6a}
$$

$$
\begin{bmatrix} \boldsymbol{p}_{gps}(t) \\ \boldsymbol{f}_{imu}(t - \tau_d) \end{bmatrix} = \begin{bmatrix} \boldsymbol{I} & \boldsymbol{0} & \boldsymbol{0} & \boldsymbol{0} \\ \boldsymbol{0} & \boldsymbol{0} & \boldsymbol{R}^\top & -\boldsymbol{R}^\top \end{bmatrix} \begin{bmatrix} \boldsymbol{x}_1 \\ \boldsymbol{x}_2 \\ \boldsymbol{x}_3 \\ \boldsymbol{x}_4 \end{bmatrix}(t - \tau_d) + \begin{bmatrix} \boldsymbol{v}_g \\ \boldsymbol{w}_a \end{bmatrix}(t), \tag{6b}
$$

where $\boldsymbol{x}_1 = [x, y]^\top$ denotes the position vector indicating the location of the sensors at the hub, $\boldsymbol{x}_2 = [v_x, v_y]^\top = \dot{\boldsymbol{x}}_1$ is the velocity vector in $\{n\}$, $\boldsymbol{x}_3 = [a_x, a_y]^\top = \dot{\boldsymbol{x}}_2$ is the acceleration vector in $\{n\}$, $\boldsymbol{x}_4 = -\boldsymbol{b}_a + \boldsymbol{g} = [b_{ax}, b_{ay}]^\top$ with $\boldsymbol{b}_a = \boldsymbol{R}\boldsymbol{b}_a^b$ refers to the combined bias and gravity vector, $\boldsymbol{w}_b \sim (0, \boldsymbol{Q}_b)$ with $\boldsymbol{Q}_b \in \mathbb{R}^{2 \times 2}$, $\boldsymbol{w}_a = \boldsymbol{R}\boldsymbol{w}_a^b \sim (0, \boldsymbol{Q}_a)$, and $\boldsymbol{v}_g \sim (0, \boldsymbol{Q}_g)$ with $\boldsymbol{Q}_g \in \mathbb{R}^{2 \times 2}$. The diagonal elements of $\boldsymbol{Q}_g \in \mathbb{R}^{2 \times 2}$ and $\boldsymbol{Q}_a \in \mathbb{R}^{2 \times 2}$ represent the covariances of the GPS noise and accelerometer noise, respectively. The vector form is

$$
\Sigma_1 : \begin{cases} \dot{\boldsymbol{x}}(t - \tau_d) = \boldsymbol{A}\boldsymbol{x}(t - \tau_d) + \boldsymbol{E}\boldsymbol{w}(t - \tau_d), & \text{(a)} \\ \boldsymbol{z} = \boldsymbol{H}\boldsymbol{x}(t - \tau_d) + \boldsymbol{v}_s(t), & \text{(b)} \end{cases} \tag{7}
$$

where $\boldsymbol{x} = [\boldsymbol{x}_1^\top, \boldsymbol{x}_2^\top, \boldsymbol{x}_3^\top, \boldsymbol{x}_4^\top]^\top \in \mathbb{R}^8$, $\boldsymbol{z}(t) = [\boldsymbol{p}_{gps}^\top(t), \boldsymbol{f}_{imu}^\top(t - \tau_d)]^\top \in \mathbb{R}^4$, $\boldsymbol{A} \in \mathbb{R}^{8 \times 8}$, $\boldsymbol{H} \in \mathbb{R}^{4 \times 8}$, and $\boldsymbol{w} = \boldsymbol{w}_b \in \mathbb{R}^2 \sim (0, \boldsymbol{Q})$ and $\boldsymbol{v}_s = [\boldsymbol{v}_g^\top, \boldsymbol{w}_a^\top]^\top \in \mathbb{R}^4 \sim (0, \Omega)$ with diagonal matrices $\boldsymbol{Q} = \boldsymbol{Q}_b$ and $\Omega = \text{diag}(\boldsymbol{Q}_g, \boldsymbol{Q}_a)$. The trends illustrated by Eq. (6) have been proven [45].

3.2. Process model for the predictor and MHE

Another approach is to let the acceleration be an input that drives the position/velocity dynamics. The aim of this model is to design the MHE. Similar to Σ_1, the model is then given by

$$
\begin{bmatrix} \dot{\boldsymbol{x}}_1 \\ \dot{\boldsymbol{x}}_2 \\ \dot{\boldsymbol{x}}_4 \end{bmatrix}(t - \tau_d) = \begin{bmatrix} \boldsymbol{0} & \boldsymbol{I} & \boldsymbol{0} \\ \boldsymbol{0} & \boldsymbol{0} & \boldsymbol{I} \\ \boldsymbol{0} & \boldsymbol{0} & \boldsymbol{0} \end{bmatrix} \begin{bmatrix} \boldsymbol{x}_1 \\ \boldsymbol{x}_2 \\ \boldsymbol{x}_4 \end{bmatrix}(t - \tau_d) + \begin{bmatrix} \boldsymbol{0} \\ \boldsymbol{I} \\ \boldsymbol{0} \end{bmatrix} \boldsymbol{R}\boldsymbol{f}_{imu}(t - \tau_d) + \begin{bmatrix} \boldsymbol{0} & \boldsymbol{0} \\ \boldsymbol{I} & \boldsymbol{0} \\ \boldsymbol{0} & \boldsymbol{I} \end{bmatrix} \begin{bmatrix} \boldsymbol{w}_a \\ \boldsymbol{w}_b \end{bmatrix}(t - \tau_d), \tag{8a}
$$

$$
\boldsymbol{z}(t) = \begin{bmatrix} \boldsymbol{I} & \boldsymbol{0} & \boldsymbol{0} \end{bmatrix} \begin{bmatrix} \boldsymbol{x}_1 \\ \boldsymbol{x}_2 \\ \boldsymbol{x}_4 \end{bmatrix}(t - \tau_d) + \boldsymbol{v}_g(t), \tag{8b}
$$

where $\boldsymbol{x}_1 = [x, y]^\top$, $\boldsymbol{x}_2 = [v_x, v_y]^\top = \dot{\boldsymbol{x}}_1$, $\boldsymbol{x}_4 = -\boldsymbol{b}_a + \boldsymbol{R}\boldsymbol{g} = [b_{ax}, b_{ay}]^\top$, and $\boldsymbol{z}(t) = \boldsymbol{p}_{gps}(t)$. The vector form is

$$
\Sigma_2 : \begin{cases} \dot{\boldsymbol{x}}(t - \tau_d) = \boldsymbol{A}\boldsymbol{x}(t - \tau_d) + \boldsymbol{B}\boldsymbol{u}(t - \tau_d) + \boldsymbol{E}\boldsymbol{w}(t - \tau_d), & \text{(a)} \\ \boldsymbol{z}(t) = \boldsymbol{H}\boldsymbol{x}(t - \tau_d) + \boldsymbol{v}_s(t), & \text{(b)} \end{cases} \tag{9}
$$

where $\quad \boldsymbol{x} = \left[\boldsymbol{x}_1^\top, \boldsymbol{x}_2^\top, \boldsymbol{x}_3^\top\right]^\top \in \mathbb{R}^6, \quad \boldsymbol{u} = \boldsymbol{R}\boldsymbol{f}_{imu} \in \mathbb{R}^2, \quad \boldsymbol{A} \in \mathbb{R}^{6\times6}, \quad \boldsymbol{B} \in \mathbb{R}^{6\times2}, \quad \boldsymbol{H} \in \mathbb{R}^{2\times6}, \quad \boldsymbol{w} = \left[\boldsymbol{w}_a^\top, \boldsymbol{w}_b^\top\right]^\top \in \mathbb{R}^4 \sim (0, \boldsymbol{Q})$ with $\boldsymbol{Q} = \text{diag}(\boldsymbol{Q}_a, \boldsymbol{Q}_b)$, and $\boldsymbol{v}_s = \boldsymbol{v}_g \in \mathbb{R}^2 \sim (0, \Omega)$ with $\Omega = \boldsymbol{Q}_g$.

3.3. Discrete system

Using a shift register to receive $\boldsymbol{f}_{imu}(t)$, the effects of time delay are canceled. Discretizing the continuous system (7) or (9) and ignoring the system disturbance and measurement noise yields

$$\boldsymbol{x}_{k+1}(k - N_d) = \begin{cases} \boldsymbol{A}_d\boldsymbol{x}_k(k - N_d) & (\Sigma_1) \\ \boldsymbol{A}_d\boldsymbol{x}_k(k - N_d) + \boldsymbol{B}_d\boldsymbol{u}(k - N_d) & (\Sigma_2) \end{cases}, \tag{10a}$$

$$\boldsymbol{z}_k(k - N_d) = \boldsymbol{H}\boldsymbol{x}_k(k - N_d), \tag{10b}$$

where the subscript k denotes the time instance $t_k = kT_s$, where T_s is the sampling interval. In this paper, $T_s = T_a$. The discrete matrices are

$$\boldsymbol{A}_d = e^{\boldsymbol{A}T_a} = \begin{cases} \boldsymbol{I}_{8\times8} + \boldsymbol{A}T_a, & (\Sigma_1) \\ \boldsymbol{I}_{6\times6} + \boldsymbol{A}T_a, & (\Sigma_2) \end{cases} \tag{10c}$$

$$\boldsymbol{B}_d = T_a\boldsymbol{B} + \frac{T_a^2}{2}\boldsymbol{A}\boldsymbol{B}, \tag{10d}$$

$$\boldsymbol{Q}_d = \int_0^{T_a} e^{\boldsymbol{A}\tau}\boldsymbol{Q}e^{\boldsymbol{A}^\top\tau}d\tau = \boldsymbol{Q}T_a + \boldsymbol{Q}\boldsymbol{A}T_a^2 + \boldsymbol{A}\boldsymbol{Q}\boldsymbol{A}^\top\frac{T_a^3}{3}, \tag{10e}$$

$$\Omega_d = \Omega/T_a. \tag{10f}$$

4. State estimation and prediction algorithms

A state estimation algorithm that compensates the GNSS delay and provides real-time monitoring of the hub position, velocity, and acceleration is required. We propose two algorithms in this section. The hub motion estimator 1 (HME1) has a low complexity because it does not include a moving horizon estimator and a nonlinear program solver. Based on HME1, the hub motion estimator 2 (HME2) is developed to improve the prediction performance for the system with longer natural period by introducing an MHE.

4.1. Algorithm 1 – HME1

The workflow diagram is presented in Fig. 6, and its steps are tabulated in Algorithm 1. Only Σ_1 in (7) is necessary, and the observer runs at a high frequency with an interval T_a. For every time step, the shift register #1 stores the real-time IMU specific force measurement. The MKF estimates the states, based on the delayed GPS measurement and the delayed acceleration measurement. In a GPS sampling interval, the position measurements inputs to the MKF once. Shift register #4 stores the data $\hat{\boldsymbol{x}}(t - \tau_d)$ and the covariance matrices. Then the stored data are supplied to the online smoother. The online Rauch, Tung, and Striebel (RTS) smoother conducts backward smoothing [46]. The additional delay caused by the smoother is τ_s so
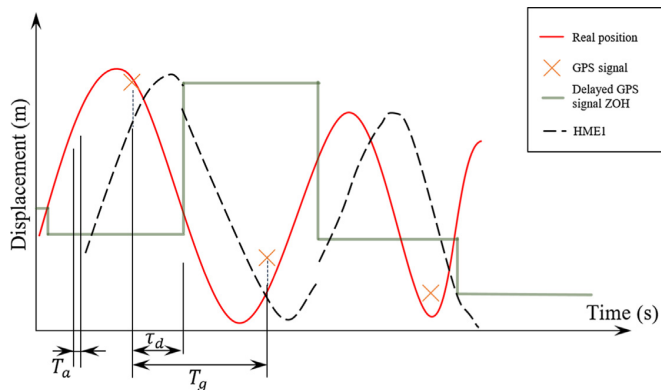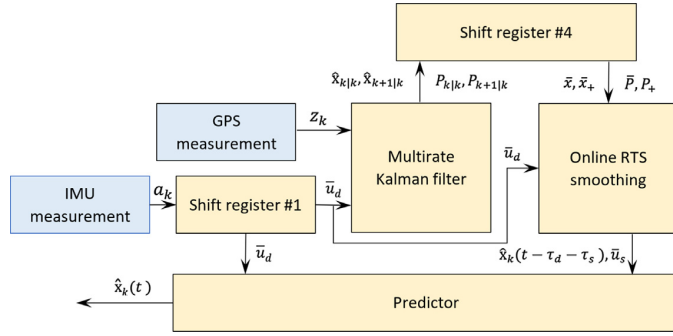

Fig. 5. Sketch of how the HME1 works.

Fig. 6. Workflow diagram of the proposed algorithm (HME1).

that the estimate becomes $\hat{\boldsymbol{x}}(t - \tau_d - \tau_s)$. A predictor is used to bring forward the estimates to the present time t. Then, the process moves on to the next step, and the above procedures are repeated. See Algorithm 1.

Algorithm 1 HME1.

    Monopile hub position estimation$(\boldsymbol{z}_k, \boldsymbol{a}_k, t, T_g, N_d, N_s)$
    Initialize: $\bar{\boldsymbol{u}}_d = \boldsymbol{0}_{2 \times N_d}, \bar{\boldsymbol{u}}_s = \boldsymbol{0}_{2 \times N_s}, \bar{\boldsymbol{x}} = \boldsymbol{0}_{9 \times N_s}, \bar{\boldsymbol{x}}_+ = \boldsymbol{0}_{9 \times N_s}, \overline{\boldsymbol{P}} = \boldsymbol{0}_{9 \times 9 \times N_s}, \overline{\boldsymbol{P}}_+ = \boldsymbol{0}_{9 \times 9 \times N_s}$
1: **while** k **do**
2:    $\bar{\boldsymbol{u}}_d$ = Shift register #1$(\boldsymbol{a}_k)$
3:    $\left[\hat{\boldsymbol{x}}_{k|k}, \boldsymbol{P}_{k|k}, \hat{\boldsymbol{x}}_{k+1|k}, \boldsymbol{P}_{k+1|k}\right]$ = Multirate Kalman filter $(\boldsymbol{z}_k, \bar{\boldsymbol{u}}_d, t, T_g)$
4:    $\left[\bar{\boldsymbol{x}}, \overline{\boldsymbol{P}}, \bar{\boldsymbol{x}}_+, \overline{\boldsymbol{P}}_+\right]$ = Shift register #2$(\hat{\boldsymbol{x}}_{k|k}, \boldsymbol{P}_{k|k}, \hat{\boldsymbol{x}}_{k+1|k}, \boldsymbol{P}_{k+1|k})$
5:    $[\hat{\boldsymbol{x}}_k(t - \tau_d - \tau_s), \bar{\boldsymbol{u}}_s]$ = Online RTS smoothing $(\bar{\boldsymbol{x}}, \overline{\boldsymbol{P}}, \bar{\boldsymbol{x}}_+, \overline{\boldsymbol{P}}_+, \bar{\boldsymbol{u}}_d)$
6:    $\hat{\boldsymbol{x}}_k(t)$ = Predictor$(\hat{\boldsymbol{x}}_k(t - \tau_d - \tau_s), \bar{\boldsymbol{u}}_d, \bar{\boldsymbol{u}}_s, N_d, N_s)$
7:    $k = k + 1$
8: **end while**
    return $\hat{\boldsymbol{x}}_k(t)$

4.2. Algorithm 2 – HME2

Based on the periodic motion of the hub, it is possible to predict the hub motion at a time instant in the near future based on past observations. Moreover, the predictor in HME1 is a simple deterministic open-loop simulation that does not take into account the stochastic properties of the measurements. Hence, to further improve the estimation performance, a more optimal HME2 is proposed. The differences between HME1 and HME2 are illustrated in Fig. 7. In Algorithm 2, we introduce an MHE. This gives optimal predictions to the states during the gap between two GPS updates, i.e., the MHE resamples the GPS
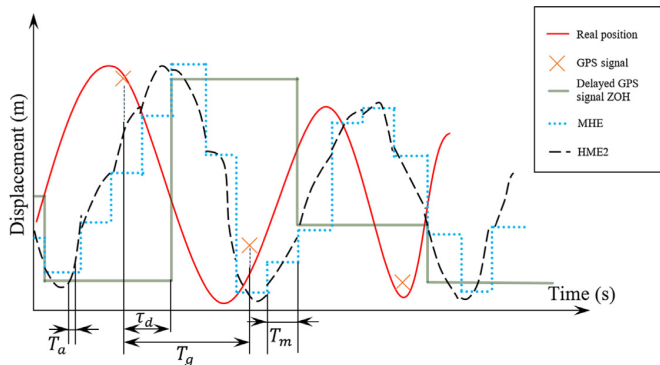

Fig. 7. Sketch of how the HME2 works with MHE.

sampling interval with a number of optimal position predictions according to past measurements and the process model Σ_2. This approach is equivalent to increasing the position sampling rate. Consequently, the MKF position estimation is corrected at a higher frequency, which helps overcome large drifts accumulated during a GPS sampling interval.

It is noted that the fidelity of the predictions, according to the discrete GPS signal sequences, depends on the first fore-aft natural frequency of the hub. Similar to the aliasing effect, limited GPS sampling points from the continuous narrow-band hub position history implies lost information regarding the dynamics and a less accurate prediction. Therefore, HME2 is more suitable for oscillations with a longer natural period.

The workflow diagram and process are presented in Fig. 8 and Algorithm 2. The calculation interval of the MHE solver is T_m, i.e., $T_a < T_m < T_g$. Shift register #2 updates every T_g and outputs stored data with delayed IMU specific force and GPS measurements every T_m. Together with the initial value provided by shift register #3, $\boldsymbol{x}_{m0,k}$, the MHE solver calculates the delayed states $\boldsymbol{x}_m(t - \tau_d)$ using nonlinear programming. The yellow blocks (multirate Kalman filter, smoother, and predictor) remain the same as those used in HME1 by taking the position $\hat{\boldsymbol{z}}_k$ from $\boldsymbol{x}_m(t - \tau_d)$, instead of taking $\boldsymbol{z}_k$ directly from the GPS measurements.

Algorithm 2 HME2.

  Monopile hub position estimation$(\boldsymbol{z}_k, \boldsymbol{a}_k, t, T_g, T_m, N_d, N_s, N_m)$
  Initialize: $\bar{\boldsymbol{u}}_d = \boldsymbol{0}_{2 \times N_d}, \bar{\boldsymbol{u}}_s = \boldsymbol{0}_{2 \times N_s}, \bar{\boldsymbol{x}}_m = \boldsymbol{0}_{2 \times N_m}, \bar{\boldsymbol{x}} = \boldsymbol{0}_{9 \times N_s}, \bar{\boldsymbol{x}}_+ = \boldsymbol{0}_{9 \times N_s}, \overline{\boldsymbol{P}} = \boldsymbol{0}_{9 \times 9 \times N_s}, \overline{\boldsymbol{P}}_+ = \boldsymbol{0}_{9 \times 9 \times N_s}$
 1: **while** k **do**
 2:   $\bar{\boldsymbol{u}}_d$ = Shift register #1$(\boldsymbol{a}_k)$
 3:   $[\bar{\boldsymbol{u}}_k, \bar{\boldsymbol{z}}_k]$ = Shift register #2$(\bar{\boldsymbol{u}}_d, \boldsymbol{z}_k)$
 4:   $\boldsymbol{x}_{m0,k}$ = Shift register #3$(\boldsymbol{x}_{k|k})$
 5:   $\hat{\boldsymbol{z}}_k$ = Moving horizon estimator$(\bar{\boldsymbol{u}}_k, \bar{\boldsymbol{z}}_k, \boldsymbol{x}_{m0,k})$
 6:   $[\hat{\boldsymbol{x}}_{k|k}, \boldsymbol{P}_{k|k}, \hat{\boldsymbol{x}}_{k+1|k}, \boldsymbol{P}_{k+1|k}]$ = Multirate Kalman filter $(\hat{\boldsymbol{z}}_k, \bar{\boldsymbol{u}}_d, t, T_m)$
 7:   $[\bar{\boldsymbol{x}}, \overline{\boldsymbol{P}}, \bar{\boldsymbol{x}}_+, \overline{\boldsymbol{P}}_+]$ = Shift register #4$(\hat{\boldsymbol{x}}_{k|k}, \boldsymbol{P}_{k|k}, \hat{\boldsymbol{x}}_{k+1|k}, \boldsymbol{P}_{k+1|k})$
 8:   $[\hat{\boldsymbol{x}}_k(t - \tau_d - \tau_s), \bar{\boldsymbol{u}}_s]$ = Online RTS smoothing$(\bar{\boldsymbol{x}}, \overline{\boldsymbol{P}}, \bar{\boldsymbol{x}}_+, \overline{\boldsymbol{P}}_+, \bar{\boldsymbol{u}}_d)$
 9:   $\hat{\boldsymbol{x}}_k(t)$ = Predictor$(\hat{\boldsymbol{x}}_k(t - \tau_d - \tau_s), \bar{\boldsymbol{u}}_d, \bar{\boldsymbol{u}}_s, N_d, N_s)$
 10:     $k = k + 1$
 11: **end while**
    return $\hat{\boldsymbol{x}}_k(t)$

4.3. Implementation

4.3.1. Delayed IMU measurement and stored signals

To input the delayed IMU measurement, Algorithm 3 is applied to shift the measurement N_d steps. Furthermore, the IMU specific force measurement during the delay is stored and input to the predictor in Algorithm 9.
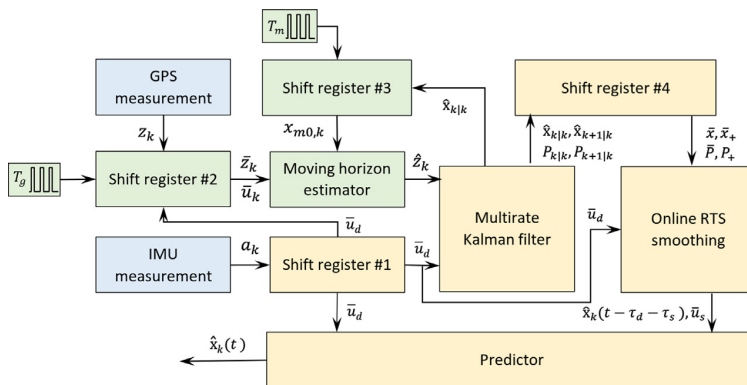

Fig. 8. Workflow diagram of the proposed algorithm with moving horizon estimator (HME2).

Algorithm 3 Shift register #1.

Shift register #1($\boldsymbol{a}_k$)
1: $\bar{\boldsymbol{u}}_d = [\boldsymbol{u}_d(:, 2 : N_d), \boldsymbol{a}_k]$
   return $\bar{\boldsymbol{u}}_d$

4.3.2. Moving horizon estimator

The GPS and IMU do not sample synchronously. The aim of the MHE is to fill the gap between two subsequent GPS updates with reasonable state predictions. For a discrete dynamics model Σ_2, the current state ($\boldsymbol{x}_k$) depends on the sequence of past inputs $\boldsymbol{U}_k = \text{col}(\boldsymbol{u}_{k-N} \cdots \boldsymbol{u}_{k-N})$ and its initial value $\boldsymbol{x}_{k-N}$. The measurement $\boldsymbol{z}_k$ is a mapping of the states $\boldsymbol{x}_k$. Therefore, the states $\boldsymbol{X}_k = \text{col}(\boldsymbol{x}_{k-N} \cdots \boldsymbol{x}_{k-N})$ are estimated with a sequence of measurements $\boldsymbol{Z}_k = \text{col}(\boldsymbol{z}_{k-N} \cdots \boldsymbol{z}_{k-N})$ by minimizing the error of the measurement error and the disturbance. The states at the last step can be treated as filtered signals. Then, the position estimation from the MHE inputs to the MKF. First, two shift registers are required to provide the historic measurements and inputs, as well as the initial value for the MHE solver; see Algorithms 4 and 5.

Algorithm 4 Shift register #2.

Shift register #2($\bar{\boldsymbol{u}}_d, z_k$)
1: $\boldsymbol{u}_k = \bar{\boldsymbol{u}}_d(:, 1)$
2: $\bar{\boldsymbol{u}}_k = [\boldsymbol{u}_d(:, 2 : N_d), \boldsymbol{u}_k]$
3: $\bar{\boldsymbol{z}}_k = [\boldsymbol{u}_d(:, 2 : N_d), \boldsymbol{z}_k]$
   return $\bar{\boldsymbol{u}}_k, \bar{\boldsymbol{z}}_k$

Algorithm 5 Shift register #3.

Shift register #3($\boldsymbol{x}_{k|k}$)
1: $\bar{\boldsymbol{x}}_m = [\boldsymbol{u}_m(:, 2 : N_m), \boldsymbol{x}_{k|k}]$
2: $\boldsymbol{x}_{m0,k} = \bar{\boldsymbol{x}}_m(:, 1)$
   return $\boldsymbol{x}_{m0,k}$

$\boldsymbol{Z}$ and $\boldsymbol{U}$ update every T_g, and the MHE solves the nonlinear program with an interval T_m. At all steps except the MHE updating time, i.e., $\text{rem}(t, T_m) = 0$, the MHE should predict the current state based on past measurements and inputs. The cost function is given by

$$\min_{S,Q} \sum_{i=k-N_m+1}^{k-1} \|\boldsymbol{w}_i\|_{\mathcal{Q}} + \sum_{i=k-N_m}^{k-1} + \|\boldsymbol{v}_i\|_{\mathcal{R}} + \|\boldsymbol{v}_k\|_{\mathcal{R}_f}, \tag{11a}$$

$$\text{s.t.} \boldsymbol{w}_i = \boldsymbol{x}_{i+1} - (\boldsymbol{A}_d \boldsymbol{x}_i + \boldsymbol{B}_d \boldsymbol{u}_i), \qquad i = k - N_m + 1, \cdots, k - 1, \tag{11b}$$

$$\boldsymbol{v}_i = \boldsymbol{z}_i - \boldsymbol{C}_d \boldsymbol{x}_i, \qquad i = k - N_m, \cdots, k - 1, \tag{11c}$$

$$\boldsymbol{w}_k = \boldsymbol{x}_k - (\boldsymbol{A}_{df} \boldsymbol{x}_{k-1} + \boldsymbol{B}_{df} \boldsymbol{u}_{k-1}), \tag{11d}$$

$$\boldsymbol{v}_k = \boldsymbol{z}_k - \boldsymbol{C}_d \boldsymbol{x}_k, \tag{11e}$$

$$t_f = T_g + \text{rem}(t, T_g) \tag{11f}$$

$$\boldsymbol{A}_{df} = \boldsymbol{I}_{6\times6} + t_f \boldsymbol{A}, \tag{11g}$$

$$\boldsymbol{B}_{df} = t_f \boldsymbol{B} + t_f^2/2 \boldsymbol{AB}, \tag{11h}$$

$$\mathcal{R}_f = \begin{cases} \mathcal{R} > 0, & \text{if } t_f = 0, \\ \boldsymbol{0}, & \text{otherwise}, \end{cases} \tag{11i}$$

where $\text{rem}(a, b)$ is the remainder after division of a by b, $\mathcal{Q}$ and $\mathcal{R}$ are positive-definite diagonal weighting matrices, and the weighted Euclidean norm is expressed as $\|\boldsymbol{w}_i\|_Q^2 = \boldsymbol{w}_i^\top \mathcal{Q} \boldsymbol{w}_i$.

4.3.3. Multirate Kalman filter

A Kalman filter is used to filter the noisy measurements in the state equation Σ_1. Because the sampling frequency in the GPS and the IMU are different, the MKF is modified from the classic Kalman filter, as illustrated in Fig. 5. The MKF works at the same frequency as the IMU. When the GPS signal is available, i.e., at $t/T_g =$ integer steps, the GPS signal corrects the estimate. Otherwise, at a moment when the GPS measurement is not available, i.e., at $t/T_g \neq$ integer, the part of the Kalman gain matrix $\boldsymbol{K}$ according to the position measurements is set to zero, and the estimate is updated with merely the acceleration measurements as a state in Eq. (7) or as an input in Eq. (9). The error grows until it is corrected at the next GPS update. The summarized algorithm is tabulated in Algorithm 6. At this stage, the MKF calculates the delayed estimate $t - \tau_d$.

Algorithm 6 Multirate Kalman filter.

Multirate Kalman filter$(\hat{\boldsymbol{z}}_k, \bar{\boldsymbol{u}}_d, t, T)$
1: **Initialize:** $\hat{\boldsymbol{x}}_{0|0}, \boldsymbol{P}_{0|0} = \boldsymbol{I}_{6\times 6}$
2: $\boldsymbol{u}_k = \bar{\boldsymbol{u}}_d(:, 1)$
3: $\hat{\boldsymbol{x}}_{k+1|k} = \boldsymbol{A}_d\hat{\boldsymbol{x}}_{k|k} + \boldsymbol{B}_d\boldsymbol{u}_k$
4: $\boldsymbol{P}_{k+1|k} = \boldsymbol{A}_d\boldsymbol{P}_{k|k}\boldsymbol{A}_d^{\top} + \boldsymbol{Q}_d$
5: $\boldsymbol{K}(k+1) = \boldsymbol{P}_{k+1|k}\boldsymbol{H}^{\top}\left[\boldsymbol{H}\boldsymbol{P}_{k+1|k}\boldsymbol{H}^{\top} + \Omega_d\right]^{-1}$
6: **if** $t/T \neq$ integer **then**
7:     $K(1:2, :) = \boldsymbol{0}_{2\times 4}$
8: **end if**
9: $\hat{\boldsymbol{x}}_{k+1|k+1} = \hat{\boldsymbol{x}}_{k+1|k} + \boldsymbol{K}(k+1)\left[\hat{\boldsymbol{z}}_{k+1} - \boldsymbol{H}\hat{\boldsymbol{x}}_{k+1|k}\right]$
10: $\boldsymbol{P}_{k+1|k+1} = (\boldsymbol{I} - \boldsymbol{K}_k\boldsymbol{H}_k)\boldsymbol{P}_{k+1|k}$
    return $\hat{\boldsymbol{x}}_{k|k}, \boldsymbol{P}_{k|k}, \hat{\boldsymbol{x}}_{k+1|k}, \boldsymbol{P}_{k+1|k}$,

---

4.3.4. Smoothing

The MKF leads to discontinuous points when $t/T_g =$ integer. Therefore, smoothing is conducted to smooth the estimate along the time history. There are three categories of smoothing: fixed-interval smoothing, fixed-point smoothing, and fixed-lag smoothing.

A widely used offline fixed-interval smoothing method is the RTS smoother, also referred to as the two-pass smoother [46]. A forward pass is the Kalman filter, which computes the filtered quantities, $\hat{\boldsymbol{x}}_{k|k}, \boldsymbol{P}_{k|k}, \hat{\boldsymbol{x}}_{k+1|k}, \boldsymbol{P}_{k+1|k}$, and stores them in the memory. The backward pass smooths the estimate. However, the RTS smoother is an offline algorithm that process the stored estimate data from the Kalman filter. At the end of an estimation on a given dataset, the RTS smoother normally runs once. For a real-time application, however, the algorithm is insufficient. Thus, to ensure an online application, a window function is employed to accomplish the backward pass for each step, where N_s is the length of the moving window. The procedure is summarized in Algorithm 7 and 8. Due to the additional phase shift of the online smoothing, the estimate is now further delayed by $t - \tau_d - \tau_s$.

Algorithm 7 Shift register #4.

Shift register#4 $\left(\hat{\boldsymbol{x}}_{k|k}, \boldsymbol{P}_{k|k}, \hat{\boldsymbol{x}}_{k+1|k}, \boldsymbol{P}_{k+1|k}\right)$
1: $\bar{\boldsymbol{x}} = \left[\bar{\boldsymbol{x}}_{k|k}(:, 2:N_s), \hat{\boldsymbol{x}}_{k|k}\right]$
2: $\overline{\boldsymbol{P}} = \left[\overline{\boldsymbol{P}}_{k|k}(:, :, 2:N_s), \boldsymbol{P}_{k|k}\right]$
3: $\bar{\boldsymbol{x}}_+ = \left[\bar{\boldsymbol{x}}_{k+1|k}(:, 2:N_s), \hat{\boldsymbol{x}}_{k+1|k}\right]$
4: $\overline{\boldsymbol{P}}_+ = \left[\overline{\boldsymbol{P}}_{k+1|k}(:, :, 2:N_s), \boldsymbol{P}_{k+1|k}\right]$
    return $\bar{\boldsymbol{x}}, \overline{\boldsymbol{P}}, \bar{\boldsymbol{x}}_+, \overline{\boldsymbol{P}}_+$

Table 5
Sensor parameters in the simulations.

Parameter	Value	Unit
GPS accuracy	±0.03	m
GPS sampling rate	1	Hz
GPS delay	0.2	s
Accelerometer accuracy	±0.15	m/s^2
Accelerometer sampling rate	100	Hz

Algorithm 8 Online RTS smoothing

Online RTS smoothing $(\bar{\pmb{x}}, \bar{\pmb{P}}, \bar{\pmb{x}}_+, \bar{\pmb{P}}_+, \pmb{u}_k)$

Initialize: $\hat{\pmb{x}}_{N_s|N_s} = \bar{\pmb{x}}(:, N_s)$, $\pmb{P}_{N_s|N_s} = \bar{\pmb{x}}(:,:, N_s)$

1: $\bar{\pmb{u}}_s = [\bar{\pmb{u}}_s(:, 2 : N_s), \bar{\pmb{u}}_d(:, 1)]$
2: **if** $k \leqslant N_s$ **then**
3:    $\hat{\pmb{x}}_k = \bar{\pmb{x}}(:, 1)$
4: **else**
5:    **for** $j = N_s - 1 : -1 : 0$ **do**
6:        $\hat{\pmb{x}}_{j|j} = \bar{\pmb{x}}(:, j)$, $\hat{\pmb{x}}_{j+1|j} = \bar{\pmb{x}}_+(:, j)$, $\pmb{P}_{j|j} = \bar{\pmb{P}}(:,:, j)$, $\pmb{P}_{j+1|j} = \bar{\pmb{P}}_+(:,:, j)$
7:        $\pmb{A}(j) = \pmb{P}_{j|j}\pmb{A}_d^\top \pmb{P}_{j+1|j}^{-1}$
8:        $\hat{\pmb{x}}_{j|N_s} = \hat{\pmb{x}}_{j|j} + \pmb{A}(j)\left[\hat{\pmb{x}}_{j+1|N_s} - \hat{\pmb{x}}_{j+1|k}\right]$
9:        $\pmb{P}_{j|N_s} = P_{k|k} + \pmb{A}(k)\left[\pmb{P}_{k+1|N_s} - \pmb{P}_{k+1|k}\right]\pmb{A}^\top(k)$
10:   **end for**
11:   $\hat{\pmb{x}}_k(t - \tau_d - \tau_s) = \hat{\pmb{x}}_{0|N_s}$
12: **end if**
    return $\hat{\pmb{x}}_k(t - \tau_d - \tau_s), \bar{\pmb{u}}_s$

4.3.5. Predictor

To move the estimated states forward to the present time t, a predictor is proposed. The time delay $\tau_d + \tau_s$ is still small; thus, the integration drift caused by the accelerometer bias is not significant until the next GPS correction. During the time delay, all acceleration inputs to Eq. (10a) are known. Therefore, the present estimate is achieved by updating Eq. (10a) for $N_d + N_s$ steps with the input vectors $\bar{\pmb{u}}_d$ and $\bar{\pmb{u}}_s$. The process is illustrated in Algorithm 9.

Algorithm 9 Predictor

Online RTS smoothing$(\hat{\pmb{x}}_k(t - \tau_d - \tau_s), \bar{\pmb{u}}_d, \bar{\pmb{u}}_s, N_d, N_s)$
1: **for** $i = 1 : N_d - 1$ **do**
2:    $\hat{\pmb{x}}_k = \pmb{A}_d\hat{\pmb{x}}_k + \pmb{B}_d\bar{\pmb{u}}_d(:, i)$
3: **end for**
4: **for** $i = 1 : N_s$ **do**
5:    $\hat{\pmb{x}}_k = \pmb{A}_d\hat{\pmb{x}}_k + \pmb{B}_d\bar{\pmb{u}}_s(:, i)$
6: **end for**
    return $\hat{\pmb{x}}_k(t)$

---

5. Verification of the proposed algorithms

5.1. Simulation overview

The simulation is conducted with HAWC2 and MATLAB [47]. The model mentioned in Section 2.2 is adopted in the following simulations. The monopile is exposed to irregular waves and a turbulent wind field. The environmental parameters are listed in Table 2. HAWC2 outputs high-frequency position, velocity, and acceleration at the hub, which are considered as the real values in the simulations. After adding zero-mean white noise processes and a slow-varying bias, and resampling with specific sample rates with delays, the resulting position and acceleration signals are used as measurements from GNSS and IMU. The important sensor parameters are listed in Table 5. The time step T_a is selected as 10 ms. The biases on the IMU specific force measurements are simulated as Wiener processes.

To evaluate of the performance of the state estimator, the mean square error (MSE) is introduced as criterion as follows:

$$MSE := \frac{1}{N}\sum_{k=1}^{N}(x_k - \hat{x}_k)^2, \tag{11j}$$

where N is the total number of steps used in the estimate.

5.2. Simulation results

The simulation results are presented in Figs. 9–14. The double integration of the acceleration measurement drifts off significantly due to the IMU bias, as expected. The performance of HME1 and HME2 are similar. Both HME1 and HME2 provide a
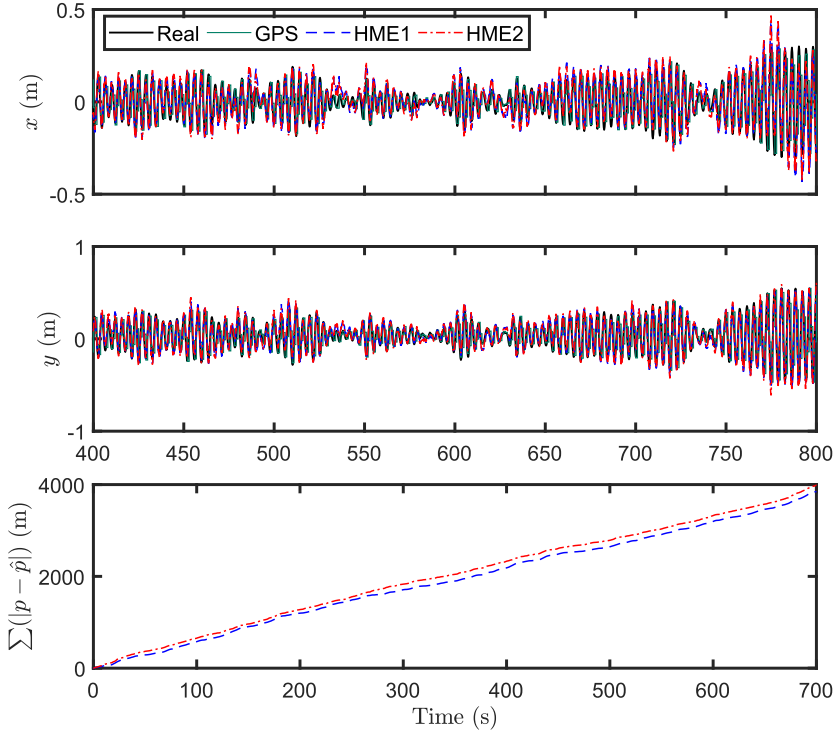

Fig. 9. Position estimate, $H_s = 2$ m, $T_p = 6$ s, $\beta_{wave} = 30°$, $S_{wave} = 10$, $U_w = 8$ m/s, $TI = 0.146$, and $S_{TI} = 596$.
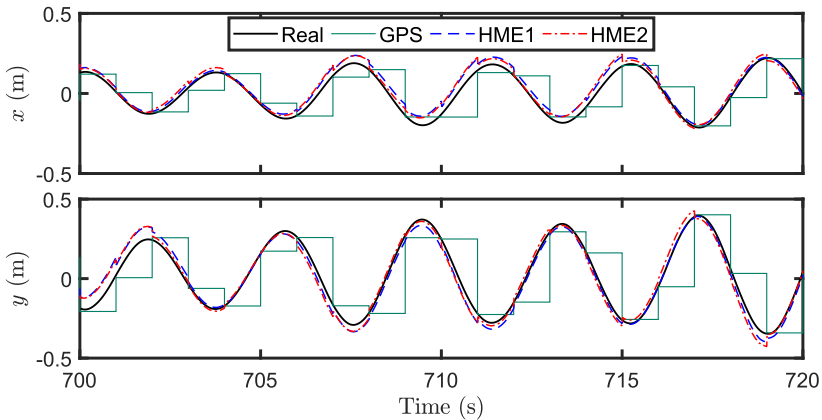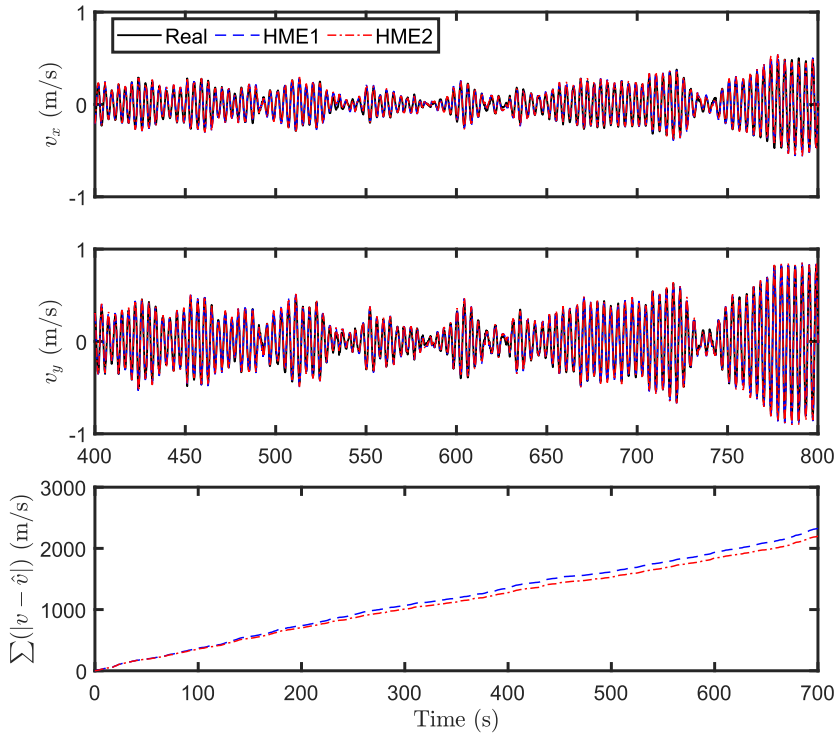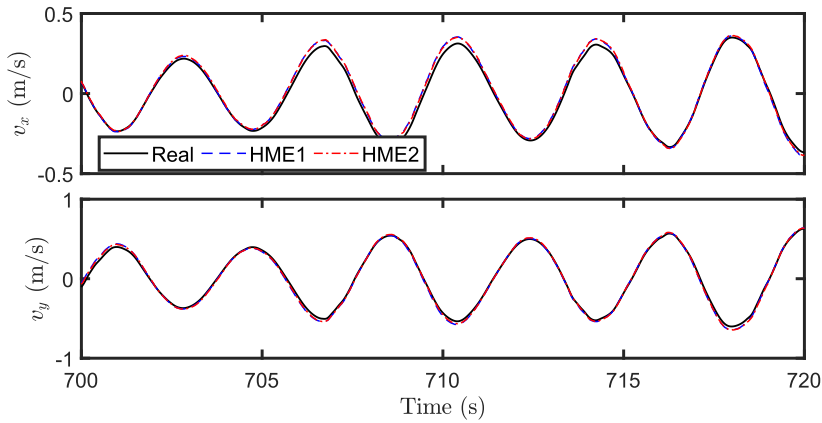

Fig. 10. Position estimate, zoomed in, $H_s = 2$ m, $T_p = 6$ s, $\beta_{wave} = 30°$, $S_{wave} = 10$, $U_w = 8$ m/s, $TI = 0.146$, and $S_{TI} = 596$.

Fig. 11. Velocity estimate, $H_s = 2$ m, $T_p = 6$ s, $\beta_{wave} = 30°$, $S_{wave} = 10$, $U_w = 8$ m/s, $TI = 0.146$, and $S_{TI} = 596$.

Fig. 12. Velocity estimate, zoomed in, $H_s = 2$ m, $T_p = 6$ s, $\beta_{wave} = 30°$, $S_{wave} = 10$, $U_w = 8$ m/s, $TI = 0.146$, and $S_{TI} = 596$.

high-frequency real-time motion estimation. Although the GPS sampling rate of 1 Hz is quite low, the MKF accurately esti-mates the position and velocity of the hub, including the sensor bias. The MKF suppresses the GPS measurement noise, and the estimate approaches the real state. The online smoother smooths the trajectory in the case of sudden changes which may cause high derivatives. The predictor corrects the delay between the smoothed estimate and the real values. The proposed GNSS/IMU integration scheme greatly improves the GPS measurement in terms of both the accuracy and sampling rate. As
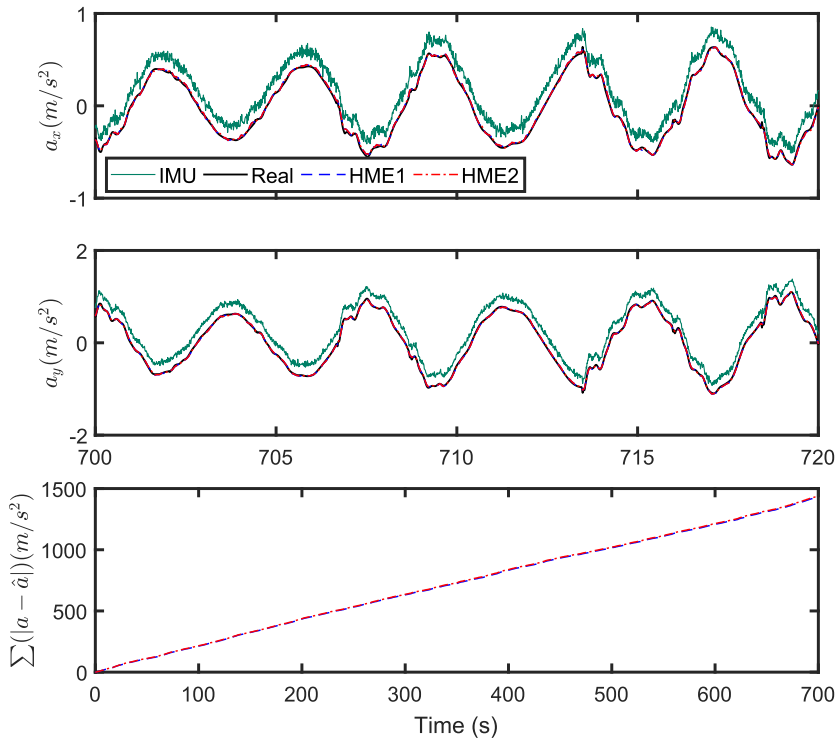
Fig. 13. Acceleration estimate, $H_s = 2$ m, $T_p = 6$ s, $\beta_{wave} = 30°$, $TI = 0.146$, $S_{wave} = 10$, $U_w = 8$ m/s, and $S_{TI} = 596$.
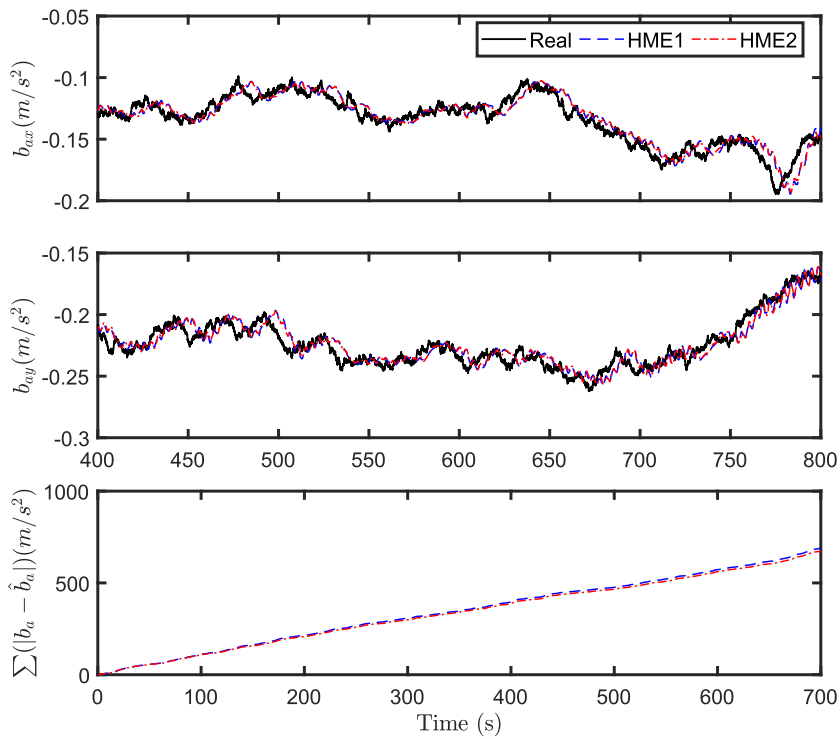

Fig. 14. Accelerometer bias estimate, $H_s = 2$ m, $T_p = 6$ s, $\beta_{wave} = 30°$, $TI = 0.146$, $S_{wave} = 10$, $U_w = 8$ m/s, and $S_{TI} = 596$.
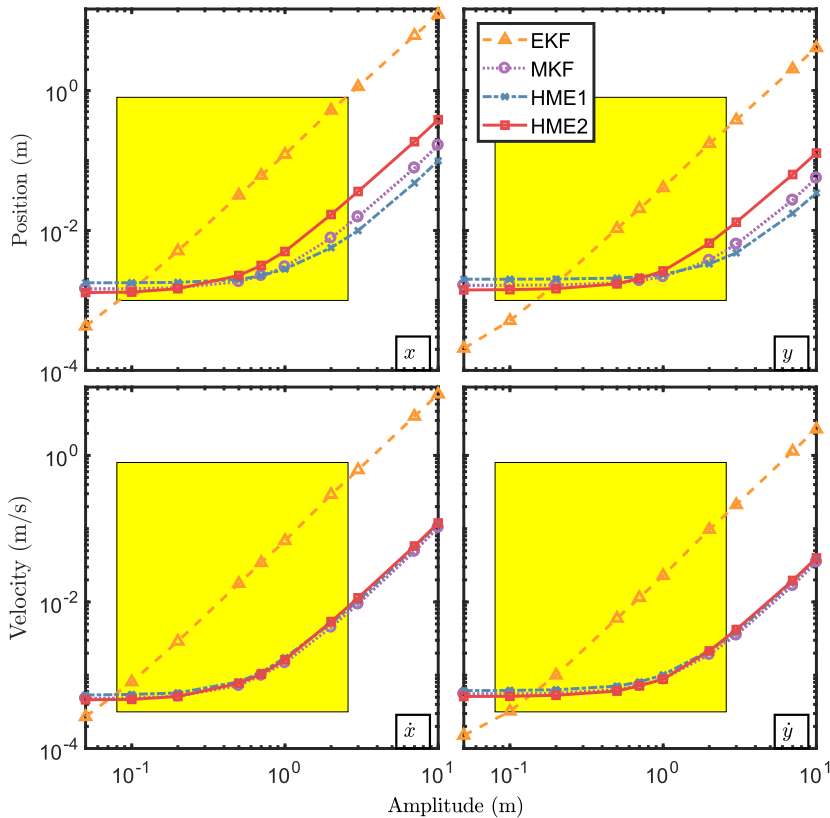
Fig. 15. MSE of hub motion estimates using different methods in various hub motion amplitudes, natural period 4 s.

shown in Figs. 11–13, the velocity and acceleration estimates converge to the real values. The error of the velocity estimate is within 0.05 m/s; see Fig. 12.

From the accumulated absolute errors (Figs. 9 and 11), HME1 has a better position estimation, whereas the velocity and bias estimates from HME2 are slightly better. In the case study, the monopile natural period is 3.8 s, for which the GPS sampling interval is too large. Hence, the moving horizon estimator struggles to predict precisely according to the sampled data. In summary, in this scenario, HME1 is preferred because of its lower complexity and sufficient accuracy.

5.3. Sensitivity study on the oscillation amplitude

In Section 5.2, the simulation results show that the estimation performance of HME2 is not improved by MHE. In this section, a sensitivity study is conducted to show how the environmental conditions influence the performance of HME1 and HME2. A series of simulations are conducted. The time series generated by the fitted spectra (Eq. 1) in Table 4 are selected as standard measurements and inputs with an oscillation amplitude less than 1 m. The generated time series is multiplied by a coefficient $N_a \in \{0.05, 0.1, 0.2, 0.5, 0.7, 1, 2, 3, 7, 10\}$ to simulate the oscillations with distinct amplitudes. All the other parameters, e.g., the GPS and IMU measurement noises, remain the same in all the simulations. The incoming direction of the wave is 30°, i.e., $\beta_{wave} = 30°$. To analyze the performance of the HME1 and HME2 algorithms, we also implement an EKF and an MKF for comparison. The EKF is implemented based on the plant model (6), where the innovation from the GPS signal is set to zero when the GPS signal is not available. Similarly, the MKF is implemented based on the delayed GPS signals.

Taking the natural periods 4, 6, and 8 s as examples, the influence of the oscillation amplitudes on the various estimation schemes are shown in Figs. 15–17. It is easy to notice that the MSEs of both position and velocity estimates increase with the motion amplitude. The EKF shows the best performance when the oscillation amplitude is less than 0.1 m, i.e., when the
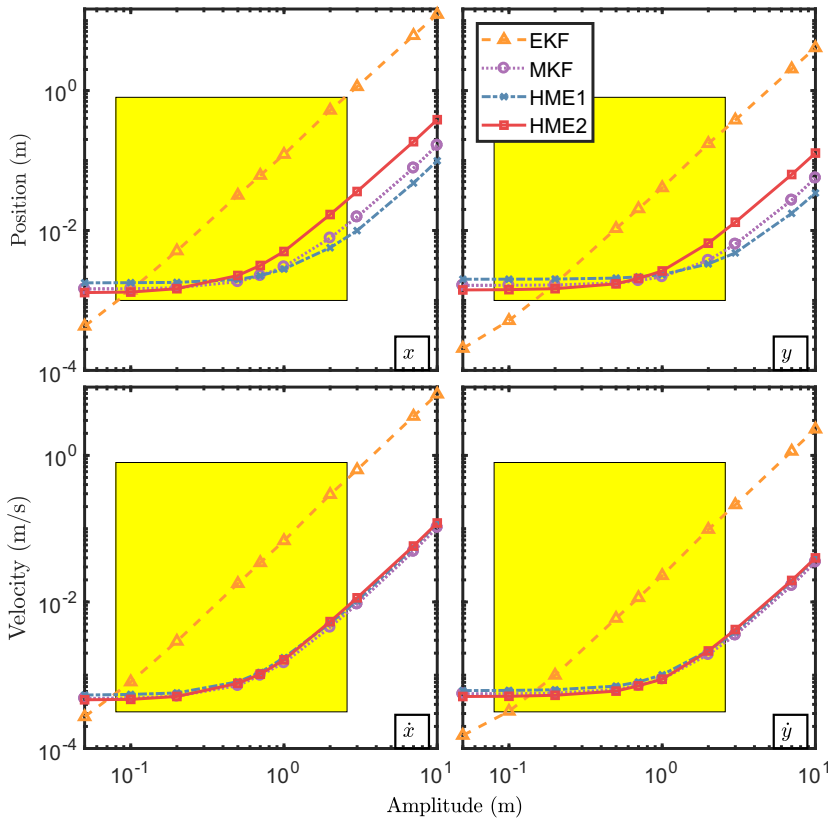
Fig. 16. MSE of hub motion estimates using different methods in various hub motion amplitudes, natural period 6 s.

motion estimator is not necessary. However, the EKF fails to accurately monitor the motion when $N_a \geqslant 0.1$. Use of only the MKF (Algorithm 6) without shift register #1 (Algorithm 3) yields medium performance results as compared with HME1 and HME2. Because of the GPS delay, there is always a delay between its estimate and the real value. With the correction by the predictor, the delay increases when the MKF updates with the delayed IMU specific force measurement from shift register #1. Both HME1 and HME2 estimate the velocity well.

For an OWT with a first fore-aft natural period 4 s, HME2 estimates the position better when the oscillation amplitude is less than 0.3 m, whereas HME1 shows better performance when the amplitude is larger than 0.3 m; see Fig. 15. For an OWT with a 6-s natural period, the performance boundary is at an amplitude of 1 m; see Fig. 16. Normally, the hub motion amplitude is located in the yellow envelope. Hence, both the HME1 and HME2 will improve the estimation performance over a single MKF.

Applying HME2 when the oscillation amplitude is less than the specific amplitude boundary, and adopting HME1 for the cases with oscillation amplitudes larger than the boundary, appear to achieve the best estimation performance.

5.4. Sensitivity study on the natural period and oscillation amplitude

Allowing the natural period to be from 3 to 8 s, the results of the best algorithms are illustrated in Fig. 18, using the criterion of minimum MSE. The yellow area shows the normal envelope of oscillation amplitude and natural period for an OWT. The detailed MSE results in three example conditions are presented in Tables 6–9. HME1 provides the best position estimate at upper left corner in Fig. 18, while HME2 is the best choice, shown in the lower right corner. MKF is the best scheme to use at two points ([0.5 m, 4 s] and [0.5 m, 5 s]), where the performance of MKF, HME1, and HME2 are very similar; see Fig. 15 The velocity estimate by HME2 is slightly better than the one from HME1. The performance of HME2 improves with an increasing natural period of the hub and with a decreasing oscillation amplitude. For the conditions in Tables 6–8, HME2 improves the estimate by approximately 20–30%. However, the estimate from HME1 is more accurate when the natural period is small; see Table 9.
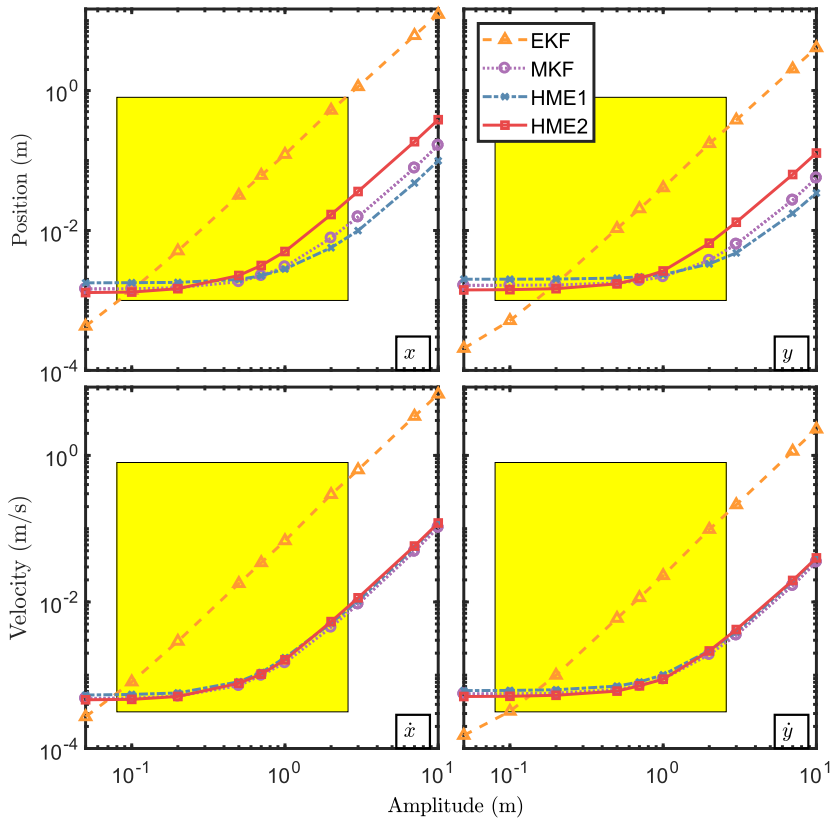
Fig. 17. MSE of hub motion estimates using different methods in various hub motion amplitudes, natural period 8 s.

Because of the low sampling rate of the GPS and the relatively high hub oscillation frequency, the moving horizon estimator struggles to accurately estimate using the sampled GPS signal and specific force measurements when the natural period of the OWT is low. HME2 greatly improves the estimate in the low-amplitude and long-natural-period region, whereas HME1 performs better in the region with higher motion amplitudes. Therefore, the suitable scheme can be decided by the oscillation amplitude and frequency.

6. Conclusions

Due to the slow GNSS sampling interval and GNSS delay, traditional discrete methods fail to provide good real-time motion estimations for a system with higher frequency. This paper proposes two GNSS/IMU integration schemes to estimate the offshore wind turbine hub position with a bottom-fixed foundation during the mating process. The systems include a multirate Kalman filter, an online RTS smoother, a moving horizon estimator, and a predictor. Simulations have verified that in the fast system, the estimators are sufficiently accurate. The estimates agree well with the real values for position, velocity, acceleration, and bias. The state observer filters the noise in the GPS and the IMU, overcomes the GPS delay, and achieves high-frequency displacement and velocity monitoring functionalities in real time.

Based on a comparison with the EKF and the MKF, the HME1 algorithm performs significantly better used as a real-time hub motion estimator during blade installation under some relevant conditions, while HME2 performs significantly better under some other relevant conditions. The performance of the state estimators is affected by the oscillation amplitude and the natural period of the hub structure. HME2 works well in the low-amplitude and low-frequency region, whereas HME1 shows superior performance in the region with higher motion amplitudes. Hence, both estimators could be implemented with a supervisory switching logic [48]. Both algorithms provide a sufficiently accurate estimate of the hub motion states in relevant conditions, thereby providing improved hub monitoring and increased safety and efficiency in practical applications.
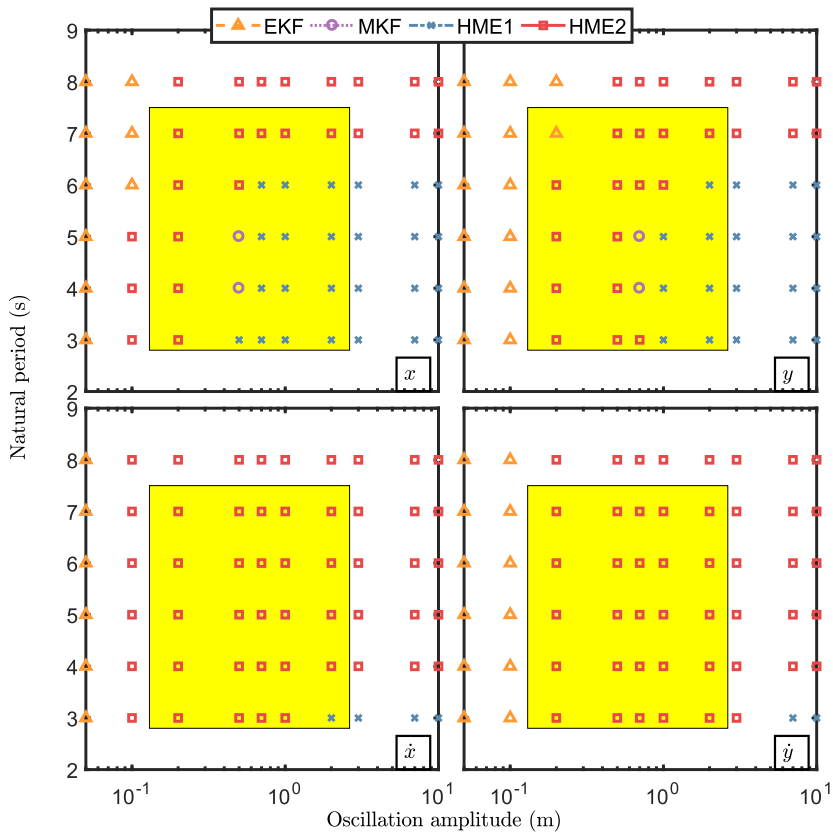
Fig. 18. The best schemes with different oscillation amplitudes and natural periods.

Table 6
The MSE of different algorithms, monopile natural period 4 s, oscillation amplitude 0.2 m.

Natural period (s)	x	y	v_x	v_y
EKF	5.98e−3	2.07e−3	3.53e−3	1.25e−3
MKF	1.52e−3	1.66e−3	0.52e−3	0.57e−3
HME1	1.79e−3	2.02e−3	0.57e−3	0.63e−3
HME2	1.42e−3	1.46e−3	0.49e−3	0.52e−3

Table 7
The MSE of different algorithms, monopile natural period 8 s, oscillation amplitude 0.2 m.

Natural period (s)	x	y	v_x	v_y
EKF	3.42e−3	1.25e−3	1.98e−2	0.74e−3
MKF	1.63e−3	1.71e−3	0.56e−3	0.58e−3
HME1	1.88e−3	2.05e−3	0.59e−3	0.64e−3
HME2	1.38e−3	1.45e−3	0.49e−3	0.52e−3

Table 8
The MSE of different algorithms, monopile natural period 8 s, oscillation amplitude 1 m.

Natural period (s)	x	y	v_x	v_y
EKF	8.46e−2	2.82e−2	4.78e−2	1.59e−2
MKF	7.81e−3	3.89e−3	3.25e−3	1.50e−3
HME1	6.59e−3	3.68e−3	2.81e−3	1.39e−3
HME2	4.99e−3	2.60e−3	1.73e−3	0.92e−3

Table 9
The MSE of different algorithms, monopile natural period 3 s, oscillation amplitude 2 m.

Natural period (s)	x	y	v_x	v_y
EKF	5.23e−1	1.74e−1	2.92e−1	0.98e−1
MKF	8.61e−3	4.05e−3	4.06e−3	1.75e−3
HME1	2.25e−3	2.17e−3	2.89e−3	1.40e−3
HME2	13.61e−3	5.52e−3	2.96e−3	1.34e−3

Acknowledgments

References

[1] Z. Jiang, W. Hu, W. Dong, Z. Gao, Z. Ren, Structural reliability analysis of wind turbines: a review, Energies 10 (2017) 2099.
[2] P. Murtagh, A. Ghosh, B. Basu, B. Broderick, Passive control of wind turbine vibrations including blade/tower interaction and rotationally sampled turbulence, Wind Energy 11 (4) (2008) 305–317.
[3] T. Yang, X. Yang, Y. Li, B. Fang, Passive and adaptive vibration suppression of pipes conveying fluid with variable velocity, J. Vib. Control 20 (9) (2014) 1293–1300.
[4] T.J. Larsen, T.D. Hanson, A method to avoid negative damped low frequent tower vibrations for a floating, pitch controlled wind turbine, J. Phys: Conf. Ser. 75 (1) (2007) 012073.
[5] J. Li, Z. Zhang, J. Chen, Experimental study on vibration control of offshore wind turbines using a ball vibration absorber, Energy Power Eng. 4 (03) (2012) 153.
[6] T.J. Stehly, D.M. Heimiller, G.N. Scott, 2016 cost of wind energy review, Tech. rep., National Renewable Energy Lab. (NREL), Golden, CO (United States), 2017.
[7] M. Gaunaa, J. Heinz, W. Skrzypiński, Toward an engineering model for the aerodynamic forces acting on wind turbine blades in quasisteady standstill and blade installation situations, J. Phys: Conf. Ser. 753 (2) (2016) 022007.
[8] Z. Jiang, Z. Gao, Z. Ren, Y. Li, L. Duan, A parametric study on the final blade installation process for monopile wind turbines under rough environmental conditions, Eng. Struct. 172 (2018) 1042–1056.
[9] P. Zhang, Y. Han, H. Ding, S. Zhang, Field experiments on wet tows of an integrated transportation and installation vessel with two bucket foundations for offshore wind turbines, Ocean Eng. 108 (2015) 769–777.
[10] A.S. Verma, Z. Jiang, N.P. Vedvik, Z. Gao, Z. Ren, Impact assessment of a wind turbine blade root during an offshore mating process, Eng.Struct. 180 (2019) 205–222.
[11] Z. Ren, Z. Jiang, R. Skjetne, Z. Gao, An active tugger line force control method for single blade installations, Wind Energy 21 (2018) 1344–1358.
[12] Z. Ren, R. Skjetne, Z. Gao, A Crane Overload Protection Controller for Blade Lifting Operation Based on Model Predictive Control, Energies 12 (1) (2019) 50.
[13] W. Yang, P.J. Tavner, C.J. Crabtree, Y. Feng, Y. Qiu, Wind turbine condition monitoring: technical and commercial challenges, Wind Energy 17 (5) (2014) 673–693.
[14] B. Lu, Y. Li, X. Wu, Z. Yang, A review of recent advances in wind turbine condition monitoring and fault diagnosis, 2009. IEEE PEMWA 2009 Power Electronics and Machines in Wind Applications, IEEE, 2009, pp. 1–7.
[15] T.I. Fossen, Handbook of Marine Craft Hydrodynamics and Motion Control, John Wiley & Sons, 2011.
[16] T.H. Bryne, J.M. Hansen, R.H. Rogne, N. Sokolova, T.I. Fossen, T.A. Johansen, Nonlinear observers for integrated INS/GNSS navigation: implementation aspects, IEEE Control Syst. Mag. 37 (3) (2017) 59–86.
[17] W. Shi, H.-C. Park, J.-H. Baek, C.-W. Kim, Y.-C. Kim, H.-K. Shin, Study on the marine growth effect on the dynamic response of offshore wind turbines, Int. J. Precision Eng. Manuf. 13 (7) (2012) 1167–1176.
[18] A. Noureldin, T.B. Karamat, J. Georgy, INS/GPS Integration, Springer, Berlin Heidelberg, 2013, pp. 247–271.
[19] R. Mahony, T. Hamel, J.-M. Pflimlin, Nonlinear complementary filters on the special orthogonal group, IEEE Trans. Autom. Control 53 (5) (2008) 1203–1218.
[20] R.G. Brown, P.Y. Hwang, Introduction to random signals and applied kalman filtering: with matlab exercises and solutions, Introduction to random signals and applied Kalman filtering: with MATLAB exercises and solutions, by Brown, Robert Grover.; Hwang, Patrick YC New York: Wiley, c1997.
[21] M. Zhu, A. Hahn, Y.-Q. Wen, Identification-based controller design using cloud model for course-keeping of ships in waves, Eng. Appl. Artif. Intell. 75 (2018) 22–35.
[22] T.A. Johansen, T.I. Fossen, The exogenous Kalman filter (XKF), Int. J. Control 90 (2) (2017) 161–167.
[23] F. Caron, E. Duflos, D. Pomorski, P. Vanheeghe, Gps/imu data fusion using multisensor kalman filtering: introduction of contextual aspects, Inf. Fusion 7 (2) (2006) 221–230.
[24] A. Smyth, M. Wu, Multi-rate Kalman filtering for the data fusion of displacement and acceleration response measurements in dynamic system monitoring, Mech. Syst. Sig. Process. 21 (2) (2007) 706–723.
[25] Y. Bock, D. Melgar, B.W. Crowell, Real-time strong-motion broadband displacements from collocated gps and accelerometers, Bull. Seismol. Soc. Am. 101 (6) (2011) 2904–2925.
[26] H. Lan, C. Yu, N. El-Sheimy, An integrated pdr/gnss pedestrian navigation system, in: China Satellite Navigation Conference (CSNC) 2015 Proceedings: Volume III, Springer, 2015, pp. 677–690.
[27] B. Zhao, R. Skjetne, M. Blanke, F. Dukan, Particle filter for fault diagnosis and robust navigation of underwater robot, IEEE Trans. Control Syst. Technol. 22 (6) (2014) 2399–2407.
[28] T.H. Bryne, R.H. Rogne, T.I. Fossen, T.A. Johansen, A virtual vertical reference concept for aided inertial navigation at the sea surface, Control Eng. Practice 70 (2018) 1–14, https://doi.org/10.1016/j.conengprac.2017.09.009.
[29] H.F. Grip, T.I. Fossen, T.A. Johansen, A. Saberi, Globally exponentially stable attitude and gyro bias estimation with application to GNSS/INS integration, Automatica 51 (2015) 158–166.
[30] J.M. Hansen, T.I. Fossen, T.A. Johansen, Nonlinear observer design for GNSS-aided inertial navigation systems with time-delayed GNSS measurements, Control Eng. Practice 60 (2017) 39–50.
[31] T.J. Larsen, A.M. Hansen, How 2 HAWC2, the user's manual Tech. rep, Risø National Laboratory, 2007.

[32] W. Shi, H.C. Park, C.W. Chung, H.K. Shin, S.H. Kim, S.S. Lee, C.W. Kim, Soil-structure interaction on the response of jacket-type offshore wind turbine, Int. J. Precision Eng. Manuf.-Green Technol. 2 (2) (2015) 139–148.

[33] P. Zhang, W. Wei, N. Jia, H. Ding, R. Liu, Effect of seepage on the penetration resistance of bucket foundations with bulkheads for offshore wind turbines in sand, Ocean Eng. 156 (2018) 82–92.

[34] H. Matlock, L.C. Reese, Generalized solutions for laterally loaded piles, J. Soil Mech. Found. Div. 86 (5) (1960) 63–94.

[35] American Petroleum Institute, API RP 2A-WSD Recommended Practice for Planning, Designing and Constructing Fixed Offshore Platforms: Working Stress Design, American Petroleum Institute, 2000.

[36] S. Bhattacharya, S. Adhikari, Experimental validation of soil–structure interaction of offshore wind turbines, Soil Dyn. Earthquake Eng. 31 (5) (2011) 805–816.

[37] T. Yang, Y. Tang, Q. Li, X.-D. Yang, Nonlinear bending, buckling and vibration of bi-directional functionally graded nanobeams, Compos. Struct.

[38] L. Arany, S. Bhattacharya, J.H. Macdonald, S.J. Hogan, Closed form solution of eigen frequency of monopile supported offshore wind turbines in deeper waters incorporating stiffness of substructure and ssi, Soil Dyn. Earthquake Eng. 83 (2016) 18–32.

[39] J. Jonkman, S. Butterfield, P. Passon, T. Larsen, T. Camp, J. Nichols, J. Azcona, A. Martinez, Offshore code comparison collaboration within IEA wind annex XXIII: phase ii results regarding monopile foundation modeling Tech. rep, National Renewable Energy Laboratory (NREL), Golden, CO, 2008.

[40] J. Jonkman, W. Musial, Offshore code comparison collaboration (oc3) for iea wind task 23 offshore wind technology and deployment, Tech. rep., National Renewable Energy Lab.(NREL), Golden, CO (United States) (2010).

[41] IEC 61400-1, Wind turbine generator systems-part 1: Safety requirements, Standard, International Electrotechnical Commission and others, Geneva, Switzerland (Aug. 2005).

[42] M. Zhu, A. Hahn, Y.-Q. Wen, A. Bolles, Identification-based simplified model of large container ships using support vector machines and artificial bee colony algorithm, Appl. Ocean Res. 68 (2017) 249–261.

[43] W. Deng, R. Yao, H. Zhao, X. Yang, G. Li, A novel intelligent diagnosis method using optimal ls-svm with improved pso algorithm, Soft. Comput. (2017) 1–18.

[44] W. Deng, S. Zhang, H. Zhao, X. Yang, A novel fault diagnosis method based on integrating empirical wavelet transform and fuzzy entropy for motor bearing, IEEE Access 6 (2018) 35042–35056, https://doi.org/10.1109/ACCESS.2018.2834540.

[45] P. Batista, C. Silvestre, P. Oliveira, On the observability of linear motion quantities in navigation systems, Syst. Control Lett. 60 (2) (2011) 101–110.

[46] H.E. Rauch, F. Tung, C.T. Striebel, et al, Maximum likelihood estimates of linear dynamic systems, AIAA J. 3 (8) (1965) 1445–1450.

[47] Z. Ren, Z. Jiang, R. Skjetne, Z. Gao, Development and application of a simulator for offshore wind turbine blades installation, Ocean Eng. 166 (2018) 380–395.

[48] V. Hassani, A.M. Pascoal, A.J. Srensen, Detection of mooring line failures using dynamic hypothesis testing, Ocean Eng. 159 (2018) 496–503, https://doi.org/10.1016/j.oceaneng.2018.01.021.

Paper A5

Dynamic simulation and control of an active roll reduction system using free-flooding tanks with vacuum pumps

Jiafeng Xu, Zhengru Ren, Yue Li, Roger Skjetne, and Karl Henning Halse

Paper A6

Mating control of a wind turbine tower-nacelle-rotor assembly for a catamaran installation vessel

Zhiyu Jiang, Zhengru Ren, Zhen Gao, Karl Henning Halse, and Peter Christian Sandvik

Mating Control of a Wind Turbine Tower-Nacelle-Rotor Assembly for a Catamaran Installation Vessel

Zhiyu Jiang[1,2], *Zhengru Ren*[1,2,3], *Zhen Gao*[1,2,3]
Peter Christian Sandvik[2,4], *Karl Henning Halse* [2,5], *Roger Skjetne*[1,2,3]
1 Department of Marine Technology, Norwegian University of Science and Technology (NTNU), Trondheim, Norway
2 Centre for Research-based Innovation of Marine Operations (SFI MOVE), NTNU
3 Centre for Autonomous Marine Operations and Systems (SFF AMOS), NTNU, Trondheim, Norway
4 PC Sandvik Marine, Trondheim, Norway
5 Department of Ocean Operations and Civil Engineering, NTNU, Ålesund, Norway

ABSTRACT

The assembly and installation costs of an offshore wind farm can approach 20% of the capital expenditures; therefore, time efficient installation methods are needed for installing offshore wind turbines. This study investigates the feasibility of a novel wind turbine installation concept using a catamaran. The catamaran is designed to carry wind turbine assemblies on board and to perform installation using lifting grippers. The installation of a rotor-tower-assembly onto a spar foundation is considered with a focus on the mating process of a tower-nacelle-rotor assembly. The spar foundation has been pre-installed at a representative site in the North Sea, and the catamaran has thrusters regulated by a dynamic positioning system. Numerical modelling of various components of the concept are introduced. Time-domain simulations of the system are performed in irregular waves, and the relative motion and velocity between the tower bottom and the spar top are analysed during the mating process. It was found that the active heave compensator can effectively reduce the relative heave velocity and the risks of structural damage during the mating process.

KEY WORDS: Offshore wind turbine installation; catamaran; mating; active heave compensator; motion control.

INTRODUCTION

The offshore wind industry has witnessed continuous growth in the past decade. To improve the cost effectiveness of offshore wind power, there is a trend to design larger wind turbines for greater water depths. Various types of supporting structures have been proposed for offshore wind turbines (OWTs). Generally, for water depth less than 40 meters, monopile, gravity-based, and jacket foundations are the most commercially competitive (Pieda and Tardieu, 2010). For water depths greater than 100 m, floating foundations including spar, semisubmersible, and tension leg platforms are viable solutions, although their commercialisation is still

at a preliminary stage because of costs.

Offshore installation is expensive. According to a recent study (Moné et al., 2017), the assembly and installation cost contributes approximately 20% to the capital expenditures of a bottom-fixed offshore wind farm. The installation costs are partly due to the rental of installation vessels and weather-restrictive nature of traditional marine operations (e.g. significant wave height $\leq$ 2.0 m). The turbulent wind condition is another factor that poses constraints. To avoid delays during offshore installation and to increase profit margins of the offshore wind industry, innovative and cost-effective methods for installing OWTs are desired. For instance, Sarkar and Gudmestad (2017) suggested an installation approach using a floating vessel with a floatable subsea structure for installation of monopile-type wind turbines. Guachamin-Acero et al. (2017) proposed another method for installing bottom-fixed wind turbines based on the inverted pendulum principle. Yet, these installation methods are not readily applicable to floating wind turbines.

A novel concept was proposed in the SFI MOVE project for installing bottom-fixed and floating OWTs (Hatledal et al., 2017). This concept utilises a catamaran vessel which carries a maximum of four tower-nacelle-rotor assemblies in an installation task. Unlike the split method (Jiang et al., 2018a) which requires several lifts of blades or nacelle, the catamaran installation concept is more efficient - it requires only one lift for each wind turbine assembly. Figure 1 illustrates a visual impression of this concept during an installation task. In general, the procedure for installing a spar-type floating wind turbine can be divided into the following major stages:

(a) The catamaran approaches the pre-installed spar foundation;

(b) The crew wait for allowable weather;

(c) The catamaran gets connected to the spar foundation via sliding grippers;

(d) The lifting mechanism grips, lifts up, and transports a wind turbine assembly to the aft;

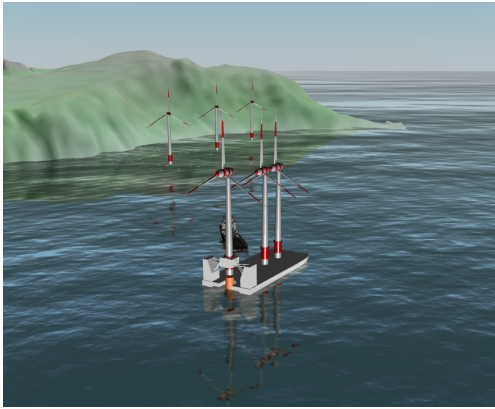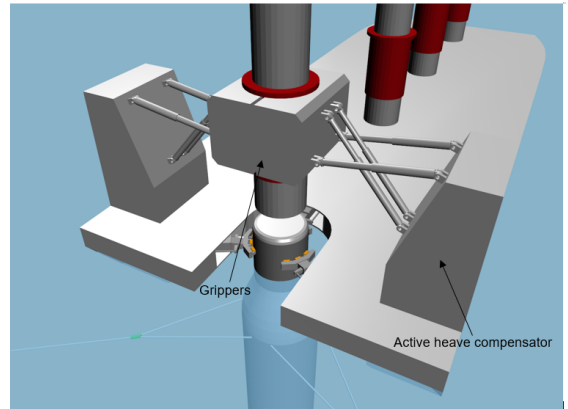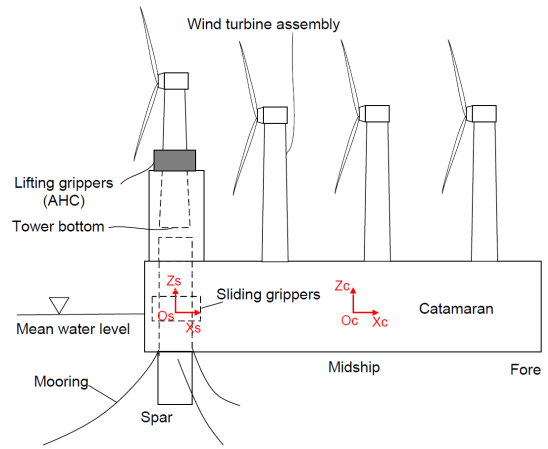(e) The relative motion between the tower bottom and the spar top is

Fig. 1 Illustration of an offshore wind farm installed by the catamaran installation vessel.

monitored;

(f) The tower bottom and the spar foundation is mated;

(g) Bolting of the tower bottom takes place;

(h) The catamaran releases the spar foundation.

All critical stages should be evaluated to ensure technical feasibility of this installation concept. At stage (c), manual mode of the dynamic positioning (DP) system may be applied. After connection of the spar and the catamaran, the sliding grippers will only constrain the relative surge and sway motions of the two bodies but allow relative pitch and roll motions. Hatledal et al. (2017) focused on stage (c) and used the virtual prototyping framework Vicosim to study the contact forces between the grippers and the foundation. Jiang et al. (2018b) performed numerical analysis for stage (e) and identified factors affecting the relative motions in the horizontal plane. These studies are preliminary, and further numerical simulations and experiments are needed for assessment of the concept.

In this study, we focus on the mating phase (stage (f)) and investigate the relative heave motion between the lifted wind turbine assembly and the spar foundation. There are different methods to achieve heave compensation. Passive and active systems are two main categories, and hybrid active-passive systems also exist which combine features of both. Passive systems are mostly open-loop systems which do not require any energy input, and pneumatic-hydraulic systems are widely used (Huster et al., 2009). In contrast, active systems involve closed-loop control and require energy input. An active system usually involves electronics, sensors and controlled actuators, and should be used when the relative motion between two independently moving references need to be compensated (Woodacre et al., 2015). A great number of examples can be found regarding modeling and control of active hydraulic systems; see Korde (1998), Jelali and Kroll (2012) and Mintsa et al. (2012), and applications can be found in deep-water mining (Chung 2010) and lifting operation (Nam et al., 2013). Here, a representative hydraulic active heave compensator (AHC) is numerically modelled for the lifting mechanism of the whole system that consists of a dynamically positioned catamaran, a spar foundation with mooring lines, and sliding grippers.

(a)

(b)

Fig. 2 Schematic of the mating of a wind turbine assembly (a) aft view (b) side view.

PROBLEM FORMULATION

Problem statement

As shown in Fig. 2, during the mating phase, the wind turbine assembly is gripped by the lifting grippers and laid upon the spar foundation. Because of the wave-induced motions on the catamaran and spar, uncontrolled landing of the wind turbine assembly on the spar foundation could result in large impact loads. To avoid this, motions of the lifting grippers should be controlled, compensating for the relative motions between the tower bottom and the spar top. The AHC should be located at both sides of the catamaran.

A hydraulic system is considered for the AHC consisting of a motor, a pump, valves, hydraulic fluid, and a hydraulic cylinder. Figure 3 gives an overview of the system components. In the figure, the wind turbine assembly is simplified as a mass, and the lifting grippers are represented by a cylinder connected to the wind turbine. Two right-hand coordinate systems are adopted, the global frame and the global vertical frame. The global coordinate system is fixed and initially aligned with body coordi-
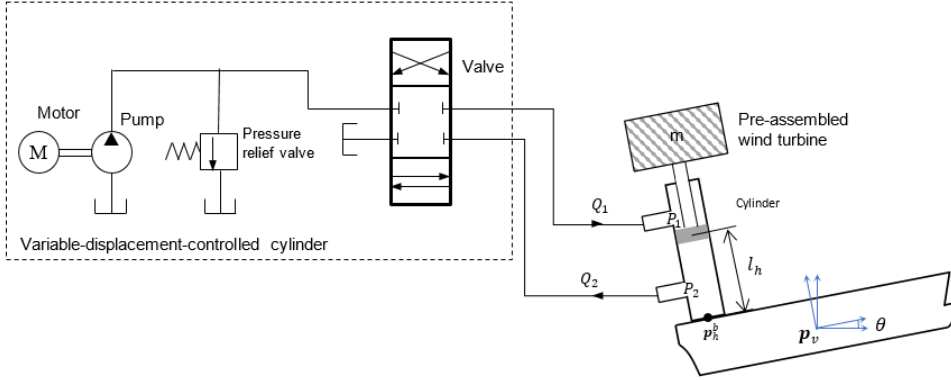
Fig. 3 Simplification of the AHC considered in the study.

nate system of the spar, with the origin point at the mean water level and x- and y-axes pointing to the north and east, respectively; see Fig. 2(b). In the body-fixed frame of the catamaran, the x^b- and y^b- axes point to the bow and port, respectively. It is assumed that the spar-top motions can be effectively measured by sensors, and the relative motions in pitch and roll are less important. The control objective is to reduce the relative heave motion between the tower bottom and the spar top in the global z-axis when exposed to oscillatory wave motions. The control input is the pump displacement.

System modelling

The main assumptions for the modelling are as follows:

- The reacting force from the hydraulic actuator does not influence the vessel motion;

- There is a rigid connection between the lifting grippers and the wind turbine assembly; see Fig.2(a);

- Hydraulic fluid density is constant;

- Pipeline distance is neglected;

- The effective bulk modulus of the hydraulic fluid is constant.

The position of the tower bottom in the global reference frame $\boldsymbol{p}_b$ becomes

$$\boldsymbol{p}_b = \boldsymbol{p}_v + \boldsymbol{R}(\boldsymbol{\Phi})(\boldsymbol{p}_h^b + \boldsymbol{d}_h), \tag{1}$$

where $\boldsymbol{p}_v$ stands for the position of the body origin of the catamaran in the global coordinate, $\boldsymbol{R}(\boldsymbol{\Phi})$ denotes the rotation matrix from the body-fixed to global reference frame parametrised by the Euler angle vector $\boldsymbol{\Phi}$, $\boldsymbol{p}_h^b$ is the position of the hydraulic lifting device in the body-fixed frame, and $\boldsymbol{d}_h = [0, 0, -l_h]^\top$ where $l_h > 0$ refers to the moving distance of the lifting grippers.

The velocity $\boldsymbol{v}_b$ of the tower bottom in the global frame is given by

$$\boldsymbol{v}_b = \boldsymbol{v}_v + \boldsymbol{R}(\boldsymbol{\Phi})\boldsymbol{S}(\omega_v)(\boldsymbol{p}_h^b + \boldsymbol{d}_h) + \boldsymbol{R}(\boldsymbol{\Phi})\boldsymbol{v}_h, \tag{2}$$

where $\boldsymbol{v}_v$ is the velocity of the body origin of the catamaran in the global coordinate, $\boldsymbol{S}$ is a three-by-three skew-symmetric matrix used to represent cross products, and $\boldsymbol{v}_h = [0, 0, -\dot{l}_h]^\top$.

In this work, a simplified variable-displacement controlled cylinder is considered for the hydraulic system (Wang et al., 2012). As illustrated in Fig. 3, this cylinder will act as an equivalent of the actual system using

a set of cylinders. The position of the cylinder is regulated by the oil pumped into and out of it. The load pressure P is defined as

$$P = \begin{cases} P_1 - P_r, & \text{if } P_1 > P_r \\ P_r - P_2, & \text{if } P_2 > P_r \end{cases} \tag{3}$$

where P_r denotes the return pressure which is considered to a constant, and P_1 and P_2 are the pressures on the two chambers of the cylinder. The state-space equation of the one-degree variable displacement controlled cylinder system is

$$\dot{l}_h = v_h, \tag{4a}$$

$$\dot{v}_h = \frac{1}{m}(-f_c v_h + PA + F_{ext}), \tag{4b}$$

$$\frac{V}{\beta}\dot{P} = -Av_h - c_l P + u. \tag{4c}$$

where v_h denotes the moving velocity of the lifting grippers, m is the total mass including the mass of the hydraulic cylinder m_h and the mass of the turbine assembly m_t, f_c is the friction coefficient, A is the cross-section area of the cylinder, F_{ext} is the external force due to gravity of the turbine assembly, $V = V_0 + Al_h$ is the effective volume of the cylinder, V_0 is the fluid volume in the pipelines, β is bulk modulus of the hydraulic fluid, c_l is the fluid leakage coefficient, and u is equivalent to the axis rotating speed of the pump ω times pump displacement D_p.

FEEDBACK CONTROL SYSTEM

For the sake of simplification, the observer design is not included in this paper.

Trajectory generator

From Eq. (1), the desired length of the hydraulic piston l_{hd} is at the time instant t_k is calculated from

$$l_{hd}(t_k) = \left[\boldsymbol{p}_h^b - \boldsymbol{R}^\top(\boldsymbol{p}_s(t_k) - \boldsymbol{p}_v(t_k))\right]_3, \tag{5}$$

where $\boldsymbol{p}_s$ is the position of the spar top in the global reference frame, and $[\boldsymbol{a}]_3$ denotes the 3rd element of the vector $\boldsymbol{a}$. A reference model is used to generate smooth trajectories $l_{hr}(t)$ and $\dot{l}_{hr}(t)$ for a series of desired lengths l_{hd}. The transfer function is given by

$$\frac{l_{hr}}{l_{hd}}(s) = \frac{\omega_r^3}{(s + \omega_r)(s^2 + 2\zeta_r\omega_r + \omega_r^2)}, \tag{6}$$

where s is the frequency, ζ_r denotes the damping ratio, and ω_r is a frequency parameter. $\zeta_r = 1$ is selected to ensure critical damping. The parameter ω_r influences the tacking speed, i.e., the higher the ω_r, the faster the tracking speed.

Because of the lowpass-filter characteristic of the reference system, there is a lag between the trajectory and the actual position. Its consequence is the unwanted impact during the final mating phase. To reduce this lag, a higher ω_r is needed. Otherwise, l_{hd} can be selected with a prediction over a short time horizon.

Control law design

In the control law design stage, it is assumed that the real-time measurements of the positions and orientations of the catamaran and spar are available. Because of the high bulk modulus β of the hydraulic fluid, $\frac{\beta}{V}$ has a large value that causes fast dynamics in the system. Therefore, the natural frequency for the system (4a)–(4b) is much smaller than for (4c). Singular perturbation theory is used to handle such problems in order to transfer the high-order system into a low-order model by dividing the system into a slow model and a fast model.

Define two error variables $e_1 = l_h - l_{hr}$ and $e_2 = \dot{e}_1 = v_h - \dot{l}_{hr}$. The system model with error dynamics is then given by

$$\left. \begin{aligned} \dot{e}_1 &= e_2 \\ \dot{e}_2 &= \frac{1}{m}(-f_c v_h + PA + F_{ext}) - \ddot{l}_{hr} \end{aligned} \right\} \quad \dot{e} = f(e, P), \tag{7a}$$

$$\varepsilon \dot{P} = -A(e_2 + \dot{l}_{hr}) - c_l P + u := g(e, P, u), \tag{7b}$$

where Eq. (7a) is the slow model and Eq. (7b) is the fast model with $e = [e_1, e_2]^{\top}$ and $\varepsilon = \frac{V}{\beta}$. As β gets very large, $\varepsilon \to 0$, and the isolated root of $g = 0$ is

$$\bar{P} = \frac{1}{c_l}(u - A\dot{l}_h) =: h_1(u) \tag{8}$$

Substituting $P = \bar{P}$ of Eq. (8) into Eq. (7a) yields,

$$\begin{aligned} \dot{e}_2 &= \frac{1}{m}[-f_c(e_2 + \dot{l}_{hr}) + \frac{A}{c_l}(u - A\dot{l}_h) + F_{ext}] - \ddot{l}_{hr} \\ &= \Upsilon u + \Psi, \end{aligned} \tag{9}$$

where $\Upsilon = \frac{A}{mc_l}$ and $\Psi = -\frac{A^2}{mc_l}\dot{l}_h + \frac{1}{m}(-d_h v_h + F_{ext}) - \ddot{l}_{hr}$. Υ is a positive constant by assuming that c_l is a constant.
Therefore the PID control law is given by

$$u = \frac{1}{\Upsilon}(-\Psi - c_1 e_1 - c_2 e_2 - c_3 \int e_1 \, dt) := h_2(e), \tag{10}$$

where c_1, c_2, and c_3 are positive constants. By using the pole placement technique, identical real eigenvalues are selected i.e., $\lambda_1 = \lambda_2 = \lambda^* < 0$. Hence, $c_1 = \lambda_1 \lambda_2 = 2\lambda^*$ and $c_2 = -\lambda_1 - \lambda_2 = -2\lambda^*$. The integral control gain c_3 is tuned to handle the bias existed in the equilibrium points (8) caused by F_{ext} in u.

ANALYSIS PROCEDURE

Figure 5 shows the analysis procedure followed in this paper to assess the performance of the AHC on the mating process. Here, the coupled system refers to the catamaran, spar and positioning system. In the analysis, several sea states are selected for the numerical simulation first. Then, numerical simulations were performed in the time domain. Based on the simulation results, the absolute and relative heave motions between the spar top and the tower bottom will be analysed, and the effect of the AHC will be shown.
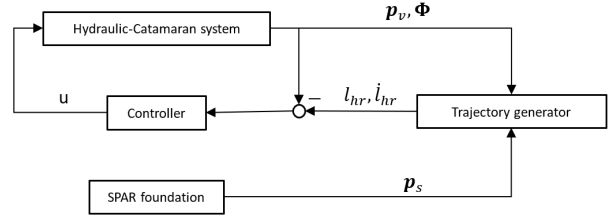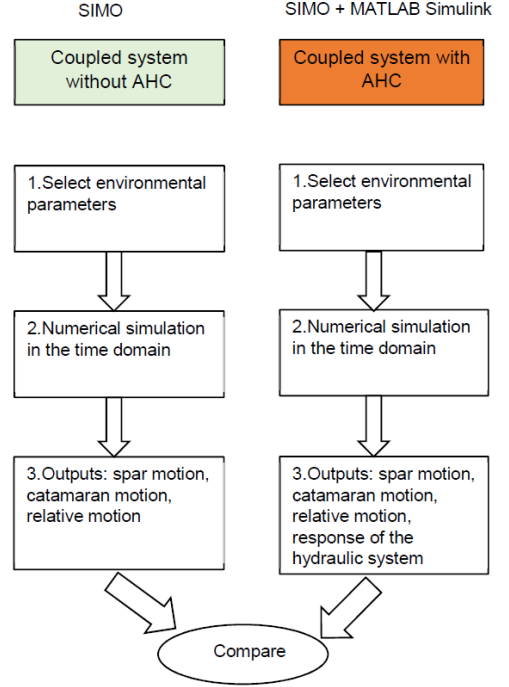

Fig. 4 Block diagram of the control system.

Fig. 5 Analysis procedure of the study.

NUMERICAL SIMULATION

The time-domain simulation program SIMO (MARINTEK, 2016) was used to simulate the coupled dynamic responses of the catamaran-spar system with 12 degrees-of-freedom. The catamaran installation vessel and the spar foundation were modelled as two rigid bodies connected by mechanical couplings (spring-damper system) at the vessel aft. The DP of the catamaran is realised by using four thrusters distributed along the vessel. A Kalman filter-based controller was used for the positioning system. In SIMO, the equations of motion of the two-body system are solved in the time domain, and the retardation functions are calculated using frequency-dependent added mass and damping. In this study, HydroD (Det Norske Veritas, 2011) was used to obtain these hydrodynamic coefficients. The second-order hydrodynamic loads in surge, sway, and yaw were calculated based on Newman's approximation. In addition, lin-
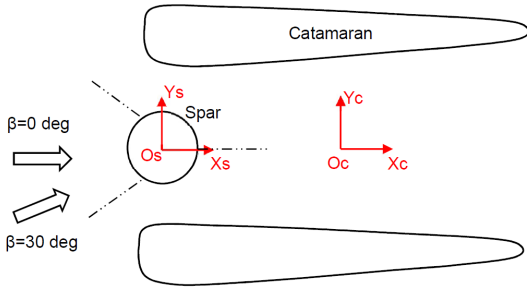
Fig. 6 Top view of the catamaran and spar at mean water level.

ear roll damping and quadratic yaw damping coefficients were specified for the catamaran to account for the viscous effects on the hull.

For the coupled system with lifting mechanism, MATLAB/Simulink was used to model the AHC, and motion responses of the catamaran and the spar from SIMO were used as inputs. In SIMO, the Newmark-Beta numerical integration method with a time step of 0.01 s was used. In MATLAB/Simulink, a 10^{-4} second sampling interval was adopted to accurately simulate the hydraulic system's fast dynamics. The control input update frequency is 10 Hz.

CASE STUDY

A catamaran vessel designed in the SFI MOVE project and a spar foundation based on the Hywind Scotland project (Steen, 2016) were considered in the case study. Figure 6 is a schematic of the initial positions of the bodies in the horizontal plane. In the figure, β denotes wave heading. The spar is constrained by a set of three mooring lines and connected to the catamaran via sliding grippers (not shown).

Tables 1–3 list the key parameters of the catamaran, wind turbine assemblies and spar. Prior to the mating operation, the spar top position, or the mating point, is located approximately 20 m above the waterline. A preliminary design of the hydraulic system was done, and the basic parameters of the hydraulic system are summarized in Table 4.

Table 1 Selected properties of the catamaran.

Parameter	Symbol	Value
Length overall (m)	L_{OA}	144
Breath moulded (m)	B	60
Draft (m)	T_c	8.0
Displacement mass (tonnes)	Δ_c	18502.9
Vertical centre of gravity (COG) above baseline (m)	KG_c	28.6
Body origin in global coordinate system (m)	(X_c,Y_c,Z_c)	(64,0,0)
Number of wind turbines on board	N_w	4

Table 5 lists the load cases under irregular waves. The significant wave height (H_S) of 2.0 m, and representative values of the spectral peak period (T_P) were chosen. A constant number of 3 was used in the directional function (Det Norske Veritas, 2010) for the directional short-crested wave spectrum, and the JONSWAP spectrum was used for wave generation. A water depth of 110 m was considered. For each load case,

Table 2 Selected properties of each wind turbine.

Parameter	Symbol	Value
Rated power (MW)	RP	10
Weight (tonnes)	M_w	1200
Hub height (m)	H_h	115

Table 3 Selected properties of the spar before mating.

Parameter	Symbol	Value
Diameter at top (m)	L_{bd1}	9.5
Diameter at waterline (m)	M_{bd1}	14
Draft (m)	T_{s1}	70
Vertical position of COG (m)	Zs_{COG1}	-51.8
Displacement mass (tonnes)	Δ_{s1}	11045
Vertical position of fairlead (m)	Z_{f1}	-15
Vertical position of mating point (m)	Z_m	20
Heave natural period (s)	T_{n3}	17.4

Table 4 Parameters of the hydraulic system.

Parameter	Symbol	Value
Cylinder cross-section area (m^2)	A	0.39
Bulk modulus (-)	β	2e9
Fluid leakage coefficient (-)	c_l	1e-7
Mass of the hydraulic piston (tonnes)	m_h	1
Friction coefficient (Ns/m)	f_c	1e5
Volume of fluid in the pipeline (m^3)	V_0	0.5

Table 5 Load cases (H_s=2.0 m).

LC	T_p	β	AHC
1	6.0	0	Yes, No
2	8.0	0	Yes, No
3	10.0	0	Yes, No
4	6.0	30	Yes, No
5	8.0	30	Yes, No
6	10.0	30	Yes, No

six 1800-s simulations with random seed numbers were performed, and the statistical results were obtained by averaging the six simulations.

RESULTS AND DISCUSSION

In this section, the simulation results of the load cases will be interpreted. The focus is to compare the relative heave motion of the mating point with and without AHC. Here, heave motion refers to the motion in the global z-direction, and heave velocity is time derivative of the heave motion.

Time series

Figures 7–8 show selected time series of the absolute heave motion and velocity of the tower bottom and the spar top. In the following, the tower bottom refers to the bottom position of the wind turbine assembly being held by the grippers. Without AHC, responses of the tower bottom were
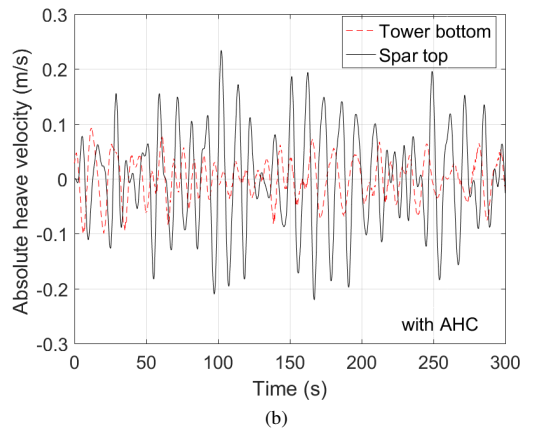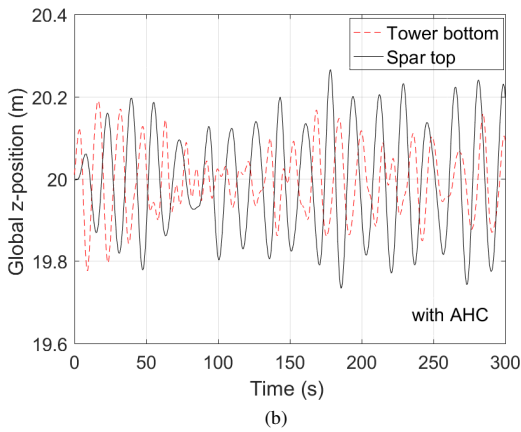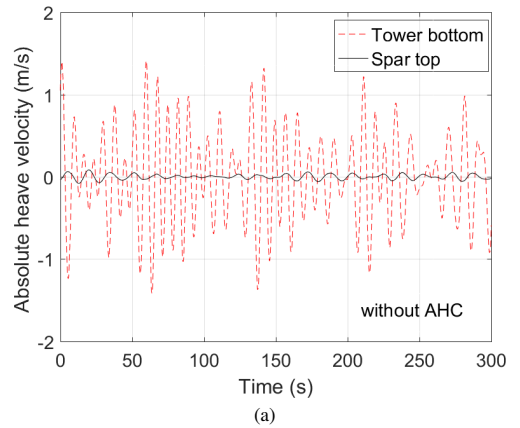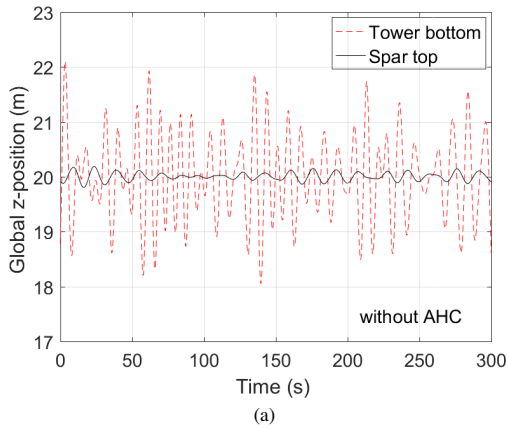
Fig. 7 Time history of the absolute heave displacement, H_S =2.0 m, T_P =10 s, β=0 deg, Seed 1 (a) without AHC (b) with AHC.

Fig. 8 Time history of the absolute heave velocity, H_S =2.0 m, T_P =10 s, β=0 deg, Seed 1 (a) without AHC (b) with AHC.

derived from rigid body motions of the catamaran, and the catamaran's heave and pitch motions contribute to the tower-bottom heave responses. As illustrated by the red dashed line in Fig. 7(a), this part is dominant compared to heave motion of the spar top. The spar-top motion is dominated by heave resonance of the spar. With AHC, heave motion of the tower bottom can be substantially compensated for, and there is generally good correspondence between the two curves in Figs. 7(b). Figure 8(a) compares the absolute heave velocities of the two bodies without AHC. Even for the short duration shown, the maximum heave velocity of tower bottom is well above 1 m/s. Because the aim of the AHC is to follow the spar-top heave motion which is quite small, AHC is also effective in reducing the heave velocity of the tower bottom (Fig. 8(b)). The maximum absolute heave velocity of the tower bottom is below 0.1 m/s in the time history.

The relative heave velocity is critical to the landing forces that occur during the mating. Figures 9–10 present the relative heave motion and velocity in the z-direction. Without AHC, the relative motion and velocity are comparable to the absolute ones. The magnitude of the relative ve-

locity, in conjunction with the large weight of the wind turbine assembly (about 1200 tonnes) indicates great landing forces. With AHC, the relative velocity is on the order of 0.2 m/s, which is expected to be handled by the protection system during the mating process.

In Fig. 11(a), movements of the hydraulic piston are shown. The moving distance follows the wave-frequency heave responses of the tower bottom. In the case with H_S =2 m and T_P =10 s, the moving distance has a mean value of 3 m and maximum of 5.6 m. The moving distance is dependent on design of the hydraulic system and longitudinal location of the mating point along the catamaran. Fig. 11(b) plots the hydraulic load pressure at the cylinder side; this pressure varies around 30 MPa during the whole simulation.

As shown in Figures 12(a)–12(b), for the suspended wind turbine tower assembly, the gripper forces from the AHC are dominant, with the mean values close to the self weight. In comparison, the inertial forces are relatively small.
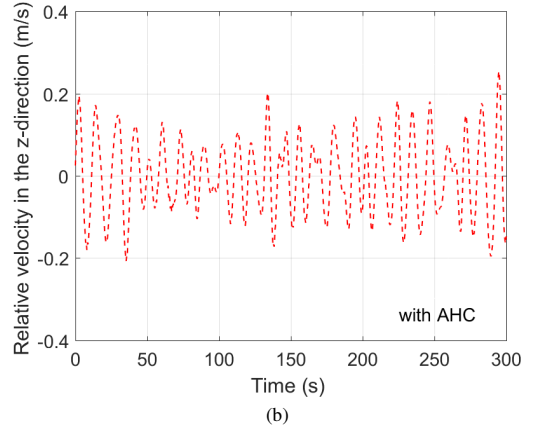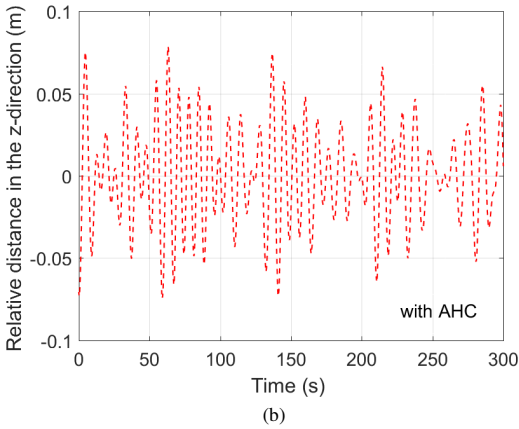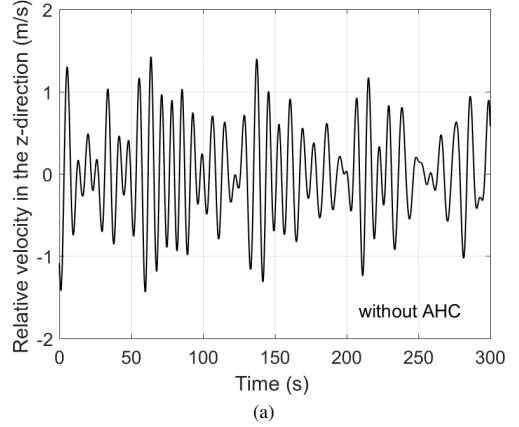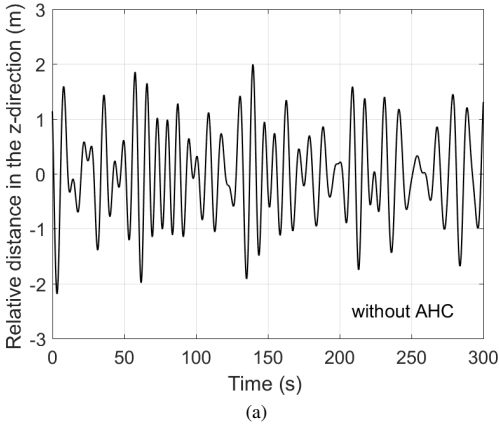
Fig. 9 Time history of the relative heave displacement between the spar top and the tower bottom, H_S=2.0 m, T_P=10 s, β=0 deg, Seed 1 (a) without AHC (b) with AHC.

Fig. 10 Time history of the heave velocity of the tower bottom relative to the spar top, H_S=2.0 m, T_P=10 s, β=0 deg, Seed 1 (a) without AHC (b) with AHC.

Statistical results

Figures 13(a)–13(b) give the statistical average of the maximum responses during 1800 s. These maxima are simply the maximum values without extrapolations. The tower-bottom motions outweigh the spar-top motions for the system without AHC, and the maximum relative distance and relative velocity approaches the maximum tower-bottom displacement and velocity, respectively. Higher T_P is correlated with larger maximum relative response, primarily due to the shape of the JONSWAP spectrum and of the catamaran's pitch response amplitude operator (not shown). In practical marine operations, lower T_P is more often encountered.

Without the AHC, the maximum responses are sensitive to the wave heading, and β=0 deg gives greater responses. With the proposed AHC, the wave heading is expected to have less impact on the heave responses of the mating point. As shown in Figs. 14(a)–14(b), when β increases from 0 to 30 deg, the magnitude of this reduction is insignificant, although a reduction in the relative displacement or velocity is observed.

Landing forces

Like the landing of subsea structures on the seabed (Det Norske Veritas, 2014), the landing of the wind turbine assembly may cause structural damage to the spar deck or to the lifting mechanism, and the risks should be assessed. According to (Graczyk and Sandvik, 2012), the following approximation can be used to evaluate the maximum force in the lift wire for a component landing on the deck

$$F_{max} = m_t g + V_{rel} \sqrt{km_t}, \tag{11}$$

where F_{max} is the maximum force in the lift wire, g is the gravitational acceleration, V_{rel} is the relative velocity between the vessel and the load, and k is the equivalent stiffness of the deck and the lift wire. In the present case, stiffness of the lifting mechanism is not negligible.
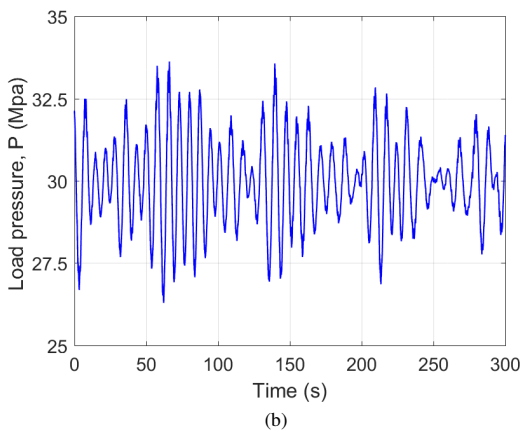
Equation (11) implies the usefulness of AHC in reducing the landing forces during mating. When the maximum relative velocity of the wind turbine assembly is kept below 0.2 m/s, the second term could be rather small. On the other hand, a radial guiding system with soft stiffness may be pre-installed on the spar. Such a system can reduce the landing forces
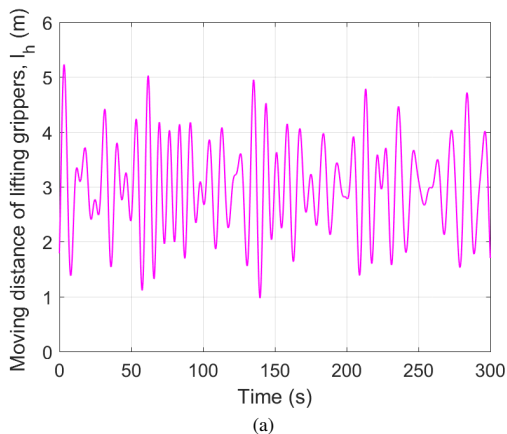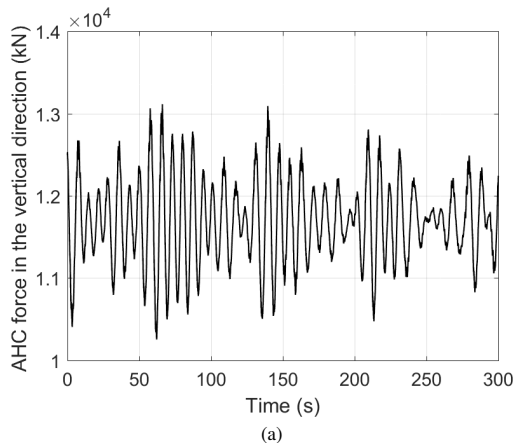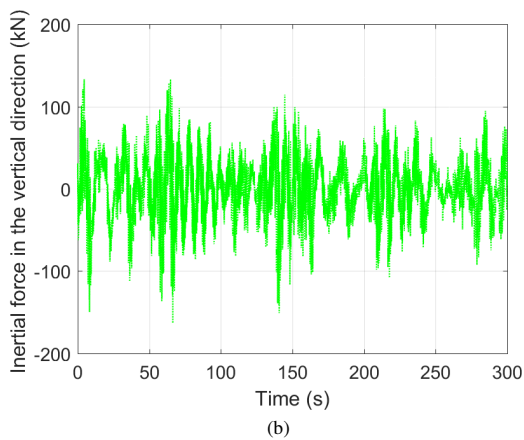
Fig. 11 Representative performance of the active heave compensator, H_S=2.0 m, T_P=10 s, β=0 deg, Seed 1 (a) moving distance of lifting grippers (b) hydraulic load pressure.

Fig. 12 Force components of the suspended tower assembly, H_S=2.0 m, T_P=10 s, β=0 deg, Seed 1 (a) gripper force (b) inertial force.

during the final contact. Because of the unknown contact stiffness, the landing forces are not calculated in this work.

CONCLUSION

This paper presents the modelling and simulation of an active heave compensator for a catamaran wind turbine installation vessel. The active heave compensator consists of a motor, a pump, valves, hydraulic fluid, and a hydraulic cylinder. Time-domain numerical simulations under irregular waves were conducted with an emphasis on the mating stage of the wind turbine installation process. A wind turbine assembly is being gripped by the lifting grippers and transferred onto a floating spar foundation.

The relative heave motion and velocity responses between the tower bottom and the spar top are compared for the cases with and without active heave compensator. It is shown that the active heave compensator can effectively reduce the relative heave velocity and can potentially improve the safety of the mating process.
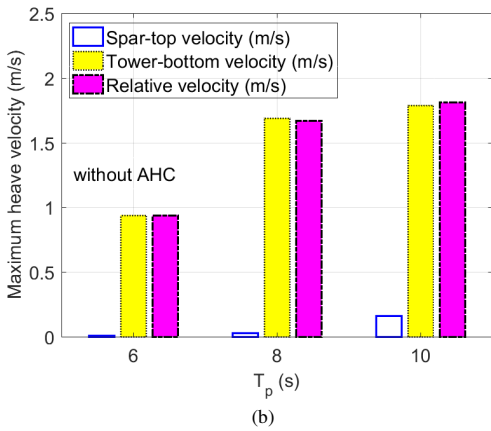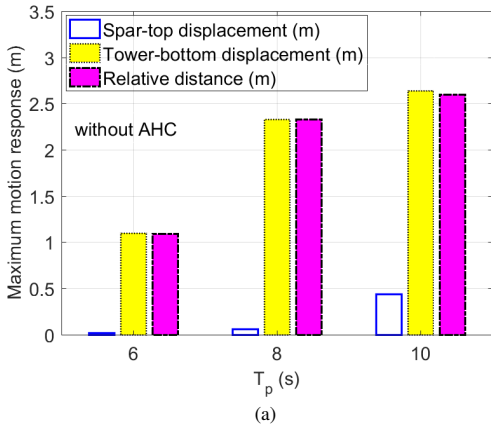
ACKNOWLEDGEMENTS

(a)

(b)

Fig. 13 Statistics of the simulation results without AHC, H_S=2.0 m, β=0 deg (a) maximum heave motion (b) maximum heave velocity.
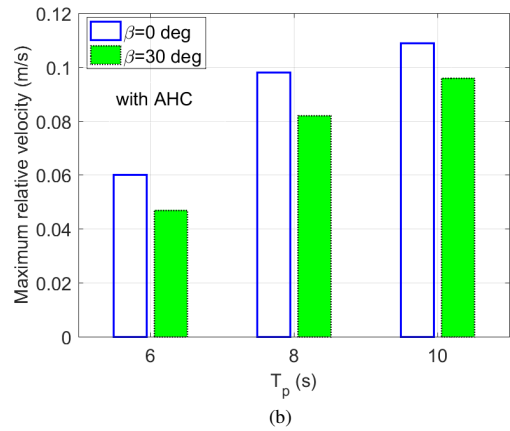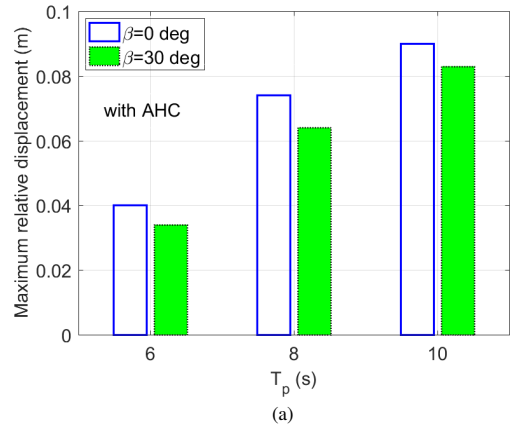

(a)

(b)

Fig. 14 Statistics of the simulation results with AHC, H_S=2.0 m (a) maximum relative heave displacement between the spar top and the tower bottom (b) maximum heave velocity between the spar top and the tower bottom.

REFERENCES

Acero, W G, Gao, Z, and Moan, T (2017). "Numerical study of a novel procedure for installing the tower and rotor assembly of offshore wind turbines based on the inverted pendulum principle ", *Journal of Marine Science and Application*, Vol 16, pp 243–260.

Chung, J S (2010). "Full-scale, coupled ship and pipe motions measured in north pacific ocean: The Hughes Glomar Explorer with a 5,000-m-long heavy-lift pipe deployed ", *International Journal of Offshore and Polar Engineering*, Vol 20, No. 1, pp 1–6.

Det Norske Veritas (2010). "Recommended Practice DNV-RP-C205 Environmental Conditions and Environmental Loads", Oslo, Norway.

Det Norske Veritas (2011). "SESAM user manual HydroD, program version 4.5".

Det Norske Veritas (2014). "Recommended Practice DNV-RP-H103 Modelling and Analysis of Marine Operations", Oslo, Norway.

Graczyk, M, and Sandvik, P C (2012). "Study of landing and lift-off operation for wind turbine components on a ship deck ", *ASME 2012 31ST International Conference on Ocean, Offshore and Arctic Engineering, OMAE2012-84273*, Rio de Janeiro, Brazil.

Hatledal, L I, Zhang, H, Halse K H, and Hilder, H P (2017). "Numerical simulation of novel gripper mechanism between catamaran and turbine foundation for offshore wind turbine installation ", *ASME 2017 36th International Conference on Ocean, Offshore and Arctic Engineering, OMAE2017-62342*, Trondheim, Norway.

Huster, A, Bergstrom, H, Gosior, J, and White, D (2009). "Design and operational performance of a standalone passive heave compensation system for a work class ROV ", *OCEANS 2009, MTS/IEEE Biloxi-Marine Technology for Our Future: Global and Local Challenges*.

Jiang, Z, Gao, Z, Ren, Z, Li, Y, and Duan, L (2018a). "A parametric study on the blade final installation process for monopile wind turbines under rough environmental conditions", *under review in Engineering Structures*.

Jiang, Z, Li, L, Gao, Z, Henning, K H, and Sandvik, P C (2018b). "Dynamic response analysis of a catamaran installation vessel during the positioning of a wind turbine assembly onto a spar foundation", *under review in Marine Structures*.

Jelali, M and Kroll, A (2012). "Hydraulic servo-systems: modelling, identification and control", *Springer Science & Business Media*.

Korde, U A (1998). "Active heave compensation on drill-ships in irregular waves ", *Ocean Engineering*, Vol 25, Issue 7, pp 541–561.

MARINTEK (2016). "SIMO Version 4.8.4 - Theory Manual".

Mintsa, H A, Venugopal, R, Kenne, J P, and Belleau, C (2012). "Feedback linearization-based position control of an electrohydraulic servo system with supply pressure uncertainty ", *IEEE/ASME Transactions on Control Systems Technology*, Vol 20, Issue 4, pp 1092–1099.

Moné, C, Hand, M, Bolinger, M, Rand, J, Heimiller, D, and Ho, J (2017). "2015 Cost of wind energy review", *Technical Report NREL/TP-6A20-66861*, National Renewable Energy Laboratory, CO, USA.

Nam, B W, Hong, S Y, Kim, Y S, and Kim, J W (2013). "Effects of passive and active heave compensators on deepwater lifting operation", *International Journal of Offshore and Polar Engineering*, Vol 23, No. 1, pp 33–37.

Pineda, I, and Tardieu, P (2016). "The European offshore wind industry key trends and statistics 2016 ", *https : //windeurope.org/about − wind/statistics/offshore/european − offshore − wind − industry − key − trends − and − statistics − 2016/*, Accessed: 2017-06-01.

Sarkar, A, and Gudmestad, O T (2013). "Study on a new method for installing a monopile and a fully integrated offshore wind turbine structure", *Marine Structures*, Vol 33, pp 160–187.

Steen, K E (2016). "Hywind Scotland - status and plans", *https : //www.sintef.no/projectweb/deepwind_{2}016/presentations/*, Accessed: 2017-02-01.

Wang, L, Book, W J, and Huggins, J D (2012). "Application of singular perturbation theory to hydraulic pump controlled systems ", *IEEE/ASME Transactions on Mechatronics*, Vol 17, Issue 2, pp 251–259.

Woodacre, J K, Bauer, R J, and Irani, R A (2015). "A review of vertical motion heave compensation systems ", *Ocean Engineering*, Vol 104, pp 140–154.

Previous PhD theses published at the Department of Marine Technology
(earlier: Faculty of Marine Technology)
NORWEGIAN UNIVERSITY OF SCIENCE AND TECHNOLOGY

Report No.	Author	Title
	Kavlie, Dag	Optimization of Plane Elastic Grillages, 1967
	Hansen, Hans R.	Man-Machine Communication and Data-Storage Methods in Ship Structural Design, 1971
	Gisvold, Kaare M.	A Method for non-linear mixed -integer programming and its Application to Design Problems, 1971
	Lund, Sverre	Tanker Frame Optimalization by means of SUMT-Transformation and Behaviour Models, 1971
	Vinje, Tor	On Vibration of Spherical Shells Interacting with Fluid, 1972
	Lorentz, Jan D.	Tank Arrangement for Crude Oil Carriers in Accordance with the new Anti-Pollution Regulations, 1975
	Carlsen, Carl A.	Computer-Aided Design of Tanker Structures, 1975
	Larsen, Carl M.	Static and Dynamic Analysis of Offshore Pipelines during Installation, 1976
UR-79-01	Brigt Hatlestad, MK	The finite element method used in a fatigue evaluation of fixed offshore platforms. (Dr.Ing. Thesis)
UR-79-02	Erik Pettersen, MK	Analysis and design of cellular structures. (Dr.Ing. Thesis)
UR-79-03	Sverre Valsgård, MK	Finite difference and finite element methods applied to nonlinear analysis of plated structures. (Dr.Ing. Thesis)
UR-79-04	Nils T. Nordsve, MK	Finite element collapse analysis of structural members considering imperfections and stresses due to fabrication. (Dr.Ing. Thesis)
UR-79-05	Ivar J. Fylling, MK	Analysis of towline forces in ocean towing systems. (Dr.Ing. Thesis)
UR-80-06	Nils Sandsmark, MM	Analysis of Stationary and Transient Heat Conduction by the Use of the Finite Element Method. (Dr.Ing. Thesis)
UR-80-09	Sverre Haver, MK	Analysis of uncertainties related to the stochastic modeling of ocean waves. (Dr.Ing. Thesis)
UR-81-15	Odland, Jonas	On the Strength of welded Ring stiffened cylindrical Shells primarily subjected to axial Compression
UR-82-17	Engesvik, Knut	Analysis of Uncertainties in the fatigue Capacity of

Welded Joints

UR-82-18	Rye, Henrik	Ocean wave groups
UR-83-30	Eide, Oddvar Inge	On Cumulative Fatigue Damage in Steel Welded Joints
UR-83-33	Mo, Olav	Stochastic Time Domain Analysis of Slender Offshore Structures
UR-83-34	Amdahl, Jørgen	Energy absorption in Ship-platform impacts
UR-84-37	Mørch, Morten	Motions and mooring forces of semi submersibles as determined by full-scale measurements and theoretical analysis
UR-84-38	Soares, C. Guedes	Probabilistic models for load effects in ship structures
UR-84-39	Aarsnes, Jan V.	Current forces on ships
UR-84-40	Czujko, Jerzy	Collapse Analysis of Plates subjected to Biaxial Compression and Lateral Load
UR-85-46	Alf G. Engseth, MK	Finite element collapse analysis of tubular steel offshore structures. (Dr.Ing. Thesis)
UR-86-47	Dengody Sheshappa, MP	A Computer Design Model for Optimizing Fishing Vessel Designs Based on Techno-Economic Analysis. (Dr.Ing. Thesis)
UR-86-48	Vidar Aanesland, MH	A Theoretical and Numerical Study of Ship Wave Resistance. (Dr.Ing. Thesis)
UR-86-49	Heinz-Joachim Wessel, MK	Fracture Mechanics Analysis of Crack Growth in Plate Girders. (Dr.Ing. Thesis)
UR-86-50	Jon Taby, MK	Ultimate and Post-ultimate Strength of Dented Tubular Members. (Dr.Ing. Thesis)
UR-86-51	Walter Lian, MH	A Numerical Study of Two-Dimensional Separated Flow Past Bluff Bodies at Moderate KC-Numbers. (Dr.Ing. Thesis)
UR-86-52	Bjørn Sortland, MH	Force Measurements in Oscillating Flow on Ship Sections and Circular Cylinders in a U-Tube Water Tank. (Dr.Ing. Thesis)
UR-86-53	Kurt Strand, MM	A System Dynamic Approach to One-dimensional Fluid Flow. (Dr.Ing. Thesis)
UR-86-54	Arne Edvin Løken, MH	Three Dimensional Second Order Hydrodynamic Effects on Ocean Structures in Waves. (Dr.Ing. Thesis)
UR-86-55	Sigurd Falch, MH	A Numerical Study of Slamming of Two-Dimensional Bodies. (Dr.Ing. Thesis)
UR-87-56	Arne Braathen, MH	Application of a Vortex Tracking Method to the Prediction of Roll Damping of a Two-Dimension Floating Body. (Dr.Ing. Thesis)

UR-87-57	Bernt Leira, MK	Gaussian Vector Processes for Reliability Analysis involving Wave-Induced Load Effects. (Dr.Ing. Thesis)
UR-87-58	Magnus Småvik, MM	Thermal Load and Process Characteristics in a Two-Stroke Diesel Engine with Thermal Barriers (in Norwegian). (Dr.Ing. Thesis)
MTA-88-59	Bernt Arild Bremdal, MP	An Investigation of Marine Installation Processes – A Knowledge - Based Planning Approach. (Dr.Ing. Thesis)
MTA-88-60	Xu Jun, MK	Non-linear Dynamic Analysis of Space-framed Offshore Structures. (Dr.Ing. Thesis)
MTA-89-61	Gang Miao, MH	Hydrodynamic Forces and Dynamic Responses of Circular Cylinders in Wave Zones. (Dr.Ing. Thesis)
MTA-89-62	Martin Greenhow, MH	Linear and Non-Linear Studies of Waves and Floating Bodies. Part I and Part II. (Dr.Techn. Thesis)
MTA-89-63	Chang Li, MH	Force Coefficients of Spheres and Cubes in Oscillatory Flow with and without Current. (Dr.Ing. Thesis
MTA-89-64	Hu Ying, MP	A Study of Marketing and Design in Development of Marine Transport Systems. (Dr.Ing. Thesis)
MTA-89-65	Arild Jæger, MH	Seakeeping, Dynamic Stability and Performance of a Wedge Shaped Planing Hull. (Dr.Ing. Thesis)
MTA-89-66	Chan Siu Hung, MM	The dynamic characteristics of tilting-pad bearings
MTA-89-67	Kim Wikstrøm, MP	Analysis av projekteringen for ett offshore projekt. (Licenciat-avhandling)
MTA-89-68	Jiao Guoyang, MK	Reliability Analysis of Crack Growth under Random Loading, considering Model Updating. (Dr.Ing. Thesis)
MTA-89-69	Arnt Olufsen, MK	Uncertainty and Reliability Analysis of Fixed Offshore Structures. (Dr.Ing. Thesis)
MTA-89-70	Wu Yu-Lin, MR	System Reliability Analyses of Offshore Structures using improved Truss and Beam Models. (Dr.Ing. Thesis)
MTA-90-71	Jan Roger Hoff, MH	Three-dimensional Green function of a vessel with forward speed in waves. (Dr.Ing. Thesis)
MTA-90-72	Rong Zhao, MH	Slow-Drift Motions of a Moored Two-Dimensional Body in Irregular Waves. (Dr.Ing. Thesis)
MTA-90-73	Atle Minsaas, MP	Economical Risk Analysis. (Dr.Ing. Thesis)
MTA-90-74	Knut-Aril Farnes, MK	Long-term Statistics of Response in Non-linear Marine Structures. (Dr.Ing. Thesis)
MTA-90-75	Torbjørn Sotberg, MK	Application of Reliability Methods for Safety Assessment of Submarine Pipelines. (Dr.Ing.

Thesis)

MTA-90-76	Zeuthen, Steffen, MP	SEAMAID. A computational model of the design process in a constraint-based logic programming environment. An example from the offshore domain. (Dr.Ing. Thesis)
MTA-91-77	Haagensen, Sven, MM	Fuel Dependant Cyclic Variability in a Spark Ignition Engine - An Optical Approach. (Dr.Ing. Thesis)
MTA-91-78	Løland, Geir, MH	Current forces on and flow through fish farms. (Dr.Ing. Thesis)
MTA-91-79	Hoen, Christopher, MK	System Identification of Structures Excited by Stochastic Load Processes. (Dr.Ing. Thesis)
MTA-91-80	Haugen, Stein, MK	Probabilistic Evaluation of Frequency of Collision between Ships and Offshore Platforms. (Dr.Ing. Thesis)
MTA-91-81	Sødahl, Nils, MK	Methods for Design and Analysis of Flexible Risers. (Dr.Ing. Thesis)
MTA-91-82	Ormberg, Harald, MK	Non-linear Response Analysis of Floating Fish Farm Systems. (Dr.Ing. Thesis)
MTA-91-83	Marley, Mark J., MK	Time Variant Reliability under Fatigue Degradation. (Dr.Ing. Thesis)
MTA-91-84	Krokstad, Jørgen R., MH	Second-order Loads in Multidirectional Seas. (Dr.Ing. Thesis)
MTA-91-85	Molteberg, Gunnar A., MM	The Application of System Identification Techniques to Performance Monitoring of Four Stroke Turbocharged Diesel Engines. (Dr.Ing. Thesis)
MTA-92-86	Mørch, Hans Jørgen Bjelke, MH	Aspects of Hydrofoil Design: with Emphasis on Hydrofoil Interaction in Calm Water. (Dr.Ing. Thesis)
MTA-92-87	Chan Siu Hung, MM	Nonlinear Analysis of Rotordynamic Instabilities in Highspeed Turbomachinery. (Dr.Ing. Thesis)
MTA-92-88	Bessason, Bjarni, MK	Assessment of Earthquake Loading and Response of Seismically Isolated Bridges. (Dr.Ing. Thesis)
MTA-92-89	Langli, Geir, MP	Improving Operational Safety through exploitation of Design Knowledge - an investigation of offshore platform safety. (Dr.Ing. Thesis)
MTA-92-90	Sævik, Svein, MK	On Stresses and Fatigue in Flexible Pipes. (Dr.Ing. Thesis)
MTA-92-91	Ask, Tor Ø., MM	Ignition and Flame Growth in Lean Gas-Air Mixtures. An Experimental Study with a Schlieren System. (Dr.Ing. Thesis)
MTA-86-92	Hessen, Gunnar, MK	Fracture Mechanics Analysis of Stiffened Tubular Members. (Dr.Ing. Thesis)

MTA-93-93	Steinebach, Christian, MM	Knowledge Based Systems for Diagnosis of Rotating Machinery. (Dr.Ing. Thesis)
MTA-93-94	Dalane, Jan Inge, MK	System Reliability in Design and Maintenance of Fixed Offshore Structures. (Dr.Ing. Thesis)
MTA-93-95	Steen, Sverre, MH	Cobblestone Effect on SES. (Dr.Ing. Thesis)
MTA-93-96	Karunakaran, Daniel, MK	Nonlinear Dynamic Response and Reliability Analysis of Drag-dominated Offshore Platforms. (Dr.Ing. Thesis)
MTA-93-97	Hagen, Arnulf, MP	The Framework of a Design Process Language. (Dr.Ing. Thesis)
MTA-93-98	Nordrik, Rune, MM	Investigation of Spark Ignition and Autoignition in Methane and Air Using Computational Fluid Dynamics and Chemical Reaction Kinetics. A Numerical Study of Ignition Processes in Internal Combustion Engines. (Dr.Ing. Thesis)
MTA-94-99	Passano, Elizabeth, MK	Efficient Analysis of Nonlinear Slender Marine Structures. (Dr.Ing. Thesis)
MTA-94-100	Kvålsvold, Jan, MH	Hydroelastic Modelling of Wetdeck Slamming on Multihull Vessels. (Dr.Ing. Thesis)
MTA-94-102	Bech, Sidsel M., MK	Experimental and Numerical Determination of Stiffness and Strength of GRP/PVC Sandwich Structures. (Dr.Ing. Thesis)
MTA-95-103	Paulsen, Hallvard, MM	A Study of Transient Jet and Spray using a Schlieren Method and Digital Image Processing. (Dr.Ing. Thesis)
MTA-95-104	Hovde, Geir Olav, MK	Fatigue and Overload Reliability of Offshore Structural Systems, Considering the Effect of Inspection and Repair. (Dr.Ing. Thesis)
MTA-95-105	Wang, Xiaozhi, MK	Reliability Analysis of Production Ships with Emphasis on Load Combination and Ultimate Strength. (Dr.Ing. Thesis)
MTA-95-106	Ulstein, Tore, MH	Nonlinear Effects of a Flexible Stern Seal Bag on Cobblestone Oscillations of an SES. (Dr.Ing. Thesis)
MTA-95-107	Solaas, Frøydis, MH	Analytical and Numerical Studies of Sloshing in Tanks. (Dr.Ing. Thesis)
MTA-95-108	Hellan, Øyvind, MK	Nonlinear Pushover and Cyclic Analyses in Ultimate Limit State Design and Reassessment of Tubular Steel Offshore Structures. (Dr.Ing. Thesis)
MTA-95-109	Hermundstad, Ole A., MK	Theoretical and Experimental Hydroelastic Analysis of High Speed Vessels. (Dr.Ing. Thesis)
MTA-96-110	Bratland, Anne K., MH	Wave-Current Interaction Effects on Large-Volume Bodies in Water of Finite Depth. (Dr.Ing. Thesis)
MTA-96-111	Herfjord, Kjell, MH	A Study of Two-dimensional Separated Flow by a Combination of the Finite Element Method and

Navier-Stokes Equations. (Dr.Ing. Thesis)

MTA-96-112	Æsøy, Vilmar, MM	Hot Surface Assisted Compression Ignition in a Direct Injection Natural Gas Engine. (Dr.Ing. Thesis)
MTA-96-113	Eknes, Monika L., MK	Escalation Scenarios Initiated by Gas Explosions on Offshore Installations. (Dr.Ing. Thesis)
MTA-96-114	Erikstad, Stein O., MP	A Decision Support Model for Preliminary Ship Design. (Dr.Ing. Thesis)
MTA-96-115	Pedersen, Egil, MH	A Nautical Study of Towed Marine Seismic Streamer Cable Configurations. (Dr.Ing. Thesis)
MTA-97-116	Moksnes, Paul O., MM	Modelling Two-Phase Thermo-Fluid Systems Using Bond Graphs. (Dr.Ing. Thesis)
MTA-97-117	Halse, Karl H., MK	On Vortex Shedding and Prediction of Vortex-Induced Vibrations of Circular Cylinders. (Dr.Ing. Thesis)
MTA-97-118	Igland, Ragnar T., MK	Reliability Analysis of Pipelines during Laying, considering Ultimate Strength under Combined Loads. (Dr.Ing. Thesis)
MTA-97-119	Pedersen, Hans-P., MP	Levendefiskteknologi for fiskefartøy. (Dr.Ing. Thesis)
MTA-98-120	Vikestad, Kyrre, MK	Multi-Frequency Response of a Cylinder Subjected to Vortex Shedding and Support Motions. (Dr.Ing. Thesis)
MTA-98-121	Azadi, Mohammad R. E., MK	Analysis of Static and Dynamic Pile-Soil-Jacket Behaviour. (Dr.Ing. Thesis)
MTA-98-122	Ulltang, Terje, MP	A Communication Model for Product Information. (Dr.Ing. Thesis)
MTA-98-123	Torbergsen, Erik, MM	Impeller/Diffuser Interaction Forces in Centrifugal Pumps. (Dr.Ing. Thesis)
MTA-98-124	Hansen, Edmond, MH	A Discrete Element Model to Study Marginal Ice Zone Dynamics and the Behaviour of Vessels Moored in Broken Ice. (Dr.Ing. Thesis)
MTA-98-125	Videiro, Paulo M., MK	Reliability Based Design of Marine Structures. (Dr.Ing. Thesis)
MTA-99-126	Mainçon, Philippe, MK	Fatigue Reliability of Long Welds Application to Titanium Risers. (Dr.Ing. Thesis)
MTA-99-127	Haugen, Elin M., MH	Hydroelastic Analysis of Slamming on Stiffened Plates with Application to Catamaran Wetdecks. (Dr.Ing. Thesis)
MTA-99-128	Langhelle, Nina K., MK	Experimental Validation and Calibration of Nonlinear Finite Element Models for Use in Design of Aluminium Structures Exposed to Fire. (Dr.Ing. Thesis)
MTA-99-	Berstad, Are J., MK	Calculation of Fatigue Damage in Ship Structures.

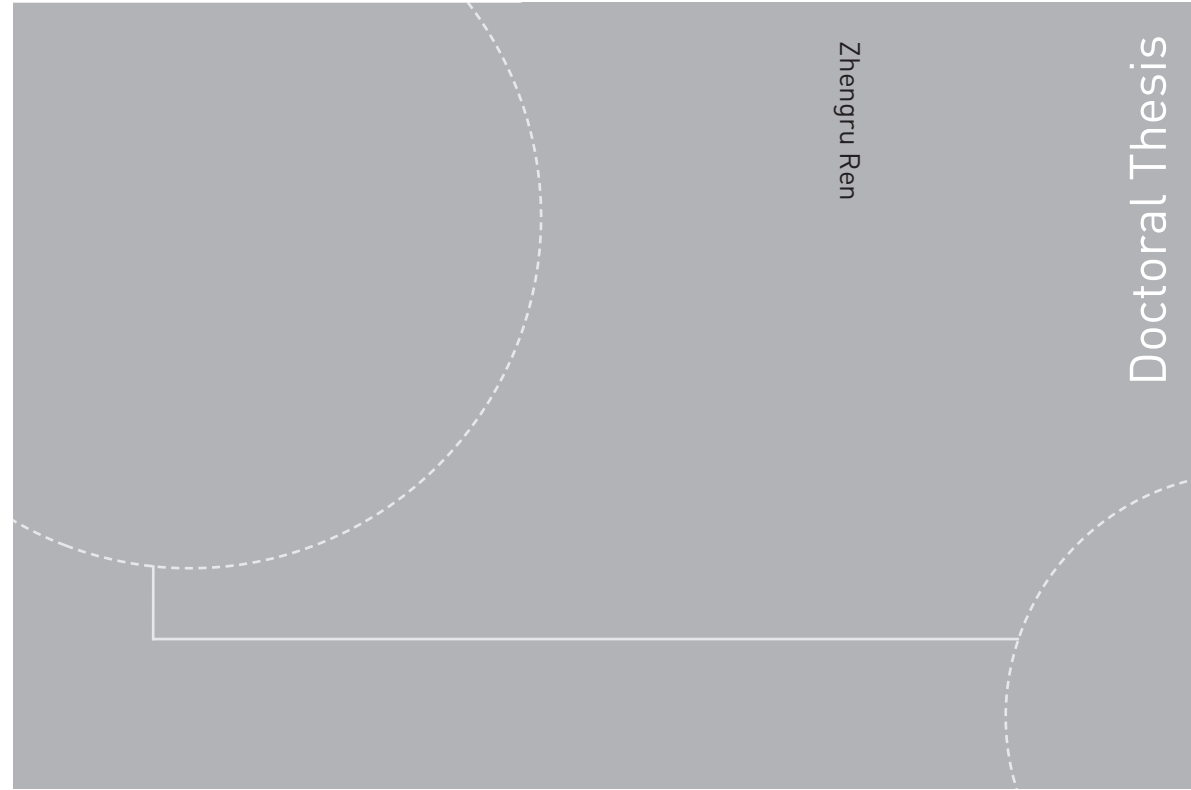|		
129		(Dr.Ing. Thesis)
MTA-99-130	Andersen, Trond M., MM	Short Term Maintenance Planning. (Dr.Ing. Thesis)
MTA-99-131	Tveiten, Bård Wathne, MK	Fatigue Assessment of Welded Aluminium Ship Details. (Dr.Ing. Thesis)
MTA-99-132	Søreide, Fredrik, MP	Applications of underwater technology in deep water archaeology. Principles and practice. (Dr.Ing. Thesis)
MTA-99-133	Tønnessen, Rune, MH	A Finite Element Method Applied to Unsteady Viscous Flow Around 2D Blunt Bodies With Sharp Corners. (Dr.Ing. Thesis)
MTA-99-134	Elvekrok, Dag R., MP	Engineering Integration in Field Development Projects in the Norwegian Oil and Gas Industry. The Supplier Management of Norne. (Dr.Ing. Thesis)
MTA-99-135	Fagerholt, Kjetil, MP	Optimeringsbaserte Metoder for Ruteplanlegging innen skipsfart. (Dr.Ing. Thesis)
MTA-99-136	Bysveen, Marie, MM	Visualization in Two Directions on a Dynamic Combustion Rig for Studies of Fuel Quality. (Dr.Ing. Thesis)
MTA-2000-137	Storteig, Eskild, MM	Dynamic characteristics and leakage performance of liquid annular seals in centrifugal pumps. (Dr.Ing. Thesis)
MTA-2000-138	Sagli, Gro, MK	Model uncertainty and simplified estimates of long term extremes of hull girder loads in ships. (Dr.Ing. Thesis)
MTA-2000-139	Tronstad, Harald, MK	Nonlinear analysis and design of cable net structures like fishing gear based on the finite element method. (Dr.Ing. Thesis)
MTA-2000-140	Kroneberg, André, MP	Innovation in shipping by using scenarios. (Dr.Ing. Thesis)
MTA-2000-141	Haslum, Herbjørn Alf, MH	Simplified methods applied to nonlinear motion of spar platforms. (Dr.Ing. Thesis)
MTA-2001-142	Samdal, Ole Johan, MM	Modelling of Degradation Mechanisms and Stressor Interaction on Static Mechanical Equipment Residual Lifetime. (Dr.Ing. Thesis)
MTA-2001-143	Baarholm, Rolf Jarle, MH	Theoretical and experimental studies of wave impact underneath decks of offshore platforms. (Dr.Ing. Thesis)
MTA-2001-144	Wang, Lihua, MK	Probabilistic Analysis of Nonlinear Wave-induced Loads on Ships. (Dr.Ing. Thesis)
MTA-2001-145	Kristensen, Odd H. Holt, MK	Ultimate Capacity of Aluminium Plates under Multiple Loads, Considering HAZ Properties. (Dr.Ing. Thesis)
MTA-2001-146	Greco, Marilena, MH	A Two-Dimensional Study of Green-Water

Loading. (Dr.Ing. Thesis)

MTA-2001-147	Heggelund, Svein E., MK	Calculation of Global Design Loads and Load Effects in Large High Speed Catamarans. (Dr.Ing. Thesis)
MTA-2001-148	Babalola, Olusegun T., MK	Fatigue Strength of Titanium Risers – Defect Sensitivity. (Dr.Ing. Thesis)
MTA-2001-149	Mohammed, Abuu K., MK	Nonlinear Shell Finite Elements for Ultimate Strength and Collapse Analysis of Ship Structures. (Dr.Ing. Thesis)
MTA-2002-150	Holmedal, Lars E., MH	Wave-current interactions in the vicinity of the sea bed. (Dr.Ing. Thesis)
MTA-2002-151	Rognebakke, Olav F., MH	Sloshing in rectangular tanks and interaction with ship motions. (Dr.Ing. Thesis)
MTA-2002-152	Lader, Pål Furset, MH	Geometry and Kinematics of Breaking Waves. (Dr.Ing. Thesis)
MTA-2002-153	Yang, Qinzheng, MH	Wash and wave resistance of ships in finite water depth. (Dr.Ing. Thesis)
MTA-2002-154	Melhus, Øyvin, MM	Utilization of VOC in Diesel Engines. Ignition and combustion of VOC released by crude oil tankers. (Dr.Ing. Thesis)
MTA-2002-155	Ronæss, Marit, MH	Wave Induced Motions of Two Ships Advancing on Parallel Course. (Dr.Ing. Thesis)
MTA-2002-156	Økland, Ole D., MK	Numerical and experimental investigation of whipping in twin hull vessels exposed to severe wet deck slamming. (Dr.Ing. Thesis)
MTA-2002-157	Ge, Chunhua, MK	Global Hydroelastic Response of Catamarans due to Wet Deck Slamming. (Dr.Ing. Thesis)
MTA-2002-158	Byklum, Eirik, MK	Nonlinear Shell Finite Elements for Ultimate Strength and Collapse Analysis of Ship Structures. (Dr.Ing. Thesis)
IMT-2003-1	Chen, Haibo, MK	Probabilistic Evaluation of FPSO-Tanker Collision in Tandem Offloading Operation. (Dr.Ing. Thesis)
IMT-2003-2	Skaugset, Kjetil Bjørn, MK	On the Suppression of Vortex Induced Vibrations of Circular Cylinders by Radial Water Jets. (Dr.Ing. Thesis)
IMT-2003-3	Chezhian, Muthu	Three-Dimensional Analysis of Slamming. (Dr.Ing. Thesis)
IMT-2003-4	Buhaug, Øyvind	Deposit Formation on Cylinder Liner Surfaces in Medium Speed Engines. (Dr.Ing. Thesis)
IMT-2003-5	Tregde, Vidar	Aspects of Ship Design: Optimization of Aft Hull with Inverse Geometry Design. (Dr.Ing. Thesis)
IMT-	Wist, Hanne Therese	Statistical Properties of Successive Ocean Wave

2003-6		Parameters. (Dr.Ing. Thesis)
IMT-2004-7	Ransau, Samuel	Numerical Methods for Flows with Evolving Interfaces. (Dr.Ing. Thesis)
IMT-2004-8	Soma, Torkel	Blue-Chip or Sub-Standard. A data interrogation approach of identity safety characteristics of shipping organization. (Dr.Ing. Thesis)
IMT-2004-9	Ersdal, Svein	An experimental study of hydrodynamic forces on cylinders and cables in near axial flow. (Dr.Ing. Thesis)
IMT-2005-10	Brodtkorb, Per Andreas	The Probability of Occurrence of Dangerous Wave Situations at Sea. (Dr.Ing. Thesis)
IMT-2005-11	Yttervik, Rune	Ocean current variability in relation to offshore engineering. (Dr.Ing. Thesis)
IMT-2005-12	Fredheim, Arne	Current Forces on Net-Structures. (Dr.Ing. Thesis)
IMT-2005-13	Heggernes, Kjetil	Flow around marine structures. (Dr.Ing. Thesis
IMT-2005-14	Fouques, Sebastien	Lagrangian Modelling of Ocean Surface Waves and Synthetic Aperture Radar Wave Measurements. (Dr.Ing. Thesis)
IMT-2006-15	Holm, Håvard	Numerical calculation of viscous free surface flow around marine structures. (Dr.Ing. Thesis)
IMT-2006-16	Bjørheim, Lars G.	Failure Assessment of Long Through Thickness Fatigue Cracks in Ship Hulls. (Dr.Ing. Thesis)
IMT-2006-17	Hansson, Lisbeth	Safety Management for Prevention of Occupational Accidents. (Dr.Ing. Thesis)
IMT-2006-18	Zhu, Xinying	Application of the CIP Method to Strongly Nonlinear Wave-Body Interaction Problems. (Dr.Ing. Thesis)
IMT-2006-19	Reite, Karl Johan	Modelling and Control of Trawl Systems. (Dr.Ing. Thesis)
IMT-2006-20	Smogeli, Øyvind Notland	Control of Marine Propellers. From Normal to Extreme Conditions. (Dr.Ing. Thesis)
IMT-2007-21	Storhaug, Gaute	Experimental Investigation of Wave Induced Vibrations and Their Effect on the Fatigue Loading of Ships. (Dr.Ing. Thesis)
IMT-2007-22	Sun, Hui	A Boundary Element Method Applied to Strongly Nonlinear Wave-Body Interaction Problems. (PhD Thesis, CeSOS)
IMT-2007-23	Rustad, Anne Marthine	Modelling and Control of Top Tensioned Risers. (PhD Thesis, CeSOS)
IMT-2007-24	Johansen, Vegar	Modelling flexible slender system for real-time simulations and control applications
IMT-2007-25	Wroldsen, Anders Sunde	Modelling and control of tensegrity structures.

(PhD Thesis, CeSOS)

IMT-2007-26	Aronsen, Kristoffer Høye	An experimental investigation of in-line and combined inline and cross flow vortex induced vibrations. (Dr. avhandling, IMT)
IMT-2007-27	Gao, Zhen	Stochastic Response Analysis of Mooring Systems with Emphasis on Frequency-domain Analysis of Fatigue due to Wide-band Response Processes (PhD Thesis, CeSOS)
IMT-2007-28	Thorstensen, Tom Anders	Lifetime Profit Modelling of Ageing Systems Utilizing Information about Technical Condition. (Dr.ing. thesis, IMT)
IMT-2008-29	Refsnes, Jon Erling Gorset	Nonlinear Model-Based Control of Slender Body AUVs (PhD Thesis, IMT)
IMT-2008-30	Berntsen, Per Ivar B.	Structural Reliability Based Position Mooring. (PhD-Thesis, IMT)
IMT-2008-31	Ye, Naiquan	Fatigue Assessment of Aluminium Welded Box-stiffener Joints in Ships (Dr.ing. thesis, IMT)
IMT-2008-32	Radan, Damir	Integrated Control of Marine Electrical Power Systems. (PhD-Thesis, IMT)
IMT-2008-33	Thomassen, Paul	Methods for Dynamic Response Analysis and Fatigue Life Estimation of Floating Fish Cages. (Dr.ing. thesis, IMT)
IMT-2008-34	Pákozdi, Csaba	A Smoothed Particle Hydrodynamics Study of Two-dimensional Nonlinear Sloshing in Rectangular Tanks. (Dr.ing.thesis, IMT/ CeSOS)
IMT-2007-35	Grytøyr, Guttorm	A Higher-Order Boundary Element Method and Applications to Marine Hydrodynamics. (Dr.ing.thesis, IMT)
IMT-2008-36	Drummen, Ingo	Experimental and Numerical Investigation of Nonlinear Wave-Induced Load Effects in Containerships considering Hydroelasticity. (PhD thesis, CeSOS)
IMT-2008-37	Skejic, Renato	Maneuvering and Seakeeping of a Singel Ship and of Two Ships in Interaction. (PhD-Thesis, CeSOS)
IMT-2008-38	Harlem, Alf	An Age-Based Replacement Model for Repairable Systems with Attention to High-Speed Marine Diesel Engines. (PhD-Thesis, IMT)
IMT-2008-39	Alsos, Hagbart S.	Ship Grounding. Analysis of Ductile Fracture, Bottom Damage and Hull Girder Response. (PhD-thesis, IMT)
IMT-2008-40	Graczyk, Mateusz	Experimental Investigation of Sloshing Loading and Load Effects in Membrane LNG Tanks Subjected to Random Excitation. (PhD-thesis, CeSOS)
IMT-2008-41	Taghipour, Reza	Efficient Prediction of Dynamic Response for Flexible amd Multi-body Marine Structures. (PhD-

Zhengru Ren

Advanced Control Algorithms to Support Automated Offshore Wind Turbine Installation

Zhengru Ren

Doctoral Thesis

NTNU
Norwegian University of
Science and Technology
Faculty of Engineering Science and Technology
Department of Marine Technology

 NTNU
Norwegian University of
Science and Technology

 NTNU
Norwegian University of
Science and Technology

 NTNU